Low Energy Electrodynamics Of Quantum Magnets

by

Nicholas J. Laurita

A dissertation submitted to The Johns Hopkins University in conformity with the requirements for the degree of Doctor of Philosophy.

Baltimore, Maryland

March, 2017

Abstract

The manner in which localized spins interact in magnetic insulators is a strongly correlated many-body problem. To date, very few exactly solvable models of such spin interactions exist and those that do are often highly idealized. Therefore, intense experimental effort is devoted to characterizing the ground states of such "quantum magnets." As nature offers a plethora of materials with various symmetries, geometries, and interactions, the resultant ground states vary from conventional, where the spins essentially behave as classical vectors, to truly quantum, where the quantum mechanical nature of spin cannot be ignored. This thesis focuses on the characterization of magnetic ground states by examining their low energy excitations through their interaction with light. A method for extracting the complex magnetic susceptibility in a transmission measurement is developed and utilized to study the magnetic field and temperature dependence of such excitations. A combination of techniques which probe from the microwave to the terahertz range are used to provide a holistic view of the low energy electrodynamics of these materials. By comparing our results to existing models, we uncover unique magnetic ordering due to low symmetry en-

ABSTRACT

vironments, classical grounds states with unconventional interactions, and quantum ground states with long range entanglement and exotic fractionalized excitations.

Primary Reader: N. Peter Armitage

Secondary Reader: Collin Broholm

Acknowledgments

Nearly all of my success today has derived from the countless lessons, discussions, and encouragement that I've received from numerous people throughout my graduate school career. Honestly, a simple "thank you" in the acknowledgement section of my thesis is completely insufficient in expressing my gratitude, but it's a start...

First and foremost I want to thank my adviser N. Peter Armitage. Your dedication and devotion to both the field and your students was obvious from the first day I met you. Your constant optimism and encouragement in the face of broken equipment, difficult experiments, and questionable results has always made it easier to regroup and retry with fervor. Your belief in me and my abilities never wavered, even when I wasn't sure of myself, and has been a tremendous part of my success. Thanks for everything Peter.

I'd also like to thank Professors Tyrel McQueen, Collin Broholm, and Oleg Tchernyshyov for your teachings, guidance, and support throughout my time at JHU. Having additional professors to turn to for discussions has been a vital part of my education these past few years.

ACKNOWLEDGMENTS

I owe a very special debt of gratitude to two former postdocs in our group, Chris Morris and LiDong Pan. In many ways I've tried my best to model myself as a scientist off of the examples that you two set. Chris taught me how to fine tune experiments and meticulously analyze data. LiDong taught me how to think critically about your results and frame them within the greater scientific context. Both of you taught me that working in a lab can be engaging, rewarding, and fun. Thank you both for everything.

I'd like to thank all the members of the Armitage group who I overlapped with, no matter how briefly. Our postdocs: Rolando Valdes Aguilar, Yuval Lubashevsky, Fahad Mahmood, Mintu Mondal, Mohammad Neshat, and Andreas Stier for your guidance throughout my career. And our graduate students: Grace Bosse, Dipanjan Chaudhuri, Bing Cheng, Prashant Chauhan, Wei Liu, Youcheng Wang, Liang Wu, and Xinshu Zhang. All of you have helped make my time at JHU invigorating through our interactions.

Many thanks to my collaborators Kate Arpino, Robert Barkhouser, Sang-wook Cheong, Joachim Deisenhofer, Seyed Koohpayeh, Guy Marcus, Priscila Rosa, Adam Phelan, and Ben Trump, without who this thesis would not be possible.

I owe many thanks to the physics department staff. Particularly the machinists Jeff Poston, Dean Carpenter, and Lyle Schwartz for turning my, often questionable, designs into reality. And also to the administrative staff, particularly Kelly Key and Pam Carmen for all the hard work they've done on my behalf and for our frequent

coffee chats, which I'll sorely miss.

I'd like to extend my deepest gratitude to the ARCS foundation, particularly Mr. and Mrs. Dilon, for their generous financial support throughout my Ph.D.

Lastly, I'd like to thank my family. My wife, Nicole Laurita, who has endured a tremendous amount while I perused my Ph.D. with nothing but the utmost patience, understanding, and respect. I'd also like to say thanks to my dog Pepper who is a constant source of enjoyment. I want to thank my father James Laurita, for teaching me the value of hard work and dedication, and my mother Christine Laurita, for teaching me to be kind, patient, and humble. It's because of your sacrifices that I get to carry the title of "Dr." for the rest of my life. I love you all and am forever grateful.

Dedication

This thesis is dedicated to my parents James and Christine Laurita,

for their unconditional love and unwavering support,

and to my wife Nicole Laurita,

for her limitless understanding, patience, and grace.

"*An expert is someone who knows some of the worst mistakes, which can be made, in a very narrow field.*" - Niels Bohr

Contents

List of Tables

List of Figures

Chapter 1

Introduction

Magnetism has captured the imagination of the human species for millennia, dating back to at least 600 B.C. when the ancient Greeks first discovered that the mineral Lodestone possessed a strange attraction to iron [10]. Since then, research in magnetism has evolved from a primarily philosophical pursuit to a rigorously quantitative science, "attracting" some of the most prominent thinkers in history along the way. What began with William Gilbert's 1600 masterpiece *De Magnete* [11] sparked a 300 year long classical pursuit of the fundamentals of magnetism, culminating in Maxwell's comprehensive theory of electricity and magnetism [12] near the end of the 19th century.

Yet, by the beginning of the 20th century observations which were unexplainable by the classical theories formulated in the previous centuries were beginning to emerge. In 1896, Pieter Zeeman demonstrated that spectral lines of incandescent

gases were split into odd multiplets when subjected to intense magnetic fields [13]. Later that same year, a classical theory put forth by Hendrik Lorentz, Zeeman's own teacher, was able to account for the effect by assuming the electron was attached to the atom by a spring whose resonant frequency was tuned by magnetic field [14]. However, continuing experiments with enhanced resolution quickly revealed experimental results outside the paradigm of Lorentz's theory. It was found that spectral lines sometimes split into even multiplets, such as the famed sodium D-lines, which was unexplainable with Lorentz's classical theory and suggested additional unaccounted for degrees of freedom of the electron.

Meanwhile, quantitative theories of magnetism in solids were in their infancy. In the early 1900's Pierre Curie developed an empirical formula to describe the temperature dependence of the magnetic susceptibility of paramagnets, materials which develop a magnetization in the presence of a magnetic field but do not retain their magnetization once the field is removed [15]. He found that the magnetic susceptibility of a paramagnet had the functional temperature dependence $\chi = C/T$ where C is a material dependent constant. Inspired by Curie's results, Peter Weiss derived a similar result for ferromagnets, materials which possess a finite magnetization even in zero applied field, by assuming that the material possessed an internal "molecular field" which acted to align all the magnetic molecules of the solid [16]. His generalized "Curie-Wiess" law, $\chi = C/(T - \Theta_{CW})$, where Θ_{CW} is a measure of the strength of the internal "Weiss" field, was found to be remarkably successful in describing the

thermodynamics of ferromagnetic materials. However, not only was a physical origin for Weiss's molecular field a mystery, it also appeared to be a direct contradiction of the Bohr-Van Leeuwen theorem [17, 18], which demonstrated that statistical mechanics always predicted the thermal average magnetization of a solid to be zero. Thus providing no classical explanation for any form of magnetism in solids.

Such controversies would be only be remedied in the follow decades with the rapid advent of quantum theory. In 1922, the famous Stern-Gerlach experiment definitively demonstrated that the angular momentum of an atom was quantized [19]. In 1925 Goudsmit and Uhlenbeck, who at the time were students of Ehrenfest, postulated the existence of an additional intrinsic electron angular momentum of $\hbar/2$ [20], thereby discovering the electron's spin. That same year Wolfgang Pauli derived his famous exclusion principle for electrons [21] and soon after the spin matricies that would also bear his name [22].

With a solid quantum foundation in place, Dirac [23] and Heisenberg [24] independently, but almost simultaneously, derived the form of the most prominent interaction between spins, the exchange interaction, which for the first time provided an account of the principles of ferromagnetism. As the interaction is derived from the exclusion principle, it is a purely quantum mechanical effect, thereby demonstrating why no classical explanation could be offered. Unbeknownst to them at the time, the discovery of the exchange Hamiltonian would launch an entire field devoted to studying such quantum interactions within solids, which today is referred to as "quantum

magnetism."

Today, quantum magnetism has blossomed into an eclectic field encompassing many subsets and applications. This thesis focuses on one such subset, magnetic insulators, in which the spins are localized to their ions at specific sites within the lattice. As we will see in this chapter, applying the exchange Hamiltonian in an insulating magnet constitutes a strongly correlated many-body problem which is rarely, except generally in the simplest possible cases, exactly solvable. Thus, there continues to be intense experimental effort devoted to studying how the underlying spin interactions within the lattice of a given material result in a particular magnetic ground state. With a plethora of quantum magnets, all of which possess various lattice geometries, symmetries, interactions, and magnetic elements, and continuing advances in solid state chemistry and materials characterization techniques, the field of quantum magnetism is undoubtedly in its prime.

The technological needs of the 21st century will revolve around energy-dense, and therefore strongly correlated, materials as well as faster more efficient computation methods. Quantum magnetism is on the forefront of addressing such needs. Many strongly correlated materials possess magnetic phases in proximity, and therefore possibly related, to additional phases with technological applications. For instance, the parent compound of high-T_c superconductors are antiferromagnetic Mott insulators which only become superconducting when charge doped. The role that magnetism may play in the superconducting properties of these materials is currently a topic of

investigation. Meanwhile, many recently proposed quantum computation methods have centered around exploiting the unusual statistics of fractional quasiparticles in certain classes of unusual quantum magnets. If such proposals are to be a reality then further research into quantum magnetism must persist.

This chapter is meant as a very brief introduction to the field of quantum magnetism, a subject so broad and diverse that only the very basics can be touched upon here. We begin by deriving the most conventional form of quantum interactions between spins, the Heisenberg Hamiltonian. Next we will discuss applying the Heisenberg Hamiltonian by examining a fundamental model of magnetism, the Ising model, to gain an understanding of the complexity of such systems and introduce topics which will arise in the context of this thesis. We then discuss excitations of the magnetic lattice and demonstrate how the ground state properties manifest in the excitation spectrum. Finally, we will move beyond the Heisenberg Hamiltonian and demonstrate how the underlying interactions between spins depend heavily on the symmetry and environment of the space in which they are embedded. We will discover that the resultant magnetic ground states can range from classical to, under special circumstances, truly quantum.

1.1 Magnetic Interactions In Solids

1.1.1 Magnetic Dipole Interactions

When a ferromagnet is cooled below some characteristic temperature T_c, known as the Curie temperature, the spins of all the electrons of the material spontaneously align such that long range magnetic order and a magnetization onset. This suggests that the spins of the ferromagnet are strongly correlated and that the long range alignment of all spins is energetically favorable. But what is the form of this interaction that drives the transition to a long range ordered phase?

From a classical physics standpoint, it is reasonable to assume that each electron behaves as a semiclassical magnetic dipole such that they interact via the conventional dipole-dipole interaction of the form:

$$U_{\text{Dip}} = \frac{1}{r^3}[m_1 \cdot m_2 - 3(m_1 \cdot \hat{r})(m_2 \cdot \hat{r})] \tag{1.1}$$

where m_1 and m_2 are the magnetic dipoles of the two electrons and r is the distance between them. We can get an approximate feel for the scale of these interactions by recalling that the dipole moment of an electron has a typical magnitude of order the Bohr magneton $\mu_B = e\hbar/m_e c$. Inserting this into Eq. 1.1 tells us that the energy

scale of dipole interactions is of order:

$$U_{\text{Dip}} \approx \frac{(\mu_B)^2}{r^3} \approx 0.1 \text{ meV or } 1 \text{ T} \tag{1.2}$$

where a typical atomic spacing of order 1 Å has been assumed [25].

This should be compared however to the actual energy scale of interactions in a ferromagnet which can be approximated by $U_{\text{Ex}} \approx k_B \text{T}_c$. With a typical Curie temperature for conventional ferromagnets (e.g. Fe, Co, Ni, Gd) ranging from $\text{T}_c \approx 10^2$ K - 10^3 K [1], we find that the interaction energy is of order:

$$U_{\text{Ex}} \approx \mu_B \text{T}_c \approx 10 - 100 \text{ meV or } 100 - 2000 \text{ T} \tag{1.3}$$

Therefore we see that dipole interactions are orders of magnitude too weak to account for the ferromagnetism in solids.

1.1.2 Quantum Magnetism: The Heisenberg Hamiltonian

So then what is the form of the interactions between spins in solids? Our goal is to derive this interaction by beginning with the simplest possible case, that of two interacting electrons. Here we present a condensed version of the Heitler-London model [26] as presented in Ref. [1]. We begin by assuming that two electrons in

a solid, both of which possess spin and orbital angular momentum, are interacting through the Hamiltonian:

$$H = \sum_{i=1}^{2} \frac{p_i^2}{2m} + V(r_1, r_2) \tag{1.4}$$

For now we disregard interactions between the electrons and the lattice although they in principle could be included in Eq. 1.4.

One can see that the Hamiltonian of Eq. 1.4 is independent of the electron's spin and therefore its eigenstates can be written as a product of an orbital state, $|\phi(r)\rangle$, and a spin state, $|S, m_s\rangle$. However, not all combinations of $|\phi(r)\rangle$ and $|S, m_s\rangle$ are permissible. As the two electrons are identical fermions they must obey the Pauli exclusion principle, which mandates the antisymmetry of the total wavefunction under particle exchange. Therefore the allowed eigenstates of the two electron system are:

$$|\Psi\rangle = |\phi(r)\rangle^{\pm} |S, m_s\rangle^{\mp} \tag{1.5}$$

where the superscripts denote the sign under particle exchange.

The addition of the spin angular momenta of two electrons is a well known result. The spins can either couple to form an antisymmetric singlet state:

$$|0, 0\rangle = \frac{1}{\sqrt{2}}(|\uparrow\downarrow\rangle - |\downarrow\uparrow\rangle) \tag{1.6}$$

or one of three symmetric triplet states:

$$\begin{aligned} |1;1\rangle &= |\uparrow\uparrow\rangle \\ |1;0\rangle &= \frac{1}{\sqrt{2}}(|\uparrow\downarrow\rangle + |\downarrow\uparrow\rangle) \\ |1;-1\rangle &= (|\downarrow\downarrow\rangle \end{aligned} \tag{1.7}$$

Which spins state is preferred is entirely chosen by the symmetry of the orbital state due to the Pauli exclusion principle. Therefore, the allowed eigenstates are:

$$\begin{aligned} |\Psi_1\rangle &= |\phi(r)\rangle^+ |0,0\rangle \\ |\Psi_2\rangle &= |\phi(r)\rangle^- |1,m_s\rangle \end{aligned} \tag{1.8}$$

with energies:

$$\begin{aligned} H|\phi(r)\rangle^+ &= E_s |\phi(r)\rangle^+ \\ H|\phi(r)\rangle^- &= E_t |\phi(r)\rangle^- \end{aligned} \tag{1.9}$$

where the subscripts "s" and "t" refer to the singlet and triplet states respectively.

Whether the parallel or antiparallel alignment of spins is preferred depends on whether E_s or E_t is the lowest energy. Again, the choice is entirely made by the spin independent Hamiltonian Eq. 1.4. However, it would be ideal if we could derive an equally valid *spin dependent* Hamiltonian which produced the same spectrum as the Hamiltonian of Eq. 1.4. To derive such a Hamiltonian, note that for spin 1/2

electrons:

$$S^2 \left|S, m_s\right\rangle = \hbar^2 S(S+1) \left|S, m_s\right\rangle = \hbar^2 \frac{3}{4} \left|S, m_s\right\rangle \tag{1.10}$$

and therefore in a similar manner the total spin of the two electron states can be written:

$$S^2 = (S_1 + S_2)^2 = S(S+1)\hbar^2 = S_1^2 + S_2^2 + 2S_1 \cdot S_2 = \frac{3\hbar^2}{2} + 2(S_1 \cdot S_2) \tag{1.11}$$

Upon rearranging we find that:

$$\frac{1}{\hbar^2}(S_1 \cdot S_2) = \frac{1}{2}S(S+1) - \frac{3}{4} \tag{1.12}$$

Therefore, the Hamiltonian:

$$H_{\text{ex}} = \frac{1}{4}(E_+ + 3E_-) - (E_+ - E_-)\frac{1}{\hbar^2}S_1 \cdot S_2 = J_0 + J_{12}S_1 \cdot S_2 \tag{1.13}$$

results in the exact same energy eigenvalues as the spin independent Hamiltonian in Eq. 1.4:

$$\begin{aligned} H_{\text{ex}} \left|\phi(r)\right\rangle \left|0,0\right\rangle &= E_s \left|\phi(r)\right\rangle \left|0,0\right\rangle \\ H_{\text{ex}} \left|\phi(r)\right\rangle \left|1,m_s\right\rangle &= E_t \left|\phi(r)\right\rangle \left|1,m_s\right\rangle \end{aligned} \tag{1.14}$$

and is therefore equivalent. With a simple redefining of the zero energy we arrive at

the spin dependent exchange Hamiltonian:

$$H_{\text{ex}} = J_{12} S_1 \cdot S_2 \tag{1.15}$$

where $J_{12} = (1/\hbar^2)(E_+ - E_-)$ is known as the exchange constant.

The spin interaction of Eq. 1.15, which was first independently derived in 1926 by both Dirac [23] and Heisenberg [24], is known today as the Heisenberg Hamiltonian and constitutes the most prominent form of spin interactions in solids. It should be noted that we arrived at the Heisenberg Hamiltonian via the Pauli exclusion principle, which acts to minimize Coulomb repulsion by separating parallel spins (although perhaps at the cost of kinetic energy). Therefore, the interaction in Eq. 1.15 is a distinctly quantum effect with the spins S_1 and S_2 in the Heisenberg Hamiltonian being quantum mechanical operators, not classical vectors. One can see by Eq. 1.15 that the strength of this interaction is parameterized by the exchange constant J_{12}, the sign of which determines whether the singlet, i.e. antiferromagnetic, or triplet, i.e. ferromagnetic, alignment is of lower energy and therefore preferred. Today, the field devoted to studying such interactions in solids is known as "quantum magnetism."

1.1.3 Generalization To Solids

The calculation presented in the previous section demonstrated the coupling between two spins is captured by Eq. 1.15, the Heisenberg Hamiltonian. However, it

is not at all clear how, or even if, such a Hamiltonian should be generalized from the simple system of two interacting electrons to a complex solid with N interacting electrons. Proving the validity of the application of the Heisenberg Hamiltonian to a magnetic solid is a highly non-trivial and complex matter. An in depth discussion on the topic can be found here [27].

However, it should be noted that in the limit of large spatial separations, such that the wavefunction overlap between electrons is very small, the exchange constant between two spins S_i and S_j can be mathematically expressed as:

$$J_{ij} = \int dr_i dr_j [\phi_i(r_i)\phi_j(r_j)] H_{\text{int}} [\phi_j(r_i)\phi_i(r_j)] \tag{1.16}$$

where H_{int} is the interacting Hamiltonian of the two electrons with themselves and the lattice. As the orbital functions $\phi_i(r_i)$ are highly localized about their ions, the exchange constant J_{ij} falls off rapidly with distance. For this reason, it is generally sufficient to only consider interactions between nearest neighboring pairs of spins in which case we arrive at the two interacting electron scenario described above.

In magnetic insulators, which will be the topic of this thesis, the wavefunction overlap between magnetic electrons is zero and no direct exchange exists between magnetic ions. Instead, exchange is often mediated by neighboring anions, for instance by the p orbitals of intermediary oxygen ions, in a mechanism known as superexchange [1]. Just as above, the coupling from superexchange interactions can be ferromagnetic or

antiferromagnetic which can be determined by the empirical Goodenough-Kanamori rules [28, 29, 30]. Amazingly, although this mechanism of exchange is different than the direct exchange described above, the Heisenberg Hamiltonian summed over next neighboring pairs still applies. Thus, the Heisenberg Hamiltonian:

$$H = \sum_{<ij>} J_{ij} S_i \cdot S_j \tag{1.17}$$

is the starting point for many investigations of magnetic insulators.

1.2 Models Of Interacting Spins

While the complexity of performing the sum in Eq. 1.17 is reduced when only interactions between neighboring pairs of spins are considered, with $\sim 10^{23}$ magnetic electrons in a solid, the sum still contains an enormous number of terms. It is clear that the Heisenberg Hamiltonian describes a many-body system of strongly correlated electrons. Frankly, it is truly amazing that Eq. 1.15 ever possesses an exact solution. However, exact results can be obtained [31], although often in highly idealized situations such as in reduced dimensions, on simple lattices, or with only uniform exchange constants. Still, while materials which approximate these idealized models are generally rare, the models themselves provide insight into more physical systems. For instance, universality guarantees that the critical exponents of phase transitions of distinct systems are identical if the Hamiltonians of the systems possess the same

dimensionality and symmetry. Therefore, while we may not be able to exactly solve the Heisenberg Hamiltonian for a given system, we may already know the critical exponents of its phase transition if it can be compared to an already solved model with identical symmetry. In this fashion, these simple models provide insight to the physics of actual systems.

This section is meant as a brief introduction in applying the Heisenberg Hamiltonian. The goal is to gain a feel for the complexity of the calculations involved as well as to introduce certain themes which will arise in the context of this thesis, such as the effect of applied magnetic fields, development of spontaneous magnetization, and critical points. We begin by solving the Heisenberg Hamiltonian on a one dimensional chain in which only the z components of the spins interact, an exactly solvable model known as the Ising model. We then discuss generalizing the model to two and three dimensions.

1.2.1 The 1D Ising model

The Ising model was developed by Wilhelm Lenz in 1920 [32] and given to his then graduate student Ernst Ising as a thesis project. The goal of the model was to identify a transition temperature at which a 1-dimensional ferromagnet spontaneously orders. Ising solved the model in 1-dimension in his 1924 thesis [33] but failed to find a spontaneous phase transition at finite temperature. Still, the Ising model today is widely regarded as the most important exactly solvable model of magnetism. Before

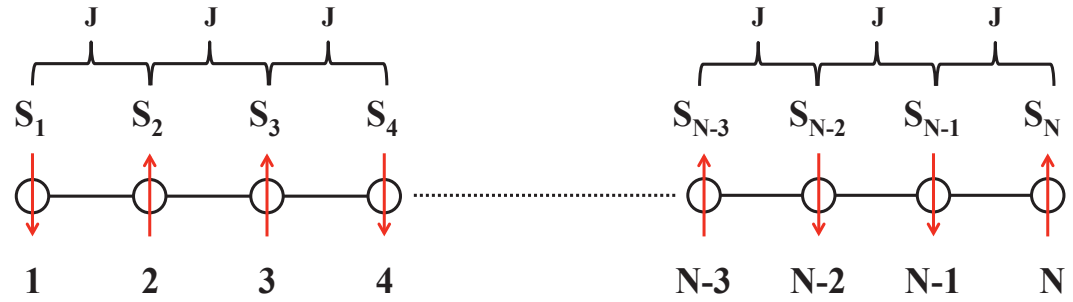

Figure 1.1: Schematic of the 1-dimensional Ising model in which each spin S_i is placed on equally spaced lattice sites N = 1, 2, ..., N and coupled to only next nearest neighbors through identical ferromagnetic exchange of strength J. Each spin is constrained to lie along the z direction, such that the only two possible states are "up" and "down."

proceeding, it should be noted that the 1-dimensional $S = 1/2$ antiferromagnet is an additional exactly solvable model whose solution was provided by Bethe in 1931 [34]. This model is interesting in its own right, with substantially different properties compared to the ferromagnetic Ising case solved below. However, for the sake of brevity this model will not be discussed.

Fig. 1.1 displays a diagram of the 1-dimensional Ising model. The model consists a one dimensional array of equally spaced spins S_i which sit at sites labeled from N = 1, 2, ..., N. Each spin is coupled to only its nearest neighbors by a ferromagnetic exchange constant $J = (0, 0, J_z)$ such that each spin is in one of two states, either "up" ($S_z = +1$) or "down" ($S_z = -1$). We additionally assume periodic boundary conditions such that $S_{N+1} \equiv S_1$. The Heisenberg Hamiltonian is then:

$$H = -J \sum_{i=1}^{N} S_i^z S_{i+1}^z - \mu_B B \sum_{i=1}^{N} S_i^z \tag{1.18}$$

where the second term accounts for Zeeman coupling to a magnetic field B applied in the z direction. Later we will examine both the zero field and finite field properties of the system.

Here we follow the Onsager transfer matrix method solution [35]. We define the transfer function $f_{i,i+1}$ as:

$$f_{i,i+1} = \exp\left(jS_i^z S_{i+1}^z + \frac{1}{2}b(S_i^z + S_{i+1}^z)\right) \tag{1.19}$$

where $j = J/k_BT$ and $b = \mu_B B/k_BT$. The transfer function is convenient as the partition function will contain terms such as:

$$\exp\left(-\beta H\right) = f_{1,2}f_{2,3}...f_{N,1} \tag{1.20}$$

where $\beta = 1/k_BT$ and the periodic boundary conditions have been utilized.

We can represent the two states of each individual spin, either up or down, by the column vectors:

$$|S_i^z = +1\rangle = \begin{bmatrix} 1 \\ \\ 0 \end{bmatrix} \quad ; \quad |S_i^z = -1\rangle = \begin{bmatrix} 0 \\ \\ 1 \end{bmatrix} \tag{1.21}$$

Our goal is then to define a transfer matrix such that:

$$\langle S_i^z | \hat{T} | S_{i+1}^z \rangle = f_{i,i+1} \tag{1.22}$$

The transfer functions, $f_{i,i+1}$, suggest that the transfer matrix must have the form:

$$\hat{T} = \begin{bmatrix} e^{j+b} & e^{-j} \\ e^{-j} & e^{j-b} \end{bmatrix} \tag{1.23}$$

which possesses eigenvalues of:

$$E_{\pm} = e^{j}\cosh(b) \pm e^{j}\sqrt{\cosh^2(b) - 2e^{-2j}\sinh(2j)} \tag{1.24}$$

With the transfer matrix determined, we can now explicitly calculate the partition function as:

$$Z_N(T,B) = Tr(\exp(-\beta H) = Tr(\hat{T}^N) = E_+^N + E_-^N \tag{1.25}$$

As $E_+ > E_-$, in the thermodynamic limit ($N \to \infty$) the partition function will be dominated by E_+^N. Therefore, we finally arrive at the partition function for the 1-dimensional Ising model:

$$Z_N(T,B) = E_+^N = \left[e^{j}\cosh(b) + e^{j}\sqrt{\cosh^2(b) - 2e^{-2j}\sinh(2j)}\right]^N \tag{1.26}$$

With the partition function in hand, we are free to calculate any thermodynamic quantity we please. Of particular importance are the magnetization per spin of the

system:

$$m(T.B) = -\frac{1}{N}\frac{\partial}{\partial B} ln(Z_N(T,B)) = \mu_B \frac{\sinh(\beta\mu_B B)}{\sqrt{\cosh^2(\beta\mu_B B) - 2\exp(2\beta J)\sinh(2\beta J)}} \tag{1.27}$$

and the zero field susceptibility:

$$\chi_M = \mu_0 (\frac{\partial m}{\partial B})_{B\to 0} = \beta\mu_B^2 \mu_0 e^{(2\beta J)} \tag{1.28}$$

Fig. 1.2 displays plots of the (a) magnetization per spin and (b) inverse susceptibility, given by Eq.'s 1.27 and 1.28 respectively, of the 1-dimensional Ising model. These plots demonstrate the counteracting effects of temperature and applied magnetic field. In zero field, thermal fluctuations overwhelm magnetic correlations such that no spontaneous transition to a long range ordered state occurs. The only critical point of the system is at zero temperature. In contrast, applied magnetic fields work against thermal fluctuations such that the system may develop a finite magnetization at a nonzero temperature. This magnetization saturates at large enough fields to the expected ± 1 μ_B per spin. A similar effect is observed in the inverse susceptibility by increasing the exchange constant. The dashed lines and colored regions represent the temperature range in which the inverse susceptibility is linear, as expected from Curie's law for paramagnetism. Increasing the exchange constant, which can be thought of as increasing the effective internal magnetic field, results in a deviation from Curie's law at higher temperatures.

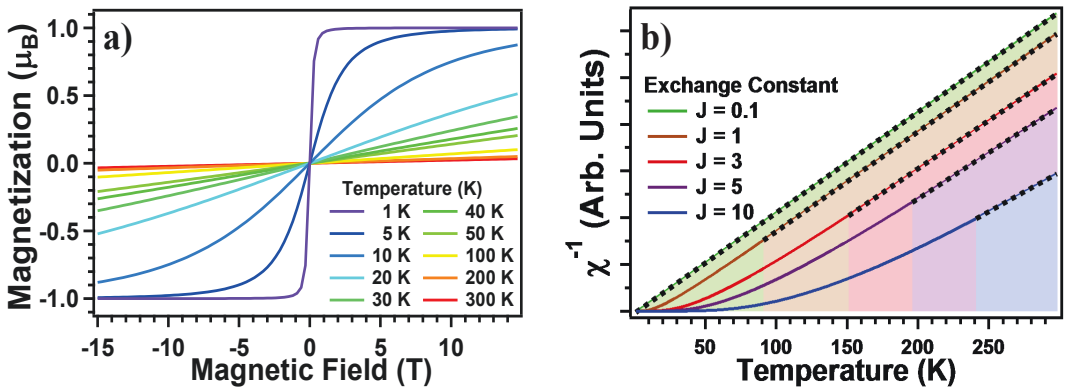

Figure 1.2: (a) Magnetization per spin and (b) inverse magnetic susceptibility of the 1-dimensional Ising model as a function of temperature, magnetic field, and exchange constant J. Dashed lines in and colored regions in (b) are the approximate temperature ranges that the inverse susceptibility obeys Curie's law, as expected for a paramagnet.

1.2.2 The 2D Ising Model

Models in two dimensions are substantially more complex than those in one dimension and, not surprisingly, exact results are therefore harder to achieve. However, the Ising model can be generalized to 2-dimensions, which it turns out is also an exactly solvable model, although only in zero applied magnetic field. Unlike the 1-dimensional model, the 2-dimensional model possesses a spontaneous phase transition at finite temperatures and is heralded today as perhaps the simplest exactly solvable model that demonstrates such a transition. The presence of a critical temperature in the model was first demonstrated in 1941 by Kramers and Wannier who were able to solve for the critical temperature by comparing expressions derived in the low and high temperature limits of the model [36]. The full derivation of the free energy of

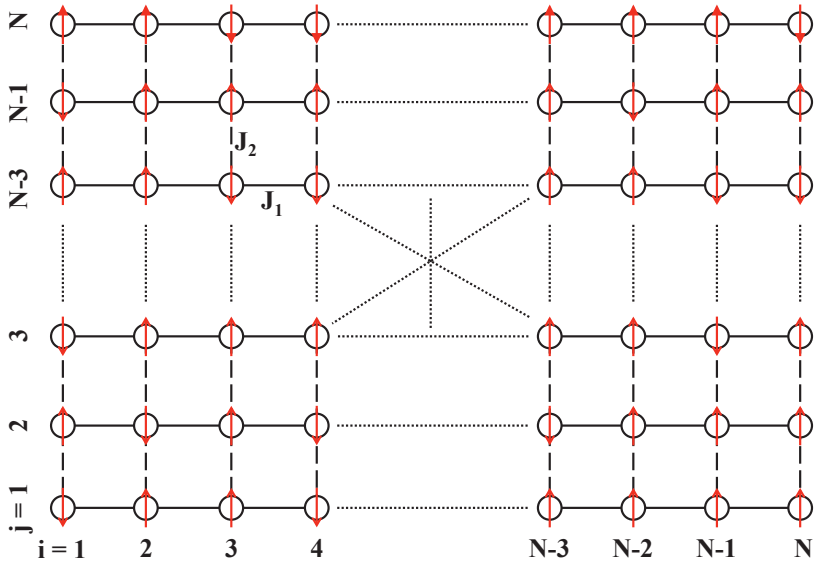

Figure 1.3: Schematic representation of the Ising model on the 2-dimensional square lattice. Each pair of spins separated horizontally are coupled by exchange constant J_1 while vertical spins are coupled by exchange J_2.

the 2-dimensional Ising model was provided in 1944 by Lars Onsager [35] whose proof was based on the transfer matrix method used in the 1-dimensional case above. The proof is far too rigorous to provide here, but we briefly define the model and quote a few of its more relevant results.

Fig. 1.3 displays the 2-dimensional Ising model on the square lattice. Like the 1-dimensional model, each spin only interacts with its nearest neighbors. However, in 2-dimensions there are now 4 nearest neighbors per spin. We generalize by allowing different exchange constants in the x and y directions, labeled J_1 and J_2 respectively in Fig. 1.3, but assume both are ferromagnetic. We also again assume periodic boundary conditions in both directions. The Heisenberg Hamiltonian can then be

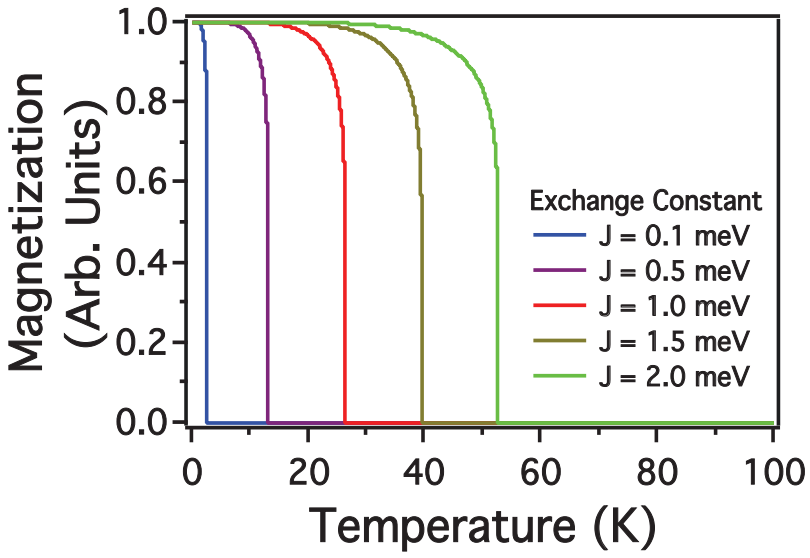

Figure 1.4: Normalized magnetization as a function of temperature of the 2-dimensional Ising model for several values of the exchange constant J. A clear phase transition to an ordered state can be seen at $T_c = 2J \ / \ [k_B \ ln(1 + \sqrt{(2)})]$.

expressed as:

$$H = -J_1 \sum_{<i,j>} S_i \cdot S_j - J_2 \sum_{<i,j>} S_i \cdot S_j \tag{1.29}$$

The additional complexity when compared to the 1-dimensional case is now obvious. In 1-dimension, each spin interacts with its two nearest neighbors such that the total number of interactions, and therefore terms in the sum of the Heisenberg Hamiltonian, is of order N. In 2-dimensions we now have an $N \times N$ array of spins which results in a total number of interactions of order N^2.

As mentioned above, a remarkable result of the model is the presence of a spontaneous phase transition to a long range ordered state at finite temperature. Within the context of the model it has been rigorously shown that the phase transition occurs

at the critical temperature T_c given by:

$$\frac{J}{k_B T_c} = \frac{1}{2} ln(1 + \sqrt{2}) = 0.44069 \tag{1.30}$$

Below this critical temperature, a temperature dependent magnetization onsets which can be expressed in normalized form as:

$$M(T) = (1 - \sinh^{-4}(\frac{2J}{k_B T}))^{1/8} \quad \text{for} \quad T \leq T_c \tag{1.31}$$

where isotropic exchange constants, $J_1 = J_2$, have been assumed. Fig. 1.4 displays the temperature dependent magnetization of the 2-dimensional Ising model plotted for a few values of the exchange constant J. Obvious critical points can be observed at which point thermodynamic quantities possess power law singularities. One can see from the expression for the magnetization given in Eq. 1.31 that the critical exponent of the magnetization $\beta = 1/8$, while other critical exponents of the model have also been calculated [1]. The ability to exactly calculate the critical exponents of the model is a major advantage as these can be generalized to systems which belong to the same universality class.

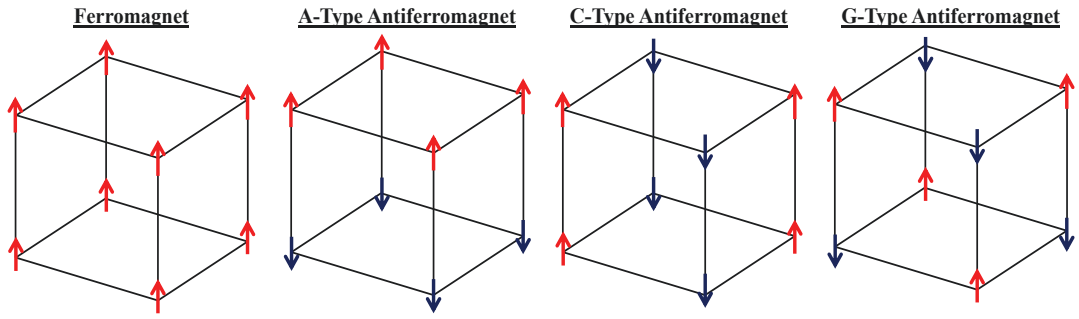

Figure 1.5: Conventional Ising-like ground states on the cubic lattice. Each arrow represents the z component of the spin with red arrows being $S_z = 1$ and blue arrows being S_z = -1. Aside from the ferromagnetic case, there are also antiferromagnetic ground states which possess opposing alignments of spins in 1, 2, or 3 directions of cube. Many other antiferromagnetic ground states exist which are not shown here.

1.2.3 3D Ising Ground States

The Ising model in 3-dimensions is not exactly solvable, although the presence of a phase transition has been proven through quasi-exact extrapolation methods [1]. In the simplest case, the lattice of the 3-dimensional model is cubic with a single spin at each corner. Much like before we sum over all neighboring pairs of spins, which in 3-dimensions results in of order N^3 interactions. The Heisenberg Hamiltonian can then be written as:

$$H = \pm J_1 \sum_{<i,j>} S_i \cdot S_j \pm J_2 \sum_{<j,k>} S_j \cdot S_k \pm J_3 \sum_{<k,i>} S_k \cdot S_i \tag{1.32}$$

where for the sake of generality we have allowed the exchange constants to be of different magnitude *and sign* along the three principle directions of the lattice. Fig. 1.5 displays a few of the more conventional Ising-like ground states typically found

on the cubic lattice. Aside from the obvious ferromagnetic ground state, there are also antiferromagnetic ground states which can possess antiferromagntic interactions between spins along 1, 2, and 3 dimensions of the cube. Many other ground state arrangements for this lattice exist.

1.3 Excitations Of The Magnetic Lattice

In the previous section we introduced the complexity of solving the Heisenberg Hamiltonian. We found that no exact solution for the 3-dimensional Ising model exist, even though the model is highly idealized. For real materials, which are often much more complex than the Ising model treated above, approximate solutions to the Heisenberg Hamiltonian can be theoretically attained either through various approximations, such as the mean field approximation, or numerical methods, such as Monte-Carlo simulations. Therefore, magnetic ground states are ultimately determined experimentally. As this thesis pertains to optical spectroscopy of magnetic materials, this section demonstrates how the excitations and dynamics of the magnetic lattice can be used to distinguish ground states. We begin with a calculation of the low energy excitations, i.e. spin-waves, of two simple, but important, magnetic ground states; the isotropic ferromagnet and two sublattice antiferromagnet. At the end of the chapter we discuss how such excitations can be studied through their interaction with light in an optical spectroscopy experiment.

1.3.1 The Isotropic Ferromagnet

Consider a 3-dimensional system with all spins coupled ferromagnetically to their nearest neighbors by the exchange constant J. We begin with the Heisenberg Hamiltonian:

$$H = -\sum_{i,j} J_{ij} S_i \cdot S_j \tag{1.33}$$

Recall that the spins in Eq. 1.17 are quantum mechanical operators and therefore follow the algebra and commutation relations appropriate for angular momentum in quantum mechanics. We can then rewrite the scalar spin product in Eq. 1.17 in terms of the raising and lowering operators, $S^+ = S_x + iS_y$ and $S^- = S_x - iS_y$ respectively, such that the Heisenberg Hamiltonian becomes:

$$S_i \cdot S_j = \frac{1}{2}(S_i^+ S_j^- + S_i^- S_j^+) + S_i^z S_j^z \tag{1.34}$$

which, with $J_{ij} = J_{ji}$, reduces the Heisenberg Hamiltonian to:

$$H = -\sum_{i,j} J_{ij}(S_i^+ S_j^- + S_i^z S_j^z) \tag{1.35}$$

To in order to determine the excitations of this model, it would be convenient if we could somehow transform the problem into one that we already know how to solve. This can be achieved by the famous Holstein-Primakoff transformation [37] which maps the problem of interaction fermions in the Heisenberg model to one of

non-interaction bosons under the appropriate approximations. The transformation of spin operators is as follows [1]:

$$\begin{aligned} \frac{1}{\hbar}S_i^z &= S - \hat{n}_i \\ \frac{1}{\hbar}S_i^+ &= \sqrt{2S}\phi(\hat{n}_i)a_i \\ \frac{1}{\hbar}S_i^- &= \sqrt{2S}a_i^\dagger\phi(\hat{n}_i) \end{aligned} \tag{1.36}$$

where $a_i^\dagger$ and a_i are the bosonic creation and annihilation operators in second quantization, and $\hat{n}_i$ and $\phi(\hat{n}_i)$ are operators given by:

$$\begin{aligned} \hat{n}_i &= a_i^\dagger a_i \\ \phi(\hat{n}_i) &= \sqrt{1 - \frac{\hat{n}_i}{2S}} \end{aligned} \tag{1.37}$$

In terms of the Holstein-Primakoff operators, the Heisenberg Hamiltonian can be rewritten as:

$$H = -N\hbar^2 S^2 J_0 + 2S\hbar^2 J_0 \sum_i \hat{n}_i - 2S\hbar^2 \sum_{ij} J_{ij}\phi(\hat{n}_i)a_i a_j^\dagger \phi(\hat{n}_j) - \hbar^2 \sum_{ij} J_{ij}\hat{n}_i\hat{n}_j \tag{1.38}$$

where $J_0 = \sum_i J_{ij} = \sum_j J_{ij}$. This equation can be simplified by expanding the square root in $\phi(\hat{n}_i)$ of Eq. 1.37 in powers of $1/S$ as:

$$\phi(\hat{n}_i) = 1 - \frac{\hat{n}_i}{4S} - \frac{\hat{n}_i^2}{23S^2} - \frac{\hat{n}_i^3}{128S^3} - ... \tag{1.39}$$

We make the "spin-wave approximation" in which the spin is assumed to be large and therefore only the first two terms in the expansion of $\phi(\hat{n}_i)$ need to be kept. The Hamiltonian then reduces to:

$$H = -N\hbar^2 S^2 J_0 + 2S\hbar^2 J_0 \sum_i \hat{n}_i - 2S\hbar^2 \sum_{i,j} a_i^\dagger a_j \tag{1.40}$$

which upon Fourier transforming can be rewritten as:

$$H = -N\hbar^2 S^2 J_0 + 2S\hbar^2 \sum_k (J_0 - J(k)) a_q^\dagger a_q \tag{1.41}$$

Here $J(k) = \frac{1}{N}\sum_{i,j} J_{i,j} \exp\left(ik(R_i - R_j)\right)$ and the sum is performed over all the wavevectors k in the first Brillouin zone.

One can see that the Hamiltonian Eq, 1.41 contains two contributions. The first term, $E_g = -N\hbar^2 S^2 J_0$ is the ground state energy of the ferromagnet. The second term represents the gain in energy which results from excitations of the magnetic lattice, which have the form of uncoupled harmonic oscillators in Eq. 1.17. The energy of these excitations is then:

$$E(k) = \hbar\omega(k) = 2S\hbar^2 (J_0 - J(k)) \tag{1.42}$$

This expression can be expanded in the small wavevector limit. For instance, for

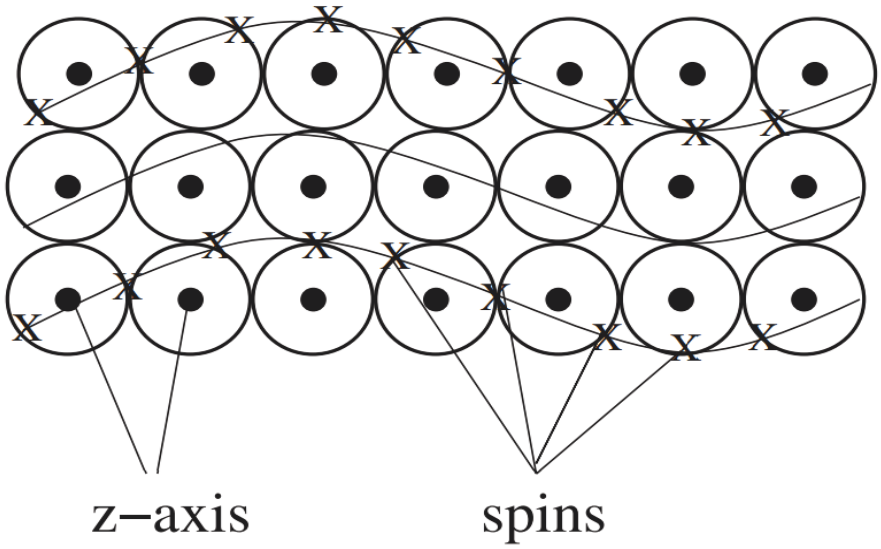

Figure 1.6: Semiclassical picture of spin-waves in a ferromagnet. Figure adapted from Ref. [1].

a cubic lattice with exchange constant J and lattice spacing a the energy becomes:

$$\hbar\omega(k) = 2SJ\hbar a^2k^2 + g_j\mu_B B_0 \tag{1.43}$$

where a Zeeman term which accounts for coupling to an applied field has been added.

The excitations discovered in the above calculation are known as "spin-waves," delocalized collective excitations of the magnetic lattice. In direct analogy to phonons being quantized lattice vibrations in solids, these "magnons" are the quanta of spin-waves. A semiclassical picture of a magnon in a ferromagnet is shown in Fig. 1.6. One can see from the excitation energy of Eq. 1.43 that each magnon reduces the

overall magnetic moment of the system by $\hbar$, thereby revealing magnons to be bosonic quasiparticles. In the spin-wave approximation, magnons are strictly non-interacting with normalized one magnon states given by:

$$|k\rangle = \frac{1}{\hbar\sqrt{2SN}} S^{-}(k)\,|0\rangle \tag{1.44}$$

where the state $|0\rangle$ represents the fully aligned ground state of the ferromagnet.

1.3.2 The Two Sublattice Antiferromagnet

We now repeat the spin-wave calculation for the case of a simple antiferromagnet. We consider a two sublattice antiferromagnet such that each spin only interacts with its nearest neighbors, all of which belong to the other sublattice. We allow for easy axis anisotropy, which we assume is along the z direction, and taken into account through the anisotropy field B_A. We begin with the Heisenberg Hamiltonian in magnetic field:

$$H = -\sum_{i,j}^{n} J_{ij} S_i \cdot S_j - g_j \frac{\mu_B}{\hbar}(B_0 + B_A)\sum_{i}^{A} S_i^z - g_j \frac{\mu_B}{\hbar}(B_0 - B_A)\sum_{i}^{B} S_i^z \tag{1.45}$$

where the last two terms account for the application of the magnetic field over sublattices A and B. The calculation then follows in a similar matter as the ferromagnetic case, the Holstein-Primakoff transformation is applied and the expansion truncated to harmonic order. The details will not be discussed here for the sake of brevity but

can be found in Ref. [1].

The magnon energies in the antiferromagnetic case are given by:

$$\hbar\omega_{\pm}(k) = \sqrt{4S^2\hbar^4(J_0^2 - J^2(k)) + g_j\mu_B B_A(g_j\mu_B B_A - 4SJ_0\hbar^2)} \pm g_j\mu_B B_0 \qquad (1.46)$$

Much like the ferromagnetic case, this expression can be expanded in the small k limit where the energies are then found to be:

$$\hbar\omega_{\pm}(k) = (2S\hbar|J_0|a\sqrt{\frac{2}{z}})k \pm g_j\mu_B B_0 \qquad (1.47)$$

in the limit of small anisotropy.

1.3.3 Optical Spectroscopy Of Magnetic Excitations

What the calculations presented in the previous sections demonstrate is that the excitation spectrum in even the simplest ferromagnets and antiferromagnets are drastically different, possessing quadratic dispersion in the ferromagnet and linear dispersion and higher degeneracy in the antiferromagnet. The excitations we examined in the low energy limit are the Goldstone modes [38] of these systems which arise due to the broken symmetries of their magnetic order. However, the excitation spectrum of most magnetic materials will also contain gapped spin-wave excitations that

are excitable with light and therefore known as optical magnons. In general, the less symmetric the magnetic ordering of a material is, the more spin-wave excitations the material will possess. In this fashion, the excitation spectrum of a material serves as a fingerprint for the ground state magnetic order and interactions. Further understanding can be obtained by applying magnetic field, which as we see in the antiferromagnetic spectrum of Eq. 1.47, splits the degeneracy of magnetic excitations.

This thesis will present low energy optical spectroscopy experiments in which we will uncover many such optical magnons. The probability of exciting a magnon through an interaction with light is given by Fermi's golden rule as:

$$P_{s\to s'} = \frac{2\pi}{\hbar^2} |\langle s' | H_{MD} | s \rangle|^2 \delta(\omega - \omega_{s'} + \omega_s) \tag{1.48}$$

where H_{MD} is the magnetic dipole operator:

$$H_{MD} = -\frac{q}{2m}(L + 2S) \cdot B \tag{1.49}$$

The symmetries of the magnetic dipole operator and the matrix element in Eq. 1.48 result in strict selection rules for making such excitations. Spin excitations can only occur if $\Delta J = 0, \pm 1$ (except $J = 0 \to J = 0$), $\Delta m_J = 0, \pm 1$, and if there is no parity change between initial and final states. Such selection rules may be exploited to uncover additional information regarding the origins of magnetic excitations.

1.4 Influences On Magnetic Interactions

The models presented in the previous section are idealizations of the actual interactions which occur in magnetic materials. In reality, nature displays a plethora of couplings, symmetries, lattice geometries, anisotropies, etc. all of which influence the interactions which work in tandem to result in a magnetic ground state. Except for in the simplest cases, real materials are much too complex to be completely described by the nearest neighbor Heisenberg model. Thus, the Heisenberg Hamiltonian is merely a starting point in investigations into quantum magnetism.

This thesis examines how the local environment of spins can influence the underlying interactions and therefore the magnetic ground state of a material. Far more has been written on this topic than could ever be summarized here. Instead, this section will give a brief overview of how a few of such factors may influence the ground state magnetic interactions of a solid. The examples given below are specific to the materials which will be discussed in this thesis.

1.4.1 Geometric Frustration

Thus far, our discussion of quantum magnetism has been primarily classical. In the Ising model each spin was treated as a classical vector, pointing either in the up or down direction. Even our spin-wave calculation, which began by using the purely quantum mechanical commutation relations of angular momentum, was eventually

mapped to a simple harmonic oscillator which we only arrived at by implicitly assuming a large (and therefore classical) spin in the expansion of the Holstein-Primakoff operators. While the fundamental interactions of these systems are indisputably quantum, the resulting ground states and excitations are often not.

We can categorize such classical ground states as product states, in which the macroscopic wave function of the system is simply the product of individual single particle wavefunctions [39]. Put another way, the system possess no quantum entanglement. Conventionally, the low temperature ground states of these systems break a symmetry, which gives rise to a macroscopic classical field, e.g an order parameter. For instance, the polarized state of a ferromagnet breaks rotational symmetry, resulting in a magnetization which can be measured and used to parameterize the system. In this sense classical physics comes to the rescue in that it allows us to understand a ground state without having to consider the enormous amount of quantum interactions which made up the ground state in the first place.

However, beyond the simplicity of the previous sections lies truly quantum ground states which do not fit this classical paradigm. These systems break no symmetries and therefore do not possess a classical order parameter. Instead such systems can only be classified by the topological properties of their wavefunctions. The quantum nature of such systems becomes apparent when one examines their excitation spectrums. Unlike the spin-waves found above, the excitations of quantum systems are often fractionalized as if the spin and charge degrees of freedoms of fundamental par-

ticles have deconfined. Such materials are currently the focus of intense investigation in solid state physics.

To see how we might arrive at such a quantum state, consider three Ising spins on the triangular lattice as shown in Fig. 1.7. If the interactions between the spins are ferromagnetic then only two ground states exist, either all the spins point up or they point down. However, what happens if the interactions are antiferromagnetic instead? Regardless of how the first two spins are oriented, the third spin cannot align in such a fashion as to be antiferromagnetic with both of the first two spins. An unpreferred ferromagnetic alignment between two spins, shown as the red side of each triangle in Fig. 1.7, is unavoidable. As a consequence, the ground state of a single triangle grows to 6-fold degenerate.

Systems which are unable to satisfy all pairwise interactions in this fashion are known as frustrated, in this case geometrically frustrated as the frustration is based off the geometry of the lattice [40]. The effect of frustration is to dramatically enhance the ground state degeneracy of the system. If we extrapolate the example in Fig. 1.7 to a triangular lattice of N spins then the ground state quickly becomes macroscopically degenerate. For instance, the ground state entropy of the triangular lattice has been shown to be remarkably large, $S = 0.323 k_B N$ [41]. With such large degeneracy the system has many ways that it can fluctuate without ever leaving the ground state manifold.

There is currently a lot of interest in such frustrated systems as these fluctuations

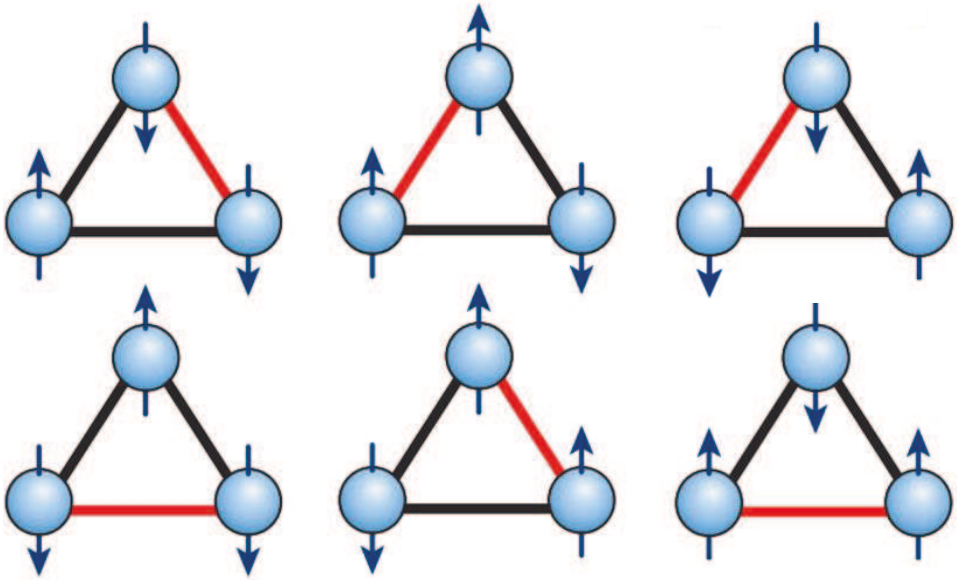

Figure 1.7: Frustrated antiferromagnetic Ising spins on the triangular lattice. All pairwise interactions cannot be satisfied resulting in a large 6-fold ground state degeneracy. Figure adapted from Ref. [2].

may result in the evasion of long range magnetic order, even at low temperatures. The ground state is then a correlated "spin liquid" as opposed to the long range ordered "spin solid" that are typically found in conventional systems. Such fluctuations can result from either classical or quantum origins. Classical fluctuations are driven by thermal energy in systems with large spins, $S > 1/2$. These systems may evade long range order until the thermal energy k_BT becomes much smaller than the exchange J at which point the spins must then either freeze or order. However systems with $S = 1/2$, which are much more perceptible to the uncertainty principle, may possess quantum zero point fluctuations preventing long range order down to absolute zero. The latter case, known as "quantum spin liquids" (QSL), were first proposed by Anderson

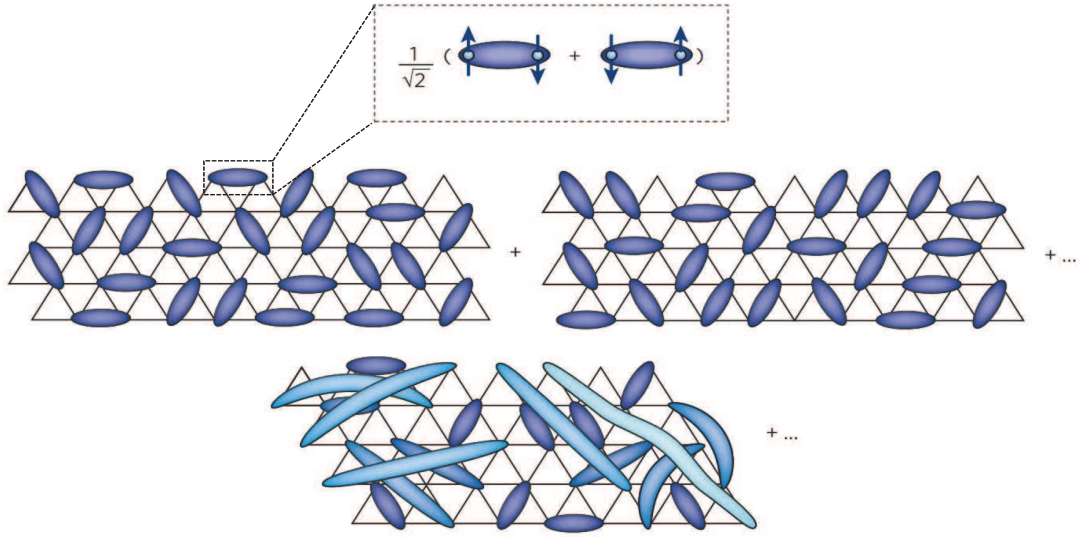

Figure 1.8: Schematic of a fluctuating 2-dimensional quantum spin liquid in which each spin participates in a highly entangled singlet. The ground state is then a highly degenerate superposition of many possible arrangements of valence bonds due to long range entanglement. Figure adapted from Ref. [2].

[42] and latter suggested as the underlying physics of high T_c superconductors [43]. Today the search a definitive QSL constitutes a major pursuit of modern condensed matter research.

As explained above, QSL ground states are believed to occur in materials with strong geometric frustration, whose lattices are often built off the triangle motif of Fig. 1.7 in 2-dimensions or corner sharing tetrahedra, shown in Fig. 1.9, in 3-dimensions. A sense of the frustration of a system can be obtained by examining the temperature dependence of the inverse susceptibility of the sample. In the paramagnetic state, $\chi^{-1} \propto$ T - Θ_{CW}, where Θ_{CW} is the Curie-Weiss constant, a measure of the sign and strength of the interactions as $\Theta_{CW} \propto J$. Therefore, Θ_{CW} represents the expected

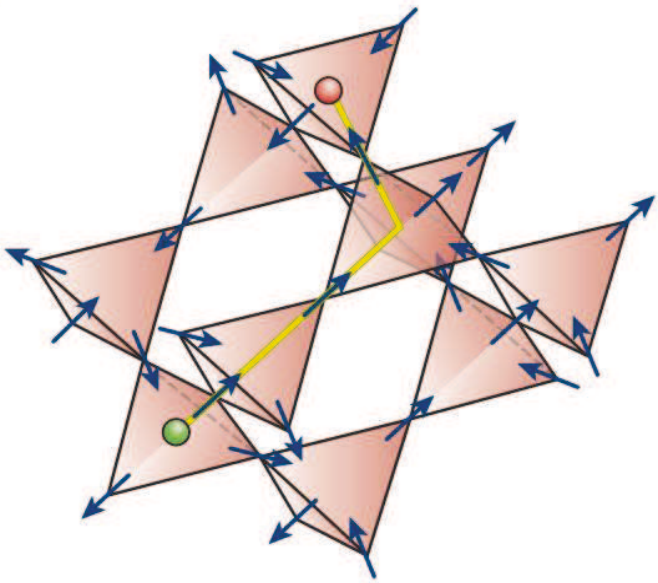

Figure 1.9: A schematic of a spin ice on the pyrochlore lattice. The excitations of these systems are magnetic monopole and anti-monopole pairs which are connected through a series of flipped spins, violating the "ice rules." Figure adapted from Ref. [2].

temperature that an unfrustrated system will magnetically order. However, frustrated systems may not magnetically order until a temperature $T_c \ll |\Theta_{CW}|$. Thus, a measure of the frustration is captured by the frustration parameter $f = |\Theta_{CW}| \ / \ T_c$, which can be as high as $f > 10^3$ in some highly frustrated systems.

Although the susceptibility of these systems within their liquid regimes may resemble that of a paramagnet, it should be noted that unlike a paramagnet a QSL is a highly correlated system often possessing power law correlations between spins [40]. Consider the spins shown in Fig. 1.8 on the triangular lattice which is a prototype of a non-magnetic QSL ground state known as a resonating valence bond state. Each spin participates in a valence bond, a maximally entangled singlet state with another

spin. Due to the high degeneracy of the ground state and the long correlation length, no ordered pattern of valence bonds is preferred. Instead the system undergoes quantum fluctuations between states with a different valence bond arrangements. As this state breaks no symmetries, it possesses no classical order parameter and instead can only be classified by the topological descriptions on its gauge fluctuations [40].

The truly quantum nature of a QSL becomes apparent when one considers its excitation spectrum. One form of excitations in a QSL are spinons, half magnon-like quasiparticles with $S = 1/2$ but no charge. In a QSL the energy cost of separating spinons does not depend on their distance form one another and they are therefore deconfined. Other excitations, such as triplons, a bound pair of spinons, exist as well. Generally, the longer range the correlations the weaker the valence bonds will be resulting more low energy excitations [2].

An additional fractionalized excitation occurs in a particular spin liquid state known as a spin ice (Fig. 1.9). These materials exist on the pyrochlore lattice which is formed by a series of corner sharing tetrahedra. The spins of the tetrahedra are Ising-like and point along the local [1,1,1] direction due to anisotropy [40]. The ground state of a single tetrahedra is a 6-fold degenerate "two-in, two-out" arrangement of spins in analogy to the Bernal-Fowler ice rules [44] for the proton configurations of water ice. Flipping a single spin of a tetrahedra creates a pair magnetic monopole - antimonopoles in neighboring tetrahedra (shown as red and green spheres in Fig. 1.9) [2]. The monopoles can then be deconfined by flipping a series of spins, creating a

"string" of magnetic flux between them. Like spin liquids, spin ices can be classical, in which fluctuations and monopole motion are driven by thermal energy, or quantum, in which non-Ising terms in the Hamiltonian govern coherent monopole tunneling between tetrahedra. Such states are currently a topic of intense interest in solid-state physics.

1.4.2 Antisymmetric Exchange

The Heisenberg Hamiltonian represents the symmetric exchange between spins as it is invariant if the spins S_1 and S_2 are interchanged. However, additional antisymmetric exchange mechanisms may exist in low symmetry environments. For instance, if inversion symmetry is broken then the antisymmetric Dyzloshinskii-Moyria (DM) exchange interaction:

$$H_{\mathrm{DM}} = \sum_{ij} D_{ij} \cdot S_i \times S_j \tag{1.50}$$

is permitted [45, 46]. One can see that broken inversion symmetry is required as the cross product is not invariant if S_i and S_j are interchanged. The vector D_{ij}, which parameterizes the strength of the interaction, is constrained to lie in the $r_i \times r_j$ direction by symmetry where r_i is the distance from the "ith" ion to the non-magnetic ion through which the superexchange interaction is mediated.

The effect of this exchange is unique from the symmetric exchange in that it is minimized by a perpendicular arrangement of the spins S_1 and S_2. However,

DM interactions are derived from spin-orbit coupling and are therefore generally much weaker than symmetric Heisenberg exchanges. i.e. $|D_{ij}| \ll |J_{ij}|$. Thus, this interaction is often a source of weak ferromagnetism in antiferromagnets and visa versa.

1.4.3 Orbital Degeneracy

Thus far, we have only considered interactions between spins. However, spins can also couple to any additional degree of freedom which may behave as a spin, i.e. a pseudospin. In the context of this thesis we will find that under certain conditions the orbital angular momentum of an electron may act as such a psuedospin. This effect becomes particularly important when a system possesses orbital degeneracy, i.e. when two orbital states possess the same energy such that neither is preferred. In this case, Kugel and Khomskii [47] derived a superexchange interaction Hamiltonian between spins and orbital degrees of freedom of the form:

$$H = J \sum_{<ij>} \left[4(S_i \cdot S_j)(\tau_i^\alpha - \frac{1}{2})(\tau_j^\alpha - \frac{1}{2}) + (\tau_i^\alpha + \frac{1}{2})(\tau_j^\alpha + \frac{1}{2}) - 1 \right] \tag{1.51}$$

where the τ_i are orbital psuedospin operators with total moment $S = 1/2$.

1.4.4 Higher Order Couplings

Additional spin coupling beyond the bi-linear interactions of the Heisenberg Hamiltonian and DM interaction are also possible. Such interactions are typically assumed to be much weaker than the aforementioned couplings but in certain situations when they are symmetry permitted they can be large enough to influence the ground state in a measurable fashion. For instance, in $HoMnO_3$ we will encounter an unusual trigonal exchange mechanism between distinct magnetic sublattices of the form:

$$H = K \sum_{ij} S^z_{Hi} S^y_{Mj} [3(S^x_{Mj})^2 - (S^y_{Mj})^2], \tag{1.52}$$

where S_H and S_M refer to the Ho and Mn spins, which are both magnetic in $HoMnO_3$, respectively [48].

1.5 Thesis Overview

This thesis investigates the role that symmetry, frustration, and unusual couplings play in the development of the low temperature magnetic ground states of quantum magnets by examining the low energy electrodynamics of their excitations. In Ch. 2, I introduce time-domain terahertz spectroscopy - the primary experimental technique of this thesis. I explain why such a technique is beneficial for the study of quantum magnetism before detailing specifics such as the modified experimental design and equipment used in our lab. I also give an in-depth description of the data analy-

sis procedure in which the magnetic susceptibility can be extracted from an optical transmission measurement. In Ch. 3, I introduce an additional optical technique, microwave cavity perturbation technique, which will be used to access the optical response of samples at a lower frequency than what is available with time-domain terahertz spectroscopy. Chapters 4 - 7 present an analysis of the low energy electrodynamics of several quantum magnets: $FeSc_2S_4$, $CuOSeO_3$, $HoMnO_3$, and $Yb_2Ti_2O_7$. From these analyses we will find that the underlying spin interactions depend heavily on the symmetry of the space in which they are embedded. Accordingly, the ground states of these materials will be shown to range from conventional to quantum. In Ch. 8, I summarize the work presented in this thesis.

In the appendices, I summarize work that I did during my Ph.D. thesis that does not fit neatly into the field of quantum magnetism, but are areas that I have still made contributions. Appendix A presents an analysis of the low energy electrodynamics of the potential topological Kondo insulator SmB_6. We will find an anomalous amount of dissipation within the Kondo gap of SmB_6 which we demonstrate does not fit the phenomenology of impurities. We additional use a detailed error analysis to put limits on the surface state conductance in this potential topological insulator. Appendix B presents an analysis of the temperature dependent optical conductivity of the potential topological superconductor Tl_5Te_3. We will find that the data is generally consistent with *s*-wave superconductivity but with a large residual conductivity at low temperatures. We suggest that such conduction may result from

topological surface states which exist within the superconducting phase. Appendix C presents a guide for operating the microwave cavity perturbation experiment used in the Armitage group.

Chapter 2

Time-Domain Terahertz Spectroscopy

2.1 History Of Time-Domain THz Spectroscopy

Picosecond time scales have historically been challenging to probe as their natural terahertz (THz) frequencies lie within an experimentally difficult region of the electromagnetic spectrum to generate and detect light. This so called "terahertz gap", spanning from roughly 100 GHz - 3 THz, lies above the capabilities of traditional electronics but below the range of optical generators and detectors (Fig. 2.1). However, advances in recent years of terahertz generation and detection methods have resulted

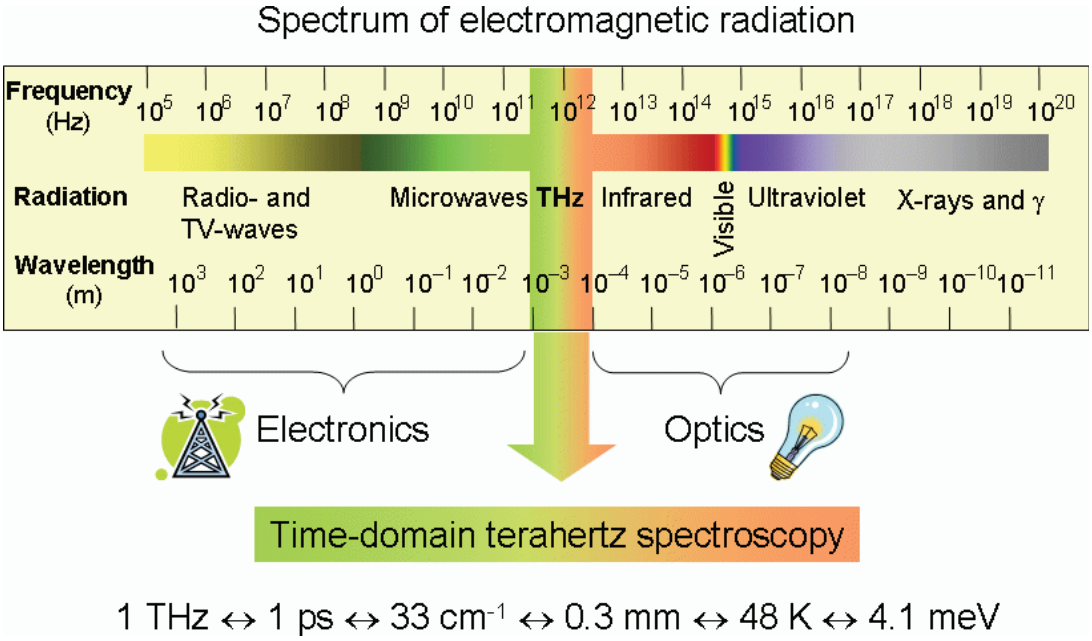

Figure 2.1: The electromagnetic spectrum with the THz range highlighted. Traditionally, the THz range has been a difficult region of the spectrum to generate and detect light as these frequencies lie between the accessible ranges of electronic and optical techniques. Shown at the bottom is a conversion guide of 1 THz in various units.

in a multitude of techniques with dramatically improved capabilities in the terahertz spectral range. Among these techniques, time domain terahertz spectroscopy (TDTS) [49, 50] has evolved into a common tool in both commercial applications as well as academic research.

The origins of TDTS can be traced back to the 1980's when David Auston found that certain photo-conductive switches, today known as "Auston switches," effectively coupled low energy single cycle picosecond pulses of radiation to free space [51, 52]. The design was later improved upon by Grischkowsky, who implemented a substrate lens on top of the Auston switch, reducing the impedance mismatch be-

tween the switch and free space and thereby enhancing the forward coupling of THz radiation [53]. Amazingly, Auston switches can also act as coherent detectors of THz pulses. Prior to these discoveries, frequencies up to about 1 THz were generated with backwards wave oscillator (BWO) techniques that possessed limited frequency adjustability, suffered from experimental artifacts related to standing wave resonances in the instrument, and relied on He-3 or pumped He-4 systems to sufficiently cool bolometers for detection [54]. With the advent of the Auston switch, broadband THz radiation could now be generated and detected at room temperature with vastly improved resolution over BWOs and similar techniques. Today, TDTS has almost entirely replaced BWO techniques as the preferred method of spectroscopy in the THz range.

The utility of TDTS becomes obvious when one considers the ubiquity of natural phenomena which exhibit energy scales of 0.5 meV - 20 meV or time scales of 0.5 ps - 10 ps. For instance, the resonant period of electrons in semiconductors, relaxation times of frustrated molecular rotations, protein folding/unfolding times, and the scattering times of electrons in metals all exist within this range. In condensed matter we are often interested in the elementary collective excitations of solids, many of which also can often be found in the THz range. For instance, low energy optical phonons, the Cooper pair binding energy in conventional superconductors, and the energy and scattering rate of spin waves or "magnons" in magnetic materials are all observable phenomena that occur within the range of TDTS. In addition to academic research,

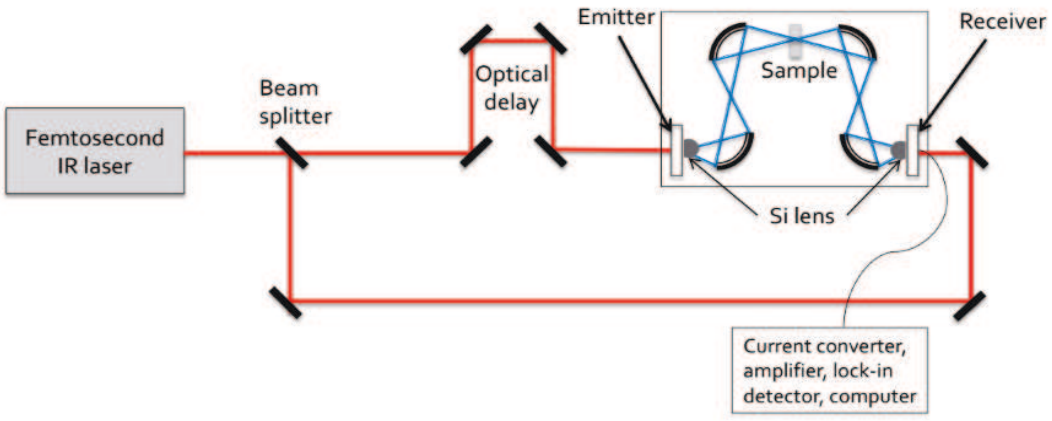

Figure 2.2: A typical TDTS experimental set-up with photoconductive Auston swtiches as generators and detectors of THz radiation.

TDTS has also made significant contributions to industrial applications in the fields of pharmaceuticals [55], medical imaging [56, 57, 58, 59, 60], protein detection [61], and biohazard applications [62, 63].

A typical TDTS experimental set up is shown in Fig 2.2. The experiment begins when a femtosecond laser pulse of infrared radiation ($\lambda \approx 800$nm) is split by a beam splitter. One infrared pulse is directed through an optical delay before being incident on a photoconductive Auston switch. Upon illumination by the infrared laser, the Auston switch, known as "the emitter," generates a pulse of THz light. The THz radiation is then directed through the spectrometer by off-axis parabolic mirrors before being incident on an identical Auston switch, known as "the receiver," which acts as a detector. Much like the emitter, the receiver is only "on" when illuminated by an infrared laser pulse. Therefore, the second infrared pulse travels around the spectrometer and arrives at the backside of the receiver just as the THz pulse is

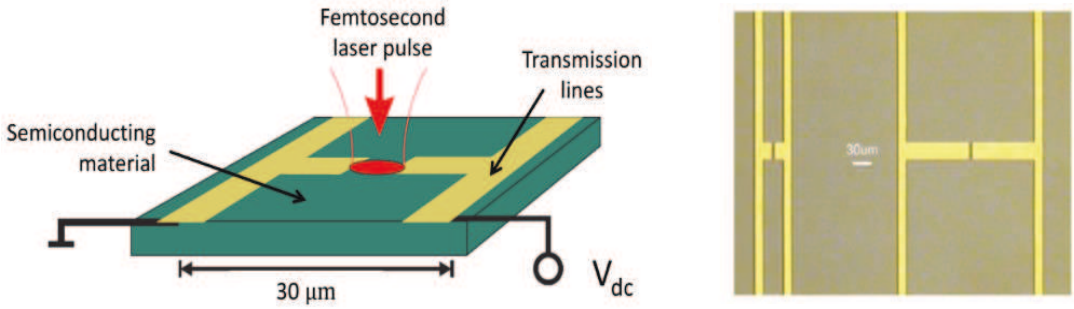

Figure 2.3: (left) An Auston switch is comprised of a strip line antenna separated by a small gap. When illuminated by an infrared laser pulse, photocarriers excited in the semiconductor are accelerated by an applied bias voltage, emitting radiation. Figure adapted from Ref. [3]. (right) An in-house built Auston switch with two gold antennas evaporated on a LT-GaAs substrate developed by Luke Bilbro [4].

arriving at the front. Now turned on by the infrared laser pulse, the incoming THz electric field generates a photocurrent in the receiver which is measured, amplified, and read by a lock-in amplifier. By adjusting the length of the optical delay, the complex electric field of the THz pulse can be coherently measured as a function of real time.

2.2 THz Generation, Coupling To Free Space, and Detection

2.2.1 THz Generation

An Auston switch consists of a semiconducting substrate (LT-GaAs in the present work) with a small metallic antenna patterned on its surface (Fig. 2.3). The most

conventional design is two parallel stripline electrodes separated by a small gap. An external bias voltage is applied across the gap which is known as the "active region" [64]. The choice of bias voltage depends on the specifications of the Auston switch but it is preferable to keep the electric field in the active region below 1 V/μm. Both a DC or AC bias can be used however improved resolution from reduced $1/f$ noise can be achieved with an AC bias. In our experiments, a bias voltage of either 15V - 25V DC or 25V - 35V AC at 15 kHz, is used. Before illumination by the femtosecond laser pulse, the switch is in the "off" state as there is no free charge in the semiconductor that can respond to the bias voltage. However, upon illumination from the infrared laser, whose energy is greater than the band gap of the semiconductor, electron-hole pairs are created in the semiconductor which are then accelerated across the antenna by the bias voltage generating a transient time dependent photocurrent $\vec{j}_{\text{emit}}(t)$ and associated dipole moment $\vec{p}(t)$ [64]. The time dependent dipole moment radiates electromagnetic waves whose electric field can be expressed via Maxwell's equations in the far field limit as [3]

$$\vec{E}_{\text{THz}}(\vec{r},t) = \frac{1}{4\pi\epsilon_0, c^2 r}[\vec{r} \times (\vec{r} \times \frac{d^2\vec{p}(t)}{dt^2})] \tag{2.1}$$

THz generation stops when the photocarriers excited in the semiconductor recombine, returning the switch back to the off state. Repetition of this process, from illumination to recombination, creates single cycle pulses of THz radiation.

The frequency content of the emitted THz pulse is generally determined by the structure of the antenna as well as the intrinsic time scales of the generation process. The peak power of the THz pulse occurs at the resonant frequency of the antenna structure. One can show that a spacing L between the antenna striplines results in a resonant frequency $f_0 = c/2L$. The resonant frequency also partially sets the low frequency content of the THz pulse as smaller dipoles will have higher resonant frequencies but then lower power at frequencies below f_0.

The upper frequency limit of the THz pulse is determined by the time scales of the generation process, namely the infrared laser pulse width τ_L, the momentum relaxation time of the semiconductor τ_c, and the semiconductor carrier recombination time τ_r. One can see from Eq. 2.1 that the time duration of the emitted THz electric field is determined by the second derivative of the transient dipole moment: $\vec{E}_{\mathrm{THz}}(t) \propto d^2\vec{p}(t)/dt^2$. As shorter time scales correspond to a larger bandwidth in frequency [54], it stands to reason that the shortest time scale of the generation process determines the highest frequency contained within the THz pulse. With typical time scales of $\tau_L \approx 50$ fs, $\tau_c \approx 200$ fs, and $\tau_r \approx 1$ ps one can see that the infrared laser pulse width is the shortest time scale and therefore the determining factor. For a more in depth and thorough investigation into the effects of these time scales on the THz pulse content I would refer the reader to Ref. [4].

It is therefore advantageous to use a pulsed femtosecond laser with the narrowest bandwidth possible. The majority of the experiments performed in our lab use a In-

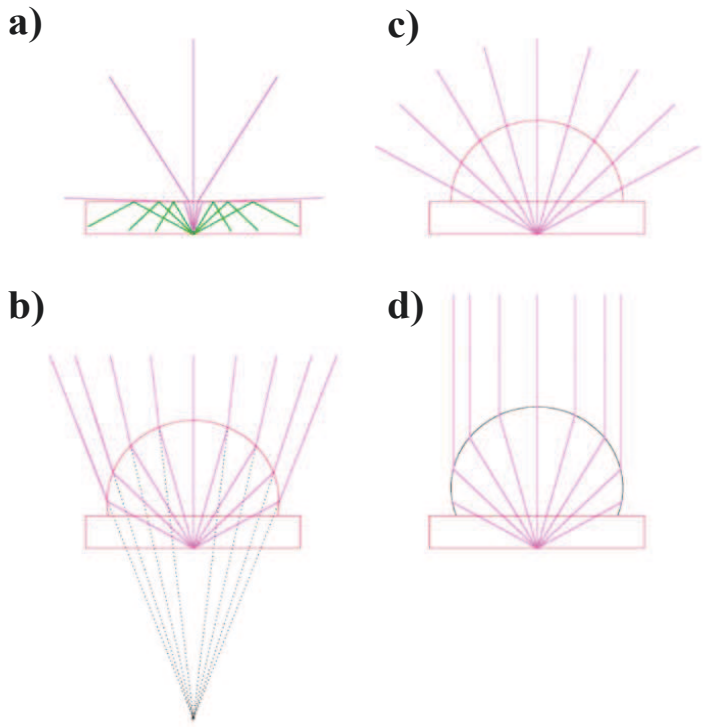

Figure 2.4: (a) Auston switch without a Si lens results in much of the THz radiation being reflected back into the substrate due to the impedance mismatch with free space. (b) A hemispherical Si lens effectively couples the THz radiation to free space but over a large solid angle. (c) A hyper-hemispherical Si lens begins to collimate the emitted THz radiation but shifts the position of the effective focus. (d) The ideal case where a hyper-hemispherical Si lens of the correct dimensions results in a collimated THz beam. See text for details. Figure adapted from Ref. [4].

tegral model Ti:Sapphire solid state laser purchased from Femtolasers. This turnkey system produces pulses of infrared radiation with a center frequency of 800 nm, bandwidth of about 40 nm, and repetition rate of 80 MHz. We additionally use a Toptica ultrafast fiber laser which operates with similar specifications as the Integral system. While the Toptica system outputs far less power when compared to the Intergral, 50 mW compared to 450 mW, it outperforms the Integral in terms of stability and price.

2.2.2 Coupling THz To Free Space

In the ideal case the antenna of the Auston switch behaves as a point source of radiation which broadcasts THz to the surrounding free space. However, the finite size of the antenna dipole and the presence of the semiconducting substrate leads to nonidealities in the emitted THz wavefronts [54]. Additionally, the impedance mismatch between the GaAs substrate (n $\approx$ 3.3) and free space (n $\approx$ 1) results in much of the generated THz radiation to be reflected back into the substrate [54] (Fig. 2.4a). These issues can be partially corrected by the placement of a Si lens [65], which has an index of refraction similar to GaAs, on the back of the Auston switch. One can see in Fig. 2.4b that the placement of a hemispherical Si lens couples THz radiation directly to free space but over a large solid angle. As the Si lens is tuned from hemispherical to hyper-hemispherical (Fig. 2.4c), by increasing the height h compared to the radius r, the emitted THz radiation tends toward collimation. The ideal case (Fig. 2.4d) in which a collimated beam is emitted from the Si lens occurs when the height of the hyper-hemispherical lens equals

$$h = r\frac{n_s}{n_s - 1} - d \tag{2.2}$$

where n_s is the index of refraction of the substrate and d is the substrate thickness [66].

2.2.3 THz Detection

Conveniently, THz radiation is detected via an identical Auston switch which we refer to as the receiver. Much like the emitter, a hyper-hemispherical Si lens is placed on top of the receiver to focus the incoming THz radiation from free space on the dipole. The difference is that while the emitter is biased by an externally applied voltage, the receiver is instead biased by the incoming transient electric field of the THz pulse. In the same fashion as the emitter, the receiver is in the off state unless illuminated by an infrared laser pulse. Therefore a THz pulse can only be measured when the infrared pulse arrives at the back of receiver at the same time that the THz pulse arrives at the front. To achieve this, an optical delay with a scanning stage is placed in the infrared beam path on either the emitter or receiver side of the experiment. In our lab we use a retroreflector mounted to a Physik Instrumente M-511.DD linear delay state with maximum scanning length of 100 mm as an optical delay. By scanning the delay stage, thereby tuning the effective path difference between the emitter and receiver arms of the experiment, one can map out the electric field of the THz pulse in real time.

It is important to note that the generated photocurrent at the receiver is proportional to the electric field of the THz pulse, $\vec{j}_{\mathrm{rec}}(t) \propto \vec{E}_{\mathrm{THz}}(t)$. Therefore the detection process is coherent, attaining both the *magnitude and phase* of the THz electric field. As we will show later, this coherent detection allows for the extraction of both the real and imaginary parts of the complex response of a sample. This sets TDTS apart

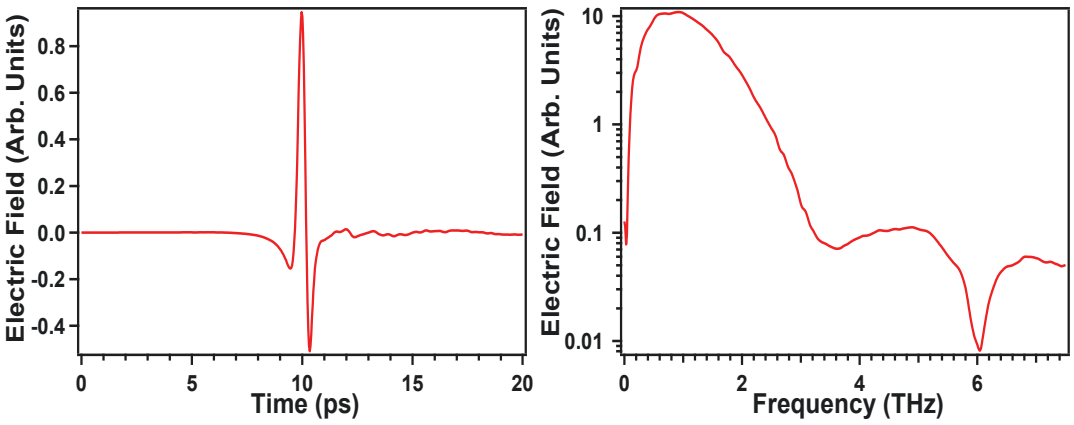

Figure 2.5: (left) The electric field of a typical THz pulse as a function of real time generated and detected by photoconductive Auston switches. (right) the Fourier transform of the pulse shown to the left revealing the spectral content of the pulse. One can see that frequencies from about 100's GHz to several THz are obtained.

from many other spectroscopy techniques which measure only the intensity of the detected electric field, $I \propto |\vec{E}(t)|^2$. With only the intensity measured, these techniques rely on measuring the real part of the response over as broad a frequency range as possible (ideally infinite) and then performing a Kramers-Kronig transform to attain the imaginary part of the optical response. Of course the accessible frequency range in any real experiment is never infinite which potentially leads to artifacts when the Kramers-Kronig transform is computed. These concerns are not a factor in TDTS experiments. Additionally, the coherent nature of detection dramatically reduces sensitivity to background thermal noise unlike traditional detectors such as bolometers [67].

The generated photocurrent in the receiver is then measured by an ammeter, amplified and converted to a voltage by a transimpedance amplifier, and then averaged

and recorded by a lock-in amplifier. A reference signal from either an optical chopper, if a DC bias is used, or the AC voltage, if an AC bias is used, is fed into the lock-in to measure the THz pulse. The time dependent electric field of a typical THz pulse generated and detected by photoconductive Auston switches is shown on the left in Fig. 2.5. A simple Fourier transform, shown on the right of Fig. 2.5, is then performed to obtain the frequency content of the THz pulse. One can see that frequencies of order 100's GHz to several THz are achieved with the Auston switches used in our lab.

2.3 THz Propagation: Modifying The $8f$ Design

Despite significant progress in developing TDTS, limiting factors of the technique remain. Perhaps the largest constraint is the technique's requirement for exceptionally large sample sizes due to large THz focal spots at the sample position. While large focal spots are partially caused by the difficulty of tightly focusing long wavelength THz radiation, 1 THz = 0.3 mm, the observed focal spot sizes of nearly 10 mm in conventional systems are far larger than the wavelength would suggest. Instead, large focal spots result from optical aberrations of the off-axis parabolic mirrors (OAPs), used to direct and focus THz radiation, and finite sized source effects [68, 69]. Correspondingly, conventional TDTS experiments typically require samples in excess of

roughly 3mm × 3mm in cross section in order to achieve sufficient signal to noise. Therefore, methods for reducing optical aberrations from OAPs in TDTS systems need to be developed. In this section we discuss the design of a new TDTS system based off a novel configuration of OAPs. We show that significantly reduced optical aberrations and smaller focal spot sizes can be achieved via this particular OAP configuration, thus easing the requirement of large sample sizes in TDTS spectroscopy.

2.3.1 The Conventional $8f$ design

Experimental configurations for directing THz radiation onto a sample under test are based on an alignment scheme of off-axis parabolic mirrors (OAPs) known as the "$8f$ configuration." This geometry, in which the total THz beam path is 8 times the reflected focal length of one OAP, allows for the passage of both low and high frequencies through the system in a consistent fashion. One can gain some understanding of wave propagation through this system from a ray optics perspective. Fig. 2.6 shows the beam path of both the low (red) and high (blue) frequencies for spectrometers based on the conventional $8f$ configuration. The THz emitter is placed at the focal spot of a 90 degree off-axis parabolic mirror, OAP 1, of reflected focal length f. A collimating hyper-hemispherical lens is placed directly after the emitter to correct finite size source effects and to more efficiently couple THz radiation to free space. In the low frequency limit, the wave fronts emerge from the hyper-hemispherical lens and quickly diverge in a Gaussian manner before OAP 1. OAP 1 then collimates

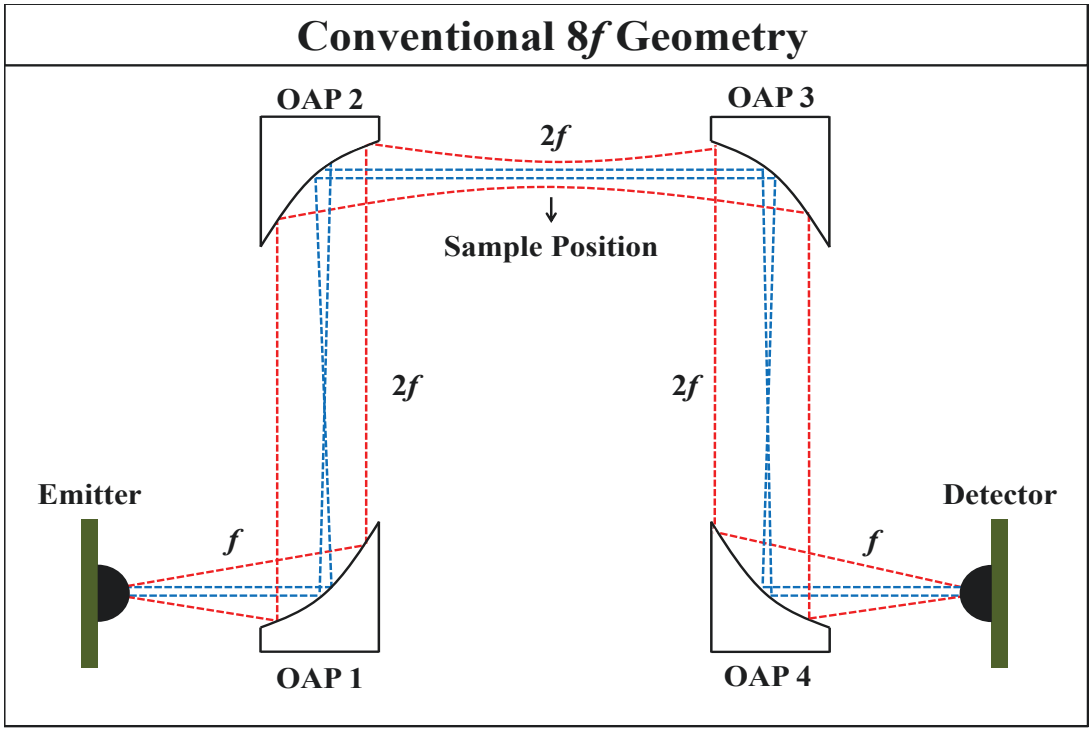

Figure 2.6: A TDTS spectrometer designed in the conventional $8f$ configuration. In this geometry the total THz path length is 8 times the reflected focal length of a single off-axis parabolic mirror (OAP). Dotted lines represent the general behavior in a ray optics perspective of both the low (red) and high (blue) frequencies contained within a THz pulse as it propagates through the system. While this design allows for the consistent passage of low and high frequency THz radiation through the system, the focal spot at the sample position is distorted from optical aberrations inherent in this design.

the low frequencies onto OAP 2 which then focuses the light halfway between OAPs 2 and 3. The high frequencies behave in the reverse manner as they emerge from the hyper-hemispherical lens collimated, are focused by OAP 1, and collimated again by OAP 2. This results in a nearly frequency independent focus, or Gaussian beam waist, formed between OAPs 2 and 3 where the sample under test is placed. The second half of the system is simply the inverse of the first half as shown in Fig. 2.6.

This analysis provides perspective on the light propagation through the system, but does not give insight into the above described optical aberrations of the system. As we discuss below, the conventional $8f$ design results in a large and distorted focal spot at the sample position due to optical aberrations that are inherent in its design.

2.3.2 Optical Aberrations Of OAPs

Off-axis parabolic mirrors are beneficial for imaging in the sub-millimeter range due to their achromatic and nearly lossless reflection properties. However, previous theoretical classical aberration analyses and ZEMAX optical design software simulations have shown that the reduction of symmetry in their off-axis design introduces optical aberrations in their imaging capabilities [68, 69]. It is known that OAPs suffer from two forms of optical aberration, coma and astigmatism, the ratio of which depends on geometrical properties of the OAP.

Our motivation for building a new TDTS system is based off the work of Brückner et al.[68], who found through numerical simulations that the imaging capability of a set of OAPs depends greatly on the alignment of one OAP to the next. While no alignment of two OAPs resulted in a complete cancellation of all optical aberrations, it was found that certain alignments perform significantly better than others. For instance, the 180 degree alignment of two OAPs, where the second OAP is a 180 degree rotation of the first (left, Fig. 2.7), resulted in an enhancement of the optical aberrations of the two OAPs and correspondingly the worst imaging capabilities of

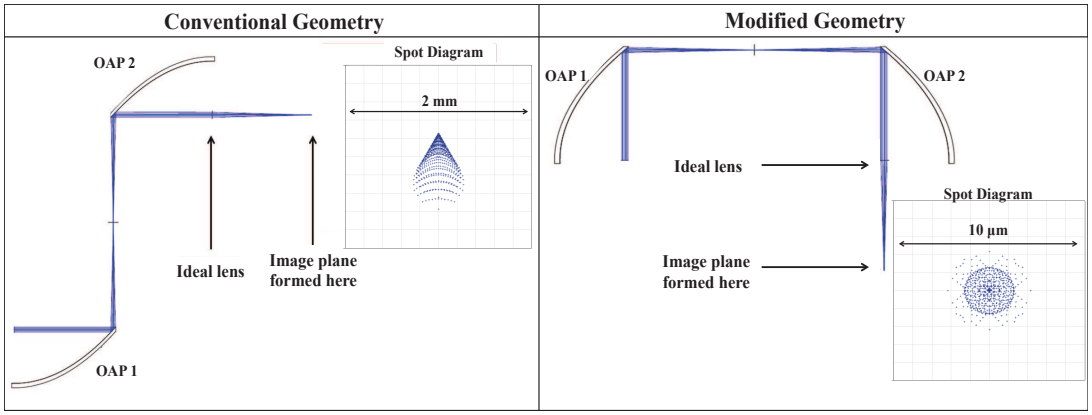

Figure 2.7: Two OAPs aligned in either the (left) conventional geometry or (right) modified geometry. Shown in blue are the results of our ZEMAX ray tracing simulations. Collimated light was sent into the first OAP to simulate the behavior of the high frequency light in TDTS spectrometers. Spot diagrams were generated by projecting the image onto a plane at the focal spot of the second OAP. One can see that the focus of the conventional geometry is highly distorted and two orders of magnitude larger than that of the modified geometry. Typical TDTS spectrometers are often based on the conventional geometry which has poor imaging capabilities.

all alignments studied. We refer to this alignment as the "conventional geometry" as it is the alignment upon which the conventional $8f$ configuration is based. However, it was found that if the second OAP is aligned such that it is the mirror image of the first OAP (right, Fig. 2.7), in which case the two parent parabolas share an axis, then the principle aberrations of the first OAP are compensated by the second OAP, resulting in a diffraction limited image. This alignment produced the best imaging results. We correspondingly refer to this alignment as the "modified geometry." Fig. 2.7 shows two OAPs aligned in the conventional (left) and modified (right) geometries with some further analysis which will be discussed below.

2.3.3 ZEMAX Simulations

The analysis of Brückner et al.[68] showed the modified geometry has reduced optical aberrations but only when light is sent into OAP 1 diverging from the focus. As discussed above, this is only consistent with the behavior of the low frequencies in the $8f$ geometry. The effects of optical aberrations for the high frequency light, which come into OAP 1 collimated (i.e. propagating into OAP 1 "backwards"), are unknown. To investigate, we collaborated with Robert Barkhouser of the Instrument Development Group at JHU who performed ZEMAX ray tracing simulations in which collimated light was sent into OAP 1. A 200 mm focal length ideal lens was used to focus the light so that the imaging performance of both the conventional and modified OAP configurations could be studied. Spot diagrams were generated by projecting the image onto a plane placed at the focus of the ideal lens.

Fig. 2.7 shows our ray tracing results for the conventional (left) and modified (right) geometries respectively. We find the image in the conventional geometry to be highly distorted from coma, as seen in the spot diagram in the left panel of Fig. 2.7. Additionally, we find the image size in this geometry to be approximately twice the image size formed by a single OAP, confirming that the aberrations are enhanced in this configuration. However, the spot diagram for the modified geometry, right panel of Fig. 2.7, shows the image to be undistorted and diffraction limited. It should be noted that the scale of the spot diagram in the modified geometry is two orders of magnitude smaller than that of the conventional geometry. This suggests that the

optical aberrations in the high frequency light are also compensated in the modified geometry. Thus the modified geometry has significantly reduced optical aberrations for the entire range of frequencies present in a typical THz pulse as shown by both our and Brückner et al.'s [68] ray tracing analysis.

2.3.4 The Modified $8f$ Design

As discussed above, TDTS spectrometers in the $8f$ configuration are composed of two copies of the OAP configurations shown in Fig. 2.7. Fig. 2.8 shows an $8f$ spectrometer based off the modified configuration of OAPs shown in the right panel of Fig. 2.7. We refer to this as the "modified $8f$ geometry." Much like the conventional $8f$ geometry, this system has a focal spot formed at the sample position between OAPs 2 and 3. However, as shown above the quality of that focal spot is determined by the relative alignment of OAPs 1 and 2 as well as OAPs 3 and 4. One can see that the conventional $8f$ geometry (Fig. 2.6) consists of the 180 degree alignment of OAPs 1 and 2 that was previously shown to produce the poorest image quality. However, our modified $8f$ geometry is based on the mirror image alignment of OAPs 1 and 2 that results in the compensation of the principle aberration and an ideally diffraction limited focal spot.

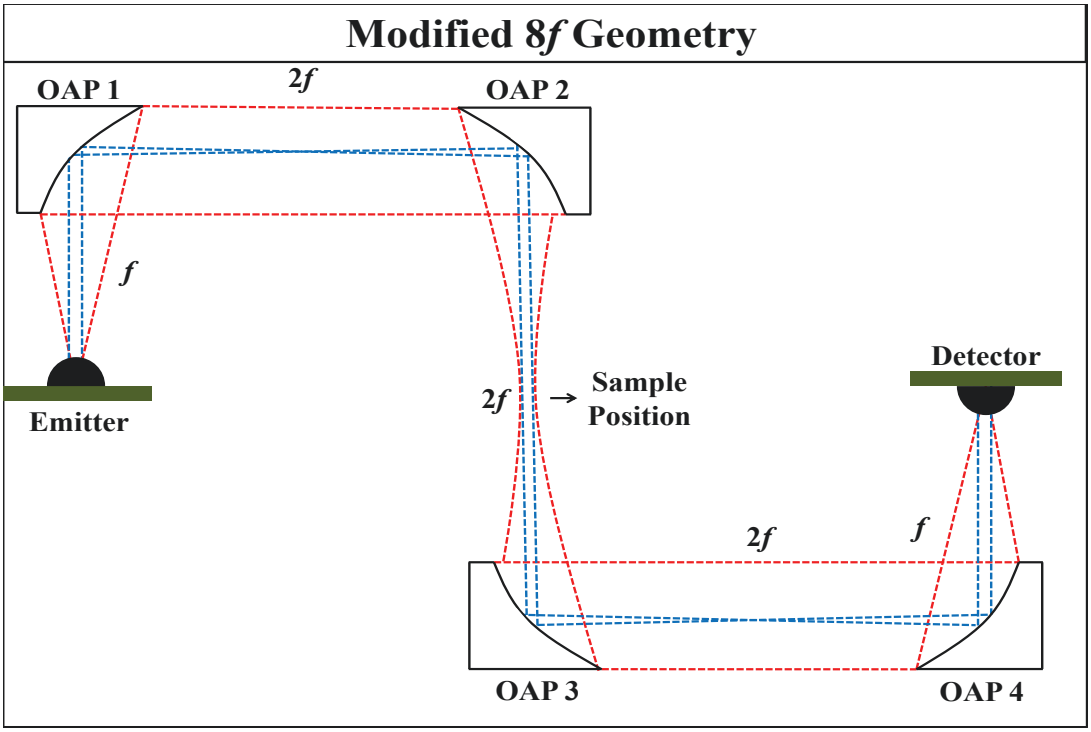

Figure 2.8: A TDTS spectrometer designed in the modified $8f$ geometry. One can see that the relative alignment of OAPs 1 and 2 (as well as OAPs 3 and 4) is based off the modified geometry of OAPs which was shown to possess the best imaging capabilities. With this design a tighter more symmetric focal spot at the sample position can be achieved.

2.3.5 Construction Of The Bilbro-Laurita-Cheng (BLC) THz Spectrometer

To test our theoretical results, a home-built TDTS spectrometer was constructed in the modified $8f$ geometry as shown in Fig. 2.8. The system utilizes aluminum coated OAPs with a diameter and reflected focal length of 2 in and 4 in respectively. All OAP degrees of freedom are locked by mounting the OAPS to aluminum holders which are fixed in position by screws and slip fit dowel pins. We find this greatly

eases the alignment of the system as only the Si lens position needs to be adjusted to fully tune up the system.

The following figures are design templates I made for the fabrication of the system. All figures are drawn completely to scale. Fig. 2.9 shows a mock-up of the system with all components in place with views from the top and side of the spectrometer respectively. Fig. 2.10 displays the design for the bottom plate, to which the all the optical components of the spectrometer are mounted. Different colors represent different screws and dowel pins used for each component, given by the legend at the top. The top figure shows the design template with only the screw and dowel pin positions of the OAPs and optical rails shown. The optical rails are used to mount the assemblies which house the Auston switches. Mounting to a rail in this fashion allows for linear adjustment to ensure the Auston switch is at the focus of OAP 1 for the emitter and OAP 4 for the receiver. The bottom diagram of Fig. 2.10 shows the design template for the bottom plate with all tapped holes shown. The gray circles represent 1/4-20 tapped holes used for mounting routine optics, e.g. polarizers, irises, etc., in between the OAPs and Auston switches. Fig. 2.11 shows a similar template for the top plate of the spectrometer which houses the cryostat. The top plate has three axis adjustability so that the sample can be positioned directly in the focus of the spectrometer.

This spectrometer is referred to in our lab as the "BLC" in honor of the students who designed the original spectrometer and those who redesigned the system in the

modified geometry as discussed above.

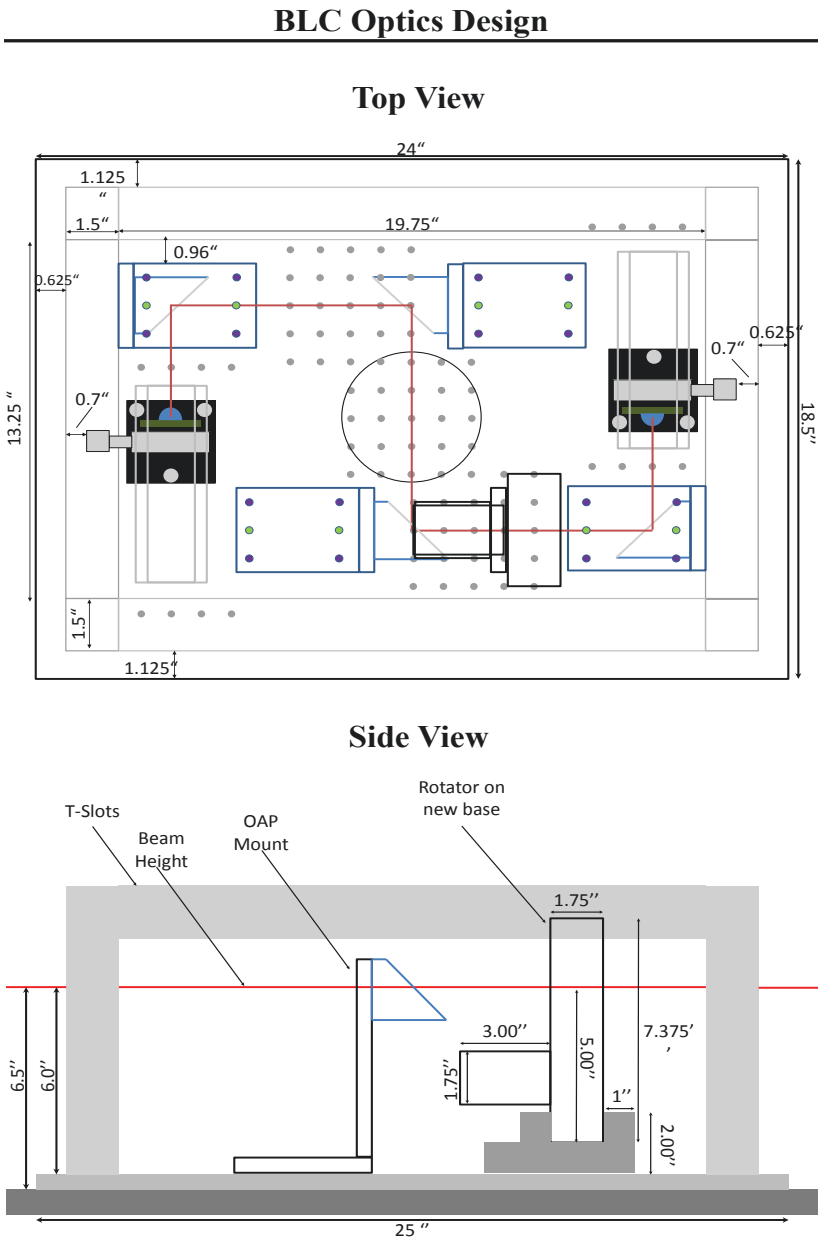

Figure 2.9: To scale drawings the BLC system with all optical components in place with views from the top and side respectively.

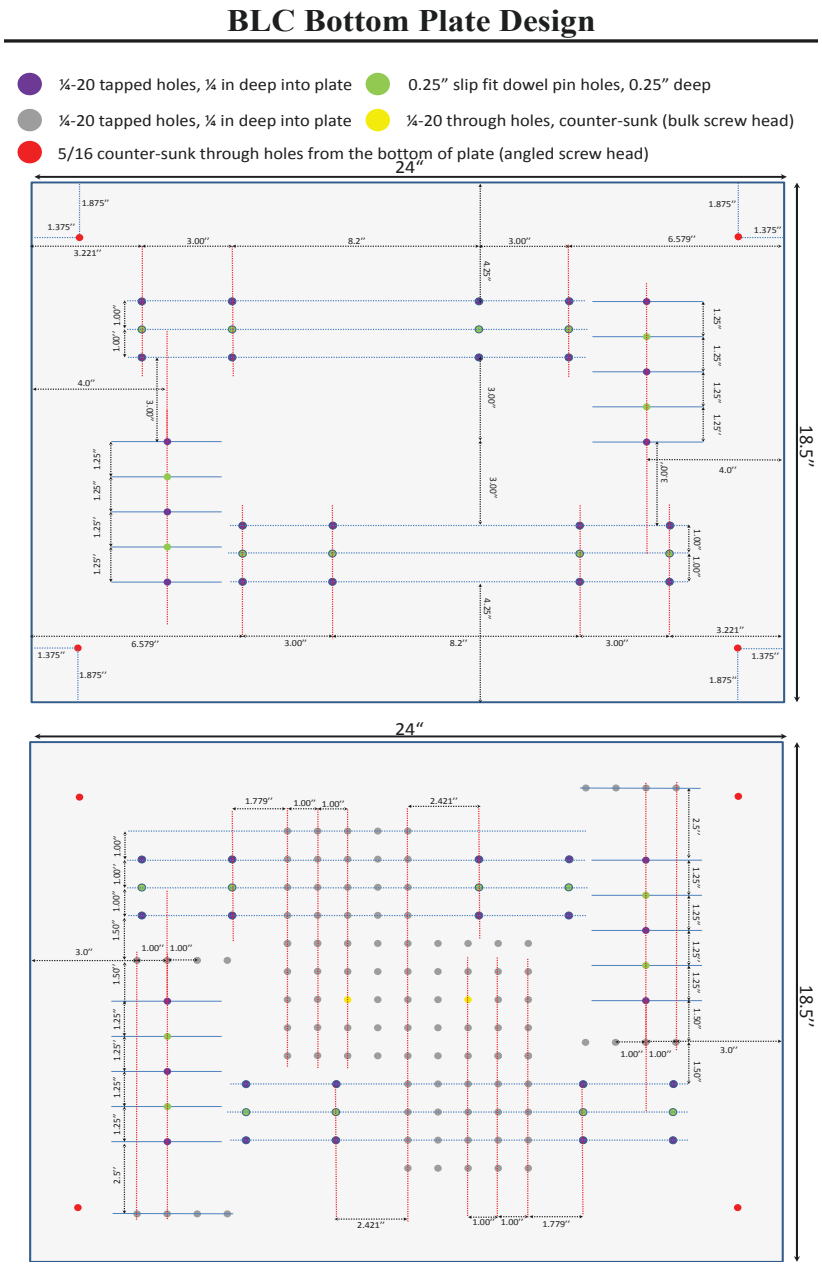

Figure 2.10: To scale drawings of the bottom plate of the BLC system. The top figures shows only the screw holes and dowel pin alignments for the OAPs and optical rails. The bottom picture displays the bottom plate with all the screw holes shown, including those used to mount routine optics.

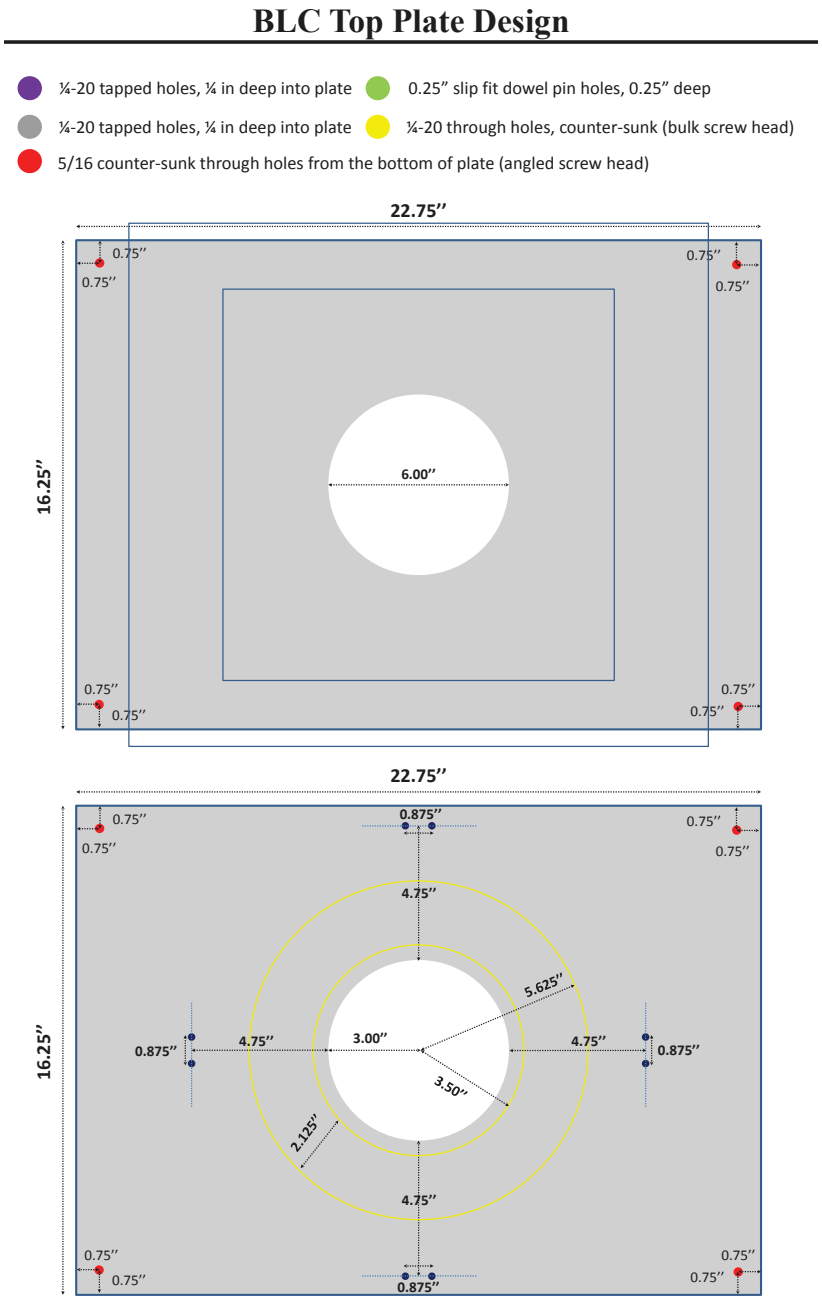

Figure 2.11: Design of the top plate of the BLC which holds the cryostat.

2.3.6 Comparison Of The Conventional and Modified $8f$ Configurations

To investigate the imaging capabilities of the modified $8f$ system, data was taken with an aperture placed at the focal spot, the size of which was then varied. The apertures used were metallic circular apertures attached to a mount with $\hat{x}$, $\hat{y}$, and $\hat{z}$ axis adjustment. The focal spot was defined as the position in which the maximum amount of signal was transmitted through the smallest aperture. For comparison, an identical aperture experiment was performed on a separate home-built THz spectrometer designed in the conventional $8f$ geometry. While this conventional system utilizes OAPs with slightly longer reflected focal lengths, we believe it to be fairly representative of the conventional $8f$ geometry.

We define the integral over all frequency of the magnitude of the Fourier transforms squared as a figure of merit to characterize each system. This quantity is identical to the integral of the electric field squared as a function of time via Parseval's theorem and is therefore proportional to the total power contained in each THz pulse.

$$P_{total} \propto \int_{-\infty}^{\infty} |E(t)|^2 dt = \int_{-\infty}^{\infty} |E(\omega)|^2 d\omega \tag{2.3}$$

This figure of merit is chosen because it allows us to quantify the focal spot size of both TDTS systems. The transmitted power $P(r, z)$ of a Gaussian beam incident on

a circular aperture of diameter d at position z is given by the equation [70],

$$P(r,z) = P_0[1 - e^{-2d^2/w(z)^2}]. \tag{2.4}$$

In this expression P_0 represents the total power, i.e. the power with no aperture is present, and $w(z)$ is beam waist diameter at position z. With an aperture placed at the focal position, $w(z)$ is a constant and represents the focal spot diameter. Thus by fitting our figure of merit to Eq. 2.4, the focal spot diameter for our TDTS spectrometers in both the conventional and modified $8f$ geometries can be extracted.

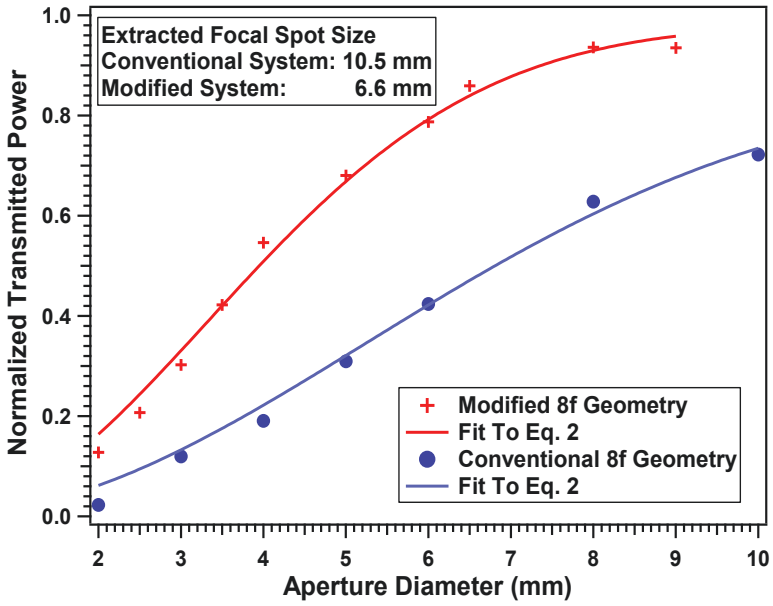

Figure 2.12: Total transmitted power as a function of aperture size for TDTS systems designed in both the modified (red, crosses) and conventional (blue, circles) configurations. Solid lines are fits of the data to Eq. 2.4 as discussed in the text. The extracted focal spot sizes for the conventional and modified geometries are 10.5 mm and 6.6 mm respectively, revealing a nearly 40% reduction in the THz focal spot size in the modified geometry.

Fig. 2.12 shows the normalized transmitted power as a function of aperture size for both the modified $8f$ (red, crosses) and conventional $8f$ (blue, circles) geometries. Normalization was performed by dividing the transmitted power of each aperture size by that of the transmitted power with no aperture present. In this way, we remove any systematic differences between the two TDTS systems. One can immediately see from Fig. 2.12 that the modified $8f$ geometry results in a dramatic improvement for all aperture sizes studied. We find more than double the signal in the modified $8f$ geometry than in the conventional $8f$ geometry for aperture sizes less than 8 mm. More importantly, the best improvement over the conventional $8f$ system is found for the smallest apertures. We find the transmitted power through a 2 mm aperture to be 4 times greater in the modified $8f$ geometry as compared to the conventional $8f$ geometry, greatly easing the typically constraining need for large sample sizes in TDTS.

Also shown in Fig. 2.12 are the fits for both the conventional $8f$ and modified $8f$ geometries to Eq. 2.4. As explained above, the focal spot diameter can be extracted by fitting these data to Eq. 2.4. We extract values of 10.5 mm and 6.6 mm for the conventional $8f$ and modified $8f$ geometries respectively. One should note that Eq. 2.4 only applies for monochromatic Gaussian beams which, as shown by the ray tracing results of Fig. 2.7, is not applicable to the conventional $8f$ system. However, we believe the larger extracted focal spot diameter is a phenomenological description of the conventional $8f$ system and still emblematic of the larger optical aberrations

in this geometry.

2.3.7 Conclusions

We demonstrated that a simple rearrangement of the off-axis parabolic mirrors results in a significantly reduced focal spot size and correspondingly improved performance of time domain terahertz spectrometers. This improvement is caused by reduced optical aberrations in our "modified $8f$ geometry" as compared to systems designed in the "conventional $8f$ geometry." We demonstrated through simulations that the aberrations in the modified geometry are compensated from one OAP to the next, instead of enhanced as they are in the conventional geometry and found that a system designed in the modified $8f$ geometry significantly out-performs a similar system designed in the conventional $8f$ geometry with the largest improvement seen at the smallest aperture size. A near 40% reduction in THz focal spot size in the modified $8f$ geometry as compared to the conventional $8f$ system was found. This design enables the study of smaller samples than what has previously been capable of in TDTS experiments.

2.4 Cryogenic Experimental Setups

2.4.1 Continuous He^4 Cryostat

Zero field measurements displayed in this thesis were performed using a continuous flow He^4 optical cryostat capable of reaching temperatures ranging from 1.6K - 300K. In order to reach temperatures below that of liquid He^4 (4.2K), the cryostat must be filled with liquid helium by completely opening the needle valve which controls the flow of He^4 into the cryostat and waiting for 10 minutes. After 10 minutes, closing the needle value allows the pump attached to the cryostat to reduce the vapor pressure of the condensed He^4 in the system, thereby reducing the temperature below 4K. While temperature control above 4K is controlled via a LakeShore 332, temperature control below 4K must be done manually by adjusting the valve attached to the pump.

All samples are mounted to circular apertures which are then placed in the THz beam through the use of a insert which mates with our cryostat. All samples are referenced to an empty aperture of identical size. By moving the insert up and down one is able to switch between either the aperture or sample in the THz beam focus.

2.4.2 Closed-Cycle Cryostat With A 7T Superconducting Magnet

Much of the data presented in this thesis will be shown as a function of magnetic field. Field dependent data was taken on a closed cycle Janis cryostat with a superconducting magnet capable of reaching fields of up 7T. Cooling on this system is achieved by introducing small amounts of ultra-pure He^4 dry gas into the sample chamber which acts as exchange gas with the cold head. This system is also capable of reaching temperatures below 4K by transferring liquid He^4 through a value on the cryostat insert. In similar manner as to the zero field cryostat, one is able to condense liquid He^4 in the sample space. Once full, the transfer of He^4 should be stopped and then the liquid He^4 can be pumped on to reach temperatures as low as 1.6K. The hold time for doing experiments in condensed He^4 depends on which temperature the experiment is performed. Generally, the lower the temperature the less hold time. I've found that experiments performed at 1.6K will generally last 35 - 45 minutes before the He^4 is depleted. However, experiments performed at 3K can last for over 90 minutes. Refilling the cryostat with liquid He^4 is a simple procedure and only takes approximately 30 minutes.

2.5 Data Acquisition and Analysis

2.5.1 Experimentally Measuring The Complex Transmission $\tilde{T}(\omega)$

The ultimate goal of a TDTS experiment is to measure the complex transmission $\tilde{T}(\omega)$ of the sample. In a sense, the complex transmission constitutes the "raw" data of a TDTS experiment as other quantities of interest, for instance the complex conductivity or complex magnetic susceptibility, can be calculated from the complex transmission under certain assumptions. To calculate the complex transmission, we first write down the experimentally measured electric field at the receiver $\tilde{E}_{\text{referance}}(t)$ as a convolution [71] of the infrared laser pulse $\tilde{L}_{\text{IR}}(t)$, the generated THz electric field of the emitter $\tilde{E}_{\text{emit}}(t)$, and the response function of the detector $\tilde{R}_{\text{rec}}(t)$:

$$\tilde{E}_{\text{reference}}(t) = \tilde{L}_{\text{IR}}(t) \otimes \tilde{E}_{\text{emit}}(t) \otimes \tilde{R}_{\text{rec}}(t) \tag{2.5}$$

We now repeat the experiment with the sample placed in the THz beam path. In a similar fashion, the electric field at the detector $\tilde{E}_{\text{sample}}(t)$ can be written as:

$$\tilde{E}_{\text{sample}}(t) = \tilde{L}_{\text{IR}}(t) \otimes \tilde{E}_{\text{trans}}(t) \otimes \tilde{R}_{\text{rec}}(t) \tag{2.6}$$

where $\tilde{E}_{\text{trans}}(t)$ represents the transmitted electric field through the sample. As convolution in the time domain is simply multiplication in the frequency domain, upon Fourier transforming the above expressions we obtain:

$$\tilde{E}_{\text{reference}}(\omega) = \tilde{L}_{\text{IR}}(\omega)\tilde{E}_{\text{emit}}(\omega)\tilde{R}_{\text{rec}}(\omega) \tag{2.7}$$

$$\tilde{E}_{\text{sample}}(\omega) = \tilde{L}_{\text{IR}}(\omega)\tilde{E}_{\text{trans}}(\omega)\tilde{R}_{\text{rec}}(\omega) \tag{2.8}$$

Once can see that while the exact form of $\tilde{L}_{\text{IR}}(\omega)$ and $\tilde{R}_{\text{rec}}(\omega)$ are not known, the transmitted electric field both with and without a sample in the THz beam path possesses an identical dependence of these quantities. Therefore, we can isolate the transmitted electric field through the sample by taking the ratio of these two measured electric fields. This ratio defines the complex transmission of the sample:

$$\tilde{T}(\omega) = \frac{\tilde{E}_{\text{sample}}(\omega)}{\tilde{E}_{\text{reference}}(\omega)} = \frac{\tilde{E}_{\text{trans}}(\omega)}{\tilde{E}_{\text{emit}}(\omega)} \tag{2.9}$$

The complex transmission is the fundamental quantity that is measured in a TDTS experiment.

2.5.2 The Analytic Expression For The Complex Transmission $\tilde{T}(\omega)$

In this section we derive the analytic expression for the complex transmission through a thick crystal of thickness d. It should be noted that the vast majority of TDTS experiments are performed either on thin films, which are too thin to measure a magnetic response, or on thick insulators where only the dielectric properties are sought. Therefore, many analytic derivations of the complex transmission begin with the assumption of a non-magnetic material, i.e. $\mu = 1$. As this thesis pertains to the THz response of magnetic insulators, this assumption does not apply and we must derive the transmission assuming the sample possesses both dielectric and magnetic properties, i.e. $\epsilon \neq 1$ and $\mu \neq 1$. In the end, certain assumptions with have to be made as both ϵ and μ are complex quantities and therefore represent four unknowns. Whereas in a TDTS measurement only two quantities are measured, the real and imaginary parts of the complex transmission. Therefore, the real and imaginary parts of both ϵ and μ are never independently extracted in a single pass transmission experiment. However, often either the electric or magnetic response can be isolated under certain assumptions or in certain limits as shown below.

We begin by assuming that a plane wave of frequency ω undergoes normal incidence on a thick slab of sample with index of refraction $n_s = \sqrt{\epsilon\mu}$, wave impedance $Z_s = \sqrt{\mu/\epsilon}$, and thickness d. The impedance mismatch between the sample and free

space, which possesses $n_0 = 1$ and $Z = Z_0 \approx 377\ \Omega$, will cause a partial reflection and partial transmission of the electromagnetic wave at the first interface of air to sample. The reflection and transmission coefficients are described by the Fresnel relations as [72]:

$$r = \frac{Z_s - Z_0}{Z_0 + Z_s} \tag{2.10}$$

$$t = \frac{2Z_s}{Z_0 + Z_s} \tag{2.11}$$

The transmitted wave will accumulate a phase while traveling through the sample given by:

$$P(d, n, \omega) = \exp\left(i\frac{\omega d}{c}n_s\right) \tag{2.12}$$

At the second interface, from sample to air, the light will again undergo a transmission and reflection given by the Fresnel relations above. Therefore we can write the total transmission through the sample as:

$$t_{\text{sample}}(\omega) = \frac{4Z_0 Z_s}{(Z_0 + Z_s)^2} \exp\left(i\frac{\omega d}{c}n_s\right) \tag{2.13}$$

We now repeat the above calculation in the absence of the sample which is used as a reference. It is best to think of this case as representing transmission of a "sample" of air with identical thickness d. In this case the magnitude of the transmission is 1, as there is no impedance mismatch to reflect radiation, however the phase that is accumulated is distinct due to the difference in index of refraction of air compared to

the sample. The reference transmission is then:

$$t_{\text{ref}}(\omega) = \exp\left(i\frac{\omega d}{c}n_0\right) = \exp\left(i\frac{\omega d}{c}\right) \tag{2.14}$$

The complex transmission through the sample in the most general form is then:

$$\tilde{T}(\omega) = \frac{t_{\text{sample}}(\omega)}{t_{\text{ref}}(\omega)} = \frac{4Z_0Z_s}{(Z_0+Z_s)^2}\exp\left(i\frac{\omega d}{c}(n_s-1)\right) \tag{2.15}$$

It should be noted that the expression for thin films can be greatly simplified from the thick crystal result. For the derivation for thin films, I would refer the reader again to Ref. [4].

For a nonmagnetic material with $\mu = 1$ the transmission expression reduces to

$$\tilde{T}(\omega) = \frac{4n_s}{(1+n_s)^2}\exp\left(i\frac{\omega d}{c}(n_s-1)\right) \tag{2.16}$$

which only contains two unknown quantities, the real and imaginary parts of the index of refraction. With both the experimentally measured transmission of the sample and the analytic expression given above one is able to use a Newton-Raphson based numerical algorithm [73] for extracting the complex index of refraction. In a non-magnetic sample one is often interested in the complex optical conductivity of the sample which can be calculated from the index of refraction.

2.5.3 Calculating The Complex Magnetic Susceptibility

The samples discussed in this thesis will be magnetic insulators in which the ultimate goal is to extract the magnetic response, generally in the form of the complex magnetic susceptibility χ_M, of the sample from the complex transmission. However, this is generally problematic for the reasons explained above, the transmission depends on both Z_s and n_s, both complex quantities, while only the complex transmission is measured. Assumptions must be made. To see how the situation is remedied we can expand the expression for the complex transmission given in Eq. 2.15 as:

$$\tilde{T}(\omega) = \frac{4\sqrt{\mu\epsilon}}{(\sqrt{\mu}+\sqrt{\epsilon})^2} \exp\left(i\frac{\omega d}{c}(\sqrt{\mu\epsilon}-1)\right) \tag{2.17}$$

With $\mu = 1 + \chi_M$, we can expand $\sqrt{\mu} \approx 1 + \chi_M/2$ under the assumption that $\chi_M \ll 1$. We can then write the complex transmission as:

$$\tilde{T}(\omega) = \frac{4\sqrt{\epsilon}(1+\chi_M/2)}{((1+\chi_M/2)+\sqrt{\epsilon})^2} \exp\left(i\frac{\omega d}{c}(\sqrt{\epsilon}(1+\chi_M/2)-1)\right) \tag{2.18}$$

Here is it is obvious that the optical response will be dominated by the exponential term in Eq. 2.18. Therefore, we can isolate χ_M by making two measurements of the sample at two distinct temperatures, one above and one below the onset of magnetism or magnetic phenomena. To see how this works, let us assume that at some

temperature, referred to as T_{ref}, the assumption $\mu \approx 1$ applies. We then perform a TDTS transmission measurement of the sample at this temperature and extract the index of refraction, $n_{ref} = \sqrt{\epsilon}$, by numerical inversion of Eq. 2.16.

Now we repeat the above procedure, but at a temperature below the onset of magnetic phenomena where the assumption that $\mu \approx 1$ no longer applies. We again carry out an identical TDTS transmission measurement of the sample. Taking the ratio of these two transmissions gives:

$$\frac{\tilde{T}(\omega)}{\tilde{T}_{ref}(\omega)} \approx \frac{\exp\left(i\frac{\omega d}{c}(\sqrt{\epsilon}(1+\chi_M/2)-1)\right)}{\exp\left(i\frac{\omega d}{c}(\sqrt{\epsilon}-1)\right)} = \exp\left(i\frac{\sqrt{\epsilon}\omega d}{2c}\chi_M\right) \tag{2.19}$$

Eq. 2.19 can then be solved for χ_M to give:

$$\chi_M(\omega) \approx \frac{2ic}{\sqrt{\epsilon}\omega d} ln(\frac{T_{ref}(\omega)}{T(\omega)}) \tag{2.20}$$

The assumption that is made here is that the dielectric properties of the sample do not appreciably change from T_{ref} to lower temperatures, which is generally a good assumption for insulating samples with T_{ref} chosen wisely. The best reference temperature to use depends on the specific details of the sample under consideration. In the best case scenario T_{ref} would be a temperature just above a magnetic ordering temperature of the sample or a temperature above the onset of magnetic fluctuations, for instance the Curie or Néel temperature for a ferromagnetic or antiferromagnetic sample respectively. In other cases magnetic excitations, such as magnetically ac-

tive crystal field levels, may persist to much higher temperatures. In these cases one must chose T_{ref} carefully but as a general rule I would not recommend using a reference temperature above 100K if it can be avoided due to proximity to the Debye temperature of most solids.

The above derivation represents a valid method for extracting the magnetic susceptibility of the sample. However, I've found that a slightly easier and very moderately more accurate method is to treat the sample as if it were nonmagnetic, Eq. 2.16, and then extract the index of refraction with the Newton-Raphson inversion in the normal way. This method makes the same assumption as the derivation above, that $\chi_M \ll 1$, but treats the permittivity as a "generalized permittivity" containing both the electric and magnetic responses. Therefore, the prefactor in the transmission expression Eq. 2.17 isn't completely ignored. Once the index of refraction is extracted as a function of temperature then a reference temperature is chosen in the same fashion as the reference temperature for the transmission above. The index of refraction at the reference temperature is given by:

$$n_{Tref} = \sqrt{\epsilon} \tag{2.21}$$

While the index of refraction at a temperature where the sample is magnetic is given by:

$$n_T = \sqrt{\epsilon(1 + \chi_M)} \tag{2.22}$$

In a similar fashion as above, the ratio of these two indicies of refraction gives:

$$\frac{n_T}{n_{Tref}} = \sqrt{(1+\chi_M)} \tag{2.23}$$

Which can be solved for χ_M as:

$$\chi_M = (\frac{n_T}{n_{Tref}})^2 - 1 \tag{2.24}$$

I've found the two methods described above to give nearly indistinguishable results, with the second method perhaps resulting in a slight improvement particularly at lower frequencies. However, the second method is generally more convenient due to the ease of running the Newton-Raphson inversion and extracting the index of refraction.

2.5.4 Transformation To The Circular Basis and Polarimetry

Often in a TDTS experiment we are not only concerned with the magnitude of the transmission but also the rotation of the plane of polarization of THz light upon transmission, i.e. Faraday rotation, or in some cases upon reflection, i.e. Kerr rotation. These effects become particularly important for experiments performed in magnetic fields as certain magneto-optical phenomena manifest as polarization

rotations. In these cases we represent the complex transmission of the sample in the Jones calculus [74] as a 2×2 complex matrix of the form:

$$\hat{T} = \begin{bmatrix} T_{xx} & T_{xy} \\ T_{yx} & T_{yy} \end{bmatrix}$$

The transmitted electric field through the sample is then given by:

$$\begin{bmatrix} T_{xx} & T_{xy} \\ T_{yx} & T_{yy} \end{bmatrix} \begin{bmatrix} E_x^i \\ E_y^i \end{bmatrix} = \begin{bmatrix} E_x^t \\ E_y^t \end{bmatrix} \tag{2.25}$$

where the superscript i and t refer to incident and transmitted electric fields respectively and the subscript x and y refer to a coordinate axis with respect to the crystal structure.

In the most general case, the transmission matrix contains four independent responses of the sample which can be probed by varying the incident polarization angle to the crystal structure of the material. However, the transmission matrix of a material must obey the same symmetries that are inherent to the material itself [75], which, except in the case of a sample with very low symmetry, generally reduces the number of independent elements in the transmission matrix. The majority of the measurements presented in this thesis were performed in Faraday geometry in which $\vec{k}_{\mathrm{THz}} \parallel \vec{H}_{\mathrm{dc}}$. In this case a material with four fold rotational symmetry, i.e. cubic, or even three fold rotational symmetry, i.e. hexagonal, is enough to restrict the transmis-

sion matrix such that it is fully antisymmetric, i.e. $T_{xx} = T_{yy}$ and $T_{xy} = -T_{yx}$ [75]. Fully antisymmetric transmission matricies can be diagonalized by a circular basis transformation, suggesting experiments performed in Faraday geometry are best understood in the circular basis. Under a circular basis transformation the transmission matrix becomes:

$$\hat{T} = \begin{bmatrix} T_l & 0 \\ 0 & T_r \end{bmatrix}$$

where T_l and T_r refer to the transmission of left and right hand circularly polarized light, the eigenpolarizations of the system, respectively.

When the transmission matrix if fully antisymmetric then off diagonal elements in the linear basis correspond to rotations of the plane of polarization by the sample. Polarization rotation experiments presented in this thesis were done through the use of a rotating wire grid polarizer [76] technique, which allows for measurement of two elements of the transmission matrix, for instance T_{xx} and T_{yx}, simultaneously. If the transmission matrix is fully antisymmetric then this rotating polarizer technique is able to determine the entire transmission matrix of the sample a single measurement. More information on this rotating polarizer technique can be found in Ref. [76]. The complex rotation angle is then given by the relation $\theta = \tan^{-1}(\frac{T_{yx}}{T_{xx}})$ in the linear basis or $\theta = \tan^{-1}(-i(\frac{T_l - T_r}{T_l + T_r}))$ in the circular basis. Much of the data in this thesis will be presented either in the circular basis or as a polarization rotation as described above.

Chapter 3

Microwave Cavity Perturbation Technique

3.1 Introduction

Measurements performed in the microwave frequency range, ($\approx$ 100 MHz - 300 GHz), have historically occurred through the use of microwave cavity resonator techniques. In the perturbation method of cavity resonators [77, 78, 79], a typical experiment begins with the measurement of the resonant frequency, ω_0, and bandwidth, Γ_0, of an empty cavity resonator. An identical measurement is then performed after the insertion of a small sample into the cavity. Upon introduction of the sample, the cavity's resonant frequency, (ω_s), and bandwidth, (Γ_s), are observed to shift due to the material properties of the sample. Assuming the sample constitutes a small

perturbation on the electromagnetic fields contained within the cavity, the complex response of the sample can be related to the frequency shifts $\Delta\omega = \omega_s - \omega_0$ and $\Delta\Gamma = \Gamma_s - \Gamma_0$. While measurements are constrained to only occur at the discreet resonant frequencies of the cavity, the "on resonance" nature results in unprecedented sensitivity, as quality factors, $Q = \omega_0/\Gamma_0$, as high as $Q \approx 10^{10}$ can be achieved with superconducting cavities at low temperatures.

In recent years, new non-resonant techniques capable of performing high resolution broadband microwave spectroscopy have emerged. For instance, measurements performed in Corbino geometry are capable of extracting the complex response of a sample from 10 MHz - 40 GHz with both low temperature and high magnetic field capabilities [80, 81]. In these measurements, microwaves are sent down a coaxial cable which is terminated by a sample arranged in the particular "Corbino" geometry. The amplitude and phase of the reflected microwaves off the sample are then measured and related to the material's complex response. Meanwhile, an additional technique capable of performing highly sensitive microwave measurements of ultra-low-loss samples has been developed [82]. In this method, a sample and a metallic reference are placed inside a rectangular transmission line to which microwaves are then inputted. By carefully measuring the increase in sample temperature resulting from absorbed microwave power, and comparing to the metallic reference, one is able to extract the surface resistance of the sample with an exceptional resolution of $\approx 1\ \mu\Omega$ [82].

However, both of these techniques are not without their faults. Corbino mea-

surements require very exacting calibrations due to the often strong temperature dependence of the impedance properties of the coaxial cables themselves [83]. Additionally, the technique is restricted to samples which possess impedances within a few orders of magnitude of that of the coaxial cable, nominally 50 Ω. While although the transmission line technique possesses high resolution, only the real part of response is measured whereas the complex response is often sought. Therefore, while more modern broadband techniques have been developed, the high sensitivity, relative simplicity, and ability to extract the sample's complex response have resulted in the continued use of cavity resonator techniques, as well as many other resonant techniques (see [84]), to this day.

In this chapter we detail the basics of microwave cavity perturbation technique (MCPT), in which the sample is entirely enclosed within the cavity resonator. We begin by discussing the basics of the cavity resonator and derive the allowed standing wave configurations, or modes, within the cavity. We then discuss the effects of introducing the sample on the modes. We will find that, in the limit of small samples, the frequency shifts of the cavity can be simply related to the complex response of the sample. At the end of this chapter I'll detail the specifics of our experimental MCPT set-up at JHU.

3.2 The Cavity Resonator

A cavity resonator is defined to be a hollow enclosed structure inside which electromagnetic fields can form standing wave configurations, or "modes" [85]. Each mode corresponds to a unique spatially varying electric and magnetic field pattern within the cavity - all oscillating at the mode's resonant frequency ω_0. Upon resonance, a maximum of the cavity's response is achieved. In the context of this thesis, the response will be characterized by transmitted microwave power through the cavity.

As we will see, the resonant frequencies of a cavity resonator are determined solely by the size and geometry of the cavity. Since each resonance corresponds to an integer number of half wavelengths between the walls of the cavity, the dimensions of the cavity are of order of the free space wavelength. With typical resonant frequencies of 1 - 100 GHz, cavity dimensions are therefore of order 1 - 10 cm. The electromagnetic fields within the cavity are easiest to calculate when the cavity is highly symmetric, i.e. of spherical, cubic, or cylindrical geometry. However, highly symmetric cavity designs result in degeneracies of resonant frequencies. That is, two or more modes with the same resonant frequency but different field configurations. Therefore, a middle ground between high and low symmetry cavity designs are preferable. For this reason, right circular cylindrical cavities whose height and diameter differ by roughly 50%, have become fairly standard [78]. Such a design will be the focus of the rest of this chapter.

3.2.1 Resonant Modes Of A Cylindrical Cavity Resonator

The goal of this section is to calculate the spatial and time dependent electromagnetic fields and corresponding resonant frequencies of each mode of a cylindrical cavity resonator. The cavity under consideration is assumed to be ideal, i.e. possessing perfectly conducting walls, with dimensions of radius R and height h. The derivation below closely follows the exposition of Ref. [86].

We begin our calculation with Maxwell's equations:

$$\begin{aligned} \nabla \cdot \mathbf{E} &= \rho \\ \nabla \cdot \mathbf{B} &= 0 \\ \nabla \times \mathbf{E} &= -\frac{\partial \mathbf{B}}{\partial t} \\ \nabla \times \mathbf{B} &= \mu_0 \mathbf{J} + \mu_0 \epsilon_0 \frac{\partial \mathbf{E}}{\partial t} \end{aligned} \tag{3.1}$$

As there are no sources of charge or current inside the cavity, we can set $\mathbf{J} = \rho = 0$. Additionally, we assume that all fields have the usual sinusoidal time dependence $e^{-i\omega t}$. Applying these conditions and uncoupling Maxwell's equations reveals that both the electric and magnetic fields must obey the Helmholtz wave equation given by:

$$(\nabla^2 + \mu\epsilon_0\omega^2)\{\begin{matrix}\mathbf{E} \\ \mathbf{B}\end{matrix}\} = 0 \tag{3.2}$$

At this stage there are still six unknowns, the three spatial components of the vectors **E** and **B**. However, thanks to Maxwell's equations, the field components are not entirely independent. In fact, it is sufficient for us to solve for only E_z *or* B_z, from which all transverse components of the fields can be derived. Solutions to Eq's. 3.2 come in three varieties: transverse electric (TE) in which $E_z = 0$, transverse magnetic (TM) in which $B_Z = 0$, or transverse electromagnetic (TEM) in which both $E_z = 0$ and $B_z = 0$. However, cavity resonators can only support TM or TE modes. Here we choose the solution for TE modes, as these modes will be more relevant for the remainder of this chapter. However, the derivation for the TM modes follows very closely and can be found in Ref. [86].

Before proceeding with the calculation, we must first specify boundary conditions. For a perfectly conducting cavity, continuity across the cavity wall dictates the boundary conditions $\mathbf{n} \times \mathbf{E} = 0$ and $\mathbf{n} \cdot \mathbf{B} = 0$, where $\mathbf{n}$ is a unit vector perpendicular to the surface of the cavity. For TE modes these reduce to $\partial B_z/\partial n|_s = 0$. Additionally, the end plates of the cavity ensure that $B_z = 0$ at $z = 0$ and $z = h$. These constraints suggest the longitude component of the magnetic field has the form:

$$H_z = \Psi(r, \theta) \sin\left(\frac{p\pi z}{h}\right) \qquad (p = 1, 2, 3, ...) \tag{3.3}$$

Inserting Eq. 3.3 into Eq. 3.2 reveals that the function $\Psi(r, \theta)$ must then satisfy the

transverse wave equation:

$$(\nabla_t + \gamma^2)\Psi(r,\theta) = 0 \tag{3.4}$$

where ∇_t is the transverse part of the Laplacian operator and γ is a constant given by:

$$\gamma^2 = \mu_0\epsilon_0\omega^2 - (\frac{p\pi}{h})^2 \tag{3.5}$$

All that remains now is to solve Eq. 3.4 for $\Psi(r,\theta)$. Once known, all field components are explicitly defined by Maxwell's equations:

$$\begin{aligned} E_z &= 0 \\ E_t &= -(\frac{i\omega\mu_0}{\gamma^2})\sin(\frac{p\pi z}{h})[\hat{z}\times\nabla_t\Psi(r,\theta)] \\ H_z &= \psi(r,\theta)\sin(\frac{p\pi z}{h}) \\ H_t &= (\frac{p\pi}{d\gamma^2})\cos(\frac{p\pi z}{h})\nabla_t\Psi(r,\theta) \end{aligned} \tag{3.6}$$

The resonant frequencies of each mode are then found by solving for ω in Eq. 3.5.

Eq. 3.4 can be solved by a standard separation of variables approach. The radial equation is solved by the cylindrical Bessel functions $J_m(\gamma_{mn}r)$ with $m = (0,1,2,...)$ while the azimuthal equation is solved in the normal fashion by $\exp(\pm im\phi)$. Together, these form the general solution:

$$\Psi(r,\theta) = H_0 J_m(\gamma_{mn}r)\exp(\pm im\theta) \qquad (m = 0,1,2,...) \tag{3.7}$$

	x_{m1}	x_{m2}	x_{m3}
$m = 0$	3.832	7.016	10.173
$m = 1$	1.841	5.331	8.536
$m = 2$	3.054	6.706	9.970
$m = 3$	4.201	8.015	11.336

Table 3.1: The first few roots of the first derivative of the cylindrical Bessel functions, i.e. the "x_{mn}" in Eq. 3.8.

The boundary condition $H_z \frac{\partial \Psi}{\partial r}|_R = 0$ mandates that the $\gamma_{mn} = x_{mn}/R$ where the x_{mn} are the"nth" roots of the first derivative of the "mth" cylindrical Bessel function. Table 3.1 displays the first few x_{mn} for TE modes.

With $\Psi(r, \theta)$ determined, the problem is now solved as all field can be calculated explicitly from Eq. 3.6. The resonant frequencies are then determined by substituting the γ_{mn} into Eq. 3.5 and solving for ω from which we find:

$$\omega_{mnp}^{TE} = \frac{1}{\sqrt{\epsilon_0 \mu_0}} \sqrt{\frac{x_{mn}^2}{R^2} + \frac{p^2 \pi^2}{h^2}} \qquad \begin{cases} m = (0, 1, 2, ...) \\ n = (1, 2, 3, ...) \\ p = (1, 2, 3, ...) \end{cases} \tag{3.8}$$

respectively. Thus, the all fields and resonant frequencies have been found.

Since the cylindrical Bessel functions (and their derivatives) have an infinite number of roots, there are an infinite number of modes which can resonate for a particular cavity geometry. Fig. 3.1 displays the resonant frequency of the 20 lowest TE (blue) and TM (red) modes found from Eq. 3.8 with $h = 18$mm and $R = 12$ mm. One can see from Table 3.1 and Fig. 3.1 that the lowest frequency TE mode is the TE_{111}

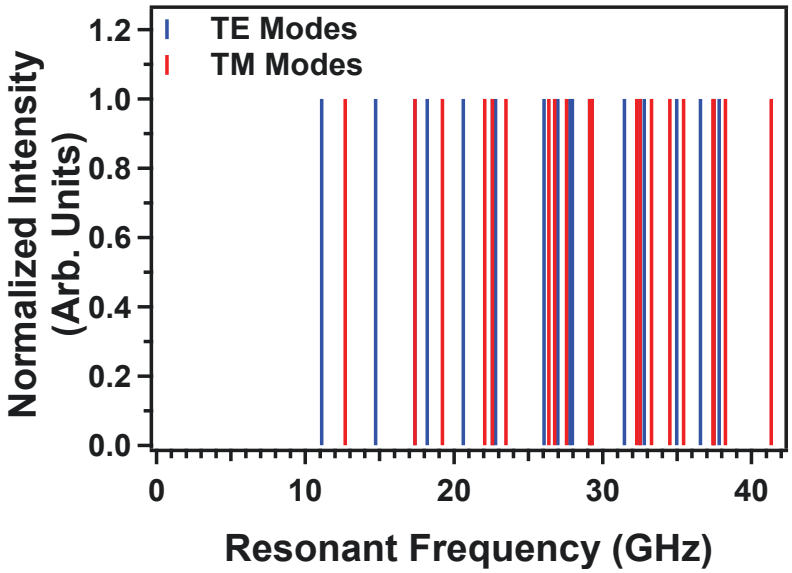

Figure 3.1: Resonant frequencies of the 20 lowest TE (blue) and TM (red) modes of a cylindrical cavity resonator of height $h = 18$mm and radius $R = 12$mm. The intensity of each mode has been normalized to unity.

mode. No resonances can exist for frequencies below that of this mode. This low frequency cut-off physically corresponds to the inability to fit an integral number of half wavelengths between the walls of the cavity. Above the TE_{111} mode there are an infinite number of resonances with increasing resonant frequencies, becoming more densely spaced as the orders of the modes increase.

By far the most important mode in cavity resonator experiments is the TE_{011} mode. As we will show later, the TE_{011} mode possesses a relatively simple, but very important, field configuration which results in the highest achieved Q-factor of all resonances [77, 78]. For this reason, many cavity experiments, including all of our own, exclusively measure with this resonance. Fig. 3.2 displays a simulation

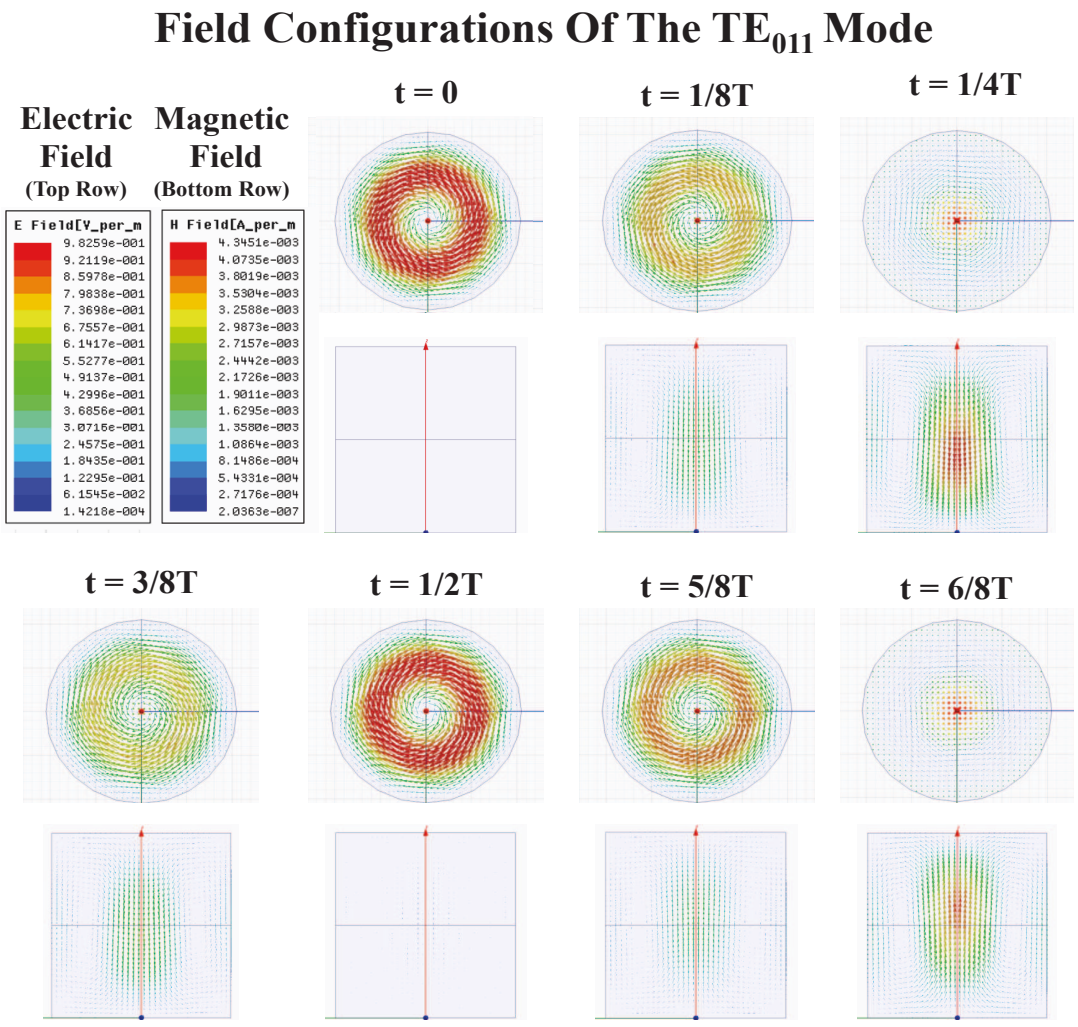

Figure 3.2: Simulations of the electric field (top row) and magnetic field (bottom row) of the TE_{011} mode of a cylindrical cavity resonator found by numerically solving Maxwell's equations inside the cavity. Each panel corresponds to a snapshot of the fields at some fraction of the overall period T.

of the electric field (top row) and magnetic field (bottom row) of the TE_{011} mode of a cylindrical cavity resonator found by numerically solving Maxwell's equations inside the cavity. More details regarding the TE_{011} mode will be provided later in this chapter.

3.2.2 Introducing Dissipation

As shown in section 3.2.1 and Fig. 3.1, an ideal perfectly conducting cavity resonates at discrete resonant frequencies. The frequency profiles of these resonances are delta functions, possessing infinitely narrow width and therefore infinite lifetimes. Of course, real cavities do not possess perfectly conducting walls and finite dissipation will occur. To see how this loss changes the resonance profile, we follow the derivation of Ref. [86] by defining the quality factor, or Q-factor, of the cavity as:

$$Q = 2\pi \frac{\text{Total energy contained in resonator}}{\text{Energy dissipated per period}} \tag{3.9}$$

If the total energy stored in the cavity is $U(t)$ then 3.9 can be written mathematically as:

$$Q = \omega_0 \frac{U(t)}{dU(t)/dt} \tag{3.10}$$

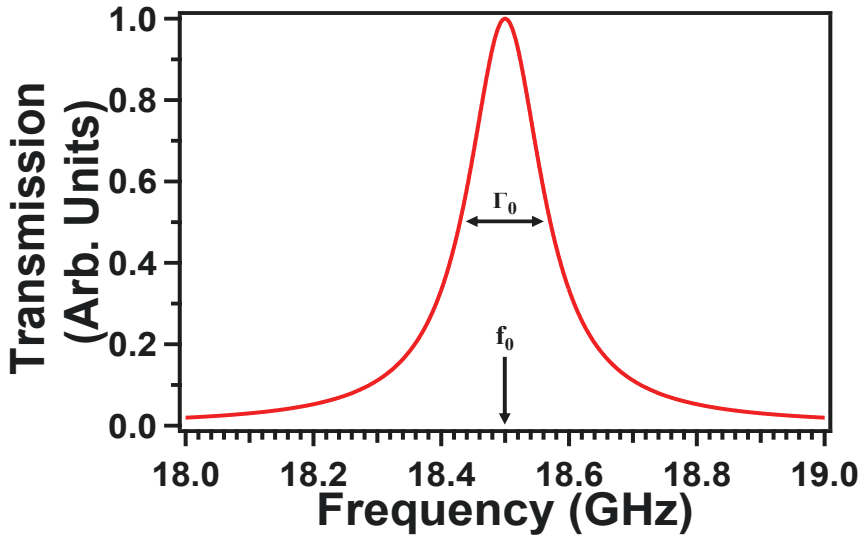

Figure 3.3: The frequency profile of a cavity resonance is a Lorentzian peak centered at f_0 with full width at half the maximum of Γ_0. Shown here is a resonance with f_0 = 18.5 GHz and a width of $\Gamma_0 = 0.2$ GHz. In actual cavities the width will often be orders of magnitude smaller than what is shown here.

where ω_0 is the resonant frequency of the lossless cavity. Solving this differential equation for $U(t)$ gives:

$$U(t) = U_0 \exp\left(-\frac{\omega_0}{Q}t\right) \tag{3.11}$$

Eq. 3.11 demonstrates that the energy stored in the cavity decays exponentially with a time constant $\tau = Q/\omega_0$. This suggests that the time dependence of the fields can be written as

$$E(t) = E_0 \exp\left(-\frac{\omega_0 t}{2Q}\right) \exp\left(-(\omega_0 + \delta\omega)t\right) \tag{3.12}$$

where a small shift in resonant frequency, $\delta\omega$ results from the damping.

The frequency profile of the transmitted power through the cavity on resonance

can then be found by squaring and Fourier transforming Eq. 3.12 to give:

$$P(\omega) \propto |E(\omega)|^2 \propto \frac{1}{(\omega - \omega_0 - \delta\omega)^2 + (\omega_0/2Q)} \tag{3.13}$$

Eq. 3.13 reveals that the power transmitted through the cavity near resonance is a Lorentzian peak centered at $\omega_0 + \delta\omega$ with full width at half maximum of $\Gamma_0 = \omega_0/Q$ (Fig. 3.3). Thus we see that loss in the cavity results in a broadening of the resonance peak, and therefore a finite lifetime, by an amount related to the dissipation. Additionally, this calculation shows that the resonance properties of the cavity can be entirely characterized by only two parameters, ω_0 and Γ_0. These are precisely the quantities measured in an MCPT experiment.

3.2.3 Maximizing Cavity Q-Factor

One can see from section 3.2.2 that the Q-factor is also indicative of measurement sensitivity as higher Q's correspond to narrower resonance peaks and therefore enhanced ability to measure resonant frequencies. Therefore, every effort when designing resonant cavities should be made to minimize dissipation and correspondingly maximize the Q-factor. Extreme care must be taken when designing a resonant cavity as the cavity dimensions, fabrication material, and choice of resonance mode all influence the ultimate Q-factor of the cavity. In this section I will elaborate on some of the more important choices that go into the design and fabrication of an excep-

tionally sensitive microwave cavity resonator. For a more in depth discussion see Ref. [78].

Energy loss in cavity resonators predominantly stems from two sources: dissipation in the cavity walls and coupling to the cavity. These two loss mechanisms, and others if present, reduce the total Q-factor by inversely adding as:

$$\frac{1}{Q_{\text{Tot}}} = \frac{1}{Q_{\text{walls}}} + \frac{1}{Q_{\text{Coupling}}} + ... \tag{3.14}$$

If large Q-factors are to be obtained, then every effort must be taken to reduce loss from these mechanisms. This is singly handedly the most important and most difficult aspect of designing an MCPT system.

Reducing loss from dissipation in the cavity walls is the easier of the two mechanisms to combat. High Q-factor cavities are often fabricated from superconducting materials, i.e. Pb or Nb, to reduce dissipation from currents running in the walls of the cavity. It is often preferable to use a superconductor with the highest T_c possible as higher T_c's correspond to larger temperature ranges in which high resolution measurements can be performed. One downside of the superconducting cavity design is that it limits the ability to perform experiments as a function of magnetic field, as strong magnetic fields may drive the cavity to the normal state. For measurements which require applied magnetic fields, cavities are typically constructed out of oxygen-free copper. However, the Q-factors attained with these cavities are orders of

magnitude lower then their superconducting counterparts.

Larger Q-factors can also be achieved through careful choice of the resonance mode used for measurements. The conventional cavity design consists of a right circular cylinder constructed in three separate parts - a top plate, a cylindrical body, and a bottom plate. These pieces are usually screwed together to form the resonator. While fabricating the cavity out of a superconducting material limits loss within one piece of the cavity, losses which occur from currents running *between* pieces of the cavity remain a serious issue as the contact resistance at these junctions can be comparatively large. This is precisely why the TE_{011} mode possesses the highest Q-factor and is the preferred mode of resonance for cavity measurements. The transverse electric nature of this mode, i.e. $E_z = 0$, ensures no current runs between any of the three pieces of the cavity. All currents in this mode run circumferentially.

Unfortunately, in cylindrical cavities the TE_{011} mode is degenerate in resonant frequency with the TM_{111} mode. If measurements are to be performed with the TE_{011} mode then this degeneracy must be broken. One method of doing so is by cutting grooves into the top and bottom of the cavity where the fields of the TM_{111} mode are maximum but the fields of the TE_{011} mode are weak. This makes the cavity appear effectively larger to the TM_{111} mode, thereby shifting it's resonance frequency well below that of the TE_{011} mode. Figure 3.4 displays the results of cutting such grooves into one of our cavities in which a groove of only $\approx$ 1-2% of the cavity diameter is enough to split the modes by $\approx$ 100 MHz. At low temperatures, within

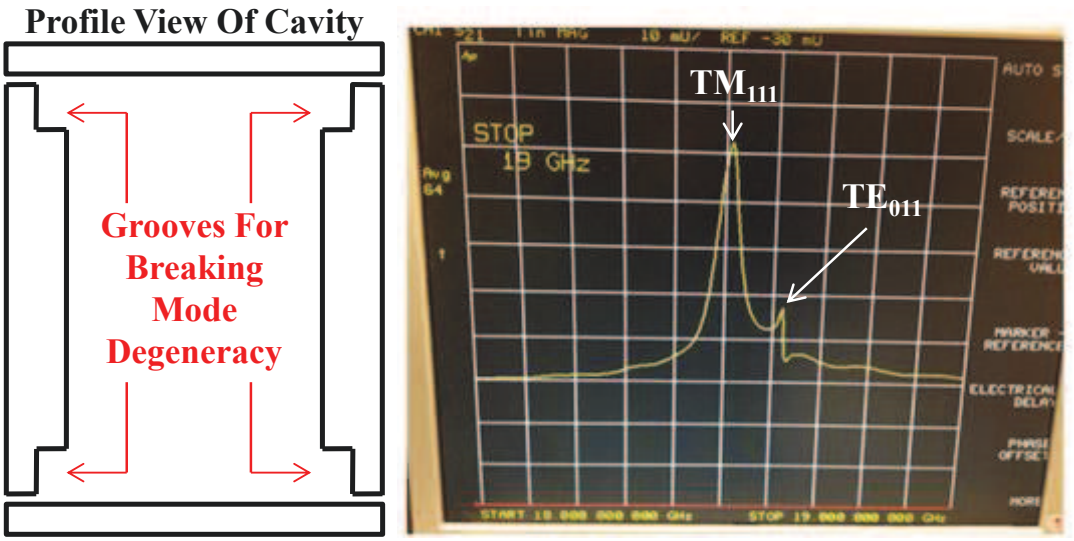

Figure 3.4: (left) Grooves cut into the top and bottom of the cylindrical body of the cavity can used to split the degeneracy between the TM_{111} and TE_{011} modes. (right) Room temperature frequency scan showing the TM_{111} and TE_{011} resonance peaks of such a resonator in our lab. Splitting of these modes by $\approx$ 100 MHz was achieved by cutting small square grooves of only 0.25 mm $\times$ 0.25 mm into a cavity with a diameter of 20 mm. One can see that the TM_{111} mode is significantly broader due to the enhanced dissipation of currents running between pieces of the cavity. Although the TE_{011} mode is sitting on the "tail" of the TM_{111} mode at room temperature, these modes will narrow considerably at low temperatures when the cavity is in the superconducting phase such that they will be well separated in frequency.

the superconducting phase of the cavity, these resonance peaks will substantially narrow such that they are well separated in frequency, allowing for measurements of only the TE_{011} mode to be performed.

Optimizing the coupling to the cavity is a much more formidable task. Coupling can be achieved either by capacitive coupling to the electric field or inductive coupling to the magnetic field of the mode of resonance. For the TE_{011} mode, the conventional method is by placing inductive antenna loops soldered to the ends of coaxial cables

at the maximum of the magnetic field of the TE_{011} mode which occurs at the ends of the cavity at roughly half the radius away from the center. When microwaves are sent down one cable, they generate a time varying current in the antenna loop which then broadcasts a time varying magnetic field to the cavity. As the antenna lies at the maximum of the magnetic field of the TE_{011} mode, this naturally couples to this particular standing wave configuration. An identical antenna, which lies at an identical position on the other side of the cavity, carries the transmitted microwave signal out of the cavity in the reverse manner.

The above description reveals exactly how coupling reduces the Q-factor of the cavity - the role of the receiving antenna is to remove energy from the cavity. Finding the correct balance between over-coupling, where the intensity of the resonance peak will be large and easily measured but the Q-factor will suffer, and under-coupling, where the Q-factor will be large but the intensity will be weak, is a major challenge of these techniques. This is further complicated by the fact that the temperatures at which you ideally want to adjust the coupling is below the superconducting transition of the cavity. The groups who perform these measurements exceptionally well have experimental set-ups where the coupling can be changed *in situ* by literally moving the coaxial cables attached to the antenna in and our of the cavity by hand. This adaptive coupling mechanism ensures the Q-factor can be optimized for every sample measurement. For experimental set-ups which do not possess this ability, optimal coupling must be achieved through a "trial and error" fashion.

Cavities which are carefully designed with the above considerations will routinely possess Q-factors on the order of 10^4 - 10^8 which corresponds to the ability to resolve resonant frequencies in the GHz range to within 1-100 Hz.

3.3 Microwave Cavity Perturbation Technique

In this section we detail how to mathematically relate the shifts in resonant frequency $\Delta\omega = \omega_s - \omega_0$ and bandwidth $\Delta\Gamma = \Gamma_s - \Gamma_0$ of a cavity resonator upon introduction of a sample to the complex response of that sample. The techniques relies on the fact that the introduction of the sample is a small perturbation on the overall structure of the electromagnetic standing wave pattern within the cavity and is therefore adiabatic. In this case, only linear effects need to be considered which greatly reduces the complexity of the calculation. After deriving the general result for cavity perturbation analysis, we discuss two distinct limits. First, the "depolarization regime," in which the microwaves completely penetrate the sample, and second, the "skin-depth regime," in which the microwaves are confined to a small regions near the sample surface.

3.3.1 The Cavity Perturbation Equation

The goal of this section is to derive the general result for cavity perturbation techniques before dealing with specific cases. Before proceeding with the calculation, we must first define the "complex frequency." It should be noted that different conventions of this definition exist. Here I use the definition provided in Ref. [85], in which the "complex" frequency shift is defined as:

$$\Delta\tilde{\omega} = \Delta\omega - \frac{i}{2}\Delta\Gamma = \omega_s - \omega_0 - \frac{i}{2}(\Gamma_s - \Gamma_0) \tag{3.15}$$

where the subscripts "0" and "s" refer to the unloaded (or empty) cavity and the loaded (containing a sample) cavity respectively.

Let us assume that the electric and magnetic fields inside the unloaded cavity in a particular resonance mode can be described as:

$$E = E_0 e^{i\omega t} \tag{3.16}$$

$$H = H_0 e^{i\omega t} \tag{3.17}$$

where E_0 and H_0 are functions of space. Upon introduction of a small, perturbative sample into the cavity. The fields are modified as:

$$E^{'} = (E_0 + E_1)e^{i(\omega+\Delta\omega)t} \tag{3.18}$$

$$H^{'} = (H_0 + H_1)e^{i(\omega+\Delta\omega)t} \tag{3.19}$$

The goal is now relate $\Delta\omega$ to the complex fields within the cavity. The remainder of this calculation involves an enormous amount of vector calculus and algebra and is not particularly enlightening. Therefore, I will only quote the result here and would direct readers to Refs. [85] or [87] for the full derivation.

The result of the calculation is:

$$\frac{\Delta\tilde{\omega}}{\omega} = \frac{\int_{V_{\text{sample}}}[(E_1 \cdot D_0 - E_0 \cdot D_1) - (H_1 \cdot B_0 - H_0 \cdot B_1)]dV}{\int_{V_{\text{cavity}}}(E_0 \cdot D_0 - H_0 \cdot B_0)dV} \tag{3.20}$$

This equation is the main result of microwave cavity perturbation. Eq. 3.20 demonstrates that a measurement of $\Delta\tilde{\omega}$ and knowledge of the fields of the unperturbed cavity can be used to calculate the fields within the sample. The fields can then be related to the sample's complex response, i.e. optical conductivity or magnetic susceptibility. This is more easily seen if we recast Eq. 3.20 as:

$$-\frac{\Delta\tilde{\omega}}{\omega} \approx \frac{\tilde{\chi_M}\mu_0}{4 < U >}\int(H \cdot H_0)dV_s + \frac{\tilde{\chi_E}\epsilon_0}{4 < U >}\int(E \cdot E_0)dV_s \tag{3.21}$$

where $\tilde{\chi_M}$ and $\tilde{\chi_E}$ are the complex magnetic and electric susceptibilities of the sample and $< U >$ is the average energy of the resonance mode in the cavity [88].

Numerical solutions to Eq. 3.20 or Eq. 3.21 are generally possible for all sample shapes and positions within the cavity. However, analytic solutions are generally

only feasible for simple sample geometries (spheres, ellipsoids, thin plates, etc.) in which case the depolarization or demagnetization factors of the sample are known. Additional simplifications occur when the sample is placed at specific positions within the cavity where it is known that either the electric field or magnetic field is zero, which greatly simplifies the right side of Eq. 3.21.

There has truly been an immense amount of calculations performed regarding various sample geometries, in various cavity positions, of various modes, of various cavity geometries [77, 78, 79, 89, 90, 91, 92, 93, 94]. Far more work has been done then could ever reasonably be written about here. Instead I will focus on the case which is specifically relevant to our own measurements. Our cavity resonator is designed such that the sample is placed at the magnetic field antinode, and therefore an electric field node, of the TE_{011} mode (Fig. 3.2) which occurs at the center of the cavity. For the calculations involving a sample placed at an electric field antinode I recommend reading Refs. [77, 78, 79].

3.3.2 Sample In The Magnetic Field Antinode Of The TE_{011} Mode

An excellent treatment of the appropriate analyses for cavity perturbation experiments performed with a sample placed in a the magnetic field maximum of the TE_{011} mode can be found in Ref. [88]. We follow their derivations here and in the

next several sections. A surprising result of placing the sample in the magnetic field antinode is that the measured frequency shift contains components from both the dielectric and magnetic responses of the sample, even though the electric field at this position is zero. It is therefore best to characterize the sample's response in terms of a generalized electromagnetic susceptibility $\tilde{\zeta}$ which contains both magnetic and electric components. Eq. 3.21 can then be rewritten in the much simpler form:

$$\Delta\tilde{\omega} = -\gamma\tilde{\zeta} \tag{3.22}$$

where γ is a geometric factor which depends on the sample geometry, cavity geometry, and mode of resonance.

With the wave vectors both outside, $k_0 = \omega/c$, and inside, $k = k_0\sqrt{\tilde{\epsilon} + i\tilde{\sigma}/\omega\epsilon_0}$, the sample defined, the generalized susceptibility can be written in the limit that $k_0 a \ll 1$ as:

$$\tilde{\zeta} = 3\frac{\tilde{\mu}-1}{\tilde{\mu}+2} + \frac{9}{10}[\frac{\tilde{\mu}^2 - 6\tilde{\mu} + 4}{(\tilde{\mu}+2)^2}(k_0 a)^2 + \frac{\tilde{\mu}}{(\tilde{\mu}+2)^2}(ka)^2] \tag{3.23}$$

where $\tilde{\mu} = \chi_M + 1$ is the permeability of the sample and a is the sample dimension.

Extracting the susceptibilities in either the depolarization regime or skin-depth regime can be done by taking the appropriate limits of Eq. 3.23 and inserting into Eq. 3.22.

3.3.3 The Depolarization Regime

In this limit, most applicable to insulating dielectrics, the microwaves are assumed to completely penetrate the sample. Extraction of either $\tilde{\chi}_M$ or $\tilde{\chi}_E$ depends on the relative strength of $\tilde{\epsilon}$ compared to $\tilde{\mu}$.

For magnetic insulators, in which $\epsilon \approx 1$ and $\sigma \approx 0$, $ka \approx k_0 a$ and $\tilde{\zeta}$ is dominated by the first term in Eq. 3.23. The complex generalized susceptibility can then be reduced to:

$$\tilde{\zeta} = \frac{\tilde{\chi}_M}{1 + N_M \tilde{\chi}_M} \tag{3.24}$$

where N_M is the demagnetization factor of the sample. In this fashion, measurement of the complex frequency shift of the cavity is a direct measure of the magnetic susceptibility of the sample.

For sample's with even moderate dielectric properties, ζ is dominated by the last term in Eq. 3.23. In this limit that $\tilde{\mu} \approx 1$, we can write the generalized susceptibility as:

$$\tilde{\zeta} = \frac{1}{10}(k_0 a)^2 \tilde{\chi}_E \tag{3.25}$$

and we therefore see that measurement of the complex frequency shift of the cavity is then a measure of the samples dielectric susceptibility.

3.3.4 The Skin-Depth Regime

An additional regime of interest pertains to samples with large conductivities in which case the microwaves are confined to a sheath close to the sample surface, i.e. the skin-depth. In this case the wave vector of the fields inside the sample becomes $ka = (1+i)a\sqrt{\mu_0\omega\tilde{\sigma}}$ and Eq. 3.22 can be written as:

$$\frac{\Delta\widetilde{\omega}}{\omega_0} = \xi\tilde{Z}_s + \lim_{\sigma\to\infty}\frac{\Delta\widetilde{\omega}}{\omega_0}, \tag{3.26}$$

where $Z_s = R_s + iX_s$ is the sample's complex surface impedance. The constants ξ and limit of $\frac{\Delta\widetilde{\omega}}{\omega_0}$ as $\sigma \to \infty$ are known as the "resonator constant" and "metallic shift" respectively, both of which depend on the mode of resonance, the sample geometry, and the sample position within the cavity. Explicit expressions for these constants for simple sample geometries can be found in [77]. Physically, the metallic shift corresponds to the expected shift in resonant frequency that would result if the sample were a perfect conductor. Of course all samples will have finite dissipation as light can penetrate the sample over small distances near the surface. The role of the term proportional to $\tilde{Z}_s$ in Eq. 3.26 is to account for this dissipation. It serves as a corrective factor which accounts for the finite skin depth (or penetration depth in the superconducting case) of the sample.

Once Z_s is known, the complex conductivity of the sample can then be calculated

from:

$$\tilde{Z}_s = \sqrt{\frac{i\omega\mu_0}{\tilde{\sigma}}} \tag{3.27}$$

3.4 Our MCPT Experiment

3.4.1 Overview

Fig. 3.5 shows a blown up schematic of our MCPT experiment at JHU. A rough description of the system is as follows. Microwaves are generated by a vector network analyzer (VNA) and fed via low loss coaxial cables into our cryogenic insert. The microwaves travel down the insert via copper coaxial cables before being fed through a vacuum connection and into a vacuum can which houses the cavity. An additional coaxial cable, which is terminated by a small antenna loop, carries the signal into the cavity resonator. When the microwave frequencies are scanned in the neighborhood of resonance, the antenna broadcasts a time dependence magnetic field which couples to the TE_{011} mode. On resonance, transmission through the cavity is maximized allowing for reception by an identical antenna placed on the other side of the cavity. The transmitted microwaves are then returned to the VNA by an identical set of coaxial cables. A LabView program then retrieves the data from the VNA, fits the resonance peak to a Lorentzian function, extracts the resonant frequency and bandwidth, and then sets the parameters on the VNA for the next scan. Repetition of this entire process as a function of temperature results in acquisition of the temperature

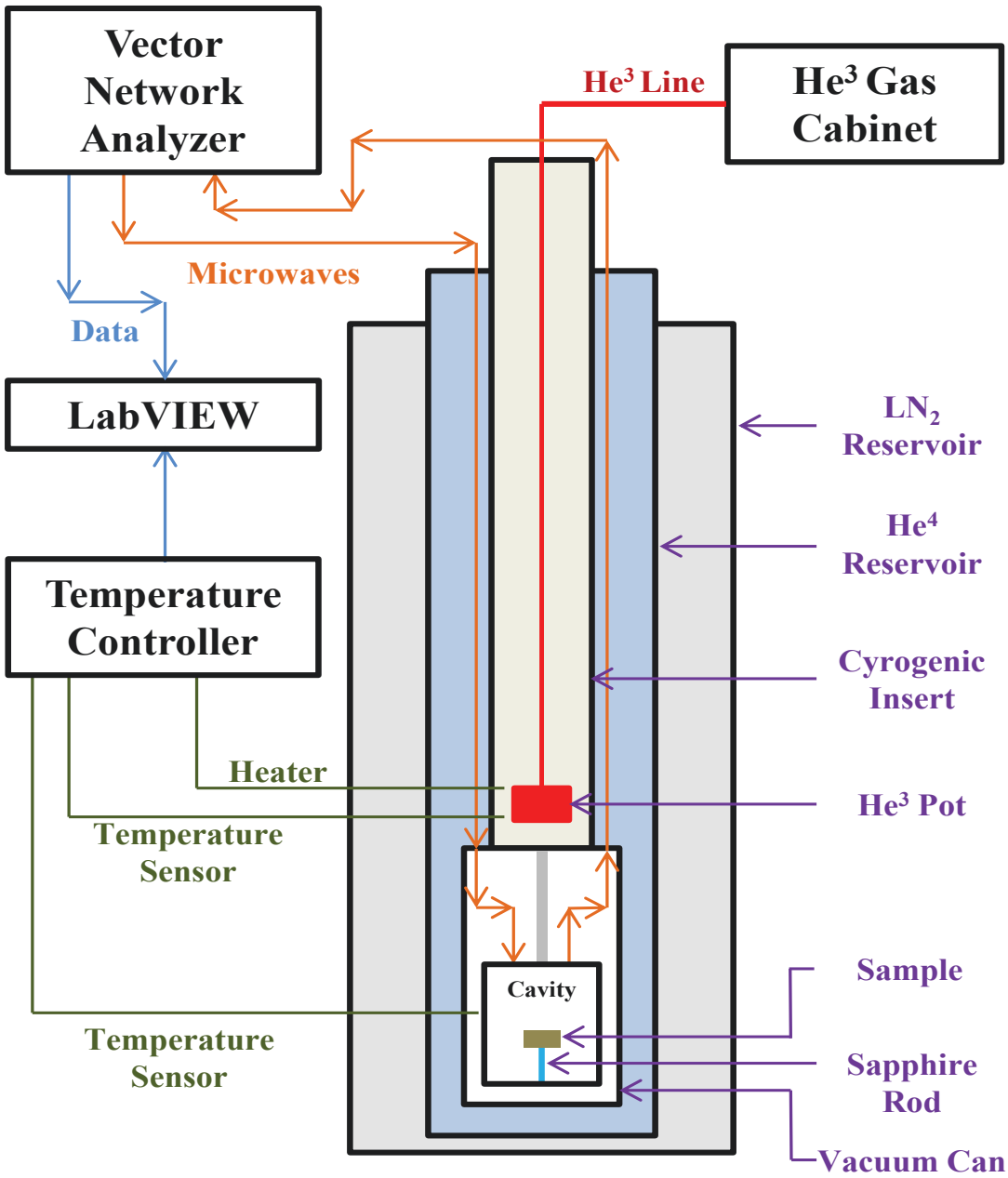

Figure 3.5: Blown up schematic of our MCPT experiment at JHU. Relative sizes of various parts have been exaggerated for clarity.

dependent complex response of the sample.

Base temperature of the experiment is reached by first filling the cryostat with liquid He^4. By pumping on the He^4 bath, thereby reducing the vapor pressure, the experiment can be cooled to $\approx$ 1.8 K. He^3 is then pumped from an external gas cabinet into a small enclosed space within the insert known as the "He^3 pot" which lies just above the cavity. At such low temperatures the He^3 condenses into a liquid which can then also be pumped on to cool the system down to temperatures as low as 350 mK. Temperature is controlled by a small 25 Ω resistor attached to the outside of the He^3 pot and monitored by separate temperature sensors placed on the He^3 pot and cavity.

In this section, I'll detail all the equipment and design considerations that went into building our MCPT experiment. Some of the equipment was recycled from use in Prof. George Grüner's group at UCLA. While other components were either bought or designed in-house here at JHU. Before proceeding it is important to say that I have kept meticulous notes regarding the design of the MCPT system. Anything not included here is almost certainly included in my lab notebook. I encourage any new user to read through it before attempting to run the experiment.

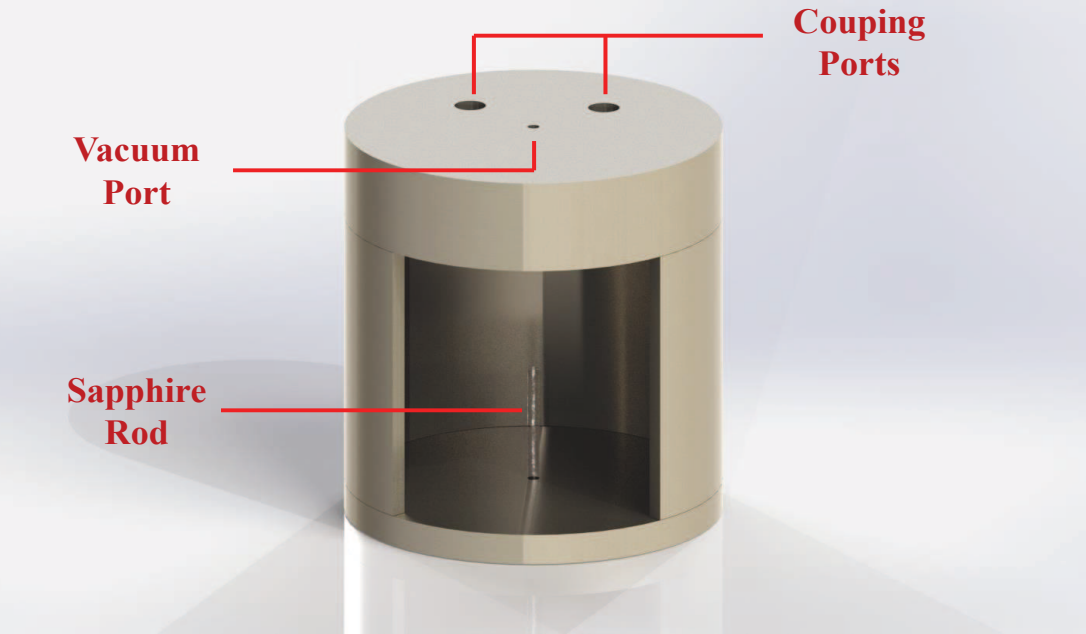

Figure 3.6: A computer generated sketch of the design of our cavity resonator. a cut away on the front is included so that the sapphire rod, used to mount a sample, is visible. The top plate contains holes for inserting coaxial cables with small antenna to couple to the cavity. These coupling ports are located at the magnetic field maximums of the TE_{011} mode. An additional hole in the top plate is used to pump out the cavity. See text for more details.

3.4.2 Equipment

3.4.2.1 The Resonating Cavity

Fig. 3.6 displays a computer generated sketch of our cavity with an opening in the front so that the inside can be viewed. Our cavity is a right circular cylinder fabricated out of NbTi, $T_c \approx 10$K, designed to resonate on the TE_{011} mode. The cavity has a height of $h = 22.3$mm and radius $R = 11.5$ mm. Rectangular grooves of 0.25mm $\times$ 0.25mm were cut into the cavity top and bottom (Fig. 3.4) to break the degeneracy between the TM_{111} and TE_{011} modes. With these dimensions, Eq. 3.8 suggests an expected resonant frequency of $\omega_0 \approx 18.68$ GHz for the TE_{011} mode which is in remarkably good agreement with our observed resonant frequency of $\omega_0 \approx 18.66$ GHz at low temperatures. With an observed bandwidth of $\Gamma_0 \approx 10$ kHz, we achieve Q-factors of $Q \approx 2 \times 10^6$. The optimal coupling was achieved by inserting of a 1 mm NbTi disc with an identical design as the top plate between the cavity body and top plate, effectively pulling the antenna further out of the cavity. Spacers of different sizes can be inserted here to further tune the coupling. Samples are inserted into the cavity by mounting to a small sapphire rod with thermal grease which places the sample at a magnetic field antinode of the TE_{011} mode. Fig. 3.7 displays the temperature dependence resonant frequency and bandwidth of our NbTi cavity. Large changes near 8K result from the superconducting transition of the cavity.

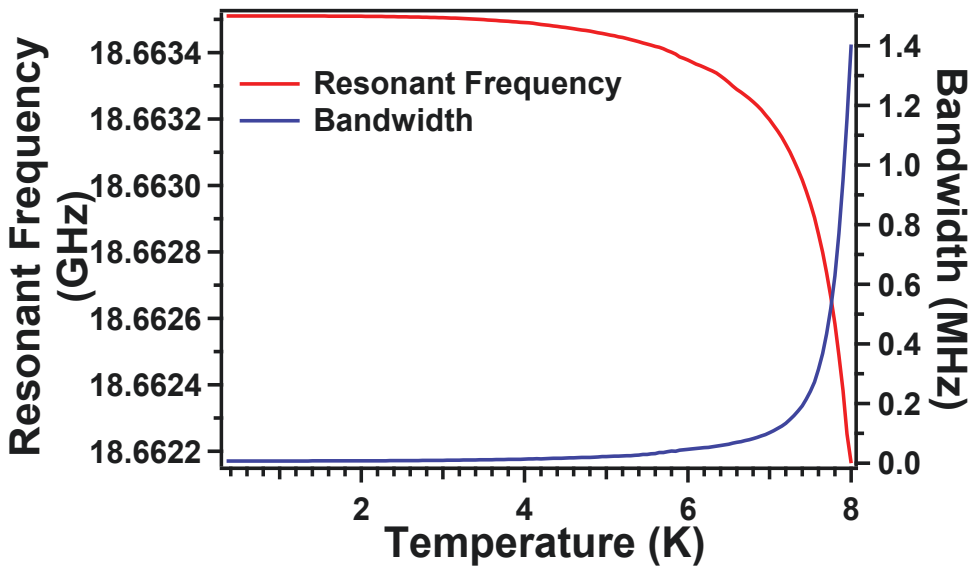

Figure 3.7: Temperature dependence of the resonant frequency and bandwidth of our NbTi cavity resonator. Large changes in both quantities near 8K result from the superconducting transition of the cavity.

3.4.3 Microwave Components

Microwaves are generated and received by a Hewlitt-Packard 8720D Vector Network Analyzer (VNA) which is capable of producing microwaves with frequencies between 50 MHz - 20 GHz. The microwaves are transported out of the VNA and into the cryogenic insert via low attenuation Cinch Connectivity Solutions Semiflex coaxial cables purchased from Digi-Key (PN: 1255-1019-ND). Microwaves are then carried down the cryogenic insert by standard 50Ω R086 semi-rigid copper coaxial cables. The copper coax cables terminate at the vacuum connections at the top of the vacuum can. From the top of the vacuum can to the just above the cavity special low thermal conductivity coaxial cables are used to limit additional heating near the

He^3 pot. The cables are model ULT-10 Keycom Characteristic Technologies cables of length 139 mm. All microwave connections on the experiment are SMA.

3.4.3.1 Cryogenics

Our cryostat is a Cryo Industries of America Inc. Model 4CR-CN Helium Research Dewar. The structure of the cryostat, from outside to inside, consists of a vacuum jacket filled with super-insulation, a liquid nitrogen reservoir, an additional vacuum jacket, and then a liquid helium (LHe) reservoir. The LHe space is cylinder with a height of 62 inches and diameter of 4 inches, capable of holding about 15 liters of LHe. A Cryomagnetics Inc model 3DA liquid He level sensor is inputted into the LHe space to measure the LHe level.

As stated above the LHe bath is pumped on to get to temperature below 4K. We use an Edwards E2M28 rotary pump to pump on the LHe bath. Temperatures below 1K are only accessible through He^3 refrigeration. The He^3 is stored and controlled via an Oxford Industries gas cabinet capable of holding about 10L of gaseous He^3. The He^3 is inputted into the experiment and returned back to the gas cabinet by an Edwards XDS10 oil-free scroll pump. Before being input into the system the He^3 is purified by an Oxford liquid nitrogen cold trap.

3.4.3.2 Temperature Control

Temperature control is done through a Lake Shore 340 temperature controller. There are two temperature sensors in the experiment. The first is a silicon diode temperature sensor which sits on the outside of the He^3 pot and reads accurately down to about 1K. The second sensor is Cernox 1010 AA that is mounted to the outside of the cavity and capable of accurately reading down to 100 mK. A simple resistive heater with resistance of 25 Ω mounted to the outside of the He^3 pot is used for temperature control.

Chapter 4

Singlet-Triplet Excitations and Long Range Entanglement In The Spin-Orbital Liquid Candidate $FeSc_2S_4$

4.1 Introduction

The search for truly quantum ground states is a central focus of modern condensed matter physics. A zero temperature spin liquid would be a prime realization of such a state [2]. Quantum spin liquids possess local moments, but, due to quantum fluctuations, do not order even at zero temperature. These fluctuations can often be

further enhanced by geometric frustration. Among their many novel features, they are proposed to possess long ranged quantum mechanically entangled wavefunctions as well as exotic fractionalized excitations. Recent proposals which suggest that these fractionalized excitations may be useful for quantum computation have only furthered interest in recent years.

To date, much focus has been devoted to fluctuations of the spin degrees of freedom, i.e. spin liquids. However, orbital degrees of freedom, which can also be disordered by quantum fluctuations [95], have received comparatively little attention. Systems with both spin and orbital fluctuations as well as spin-orbit coupling have been proposed to form a "spin-orbital liquid" ground state, characterized by entangled spin and orbital degrees of freedom but no long range order [5, 96, 97].

Among the best candidates for such a state is the A-site cubic spinel $FeSc_2S_4$, which shows no signs of magnetic ordering down to 50 mK. Instead, $FeSc_2S_4$ displays nearly perfect Curie-Weiss behavior with Θ_{CW} = -45.1K resulting in a frustration parameter, $f = |\Theta_{CW}|/T_N \geq 1000$, one of the largest ever recorded. Recent theoretical proposals and experimental studies of $FeSc_2S_4$ suggest that this large frustration parameter results from a spin-orbital liquid ground state which may lie in close proximity to a quantum critical point and a long range ordered magnetic phase. However, $FeSc_2S_4$'s true ground state or proximity to this quantum critical point is unknown.

In this chapter, we use time domain THz spectroscopy to probe the magnetic excitations of $FeSc_2S_4$. We observe a singlet-triplet excitation which displays a three-fold

splitting in magnetic field. We find the energy of this excitation to be substantially renormalized from the expected single ion value, in good agreement with the proposed spin-orbital liquid state. Using experimentally obtained parameters we compare our results to existing theoretical models to determine $FeSc_2S_4$'s proximity to the quantum critical point as well as a length scale for spin-orbital singlet correlations.

4.1.1 Spin-Orbital Singlet Formation In Single Ion Fe^{+2}

Before discussing $FeSc_2S_4$, we first demonstrate how spin and orbital degrees of freedom become entangled in the single ion Fe^{+2} from crystal field and spin orbit coupling effects. Shown in 4.1 is an energy diagram for the single ion case of Fe^{+2} ions in a tetrahedral crystal field, as is the case in $FeSc_2S_4$, with the addition of spin orbit coupling. In a tetrahedral S_4 crystal field, the $3d$ shell of each Fe^{+2} ion is split into an upper t_2 orbital triplet and a lower e orbital doublet. With Hund's coupling included, the Fe^{2+} ions assume a high spin $S = 2$ configuration with a lower ^5E orbital doublet ground state and an upper $^5T_2$ orbital triplet excited state. The ground state's two-fold orbital degeneracy is associated with the freedom to place a hole in either e orbital. Although such orbital degeneracy is often relieved by Jahn-Teller distortions, heat capacity experiments show no sign of orbital ordering down to 50 mK [96]. The possible removal of the ground state orbital degeneracy by random

strains was proposed previously [98], but the expected T^2 contribution to the specific heat [99] was not observed experimentally [96]. The orbital degeneracy's contribution to the specific heat and magnetic entropy has since been observed experimentally [96].

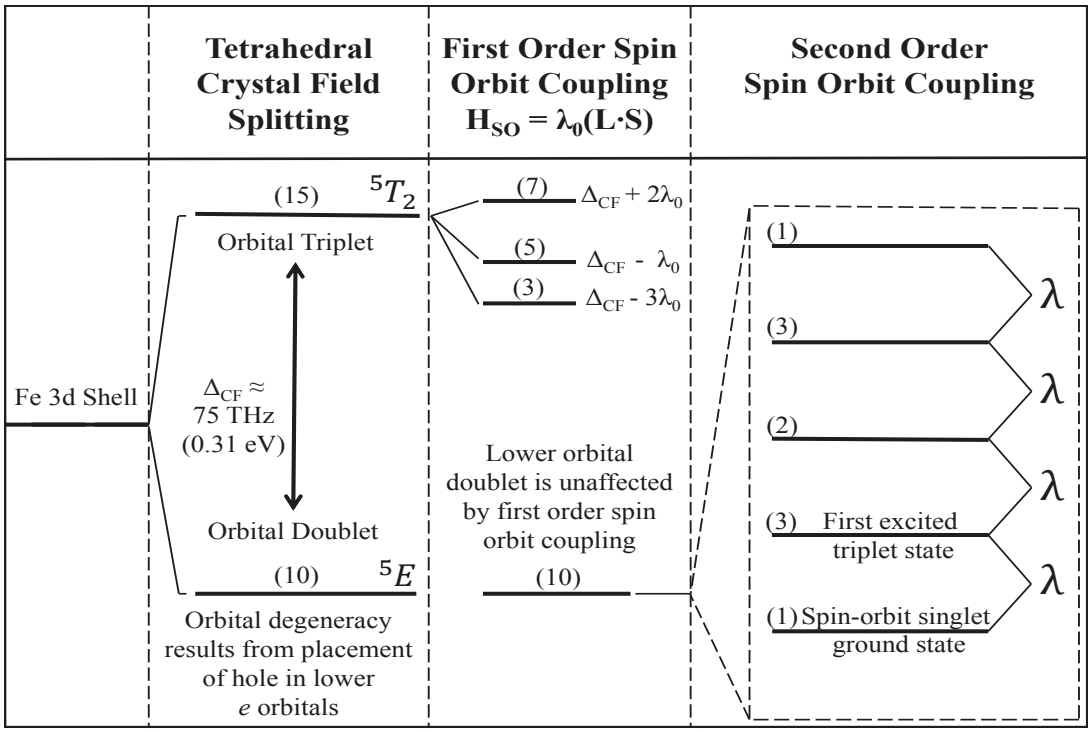

Figure 4.1: (a) Energy diagram of a Fe^{2+} single ion in an S=2 configuration after tetrahedral crystal field and first and second order spin orbit coupling effects are considered. Numbers in parenthesis represent the degeneracy of each level. Second order spin orbit coupling splits the lower ^{5}E doublet into 5 equally spaced levels separated by $\lambda = 6\frac{\lambda_0{}^2}{\Delta_{CF}}$.

Spin orbit coupling splits the upper orbital triplet into three levels with energies $\Delta_{CF} - 3\lambda_0$, $\Delta_{CF} - \lambda_0$, and $\Delta_{CF} + 2\lambda_0$, where Δ_{CF} is the ^{5}E - $^5T_2$ splitting and λ_0 is the spin orbit coupling constant [100, 101]. The potentially huge tenfold ground state degeneracy coming from the spin degeneracy of $S = 2$ and the orbital doublet

is split at second order in the spin-orbit interaction into 5 levels equally separated by $\lambda = 6\lambda_0^2/\Delta_{\rm CF}$ (Fig. 4.1). The ground state is then a spin and orbitally entangled singlet [102] with a wavefunction of the form:

$$|\psi_g\rangle = \frac{1}{\sqrt{2}}\,|3z^2{-}r^2\rangle\,|S_z{=}0\rangle + \frac{1}{2\sqrt{2}}\,|x^2-y^2\rangle\,[|S_z{=}{+}2\rangle + |S_z{=}{-}2\rangle]\,. \qquad (4.1)$$

The first excited state is a three-fold degenerate spin-orbital triplet, predicted to split Zeeman-like with g-factors of $g = \pm(1 - 2\frac{\lambda_0}{\Delta_{\rm CF}})$ [100].

4.1.2 Including Magnetic Exchange: $FeSc_2S_4$

$FeSc_2S_4$ differs from the single ion case in that the lattice now incorporates an additional energy scale, magnetic exchange, between Fe^{+2} ions. It was suggested by Refs. [5, 97] that the spin and orbitally entangled singlet character of the wavefunction is preserved when the Fe^{2+} ion is incorporated into the $FeSc_2S_4$ lattice. Chen *et al.* [5, 97] proposed that the spin orbital liquid state results from competition between magnetic spin-orbital exchange, which favors a magnetically ordered classical ground state, and on-site spin-orbit coupling, which favors a spin orbital liquid quantum disordered state. In the framework of a mean-field next-nearest neighbor (NNN) Kugel-Khomskii-type "J_2/λ"-model, in which J_2 is the NNN exchange constant and λ is the excitation energy of single ion Fe^{2+} discussed above, Chen *et al.* predict a quantum phase transition (QPT) at $x_c = 1/16$ (with $x = J_2/\lambda$), which

separates spin-orbital liquid and ordered phases (Fig. 4.2). The dominance of NNN exchange is demonstrated by the fact that the lowest energy magnetic excitations are found in neutron scattering at the wavevector for a simple Néel state $\mathbf{q} = \frac{2\pi}{a}(1, 0, 0)$ [103] and density functional theory which predicts the ratio of NNN to nearest neighbor exchange to be ≈ 37 [104]. The spin orbital liquid presumably differs from the ionic limit in that spin and orbital degrees of freedom may be entangled over longer length scales in that a spin on one site becomes entangled with the orbital of another site. Presumably this length scale diverges as the system approaches the QPT. The estimated value for x was such as to put $FeSc_2S_4$ slightly into the ordered regime. However, the actual proximity to the QPT and the nature of the ground state has yet to be verified.

Intuitively, one might expect the spectrum of $FeSc_2S_4$ in the spin-orbital liquid phase to be similar to that of the single ion Fe^{2+} described above since the spin-orbital liquid results from degeneracies on individual Fe^{2+} ions and $FeSc_2S_4$ breaks no other symmetries aside from those inherent to the crystal. Chen *et al.* [5, 97] predicted that while the first excited state would still be a spin-orbital triplet, its energy would be substantially renormalized by exchange. In the simplest case with only NNN exchange (e.g. the J_2/λ model) through an expansion in the exchange (valid at $x \ll x_c$) it was shown that the lowest singlet-triplet excitation energy of $FeSc_2S_4$ is:

$$E(q) = \lambda + 2J_2 \sum_A \cos(\mathbf{q} \cdot \mathbf{a}), \tag{4.2}$$

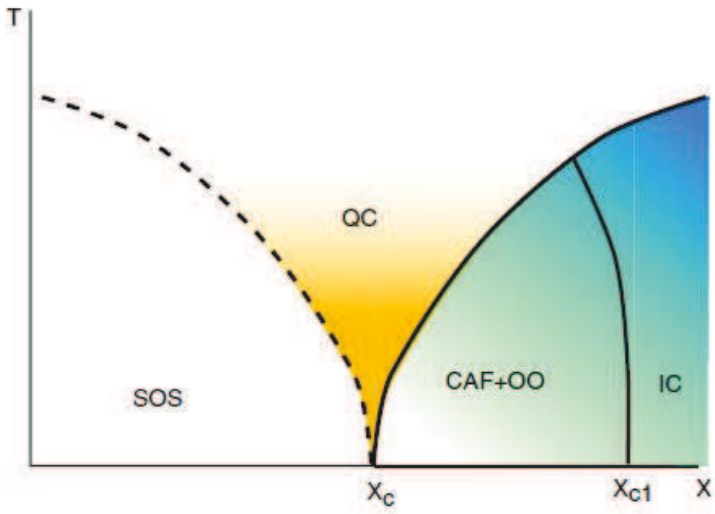

Figure 4.2: Theoretically proposed phase diagram of $FeSc_2S_4$ adapted from Ref. [5]. The bottom axis is labeled by the parameter $x = J_2/\lambda$. For $x < x_c$ the system is believed to be a spin-orbital liquid state characterized by long ranged spin-orbital singlets. For $x > x_c$ the ground state becomes an antiferromagnet with orbital ordering. It is believe that $FeSc_2S_4$ lies on the spin-orbital singlet side of the phase diagram but is in close proximity to the quantum critical point at $x_c \approx 1/16$.

where **a** represents the lattice vectors of the 12 NNN. Such excitations can be probed with optical measurements such as time domain terahertz spectroscopy (TDTS) through the magnetic dipole operator. Due to negligible momentum of light compared to the lattice scale, we probe the $\mathbf{q} \to \mathbf{0}$ limit, reducing Eq. 4.2 to $E = \lambda(1 + 24x)$. For $FeSc_2S_4$, with x of order x_c, one expects the excitation energy to be substantially renormalized from the ionic value.

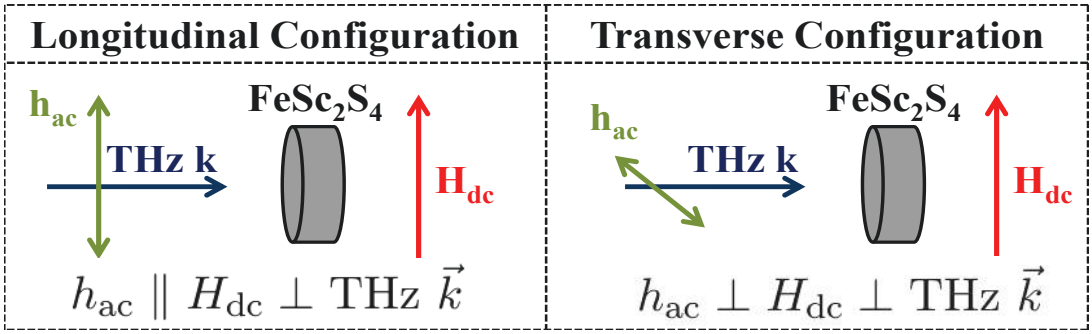

Figure 4.3: Graphic showing the two measurement geometries used in this experiment which are distinguishable by the relative orientation of the THz magnetic field ($\vec{h}_{\rm ac}$) and static magnetic field ($\vec{H}_{\rm dc}$). We refer to these alignments as the "longitudinal" ($\vec{h}_{\rm ac} \parallel \vec{H}_{\rm dc}$) and "transverse" ($\vec{h}_{\rm ac} \perp \vec{H}_{\rm dc}$) measurement configurations which are measured simultaneously via a rotating polarizer technique.

4.2 Experimental Methods

Dense polycrystalline $FeSc_2S_4$ samples were prepared by our collaborators at the University of Augsburg by spark plasma sintering at 1000°C from precursor synthesized binary sulfides Sc_2S_3 and FeS. Structural, magnetic and optical properties were found to be identical to previous samples prepared by conventional solid state synthesis [96]. TDTS transmission experiments were performed, as detailed in Ch. 2, using a home built spectrometer with applied magnetic fields up to 7 T in the Voigt geometry ($\vec{k}_{\rm THz} \perp \vec{H}_{\rm dc}$). Through the use of a rotating polarizer technique [76], we measure the sample's response to two polarization directions with respect to $\vec{H}_{\rm dc}$ simultaneously. Fig. 4.3 displays the two measurement configurations which are simultaneously measured with our rotating polarizer technique. These geometries can be labeled by the relative orientation of the incoming THz magnetic field, $\vec{h}_{\rm ac}$

and static magnetic field $\vec{H}_{\rm dc}$. We refer to these geometries as either "longitudinal," with $\vec{h}_{\rm ac} \parallel$ to $\vec{H}_{\rm dc}$ or "transverse," with $h_{ac} \perp H_{dc}$. Reflectivity measurements were performed by our collaborators in the mid-infrared frequency range from 1000 to 8000 cm^{-1} using a BRUKER IFS 113v Fourier-transform spectrometer equipped with a He flow cryostat.

4.3 Experimental Results

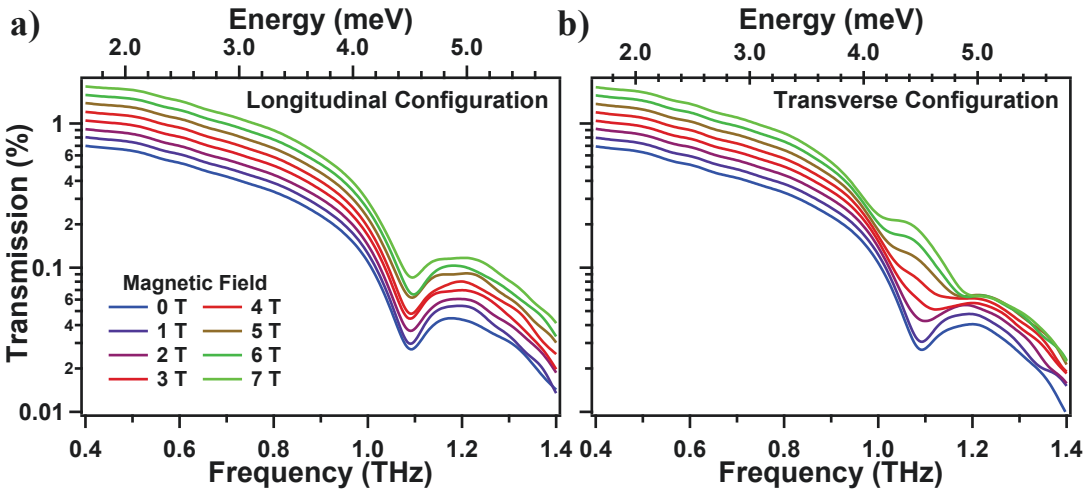

Figure 4.4: Field dependence of the magnitude of the transmission coefficient of $FeSc_2S_4$ taken at T = 5K for the (a) longitudinal configuration and (b) transverse configuration respectively. Offsets of 0.05 are included between the curves for clarity.

Figs. 4.4 displays the magnitude of the T = 5K transmission coefficient as a function of applied field for the (a) longitudinal and (b) transverse configurations respectively. In zero field, a sharp absorption develops at 1.08 THz (4.46 meV) below 10K [105]. As shown below, its energy is in reasonable agreement with the predicted

singlet-triplet excitation energy of Eq. 4.2. Further evidence for this assignment is found in the field dependence of the transmission. While no splitting is observed in the longitudinal configuration, the transverse configuration shows a clear splitting into two separate resonances with increasing field, suggesting the presence of distinct selection rules in the system.

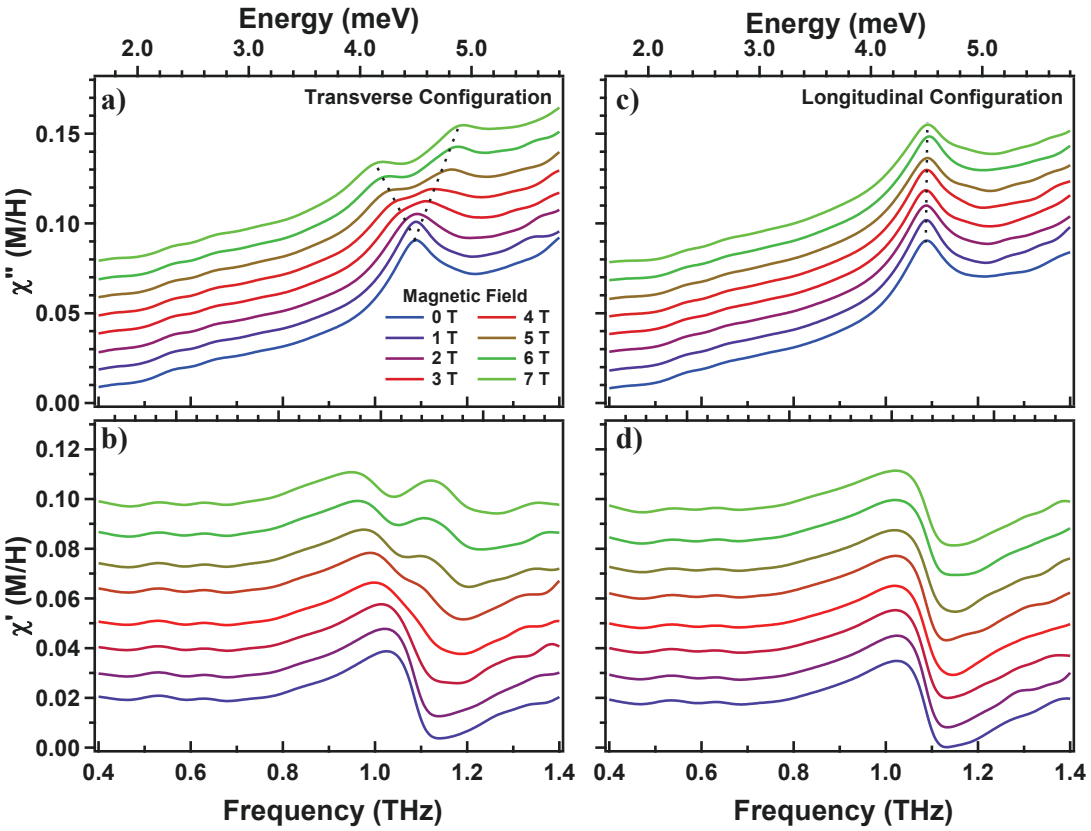

Figure 4.5: Field dependence of the imaginary χ'' and real χ' parts of the complex ac susceptibility in the (a-b) transverse and (c-d) longitudinal configurations. All spectra was taken at T = 5K. The susceptibility is shown in SI units, given by the ratio of the magnetization to applied field. Dashed lines are guides to the eye. Offsets of 0.1 are included for clarity.

To better resolve the splitting, the complex ac susceptibility of the sample was

calculated from the transmission coefficient. Fig. 4.5 shows the real and imaginary parts of the complex susceptibility in the (a-b) transverse and (c-d) longitudinal configurations respectively. The splitting of the resonance with increasing field is apparent in the transverse configuration. To extract the peak positions for both configurations the spectra was fit using Lorentzian oscillators and a linear background, which related work proposed derives from a continuum of zone boundary pairs of triplet excitations [105].

Fig. 4.6(a) shows the field dependent splitting of the excited state triplet. Quantitative values for the splittings could not be resolved below 3 T. Linear fits were performed on each branch to determine the g-factors. Only data between $5T \leq H_{dc} \leq 7T$ were used in the upper branch fit since low transmission in the high frequency range causes error below 5 T. We find g-factors of $g = 0.93$ and $g = -0.92$ for the upper and lower branches respectively.

Mid-infrared reflectivity at higher energy was performed in order to determine the crystal field splitting and spin orbit coupling constant of the sample. Fig. 4.6(b) shows the T = 5K MIR reflectivity (black, left axis) spectrum, which displays a number of prominent features. The excitation energies can be found from the maxima of the dielectric loss (indicated by red arrows), which was obtained by using a Kramers-Kronig consistent variable dielectric function fitting routine [106]. Although one only expects two optically active excitations from ^5E to $^5T_2$ states, additional and shifted absorptions are expected due to strong coupling of the $^5T_2$ levels to vibrational

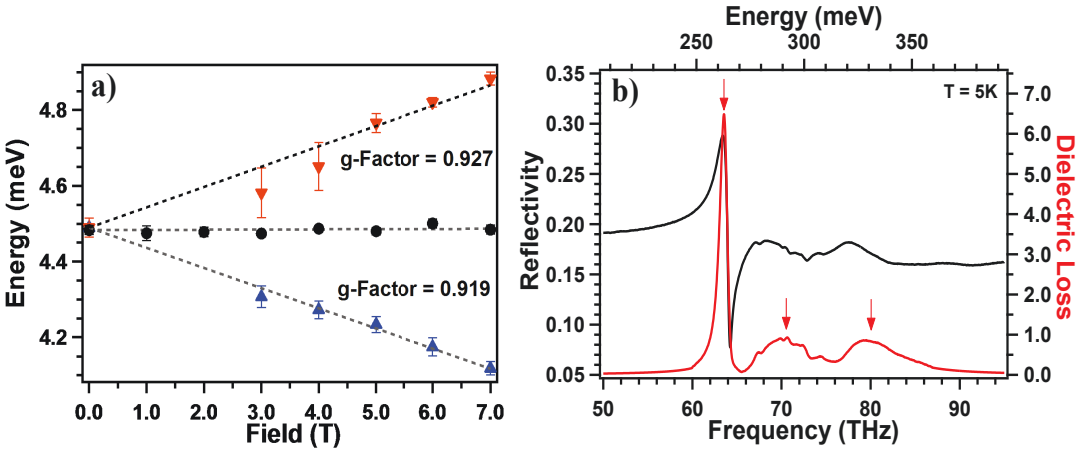

Figure 4.6: Singlet-triplet excitation energies of both measurement configurations extracted from fitting the susceptibility data shown in Fig. 4.5. Dashed lines are linear fits of the data from which the g-factors are extracted. Error bars are based on the quality of the fits. (b) Mid-infrared reflectivity data taken at T = 5K (black, left axis) along with the dielectric loss (red, right axis). Three features are seen with energies of 63.52 THz (0.262 eV), 70.32 THz (0.290 eV), 80.16 THz (0.331 eV), corresponding to crystal field excitations to the $^5T_2$ energy levels plus coupling to Jahn-Teller modes of Fe^{2+} in a tetrahedral environment.

modes [107]. Following the approach of Wittekoek *et al.* [101], the crystal field splitting, spin orbit coupling constant, Jahn-Teller coupling mode energies (E_{JT}), and coupling constants ($\hbar\omega_{\mathrm{JT}}$), can be extracted from the mode energies and intensities. We determine values of $\Delta_{\mathrm{CF}} = 71.6 \pm 5$ THz (296.1 ± 20.7 meV), $\lambda_0 = 2.14 \pm 0.30$ THz (8.85 ± 1.24 meV), $E_{\mathrm{JT}}/\lambda \approx 1.6$, and $\hbar\omega_{\mathrm{JT}}/\lambda \approx 4$. From these values we can calculate $\lambda = 6\lambda_0^2/\Delta_{\mathrm{CF}} = 0.38 \pm 0.06$ THz (1.57 ± 0.25 meV). These values correspond closely to values found in other Fe^{2+} tetrahedral compounds [108].

From our experimental value of λ and the value of J_2 extracted from the Curie-Weiss constant, we find from Eq. 4.2 an expected singlet-triplet excitation energy of 1.31 THz (5.42 meV), which is in reasonable agreement with the observed energy

of 1.08 THz (4.46 meV). Additionally, substituting our measured values into the predicted g-factor expression $g = \pm(1 - 2\frac{\lambda_0}{\Delta_{CF}})$ [100] gives expected values of $g = \pm$ 0.94, which are in excellent agreement with our observed g-factors of $g = 0.93$ and $g = -0.92$.

With the energy scales characterized, we can work backwards to determine $FeSc_2S_4$'s proximity to the QPT in the context of the theory of Chen *et al.* [5, 97]. With an observed excitation energy of 1.08 THz (4.46 meV) and our experimental value for λ we can solve Eq. 4.2 for x. Here the implicit assumption is that Eq. 4.2, which was considered valid far from the critical point as an expansion in the exchange, is still valid near the QPT for momenta far from the ordering wavevector. We find a value of $x = 0.08$, which puts $FeSc_2S_4$ slightly above the predicted $x_c = 1/16$ from mean field theory. The fact that $FeSc_2S_4$ does not order down to the lowest measured temperatures indicates that quantum fluctuations are presumably important in setting x_c. We may use this value of x to make an estimate for J_2 of 0.029 THz (0.120 meV), which is about 25% less than the value inferred from the Curie Weiss constant [5, 97].

4.4 Discussion

Pure spin singlet-triplet excitations are typically forbidden in electron spin resonance measurements due to the parity change between spin singlet and triplet states

[109] [110] and are usually only seen in the presence of a Dzyaloshinskii - Moriya (DM) [46, 111] interaction or staggered magnetization arrangements along crystallographic axes. Chen *et al.* estimate the static DM interactions to be ≈ 100 times weaker than both exchange and spin orbit couplings [5]. In principle, dynamic DM interactions can also weakly allow pure spin singlet-triplet excitations, [110] but such interactions involve a phonon and are assumed to be even weaker than static contributions. However, neither of these effects are thought to be relevant in $FeSc_2S_4$ since the spin-orbital singlet and triplet states belong to the same $S = 2$ ^{5}E-multiplet and are different from the pure spin states. In the single ion case of Fe^{2+} in tetrahedral crystal fields, it has been shown that a similar singlet-triplet excitation is magnetic dipole active with selection rules that agree with the results presented in this work [102] [107]. Therefore, we believe the observation of this singlet-triplet excitation is further evidence for the entangled spin-orbital singlet character of the ground state and establishes $FeSc_2S_4$ as a SOL.

As discussed in Ref. [5, 97], it is believed that the critical regime of this QPT can be described by a Euclidean multicomponent Φ^4 scalar field theory in 4 space-time dimensions. In such field theories a correlation length can be extracted through the relation $\xi = \frac{hv}{E}$ where E is a characteristic energy that vanishes at the QPT and v is a velocity, whose square is a proportionality between space and time derivatives in the effective Lagrangian. This length can be understood as the scale over which spin and orbital degrees of freedom are entangled. In the present case, $E \approx 0.17$ meV can be

identified with the zone boundary soft gap in neutron scattering [103]. By inspection of the terms in the action written down in Ref. [5], we can identify $v = \frac{a}{8h}\sqrt{\lambda^3/J_2}$ and find $\xi = \frac{\lambda a}{8E}\sqrt{1/x}$. Using our experimentally determined spin-orbit and exchange parameters we estimate a correlation length of $\xi/(\mathbf{a}/2) \approx 8.2$. This demonstrates the long-range entangled character of the SOL non-classical ground state in $FeSc_2S_4$.

4.5 Conclusion

In summary, we believe we have demonstrated the spin-orbital singlet character of the ground state of $FeSc_2S_4$ through the observation of a singlet-triplet excitation. Its energy is significantly renormalized from the expected single ion value by magnetic exchange, in agreement with the model of Ref. [5, 97]. This system, in close proximity to the QPT, differs from a simple ensemble of spin-orbit singlet ions through the presence of longer range correlations which we demonstrated exist over a length scale of over 8 nearest neighbors. We believe our results establish $FeSc_2S_4$ as a spin orbital liquid in very close proximity to a quantum critical point and therefore on the edge of magnetically ordering.

Since the the completion of this work, two additional neutron scattering studies have been reported and produced conflicting results. Plumb *et al.* [112] claim to observe the devlopment of magnetic Bragg peaks below 11.8 (K), indicating the onset of antiferromagnetic order, subsequent to a cubic to tetragonal structural transition

which breaks the orbital degeneracy. Although such Bragg peaks were not observed in the previous neutron study of Krimmel *et al* [103], the claim is that the new results are not inconsistent but instead the previous study did not possess the necessary sensitivity to observe the magnetic order. In this scenario, $FeSc_2S_4$ is still in proximity to the quantum critical point but on the magnetically ordered side of the phase diagram, with $x > x_c$. However, an additional neutron scattering study by Biffin *et al.* [113] did not observe such Bragg peaks and instead claim that the magnetic field dependence of the spin-orbtial triplet excitations are consistent with the spin-orbital liquid picture, placing $FeSc_2S_4$ on the spin-orbital liquid side of the phase diagram with $x < x_c$. The contradictory results of these two studies is currently an area of open investigation. However, one possibility is that $FeSc_2S_4$ is highly sensitive to disorder, impurities, and sample preparations - a hallmark of proximity to a quantum critical point. This provides a natural explanation as these two studies were preformed on samples provided by different groups. To date, a full understanding of the role of disorder of the ground state of $FeSc_2S_4$ is lacking and requires further invesitgation.

Chapter 5

Low Energy Magnon Dynamics and Magneto-Optics Of The Skyrmion Insulator Cu_2OSeO_3

5.1 Introduction

Non-trivial spin textures have become a hotbed of research in recent years due to their unique physical properties and potential applications in spintronics and information storage. Skyrmions [114], topological vortices of magnetic spins, are a prime example of such a non-trivial spin texture [115]. The existence of skyrmion phases, where a hexagonal lattice of skyrmions is formed, was recently predicted to exist in chiral magnets [116, 117], and has since been realized in the metallic B20 helimagnets:

MnSi [118], FeGe [119], and $Fe_{1-x}Co_xSi$ [120, 121]. The skyrmion phases of these materials possess unique electrodynamics [122] such that they can be manipulated via application of an electrical current or thermal gradient [123] and have accordingly attracted intense experimental interest.

Optical spectroscopy is exceptionally well-suited for studying these chiral magnets as their nearly ferromagnetic nature ensures an ordering wavevector of $\vec{k} \approx 0$ which is directly probed by optical experiments. However, high precision optical transmission experiments of single crystal skyrmion materials has thus far been impossible due to their metallic nature. This has been particularly detrimental to the optical study of their low energy magnetic response which generally requires bulk samples in the linear response regime.

Recently, a skyrmion phase with unique physical properties was recently shown to exist in the *insulating* chiral magnet Cu_2OSeO_3 [124, 125, 126]. The low symmetry crystal structure of Cu_2OSeO_3 permits multiferroism [127, 128, 129] as well as magnetoelectric coupling [130, 131, 132], which recent measurements have shown results in a finite polarization that onsets in conjunction with magnetic order at $T_c \approx 58K$ [133, 134]. This finite polarization allows for coupling between *magnetic* skyrmions and applied *electric* fields [125, 126] - a promising mechanism for technological applications and novel devices [135, 136]. Accordingly, the magnetic and magnetoelectric properties of Cu_2OSeO_3 have been the focus of intense investigation [133, 134, 137, 138, 139, 140].

CHAPTER 5. LOW ENERGY MAGNON DYNAMICS AND MAGNETO-OPTICS OF THE SKYRMION INSULATOR Cu_2OSeO_3

From an optics perspective, the large Mott insulating gap of Cu_2OSeO_3 naturally separates electric and magnetic degrees of freedom [141, 142, 143], allowing for direct access to the magnetic response via transmission optics. Spectroscopic investigations have since been performed from the microwave [144, 145, 146, 147] to the visible [143] frequency ranges. However, experiments performed at infrared or terahertz (THz) frequencies have so far only occurred at two extremes of the phase diagram, either in zero applied magnetic field [142, 148] or in large pulsed magnetic fields of order H $\approx$ 10T [149]. To date, no THz experiments have been performed in weak magnetic fields (H $\leq$ 200 mT), within the various magnetic phases of Cu_2OSeO_3, including the skyrmion phase. Additionally, a detailed investigation into the dynamics of the known THz excitations as a function of temperature and magnetic field has not yet been presented.

In this chapter, we present a comprehensive high resolution optical study of the skyrmion insulator Cu_2OSeO_3 in the THz regime via time-domain THz spectroscopy (TDTS). As our experimental energy range, $\hbar\omega$ = 1 - 10 meV, is far less than the bulk band gap, $\Delta_g \approx 1$ eV, we directly access the low energy magnetic response of Cu_2OSeO_3. Experiments are performed within three distinct regimes of magnetic field: H = 0, H $\leq$ 200 mT, and H $\geq$ 5 T. In zero field, we observe a weak excitation which is revealed to be a zone folded magnon from the zone boundary to the zone center which has not been predicted by spin-wave theory. Highly sensitive polarimetry experiments performed in weak magnetic fields observe Faraday and Kerr rotations

which are proportional to the sample magnetization, allowing for optical detection of the skyrmion phase and construction of a magnetic phase diagram. In large magnetic fields, we study the field and temperature dependent dynamics of the uniform mode of the field polarized phase. The uniform mode is found to decay through a non-Gilbert damping mechanism and to possess a finite spontaneous decay rate in the zero temperature limit. The potential damping mechanisms of this mode are discussed.

5.1.1 H-T Phase Diagram

Figure 5.1(a) shows the crystal structure of Cu_2OSeO_3 [152] which crystallizes in the cubic, but non-centrosymmetric, space group $P2_13$ [153]. The unit cell forms a distorted pyrochlore lattice with 16 Cu^{2+} (S = 1/2) ions residing on the vertices of 4 corner sharing tetrahedra. Each tetrahedron is composed of one Cu(I) site (orange spheres) and three Cu(II) sites (blue spheres), which possess distinct crystal field environments [133, 154]. This low symmetry structure results in five unique Heisenberg exchanges and five Dzyaloshinskii-Moriya (DM) [45, 46] exchanges within the unit cell. These exchanges are classified as either "strong" or "weak" depending on whether they couple two intra-tetrahedral or two inter-tetrahedral Cu^{2+} spins respectively. Experiments [150, 155] and calculations [141, 151, 156] reveal that the "strong" couplings result in a semi-classical ferrimagnetic arrangement for each tetrahedron, in which the Cu(I) spin orders antiferromagnetically to the three Cu(II) spins (Figure 5.1(b)). This ground state is well separated from the first excited state by a

large energy gap of $\Delta \approx 275$K, [141, 150, 151, 155] such that each tetrahedron can be treated as an effective S = 1 spin which form the basic magnetic building blocks of Cu_2OSeO_3. The resulting effective unit cell then consists of four S = 1 spins arranged in the Trillium lattice, a structure identical to that of the B20 helimagnets, revealing why such similar phase diagrams result from seemingly dissimilar compounds [147].

The magnetic phase diagram can then be understood as competition between the "weak" Heisenberg and "weak" DM exchanges of these effective S = 1 spins [141, 151, 156]. With $|D_{ij}| < |J_{ij}|$, the resultant magnetic order in zero field onsets at $T_c \approx 58$K in the form of a long wavelength helix ($\lambda \approx 50$ nm) [124, 157] as shown in Figure 5.1 (c). The magnetic order reduces the symmetry to the rhombohedral group R3 [133]. Weak cubic anisotropy pins these helices to degenerate high symmetry directions of the cubic structure, resulting in a"multi-domain helical phase." Application of a magnetic field cants the spins in the direction of the applied field. At H_{c1} the applied field overcomes the weak cubic anisotropy resulting in a "single-domain conical phase," shown in Figure 5.1(d), in which the helices co-align into a single domain with a conical arrangement of spins [124, 157]. Further increasing the applied magnetic field smoothly tunes the cone angle to zero at H_{c2}, thereby untwisting the magnetization, resulting in a field polarized ferrimagnetic phase as shown in Figure 5.1(e). While the exact values of the critical fields depends on the demagnetization factors of the sample, H_{c1} and H_{c2} are generally on the order of 10 mT and 100 mT respectively [124, 157].

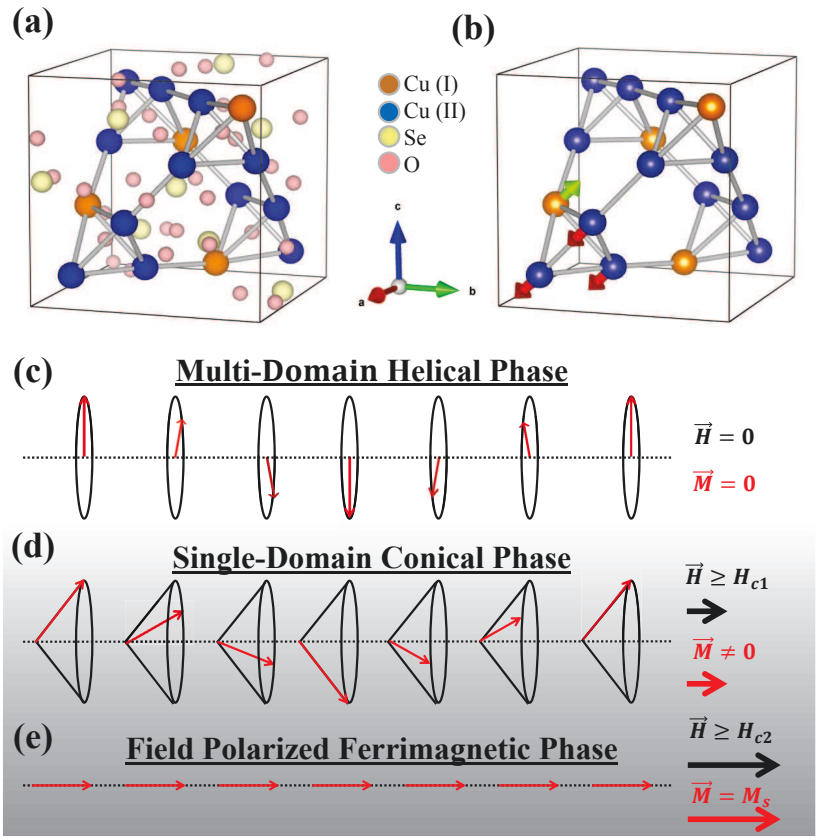

Figure 5.1: (a) Unit cell of Cu_2OSeO_3 with the Cu(I) and Cu(II) positions shown as orange and blue spheres respectively. (b) The ground state of each tetrahedron consists of a ferrimagnetic arrangement in which the Cu(I) spin (green arrow) orders antiferromagnetically to the Cu(II) spins (red arrows), creating effective S=1 spins. Shown in (c)-(e) are representations of the (b) helical, (c) conical, and (d) field polarized magnetic phases where each arrow represents the effective spin of a single tetrahedron. See text for more details.

Much like the B20 helimagnets, a skyrmion phase spanned by $\approx$ 2K and $\approx$ 30 mT just below T_c is stabilized by Gaussian thermal fluctuations [118] and has since been detected by a variety of techniques [124, 125, 126, 139, 157, 158]. In this phase, skyrmions form a hexagonal lattice much like Abrikosov vortices in type-II superconductors. Such a phase can be thought of as a double twisting of the magnetization which results from the superposition of 3 helices with $\vec{k}$ vectors at 120 degrees to one another [157]. The skyrmion diameter is identical to the helical phase wavelength, d $\approx$ 50 nm, which is three orders of magnitude larger than the inter-atomic spacing [124] revealing skyrmions to be vast macroscopic spin structures. Among other things, in the present work we show that the skyrmion phase can be detected by low frequency optics in the form of TDTS.

5.2 Experimental Methods

Phase pure single crystals of Cu_2OSeO_3 were grown by chemical vapor transport. Cu_2OSeO_3 powder was placed in an evacuated fused-silica tube with a temperature gradient of 640 °C - 530 °C, with NH_4Cl as the transport additive, using seed crystals to increase yield. Purity of single crystals were verified by magnetization and X-ray diffraction experiments, showing reproducibility of physical property behavior and good crystallinity. For more details see Ref. [159].

Time domain terahertz (TDTS) measurements were performed on a hand polished

single crystal sample with plane parallel sides of cross sectional area of $\approx$ 3 mm $\times$ 3 mm and thickness $d = 0.92$ mm. The orientation of the sample was such that the $(1,\bar{1},0)$ direction was normal to the sample surface. Experiments were performed using a home built spectrometer with applied magnetic fields up to 7 T in Faraday geometry ($\vec{k}_{THz} \parallel \vec{H}_{dc}$) [160]. The polarization was such that the THz oscillatory fields $e_{ac} \parallel c$ and $h_{ac} \parallel (110)$ directions respectively. TDTS is a high resolution method for accurately measuring the electromagnetic response of a sample in the experimentally challenging THz range. In a typical TDTS experiment, the electric field of a transmitted THz pulse through a sample is measured as a function of real time. Fourier transforming the measured electric field and referencing to an aperture of identical size allows access to the frequency dependent *complex* transmission spectrum of the sample which is given by,

$$\widetilde{T} = \frac{4\widetilde{n}}{(\widetilde{n}+1)^2} \exp\left(\frac{i\omega d}{c}(\widetilde{n}-1)\right) \tag{5.1}$$

where d is the sample thickness, ω is the frequency, c is the speed of light, $\widetilde{n}$ is the sample's complex index of refraction, and normal incidence has been assumed. A Newton-Raphson [73] based numerical inversion of the complex transmission is then used to obtain both the frequency dependent real and imaginary parts of the index of refraction.

The index of refraction, $\widetilde{n} = \sqrt{\epsilon\mu} = n + ik$, contains both the electric and magnetic responses of the sample as THz fields can couple to both electric and magnetic dipole transitions. In principle, the linear magnetoelectric properties of Cu_2OSeO_3 introduce

an additional contribution to the index of refraction such that $\widetilde{n} = \sqrt{\epsilon\mu \pm \chi^{\mathrm{ME}}}$, where χ^{ME} is the magnetoelectric susceptibility. However, at the level of sensitivity of the present experiments we observe no magnetoelectric effects in the THz range suggesting that the magnetoelectric susceptibility is small compared to the linear electric and magnetic susceptibilities, $\chi^{\mathrm{ME}} \ll \chi^{\mathrm{M}}, \chi^{\mathrm{E}}$. We therefore neglect the magnetoelectric contribution to the index of refraction in our analysis and ascribe absorptions as stemming from purely electric or magnetic effects.

The linear THz response of a sample can be represented in the Jones calculus [74] as a 2×2 complex transmission matrix of the form,

$$\hat{T} = \begin{bmatrix} T_{xx} & T_{xy} \\ T_{yx} & T_{yy} \end{bmatrix}$$

However, the overall symmetry of Cu_2OSeO_3 restricts the response such that the transmission matrix is fully antisymmetric, i.e. $T_{xx} = T_{yy}$ and $T_{xy} = -T_{yx}$ [75]. One can then identify off diagonal elements of the transmission matrix with rotation of the plane of polarization of light by the sample. Polarization rotation experiments were done through the use of a rotating polarizer [76] technique, which allows for simultaneous measurement of two elements of the transmission matrix. The complex rotation angle is then given by the relation $\theta = \tan^{-1}(\frac{T_{yx}}{T_{xx}})$. Fully antisymmetric transmission matricies can be diagonalized by a circular basis transformation, $T_r = T_{xx}$ - iT_{xy} and $T_l = T_{xx} + iT_{xy}$, suggesting experiments performed in Faraday geometry

are best understood in the circular basis. Data taken in applied magnetic field will therefore be presented as either a polarization rotation or in the circular basis.

Time-of-flight neutron scattering experiments were performed on the SEQUOIA instrument at the Spallation Neutron Source of Oak Ridge National Laboratories. To enhance the signal to noise ratio, we co-aligned more than 50 single crystals to yield a mass of $\approx$ 5g. A mosaic of less than 0.5 degrees was ensured by design of a custom mount to orient the samples according to their as-grown facets. The co-aligned mosaic was cooled to 4 K in a bottom-loading CCR and rotated by 180 degrees in 0.5 degree steps about the $(h\bar{h}0)$ axis. An incident energy of 20 meV was chosen with the fine chopper rotating at a rate of 180 Hz. These same spectrometer settings were used to measure Vanadium incoherent scattering for absolute normalization of the differential scattering cross-section. Reduction of the data was performed using Mantid [161] and subsequent analysis was done with Horace [162].

5.3 Experimental Results

5.3.1 Temperature Dependence

Figure 5.2(a) displays the magnitude of the complex zero field transmission of Cu_2OSeO_3 as a function of frequency and temperature plotted on log scale. Figure 5.2(b) displays the corresponding imaginary, or dissipative, part of the index of refraction extracted from the transmission and Eq. 5.1. One can see that the

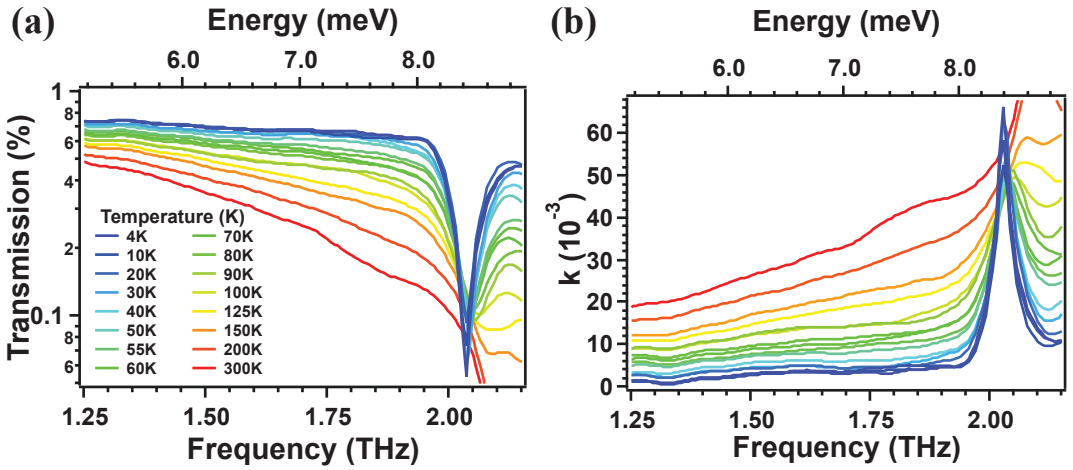

Figure 5.2: (a) Magnitude of the zero field complex transmission spectra of Cu_2OSeO_3 as a function of frequency and temperature plotted on log scale. (b) Corresponding imaginary, or dissipative, part of the index of refraction extracted from the transmission and Eq. 5.1. A clear absorption is observed at 2.03 THz which narrows and gains intensity with reducing temperature.

spectra consists of two prominent features, The first is a nearly linear background which shows decreasing dissipation as the temperature is reduced. The origin of this background is an intense infrared active phonon at 2.5 THz, which is outside our experimental frequency range [142]. The reduction of this background with reducing temperature presumably results from a narrowing of this phonon at lower temperatures. The second, and more interesting, feature in the spectra is the clear absorption with a resonant frequency of $f_0 = 2.03$ THz (8.40 meV). As shown in Figure 5.2, this excitation begins developing at T $\approx$ 120 K and displays an increasing intensity and simultaneous narrowing as the temperature is reduced.

This absorption was previously reported in far infrared experiments performed by Miller *et al.* [142] in which it was hypothesized to be a low frequency phonon. It

was reported that this absorption displayed no response to weak magnetic fields up to 14 mT applied parallel to the sample surface and no anomalous behavior at the magnetic ordering temperature $T_c \approx 58$K. Although the potential magnetic dipole or magnetoelectric character of the excitation could not be excluded as the response to larger magnetic fields or anisotropy upon change in field direction or incident polarization was not investigated.

However, the intensity of this excitation is generally problematic for the phonon interpretation. This becomes obvious when one compares the spectral weight (plasma frequency) of this excitation to that of the other known infrared optical phonons of Cu_2OSeO_3, which were also reported by Miller *et al.* [142]. In general, a phonon's plasma frequency can be related to its total spectral weight through the sum rule $\int_0^\infty \sigma_1(\omega) \propto \omega_p^2$. A comparison reveals that the spectral weight of the low frequency excitation observed in this work is a staggering 10^4 to 10^8 times weaker than any of the infrared optical phonons observed in Cu_2OSeO_3, suggesting a different origin for this excitation. Instead, the intensity of this excitation is much more consistent with magnetic excitations in single crystal samples. The weak intensity of magnetic excitations derives from the fact that the THz magnetic field interacts far more weakly with matter than the THz electric field.

Further support for the magnon interpretation of this excitation is provided by by the momentum resolved capabilities of inelastic neutron scattering. Shown in Figure 5.3(a) is a false color map of the differential scattering cross-section at 4 K (to be

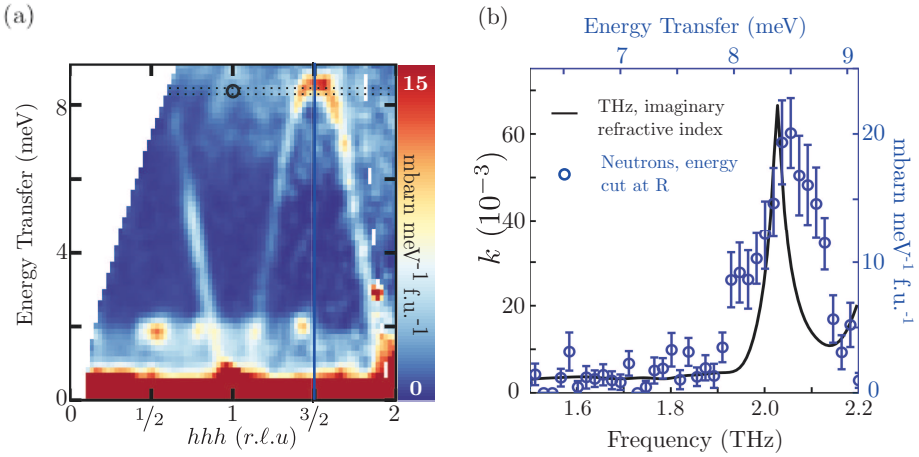

Figure 5.3: (a) **Q**-E dependence of the differential scattering cross-section along the (111) direction in reciprocal space. Perpendicular directions have been integrated within 0.1 Å. The magnon band at R_{111} is seen to be folded to the Γ_{111} zone-center. The peak (black circle) and FWHM (black dotted lines) in the THz spectrum is overlaid for comparison. (b) An energy cut (blue, right axis) along the blue line shown in (a) overlaid on the imaginary part of the index of refraction (black, left axis) measured by THz transmission. All data is obtained at T= 4.0(5) K.

detailed in a related upcoming publication [163]). The peak energy of the excitation in question has been overlaid at the (111) zone-center (Γ_{111}), where a dispersive magnon branch reaches its highest point. Judging from its energy, relatively weak intensity, and local curvature at the apogee, it appears to be a zone-folded replica of the magnon band whose intensity is strongly peaked at the zone boundary $R_{111} = (3/2\,3/2\,3/2)$ point. This observation suggests a more direct comparison between these two spectroscopic techniques.

Figure 5.3(b) shows an energy cut at R_{111}, along the blue line in Figure 5.3(a), overlaid with the dissipative part of the index of refraction k from THz spectroscopy. This presentation makes evident the agreement in energy between these modes, which

is determined by neutron scattering as f=2.05(3) THz. Differences in the excitation width result from the inherent resolution limits of the neutron spectrometer and the increased angular spread of the co-aligned mosaic as compared to that of a single crystal. Together, these observations motivate the conclusion that the mode observed by THz spectroscopy is, infact, a zone-folded magnon—a new magnetic excitation which has not been previously predicted by spin-wave theory [141, 151].

With the magnetic character of this excitation determined, the dynamical properties of this magnon can be found from fitting the spectra to a Drude-Lorentz model with the following form,

$$\mu(\omega) = \frac{S\omega_0^2}{\omega_0^2 - \omega^2 - i\omega\Gamma} + \mu_\infty \tag{5.2}$$

where, ω_0, Γ, S, and μ_∞ represent the magnon frequency, full width at half max, oscillator strength, and high frequency permeability of the lattice respectively.

Figure 5.4 displays the temperature dependent oscillator parameters, (a) $f_0 = \omega_0/2\pi$, (b) Γ, and (c) S, of the low frequency magnon as determined from fitting the spectra with Eq. 5.2. An additional linear background was included in the fits to account for the high frequency phonon at 2.5 THz. Error bars in the figure are based on the quality of the fits. Unlike the results reported from Miller *et al.* [142], we uncover a coupling of this excitation to the magnetic structure of Cu_2OSeO_3. One can see in Figure 5.4(a) that the magnon frequency displays a weak softening as

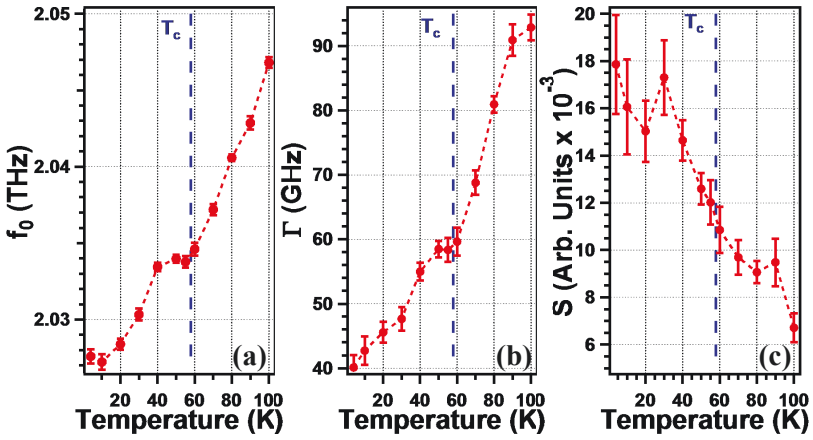

Figure 5.4: Temperature dependent oscillator parameters, (a) frequency $f_0 = \omega_0/2\pi$, (b) full width at half max Γ, and (c) oscillator strength S, of the magnon shown in Figure 5.2. Error bars are based on the quality of the fits. A clear anomaly in the magnon's frequency and width can be seen at $T_c \approx 58$K (vertical dashed lines), indicating a sensitivity to the magnetic transition.

the temperature is lowered, reducing by $\approx 1\%$ from 100K to 4K. A clear anomaly is observed in the magnon's frequency at $T_c \approx 58$K (vertical dashed lines in Figure 5.4), further supporting the magnetic character of this excitation. A similar anomaly at T_c is observed in the width of the excitation, shown in Figure 5.4(b), which also shows the general trend of reducing with lowering temperatures. The far infrared FTIR transmission spectroscopy experiments of Miller *et al.* [142] likely did not posses the level of sensitivity needed to observe these features which explains why this softening and sensitivity to the magnetic structure was not previously observed. However, our experiments are able to determine the magnon frequency to a precision of ≈ 0.5 GHz (2 μeV), allowing for detection of such subtle effects.

It may seem unusual that this magnetic excitation persists to such high tem-

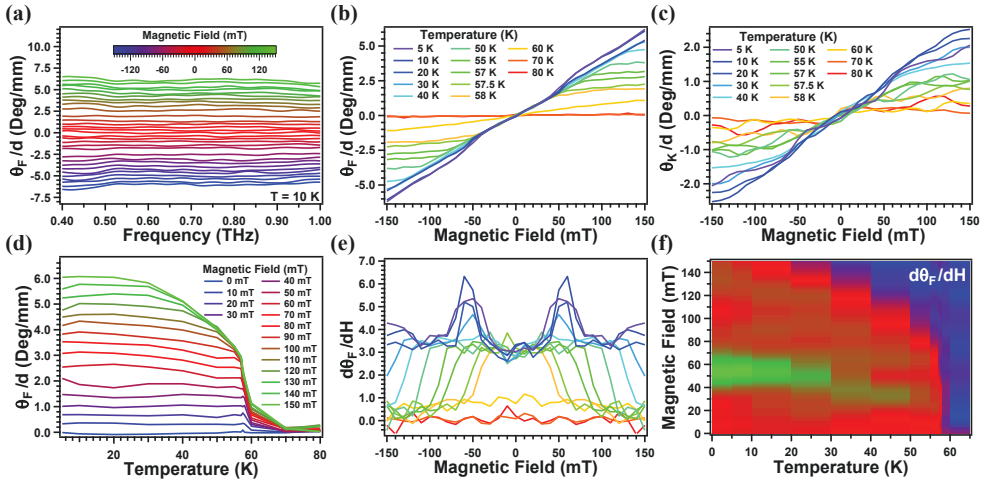

Figure 5.5: (a) Frequency dependence of the real part of the Faraday rotation normalized by sample thickness at T = 10K. (b-c) Real part of the (b) Faraday and (c) Kerr rotation as a function of magnetic field found from averaging the data over frequency range shown in (a). (d) Temperature dependence of the Faraday rotation. (e) The field derivative of the Faraday rotation as a function of magnetic field, a quantity proportional to the magnetic susceptibility of the sample. (f) Image plot of the data shown in (e) where the phase boundaries between the helical and conical phases (bright green) and conical and field polarized phases (red to blue) are clearly seen.

peratures, well above the magnetic transition at T_c. However, this mode physically corresponds to the rigid rotation of all the spins of a single tetrahedra [151]. As mentioned above, these tetrahedra remain well defined entities far above T_c due to the strong exchanges between spins within the tetrahedra. Therefore, the observation of this mode up to 120 K is consistent with the strongly entangled tetrahedra picture of Cu_2OSeO_3 [141]. Interestingly, we find this excitation does not display any discernible dependence with magnetic field for fields up to H = 7T in Faraday geometry. We discuss this lack of field dependence as well as the folding of this zone boundary mode to the zone center in the discussion below.

5.3.2 Magnetic Field Dependence

5.3.2.1 Magnetization Dependent Faraday and Kerr Rotations

Rotation of the plane of polarization of incident radiation upon transmission (Faraday rotation) or reflection (Kerr rotation) can often be related to the underlying symmetry of the material under investigation. For instance, the non-centrosymmetric chiral structure of Cu_2OSeO_3 permits "natural optical activity," rotation of the plane of polarization of linearly polarized light upon transmission in zero applied magnetic field, an effect which was recently observed in the visible range [143]. Additional gyrotropic effects can occur when time reversal symmetry is broken, for instance by the spontaneous magnetization of the sample. In this case the index of refraction matrix is fully antisymmetric with off-diagonal terms, assuming linear response, proportional to the sample magnetization [164]. A circular basis transformation reveals that linearly polarized light undergoes Faraday and Kerr rotations proportional to the sample's magnetization upon transmission [164, 165, 166, 167]. Examination of the proportionality constants reveals that the Kerr rotation is expected to be weaker than the Faraday rotation by a factor of $\approx d/\lambda$, [164] which in the case of this experiment is ≈ 3. Such magneto-optical effects allows one to treat polarization rotations as measures of the order parameter of the magnetically ordered phases and can therefore be used to construct a magnetic phase diagram.

For a single pass transmission experiment we can write the total polarization rotation of Cu_2OSeO_3 as,

$$\theta_{Tot} = \theta_{\mathrm{NOA}} + \theta_F(M(H,T)) \tag{5.3}$$

where θ_{NOA} is the natural optical activity intrinsic to the chiral lattice of Cu_2OSeO_3, $\theta_F(M(H,T))$ is magnetization dependent Faraday rotation, and higher order terms have been neglected. The natural optical activity is too weak to observe in our long wavelength THz measurements as it scales inversely with the wavelength of light. Instead, improved signal to noise is obtained by subtracting the zero field rotation from the field dependent data. This is justified as although Cu_2OSeO_3 orders in zero magnetic field, the helical phase is marked by domain formation such that the net magnetization in this phase is zero. If we define $\theta'_{\mathrm{Tot}}(H,T) = \theta_{\mathrm{Tot}}(H,T) - \theta_{\mathrm{Tot}}(H=0,T)$, then the field dependent polarization rotation, normalized by the sample thickness d, is given by,

$$\frac{1}{d}\theta'_{\mathrm{Tot}}(H,T) = \frac{1}{d}\theta_F(M(H,T)) \tag{5.4}$$

Additional information and enhanced signal to noise can be achieved by examining multiple reflections ("echos") of the THz pulse through the sample. The symmetry and finite magnetization of Cu_2OSeO_3 results in a Faraday rotation that further rotates upon reflection inside the sample. Therefore, the first echo of light, which

travels through the sample a total of three times, gains a contribution to its rotation that is three times the Faraday rotation of the first transmitted pulse. Additionally, the first echo also reflects internally off the sample surface twice, each time gaining a Kerr rotation that will also be magnetization dependent, but is expected to rotate in the opposite direction of the Faraday rotation [164]. Therefore the total polarization rotation of the first reflected pulse is given by,

$$\frac{1}{d}\theta'_{\mathrm{Tot}}(H,T) = \frac{1}{d}[3\theta_F(M(H,T)) - 2\theta_K(M(H,T))]. \tag{5.5}$$

where, the first and second terms represent the Faraday and Kerr rotations respectively. Thus, the complex Faraday and Kerr rotation angles can be measured independently if both the first transmitted and first reflected pulses of terahertz light through the sample are measured.

Figure 5.5 displays the results of our polarimetry experiments of Cu_2OSeO_3. Figure 5.5(a) shows the real part of the extracted Faraday rotation per mm of sample thickness, as defined in Eq. 5.4, as a function of frequency and applied magnetic field at T=10K. One can observe that the Faraday rotation in our spectral range shows little frequency dependence. However, structure can be found in the field dependence of the data. Figure 5.5(b) shows the real part of the Faraday rotation as a function of magnetic field obtained from averaging the data in Figure 5.5(a) over the frequency range shown at each temperature.

The proportionality between the Faraday rotation and magnetization is easily observed in Figure 5.5(b). The Faraday rotation is small at temperatures above $T_c \approx$ 58K. Below T_c, the system enters the multi-domain helical phase where magnetic order develops but with multiple domains resulting in no net magnetization. Therefore, no additional Faraday rotation that results from magnetic ordering is expected at temperatures below T_c in zero applied field. Once a magnetic field is applied the spins cant in the direction of magnetic field resulting in a linear increase in magnetization and therefore an identical trend in Faraday rotation. At H_{c1} the helices co-align and the system enters the single-domain conical phase, which is accompanied by a jump in magnetization. The corresponding increase in Faraday rotation can be observed for fields $H_{c1} \approx \pm 50$ mT at T=5K. At larger magnetic fields, $H \geq H_{c2}$, the system enters the field polarized phase, in which all spins are aligned, resulting in a saturation of the magnetization and Faraday rotation. Figure 5.5(c) displays the real part of the Kerr rotation as a function of magnetic field, obtained in a similar manner as the Faraday rotation described above and Eq. 5.5. One can see that the Kerr rotation displays an identical dependence on sample magnetization but is approximately a third that of the Faraday rotation, as expected from the ratio of d/λ.

As the Faraday and Kerr rotations are proportional to the sample magnetization, an H-T phase diagram of Cu_2OSeO_3 can be constructed from the data shown in Figure 5.5 (a)-(c). Here we focus primarily on the Faraday rotation, as the signal to noise is much better than that of the Kerr rotation due to technical aspects of our

measurement. In order to appropriately identify phase boundaries, subtle features in the data must be identified which are more easily observed in the temperature dependence and field derivatives of the Faraday rotation. Figure 5.5(d) displays the temperature dependence of the Faraday rotation at constant fields, where the phase boundary between the conical and field polarized phases is evident. Figure 5.5(e) shows the first derivative of the Faraday rotation with respect to magnetic field at constant temperatures, a quantity proportional to the magnetic susceptibility of the sample. The transition from the helical to the conical state is now easily identified as a sharp maximum in the derivative. The phase boundary between the conical and field polarized phases can be identified as the field beyond which the first derivative is zero or identically as a sharp maximum in the second derivative. Figure 5.5(f) shows an image plot of the data in Figure 5.5(e) in which clear phase boundaries at H_{c1} (bright green) and H_{c2} (red to blue) are easily observed.

Figures 5.6(a) displays our extracted H-T phase diagram of Cu_2OSeO_3 as determined from our polarization rotation experiments. Symbols are the extracted phase boundaries from the data shown in Figure 5.5 while dotted lines result from power law fits of the data given by the expression, $H_c(T) = H_c(0)(1-(T/T_c)^{\alpha})^{\beta}$, which was previously found to describe the data in both μSR [138] and ac susceptibility [168, 169] investigations. We restrict the critical exponent α=2 as has been done previously [138, 168, 169] and is expected for a three dimensional system [170]. From these fits we extract a critical temperature of $T_c = 58.4 \pm 0.4$ K and a critical exponent

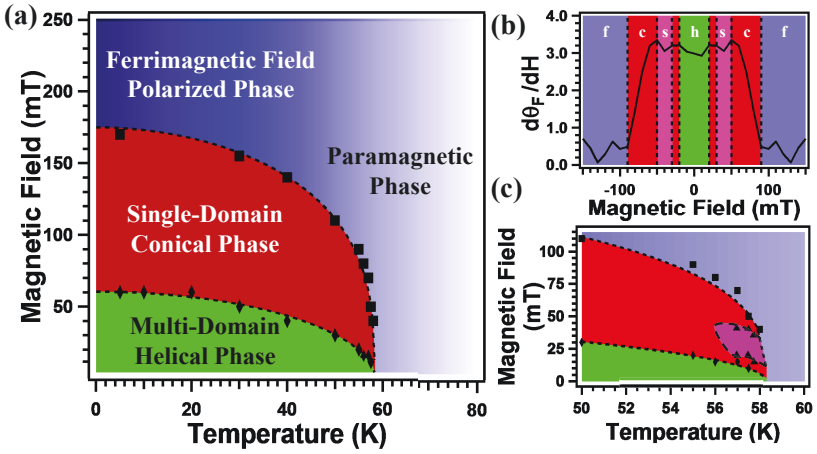

Figure 5.6: (a) The H-T magnetic phase diagram of Cu_2OSeO_3 constructed from our Faraday rotation experiments shown in Figure 5.5. (b) The first derivative of the Faraday rotation with respect to field at T=57K, a temperature at which all of the magnetic phases of Cu_2OSeO_3 can be observed. Dashed vertical lines and distinct colors signify transitions from the (h)elical, (s)kyrmion, (c)onical, and (f)errimagnetic phases. (c) Zoomed in region of the phase diagram where the skyrmion phase is observed. See text for more details.

of $\beta = 0.35 \pm 0.04$ at H_{c2}. Our extracted critical temperature is in excellent agreement with previous investigations. While our extracted value of β at H_{c2} is in reasonable agreement with the $\beta = 0.367$ of the 3D Heisenberg model and the $\beta \approx 0.37$ - 0.39 found in previous experiments of Cu_2OSeO_3 [138, 168, 169].

Figure 5.6(b) displays the derivative of the Faraday rotation with respect to field at T=57K, a temperature at which all of the magnetic phases of Cu_2OSeO_3 can be observed. Dotted lines and distinct colors mark different magnetic phases. The skyrmion phase manifests in the magnetic susceptibility, and therefore in the derivative of the Faraday rotation, as an additional minimum shown in pink in Figure 5.6(b). Figure 5.6(c) displays the phase diagram in the vicinity of T_c in which the skyrmion

phase can observed. Although our data possesses limited temperature resolution and demagnetization effects of the sample have not been taken into account, the extracted phase diagram, including the skyrmion phase, is in excellent agreement with those reported in previous studies [124, 157].

5.3.2.2 THz Dynamics of the Uniform Mode

While one can obtain an approximate understanding of the magnetic phases of Cu_2OSeO_3 by reducing the unit cell to four weakly coupled effective S=1 spins, an understanding of the excitation spectrum requires consideration of all unique exchanges in conjunction with quantum fluctuations. Such a full quantum treatment has been performed by Janson *et al.* [141] and Romhányi *et al.* [151], while corresponding neutron scattering [150, 155], high field THz ESR [149], and Raman spectroscopy [148] experiments reveal a striking agreement between the theoretical and experimentally observed excitation spectrums.

Of particular importance to this work is the lowest energy excitation of Cu_2OSeO_3. At the single tetrahedron level, the ground state is a three-fold degenerate triplet comprised of states with quantum numbers $|S, S_z\rangle = |1, -1\rangle$, $|1, 0\rangle$, $|1, 1\rangle$. Each of these states are themselves a coherent quantum superposition of four classical ground states [141, 151]. Turning on interactions between tetrahedra at the mean field level mixes single tetrahedron states with identical symmetry. The new resultant ground state is then a non-degenerate superposition of the original $|1, 1\rangle$ triplet state and a higher

energy $|2,1\rangle$ quintet state with wavefunction $|\psi\rangle_t = \cos(\alpha/2)|1,1\rangle + \sin(\alpha/2)|2,1\rangle$, where the variational parameter α controls the degree of mixing [141, 151]. One can see that the ground state wavefunction of each tetrahedron is no longer a state of definite angular momentum and states can only be labeled by their S_z components. Including quantum fluctuations into the theory renormalizes the excitation spectrum. In zero field the lowest energy excitation is a parabolicly dispersing Goldstone mode associated with the reduction of symmetry from SU(2) to U(1) in the ferrimagnetic state [141, 150, 151, 155]. Application of magnetic field gaps the Goldstone mode, which is hereafter referred to as the uniform mode, by an amount proportional to the field through Zeeman coupling [149, 171].

Figure 5.7 displays the results of our high field transmission experiments in which the uniform mode is observed. Improved signal to noise and systematics were obtained by applying a cosine window function to the data in the time-domain before Fourier transforming. Here data is presented in the right hand channel of the circular basis which, as discussed in the methods section above, is an eigenpolarization of the system. We find that the uniform mode is only active to right hand circularly polarized light, as expected for a magnetic excitation with a well defined magnetic dipole moment of ΔS_z=-1 [151]. Figure 5.7(a) displays the magnitude of the complex transmission of Cu_2OSeO_3 at T=5K as a function of magnetic field and frequency. The uniform mode enters our accessible frequency range around H $\approx$ 5T and can be seen to display an increase in resonant frequency and a narrowing width with increas-

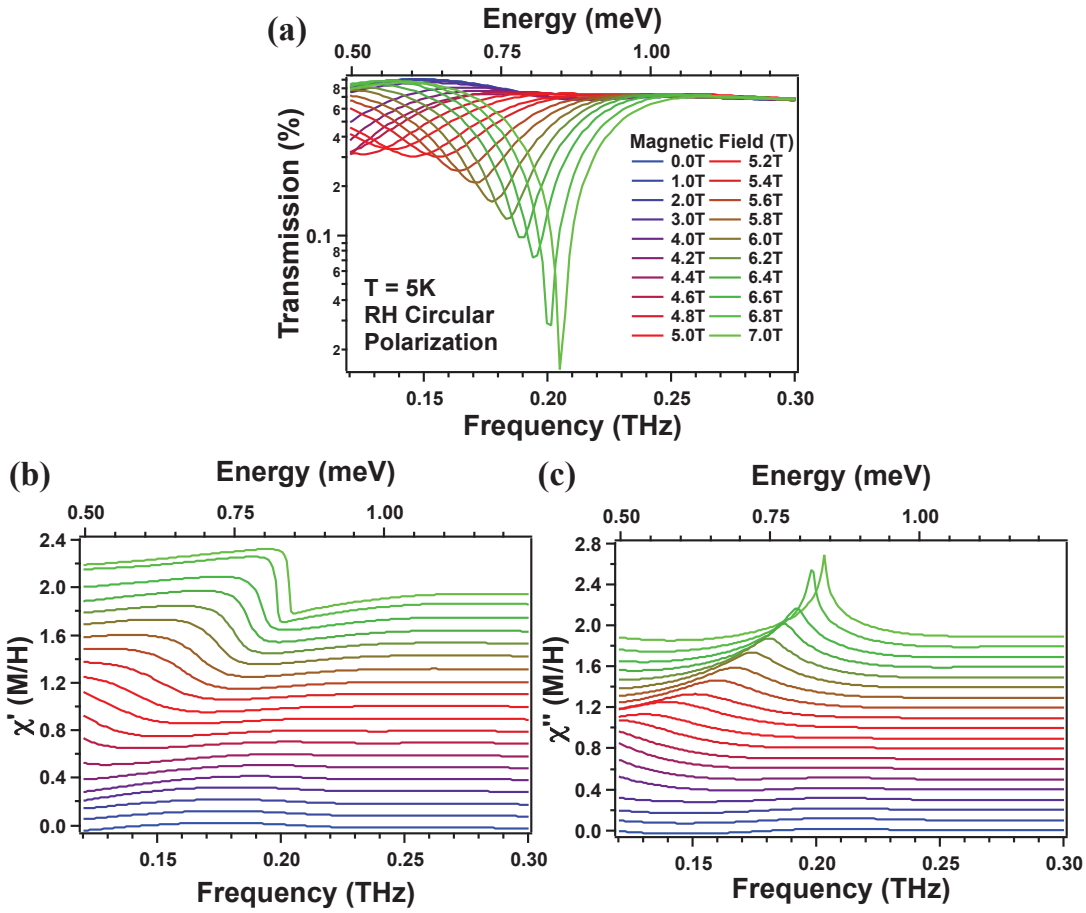

Figure 5.7: Results of our high field transmission experiments of Cu_2OSeO_3 presented in the circular basis with only the right hand channe shownl. (a) Magnitude of the complex transmission as a function of magnetic field and frequency at T=5K. A sharp magnetic absorption is observed at low frequencies which we identify as the uniform mode of the field polarized phase. (b)-(c) Corresponding (b) real $\chi^{'}$ and (c) imaginary $\chi^{''}$ parts of the complex magnetic susceptibility. Offsets of 0.1 per field have been added for clarity.

ing applied field. Figure 5.7(b)-(c) displays the (b) real and (c) imaginary parts of the magnetic susceptibility extracted from the data shown in Figure 5.7(a) and Eq. 5.1. In order to extract the magnetic susceptibility, data were referenced to identical field scans at T=100K, a temperature at which the absorption is no longer observed. The implicit assumption here is that the dielectric properties of Cu_2OSeO_3 do not appreciably change below 100K, typically a good assumption for such a large gap insulator [172].

The data presented in Figure 5.7 were fit to the general Drude-Lorentz expression given in Eq. 5.2 in order to extract the dynamical properties of the uniform mode. Figure 5.8(a) displays the extracted resonant frequencies, $f_0 = \omega_0/2\pi$, as a function of magnetic field at T=5K, the temperature at which the highest resolution of our measurement is obtained. Error bars are based on the quality of the fits. The dotted line is a linear fit of the data as expected for Zeeman coupling. From this fit we obtain an effective g-factor of $g_{\text{eff}} = 2.08 \pm 0.03$, which is in excellent agreement with the expected value for Cu^{2+} spins and the THz ESR measurements of Ozerov *et al.* [149] which previously reported $g_{\text{eff}} = 2.1 \pm 0.1$.

Additional information regarding the dynamics of this mode can be obtained by examining the width of the excitation as a function of temperature and magnetic field. In the limit of no disorder, the excitation width represents the decay rate (Γ), or the inverse lifetime, of the uniform mode. Figure 5.8(b) displays the field dependence of the width of the uniform mode at several temperatures. The width

displays an unusual approximately linear decrease in the accessible field region of our measurement for all temperatures, suggesting a dominant non-Gilbert damping mechanism. The temperature dependence of the width of the uniform mode at fields between 6T and 7T is shown in Figure 5.8(c). One can see that the width of the uniform mode broadens with increasing temperature. Such thermal broadening can be ascribed to enhanced decay through interactions with thermally excited magnons, processes which become frozen out at low temperatures.

The functional dependence of the decay rate with temperature may reveal additional information regarding the decay processes of the uniform mode. Magnon decay through magnon-magnon interactions is a well studied topic dating back to the earliest days of spin wave theory [173, 174, 175]. In the simplest case, the spin wave Hamiltonian is completely harmonic, i.e. spin waves are non-interacting plane waves. Interactions can be included by introducing anharmonic terms into the Hamiltonian which couple magnon states. In general, such interaction terms do not conserve quasiparticle number and one must rely on symmetry and conservation laws to determine which decay channels are permitted [176]. In the simplest cases, the temperature dependence of such decay processes can expressed as a polynomial expansion of temperature with terms proportional to T and T^2 for the lowest order three and four magnon interactions respectively [174]. Terms proportional to T^3 or greater result from higher order magnon-magnon interactions that are neglected in our analysis. Far less conventional are magnon decays at zero temperature, i.e. spontaneous decays,

which arise from quantum, not thermal, fluctuations [176]. The spontaneous decay rate will in general be a function of magnetic field stemming from field dependence of the kinematic requirements [176, 177] which must be satisfied for decays to occur.

Therefore we can write the total decay rate of the uniform mode as a function of both field and temperature as

$$\Gamma(T, H) = \Gamma_0(0, H) + A(H)T + B(H)T^2 \tag{5.6}$$

where the $\Gamma_0(0, H)$ is the spontaneous decay rate and the terms proportional to T and T^2 result from three and four magnon interactions respectively as described above.

Dashed lines in Figure 5.8(c) are fits of the data to Eq. 5.6. One can see that the decay rate is well described by Eq. 5.6 and that an extrapolation of the fits to the zero temperature limit reveals a finite spontaneous decay rate. Figure 5.8(d) displays the field dependence of the extracted spontaneous decay rate obtained from the fits shown in Figure 5.8(c). One can observe that the spontaneous decay rate displays an approximately negative linear dependence with magnetic field in the accessible region of our measurement. The decay processes of the uniform mode and the possible origins of the spontaneous decay rate are further addressed in the discussion below.

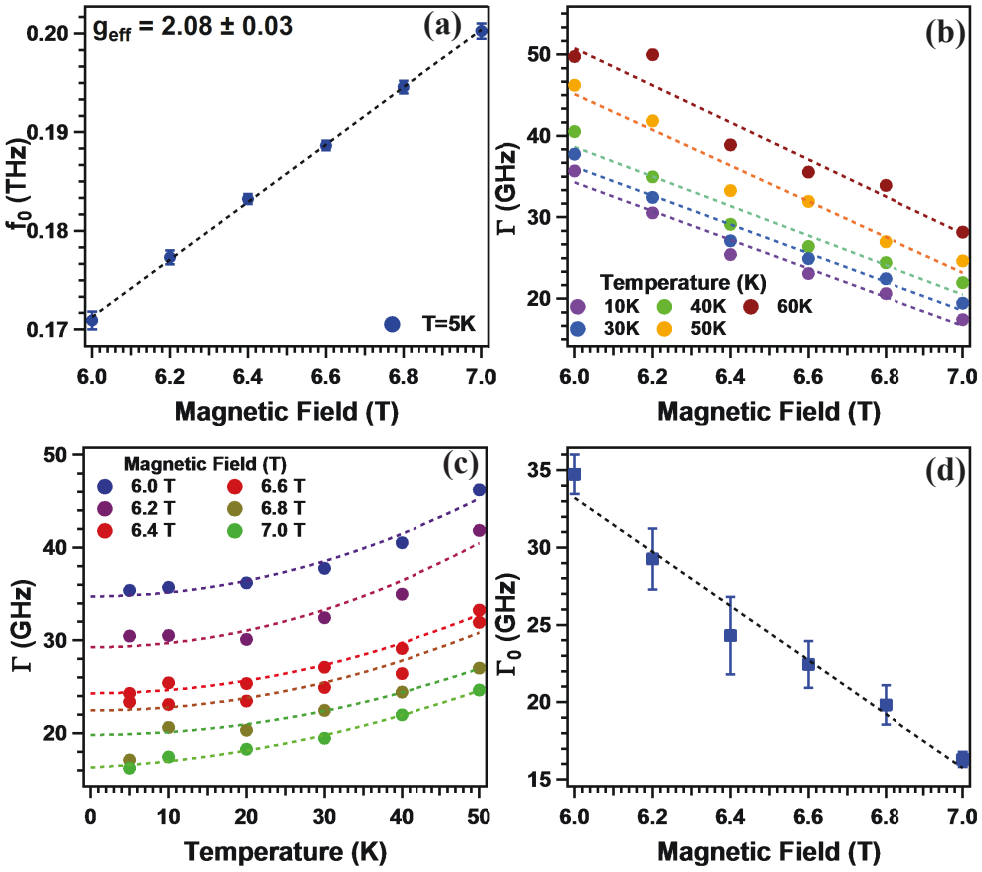

Figure 5.8: Dynamical properties of the uniform mode obtained from fitting the susceptibility shown in Figure 5.7 to Eq. 5.2. (a) Field dependence of the resonant frequency at T=5K as well as a linear fit from which a $g_{\text{eff}} = 2.08 \pm 0.03$ is obtained. (b) Field dependence of the full width at half max (Γ) of the uniform mode at several representative temperatures. (c) Temperature dependence of the Γ at several values of magnetic field. Dashed lines are fits of the data by Eq. 5.6 which reveals a zero temperature spontaneous decay rate. (d) Magnetic field dependence of the spontaneous decay rate obtained from fitting the data shown in (c). The dashed line is a linear fit of the data is meant as a guide to the eye.

5.4 Discussion

Dzyaloshinkii-Moriya (DM) interactions are obviously vital in the low energy description of chiral magnets. Yet, spin-wave calculations of Cu_2OSeO_3 [150, 151] have thus far not included DM interactions, effectively treating the system as a ferromagnet. However, DM interactions in Cu_2OSeO_3 have been suggested to be exceptionally strong. Recent calculations predict the largest DM interaction, referred to as D_4, to range from $|D_4/J_4| \approx 0.5$ [141] to $|D_4/J_4| \approx 1.95$ [127], *nearly twice the symmetric exchange*. Thus, it is reasonable to assume that DM interactions may have a more profound impact in Cu_2OSeO_3 than other chiral magnets. As it is expected that DM interactions modify the spin-wave spectrum at low energies near the Γ point [150, 151], the exact region probed by low energy optical spectroscopy, we believe that many of the observations made is this work can be attributed to such DM interactions.

In zero field, we observed a magnon with frequency $f_0 \approx 2.03$ THz (8.40 meV) which we demonstrated was folded from the zone boundary to the zone center. It should be noted that Cu_2OSeO_3 displays no change in either structural or magnetic symmetry from T_c down to at least 10K [133], suggesting a different mechanism for this folding. Assuming spin-wave calculations, which treat the unit cell as an FCC lattice, have captured the symmetry of Cu_2OSeO_3 correctly, then we attribute this new magnon excitation to DM interactions which thus far have not been included in calculations. We speculate that this mode is permitted by symmetry to exist at the Γ point but is perhaps silent in the spin-wave calculations due to vanishing

intensity. However, DM interactions, which will presumably mix magnon states, may give intensity to this otherwise silent mode. We hope this study will motivate future spin-wave calculations which include the DM interactions to further investigate.

It is currently unclear why this mode does not display discernible field dependence, but this may not be inconsistent with the mechanism described above. Spin-wave calculations predict a degeneracy between two magnon bands at the R point, the higher energy magnon being a singlet associated with rotating the spins of a single tetrahedra against the mean field exerted by neighboring tetrahedra [151]. Presumably DM interactions will mix magnon states at this point, breaking this degeneracy. We speculate that the band character at the extrema is then predominantly singlet, explaining the lack of field dependence. Again, spin-wave calculations which include DM interactions or neutron scattering measurements in magnetic field, which have not yet been performed, would be needed to investigate this further.

The helical, conical, and skyrmion phases of Cu_2OSeO_3 are stabilized by the competition between DM and Heisenberg exchanges. In this work we showed that such phases can be detected by high resolution polarimetry experiments. Here we only remark that it is surprising that the observed Faraday rotation in the THz range possesses no frequency dependence. One would generally expect that the THz spectra would display signatures of the low frequency excitations of Cu_2OSeO_3, for instance the helimagnon skyrmion [147] excitations or the uniform mode. Although these excitations lie at lower frequencies than those probed by our measurements in zero or

small magnetic fields, spectral signatures of these excitations are generally expected to extend to higher frequencies. Instead we observe Faraday and Kerr rotations with no discernible frequency dependence within our spectral range.

In large magnetic fields, we studied the field and temperature dependent dynamics of the uniform mode of Cu_2OSeO_3. We found this excitation to surprisingly narrow with increasing applied magnetic field, suggesting a dominant non-Gilbert damping mechanism. Such a narrowing with magnetic field is typically only observed in these chiral magnets in weak magnetic fields before entering the field polarized phase [147]. The origin of this narrowing is currently unclear. However, there have been predictions of an additional weak antiferromagnet order that exists on top of the ferrimagnetic order in Cu_2OSeO_3 [141], and in MnSi type crystals in general [156], which results from an additional spin canting that persists into the field polarized phase. We speculate that the narrowing of this excitation in field may stem from overcoming this canting in large fields, which would presumably reduce magnon coupling. We hope our measurements will inspire future investigations into this effect.

We also discovered that the uniform mode of Cu_2OSeO_3 possessed a spontaneous decay rate in the zero temperature limit. One may be quick to ascribe such a zero temperature decay to inhomogeneous broadening from disorder. While we cannot definitely rule out this possibility, the strong field dependence of the spontaneous decay rate may be indicative of a different origin. In fact, there are several reasons to suspect that such spontaneous decays are permitted in Cu_2OSeO_3. Spontaneous

decays, which require anharmonic magnon interactions are, generally speaking, only permitted if two criteria are met [176]. First, the spin order must be non-collinear due to symmetry and angular momentum conservation [176, 178]. Second, the magnon spectrum must be able to support magnon decays in a fashion that conserves both energy and momentum. We address these points below.

DM interactions are a natural mechanism to obtain a non-collinear spin structure and a coupling of transverse and longitudinal spin components, which may therefore permit anharmonic magnon interactions. Additionally, as we mentioned above, the uniform mode of Cu_2OSeO_3 is not a state with well defined angular momentum but is instead a superposition of several angular momentum states. One would generally expect that the quantum entangled nature of this state would result in zero point motion and therefore may lead to spontaneous decays. Finally, the proposed additional antiferromagnetic order described above would likely also couple magnon states in such a fashion to result in a spontaneous decay. Further theoretical and experimental research is needed to investigate if these effects, or perhaps others, can account for the observed spontaneous decay rate.

With such anharmonic terms possibly allowed the question remains how the uniform mode, the expected global minimum of the spin wave spectrum, can decay while conserving energy. While the minimum of the magnon band is expected to be the uniform mode at $\vec{k}$=0 from spin wave theory, weak dipolar interactions, which are always present in ferromagnets, raise the energy of the uniform mode in magnetic

field by an amount proportional to the sample magnetization [177, 179, 180, 181]. The resulting band structure then contains minima at small momenta $\vec{k}_{\min} > 0$, the exact value of which depends on sample geometry. Therefore, the uniform mode can then in principle decay by splitting into magnons at the band minima assuming the kinematic requirements are met. Such magnon splitting through dipolar effects have been extensively studied in the similar compound YIG [177, 179, 180, 181]. Theoretical treatments which include dipolar effects are needed to determine if such effects can account for the observed decay of the uniform mode in Cu_2OSeO_3.

We also note that it is also generally possible to observe a broadening of a resonance peak by non-equilibrium effects, in the form of a four magnon anharmonic interaction [182]. Such effects have been observed in microwave resonance experiments. However, the fields used in our THz measurements are substantially weaker than those of typical microwave resonance experiments and it is generally assumed that our experiments are strictly in the linear response regime. Therefore, we remark that while the spontaneous decay of the uniform mode may be caused by quantum interactions, further measurements and investigations are required to fully understand the origin of the spontaneous decay.

5.5 Conclusion

In summary, high resolution terahertz transmission and polarimetry experiments were utilized to probe the magneto-optics of the skyrmion insulator Cu_2OSeO_3. Experiments performed throughout the magnetic phase diagram uncovered a new magnetic excitation which was shown to be folded from the zone boundary to the zone center, detected the magnetic phases including the skyrmion phase, and unveiled the unusual dynamics of the uniform precession of the field polarized phase. These observations were generally attributed to the effects of DM interactions, which are particularly strong in Cu_2OSeO_3, on the low energy magnetic response of this chiral magnet. Our results underline the need for further investigation into the effects of DM interactions in these systems.

Chapter 6

Anomalous Exchange Between Ho^{+3}-Mn^{+3} Moments In h-$HoMnO_3$

6.1 Introduction

Low symmetry environments may drive spins to interact through unconventional mechanisms. Such is the case in the hexagonal rare-earth manganites h-$REMnO_3$, a remarkable class of robust multiferroic and magnetoelectric materials which display improper ferroelectricity with $T_c > 600K$ and antiferromagnetism with $T_N \approx 100K$ [183]. Magnetism in these systems is hallmarked by both rare-earth and manganese magnetic moments, the latter of which form a fully frustrated triangular lattice.

CHAPTER 6. ANOMALOUS EXCHANGE BETWEEN Ho^{+3}-Mn^{+3} MOMENTS IN h-$HoMnO_3$

As the rare-earth spins lie orthogonal to the Mn spins, the conventional Heisenberg interaction between RE and Mn moments is expected to be negligible, suggesting the presence of less conventional exchange mechanisms. Furthermore, the low symmetry crystal structure of these materials, which contains as many as 5 magnetic sublattices, permits an array of competing couplings as evidenced by the increasing complexity of the magnetic phase diagram with increasing rare-earth spin [183]. Accordingly, the role of the RE moments in the magnetic response of these materials has been the topic of intense investigation [184, 185, 186, 187].

Of this class, $HoMnO_3$ (HMO) is of particular interest as it possesses the largest effective rare-earth magnetic moment ($10.8\mu_B$) [188], making it a prototypical material for studying magnetic exchange in hexagonal manganites [189, 190, 191, 192, 193]. To date, the role of the Ho moments in the magnetic response remains controversial as many experiments have produced conflicting results [187, 194, 195, 196, 197, 198, 199, 200, 201, 202]. Additionally, few experiments have been performed at sufficiently low temperatures when full magnetic order of both Ho and Mn sublattices is believed to exist and Ho-Mn exchange is expected to be large enough to influence the ground state.

In this chapter we present a systematic study of the low energy optical response of HMO via time domain terahertz spectroscopy under applied magnetic fields. The spectra is marked by an array of Ho ($^5I_8$) crystal field excitations as well as a antiferromagnetic resonance (AFR) of the Mn sublattice. We find the AFR splits *asymmet-*

rically in applied magnetic fields with g-factors much larger than the expected Mn only values. Additionally, we find a large renormalization of the g-factors at T_{Ho} = 5K, the temperature at which the Ho spins are thought to order. We attribute these effects to exceptionally strong and unconventional Ho-Mn interactions. We speculate as to the form of this interaction and suggest that a previously proposed trigonal anisotropy exchange mechanism may potentially cause such effects.

6.1.1 Crystal Structure and Magnetic Order of HMO

Fig. 6.1 displays the hexagonal crystal structure of HMO which consists of alternating layers of corner sharing MnO_5 bipyramids and Ho ions which are stacked along the c axis. At the ferroelectric transition, T_c = 875K, the MnO_5 bipyramids buckle due to structural trimerization [203, 204, 205] resulting in opposite displacements along the c axis of 1/3 and 2/3 of the Ho ions (and neighboring O ions) respectively. The symmetry of the lattice is then reduced to the non-centrosymmetric polar space group $P6_3cm$ with a net polarization of $P_z = 5.6\ \mu Ccm^{-2}$ along the c axis [206]. In this phase, the Ho ions occupy two symmetry distinct sites, the 2a and 4b positions of the crystal lattice, with symmetries of C_{3v} and C_3 respectively.

The magnetic ordering of the Mn sublattice has been determined in recent years [195, 196, 197, 198, 201, 202]. Constrained to lie in the a-b plane by anisotropy, the

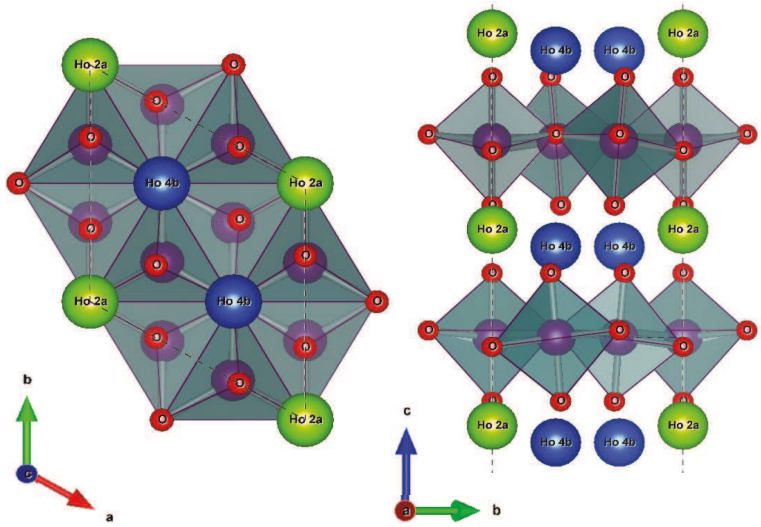

Figure 6.1: Crystal structure of HMO below the ferroelectric transition temperature, $T_c = 875K$ with views along the (left) c axis and (right) a axis of the crystal. In this phase the symmetry is that of the non-centrosymmetric polar space group $P6_3cm$, in which the two Ho^{+3} sites of the lattice posses different point group symmetries.

S=2 Mn moments form a fully frustrated triangular lattice [207]. At $T_N \approx 75K$ the Mn spins order, forming a noncollinear 120 degree structure with symmetry $P6_3'c'm$. Two additional zero field Mn sublattice transitions occur at $T_{SR} \approx 40K$ ($P6_3'cm'$) and at $T_{Ho} \approx 5K$ ($P6_3cm$), in which the Mn spins rotate by 90 degrees within the basal plane.

Consensus on the zero field ordering of the Ho moments has developed over recent years. Neutron [199] and x-ray [187] scattering measurements indicate that magnetization of the Ho sublattices onsets near 30K. Group theory analysis [187, 200] suggests that the $P6_3'c'm$ magnetic symmetry for $T_{Ho} < T < T_{SR}$ permits ordering of both the 2a and 4b Ho sublattices, which are believed to order along the c axis due to uniaxial

anisotropy. In this temperature region the Ho 2a spins align ferromagnetically within one plane and antiferromagnetically between adjacent planes. The Ho 4b sites order identically to the Ho 2a sites but in the opposite direction. Interestingly, the $P6_3cm$ symmetry below T_{Ho} does not permit ordering of the Ho 2a sites, indicating they possibly become paramagnetic at low temperatures. The Ho 4b spins would then form an antiferromagnetic ordering both within planes and between planes below T_{Ho}.

Under applied magnetic fields HMO displays a phase diagram of tremendous complexity [193, 195, 196, 197, 198, 208]. The majority of experiments are performed with applied field along the hexagonal c direction. In this case T_{SR} drops continuously and can be tuned to T_{Ho} with fields of $\approx$ 1T. A reentrant phase with symmetry $P6_3^{'}$ separates the intermediate and high temperature phases at larger applied fields. Further increasing the field returns the system to the high temperature $P6_3^{'}c^{'}m$ symmetry phase. Below T_{Ho} as many as 5 metamagnetic transitions are observed below $H_c \approx 2T$, which presumably stems from the competition between various exchange couplings of the magnetic sublattices [209]. Above H_c it is believed that full spin alignment of both Ho sublattices exists as the magnetization saturates and the suggested $P6_3c^{'}m^{'}$ symmetry permits a full ferromagnetic alignment of Ho spins [187, 200].

6.1.2 The Mn AFR As A Probe Of RE-Mn Interactions

Interactions between RE and Mn moments in hexagonal manganites can be probed by examining the excited states of the Mn sublattice. As stated above, the Mn sublattice forms a fully frustrated triangular lattice with the spins confined to the a-b plane by strong planar anisotropy. The spin Hamiltonian of the Mn spins can be written as:

$$H = J \sum_{<i,j>} S_i \cdot S_j + D \sum_i (S_i^z)^2 - H \sum_i S_i^z \tag{6.1}$$

where $< i, j >$ refers to nearest neighbor pairs, J is the exchange, D is the easy plane anisotropy, and H is the applied magnetic field along the c axis [198]. The excitation spectrum of the Hamiltonian in Eq. 6.1 is well understood. In the $k \rightarrow 0$ limit, applicable to our optical measurements, the low energy spectrum consists of three modes [210]. The first is a Goldstone mode which results from the broken rotational symmetry due to the magnetic ordering of the lattice. The remaining two excitations are a gapped antiferromagnetic resonance whose energy in magnetic fields applied along the c axis are given by:

$$\omega_{\pm}^2(H) = \frac{ab}{2} - \frac{b(a-b)}{2(a+b}H^2 \pm \frac{bH}{2(a+b)^2}\sqrt{H^2 b(b-2a) + 2ab(a+b)^2} \tag{6.2}$$

where $a = 2S_{\mathrm{Mn}}D$ and $b = 3S_{\mathrm{Mn}}J$ are proportional to the anisotropy and exchange respectively. Eq. 6.2 is more easily understood if we expand it in the weak field limit (valid for fields $H < S_{\mathrm{Mn}}J \approx 40$T in HMO) as:

$$\omega_{\pm}(H) = 6\sqrt{JD} \pm \frac{2J}{J + 2D/9}\mu_B H \tag{6.3}$$

One can see from Eq. 6.2 that these two modes are degenerate in zero field with an energy gap of $\omega(0) = 6\sqrt{JD}$ but then split symmetrically in applied fields with expected g-factors of $g = \pm 2J/(J + 2D/9))$ [211].

From Eq. 6.3 we see that the g-factors are bounded to be less than 2 for any positive values of J and D. Indeed, in hexagonal manganites which do not possess rare earth magnetism, e.g. $YMnO_3$ or $LuMnO_3$, the Mn AFR splits in magnetic field with $g \approx \pm 2$. However, hexagonal manganites which possess rare earth magnetism have been found to display g-factors much larger than 2 at low temperatures. This has been interpreted as stemming from RE-Mn interactions which act as an effective magnetic field on the Mn sublattice [186]. With the exchange and anisotropy found to be $J = 2.44$ meV and $D = 0.28$ meV respectively in HMO [198], one expects g-factors of $\pm$ 1.95 from Eq. 6.3. Instead, Talbayev *et al.* [186] observed the g-factors in HMO were much larger than 2 at 20K, although no values for the g-factors or detailed temperature dependence of the g-factors was presented.

6.2 Experimental Methods

Single crystals of HMO were grown via optical floating zone method. Two samples with the orientations of [-1,1,0] (d = 670 μm) and [0,0,1] (d = 594 μm) normal to the sample surface were measured in this study. Sample were hand polished such that they possessed plane parallel sides and a near mirror finish for optical transmission measurements. Time domain terahertz (TDTS) transmission experiments were performed using a home built spectrometer with applied magnetic fields up to 6 T in Faraday geometry ($\vec{k}_{\mathrm{THz}} \parallel \vec{\mathrm{H}}_{\mathrm{dc}}$) as detailed in Ch. 2. Data was taken in several different geometries by varying the relative orientations of the incident THz magnetic field ($\vec{\mathrm{h}}_{\mathrm{ac}}$) and static magnetic field ($\vec{\mathrm{H}}_{\mathrm{dc}}$) as compared to the c axis of the crystal. Measurements performed in magnetic field utilized a rotating polarizer technique, which allows for measurement of the sample's response to two polarization directions simultaneously [76]. Data taken in magnetic fields will be presented in the circular basis for the sample with the c axis normal to the surface, which diagonalizes the transmission matrix and is therefore the eigenpolarizations for this orientation.

6.3 Experimental Results

Figure 6.2 displays image plots of the imaginary, or dissipative, part of the index of refraction, $\tilde{n} = n + ik$, as a function of temperature and frequency for the orientations (a) $\vec{\mathrm{h}}_{\mathrm{ac}} \parallel$ c and (b) $\vec{\mathrm{h}}_{\mathrm{ac}} \perp$ c respectively. One can show that the axial symmetry of

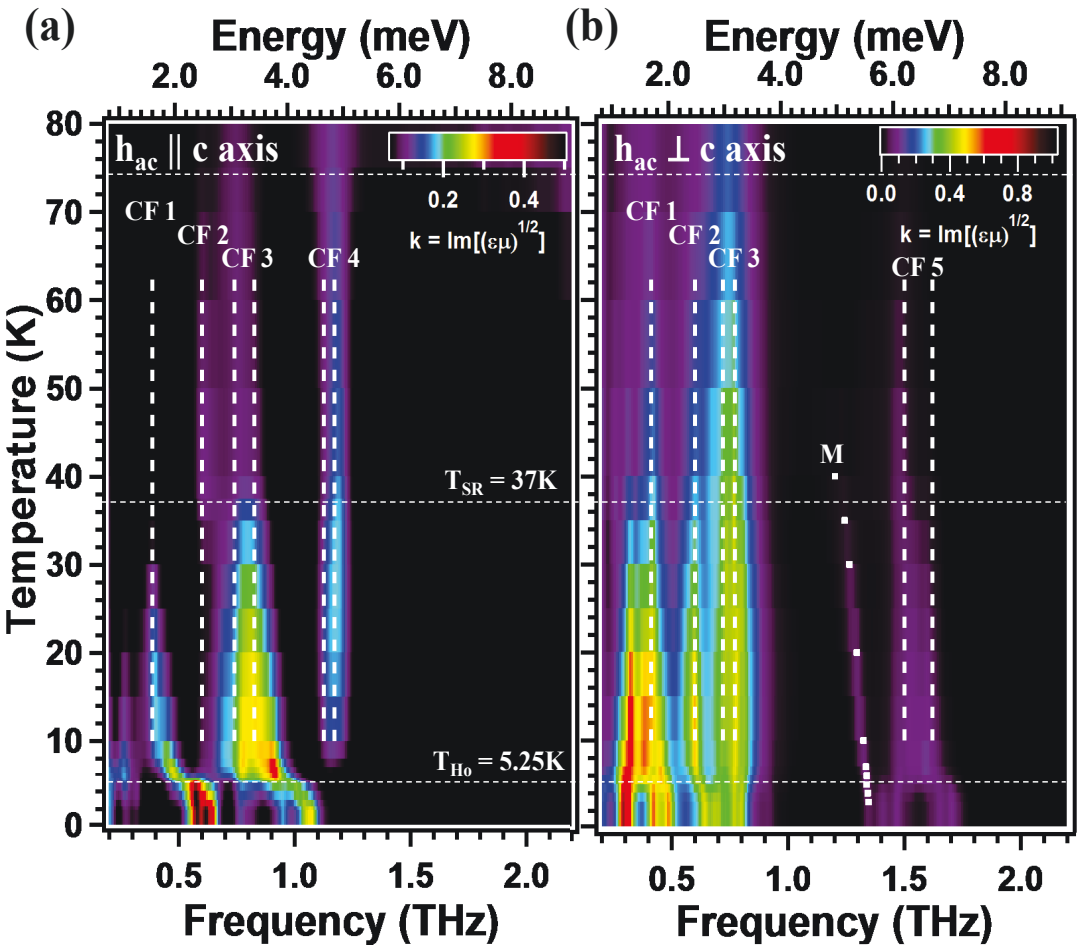

Figure 6.2: Image plots of the imaginary part of the index of refraction as a function of temperature and frequency for the (a) $\vec{h}_{ac} \parallel$ c and (b) $\vec{h}_{ac} \perp$ c geometries respectively. Horizontal dashed lines denote the three zero field transition temperatures while vertical dashed lines label the five observed Ho crystal field transitions identified at temperatures $T \geq T_N$. The excitation labeled "M" is a well known antiferromagnetic resonance of the Mn sublattice observed in all hexagonal manganites.

the lattice constrains the zero field linear response transmission matrix such that only these two orientations are unique [75]. We identify a total of 5 excitations at temperatures $T \geq T_N$, marked by vertical dashed lines in Fig. 6.2, as crystal field transitions of the Ho ($^5I_8$) ions as several excitations are in excellent agreement with previously studies [186, 198] while others are reported here for the first time. Crystal field transitions within the J=8 manifold of $^5I_8$ Ho ions have been previously discussed in a number of compounds [212, 213, 214, 215, 216]. The general expectation is a series of magnetically active singlets and doublets with selection rules that depend on the orientation of the THz $\vec{h}_{ac}$ with respect to the c axis of the crystal. It is believed that the ground state of the Ho ions is a crystal field doublet [186]. However, the $^5I_8$ state is non-Kramers such that degeneracies are not protected by symmetry. Furthermore, broken inversion symmetry allows otherwise forbidden electric dipole transitions between crystal field states while additional complications arise due to the slightly different point group symmetries of the two Ho ion positions. Therefore, while 5 crystal field levels are identified above T_N, new excitations with shifting spectral weight appear as the temperature is reduced, resulting in a spectrum of nearly degenerate clusters of excitations at the lowest temperatures. We neglect to discuss the fine details of the spectra here. However, abrupt changes in the spectra can be used to identify the three zero field transitions, which are marked by dashed horizontal lines in Fig. 6.2, at temperatures of $T_N \approx 72$K, $T_{SR} \approx 37$K, and $T_{Ho} \approx 5.25$K, which are in excellent agreement with previously reported values.

The excitation with strong temperature dependence labeled "M" in Fig 6.2 at ω_0 $\approx$ 1.2 THz in the $\vec{h}_{ac} \perp c$ orientation is the AFR of the Mn sublattice. In order to extract the resonant frequency (ω_0), width (γ), and oscillator strength (S) of the Mn AFR, the spectra were fit to a general model of a Drude-Lorentz oscillator:

$$\mu(\omega) = \frac{S\omega_0^2}{\omega_0^2 - \omega^2 - i\omega\gamma} + \mu_\infty \tag{6.4}$$

where μ_∞ is the high frequency permeability of the lattice. An additional linear background was included in the fit to account for neighboring Ho ion crystal field levels.

Fig. 6.3(a) displays the resonant frequency of the AFR as a function of temperature, extracted by fitting the spectra with Eq. 6.4. One can see that the AFR frequency increases linearly (dashed line in Fig. 6.3) as the temperature is reduced. This is in contrast to other hexagonal manganites in which the AFR frequency has been empirically found to scale with T^3 [211]. Deviations from this power law behavior were only observed at low temperatures, presumably caused by magnetic fluctuations of the rare-earth moments. The fact that the AFR frequency is not described by the expected T^3 power law over any temperature range in HMO may suggest that Ho moment fluctuations onset at T_{SR} in agreement with previous reports [187, 199].

Fig. 6.3(b) displays the temperature dependence of the width (blue, left axis) and intensity (red, right axis) of the AFR. One can see that for the temperature range

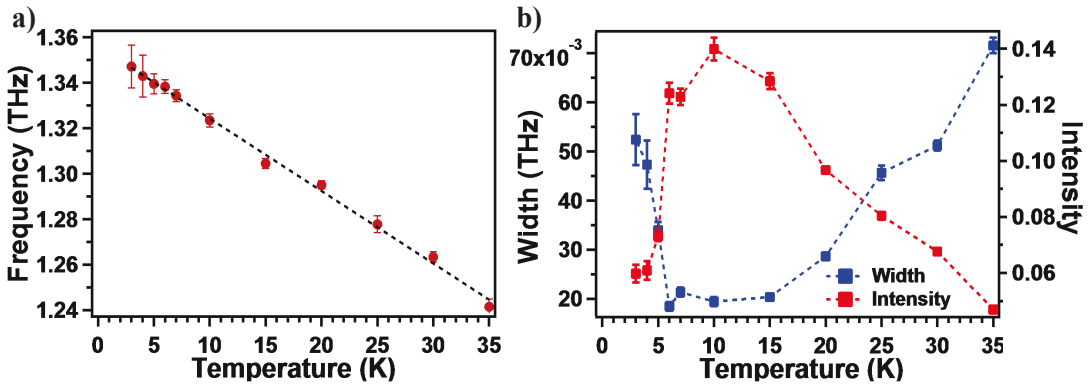

Figure 6.3: Temperature dependence of the MN AFR (a) resonant frequency and (b) width and intensity. The dashed line in (a) is a linear fit of the data while the dashed lines in (b) are meant as guides for the eye.

$T_{Ho} < T < T_{SR}$ the AFR gains intensity and considerably narrows. However, at T_{Ho} the AFR is dramatically damped and the intensity is significantly reduced. It is unclear if such effects stem from the reorientation of the Mn sublattice which occurs at T_{Ho} or if spectral weight is reduced through hybridization with nearby Ho crystal field levels which become nearly degenerate with the AFR below T_{Ho}.

In order to more fully characterize the spectra, measurements were performed as a function of magnetic field as described in Sec. 6.2. Fig. 6.4 displays image plots of the dissipative part of the index of refraction as a function of magnetic field at 20K. The right and left columns of Fig. 6.4 display the response to right and left hand circular polarizations respectively. Figs. 6.4(a-b) displays the data for the entire frequency range of our measurement. One can see the spectra is exceptionally complex with strong dissipation from Ho crystal field levels below $\approx$ 1 THz and at $\approx$ 1.5 THz. The excitation near 1.25 THz whose energy changes linearly with magnetic field is

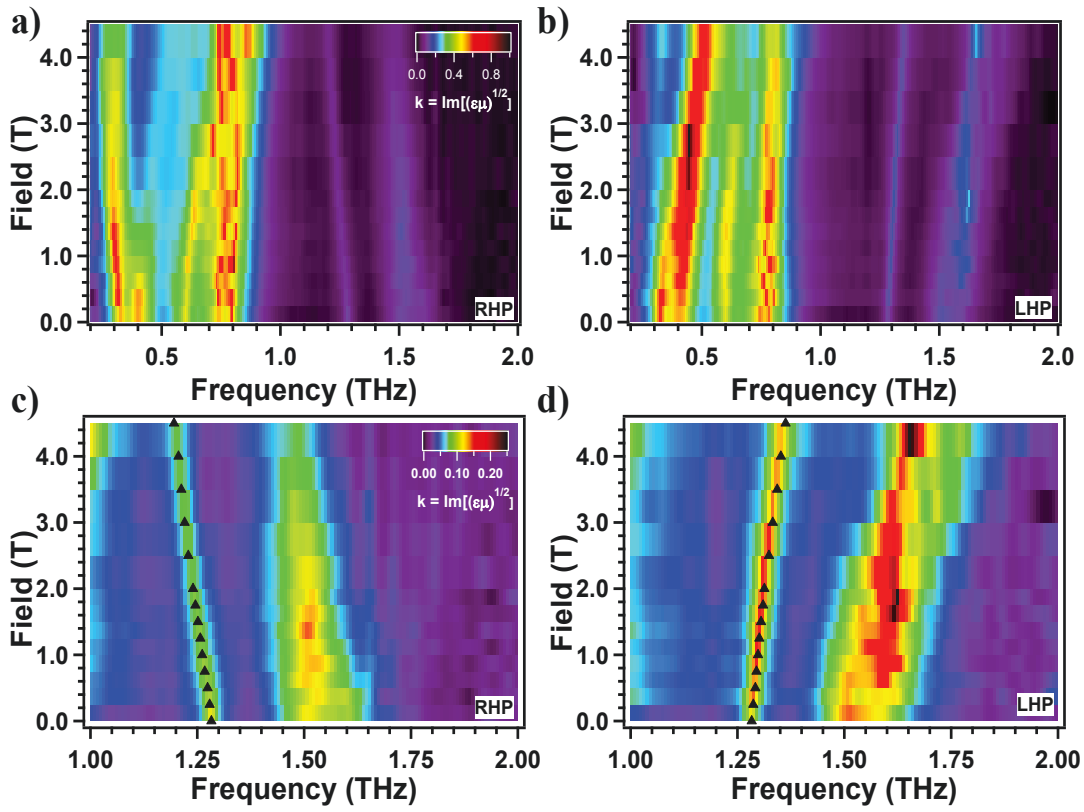

Figure 6.4: Field dependent spectra of HMO for (a) right and (b) left hand circular polarizations respectively shown for the entire frequency range of our measurement. (c-d) Identical plots in the frequency range of the Mn AFR. Black triangles represent the resonant frequencies extracted from fitting the data as described in the text.

the AFR of the Mn sublattice. Figs. 6.4(c-d) displays the same data over a smaller frequency range where the Mn AFR is observed.

One can immediately see that the two branches of the Mn AFR possess distinct selection rules to right and left hand circular polarizations, confirming that the circular basis is the correct basis for spectroscopy in HMO. Additionally, strong circular dichroism can be seen in the image plots of Figs. 6.4(c-d) as the dissipation is significantly stronger in the left hand channel than in the right. In a similar manner

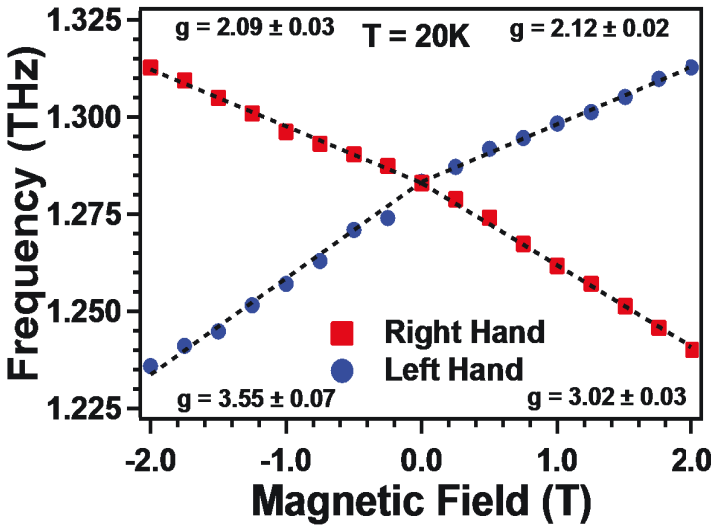

Figure 6.5: Resonant frequency of the Mn AMR as a function of magnetic field. Red squares and blue circles are the extracted resonant frequencies found by fitting the field dependent spectra for right and left hand circularly polarized light respectively. An unexpected asymmetric splitting in which the high energy branch possesses a significantly lower g-factor than the low energy branch is observed. This asymmetry extends to negative fields as well such that a kink in the AFR g-factor is seen.

as the zero field data, these spectra were fit to Eq. 6.4 to extract the magnetic field dependence of the dynamical properties of the AFR. Black triangles in Figs. 6.4(c-d) mark the resonant frequencies of the AFR found via fits of the spectra.

The g-factors of the AFR can be found by fitting the extracted resonant frequencies as a function of magnetic field. To reiterate, the expectation from the Hamiltonian given in Eq. 6.1 is a symmetric splitting of the two branches in magnetic field with g-factors of $g \approx \pm 2$. While g-factors greater than 2 are indicative of RE-Mn interactions the splitting is still expected to be symmetric, with identical g-factors for the high and low energy branches. Fig. 6.5 displays linear fits of our extracted resonant frequencies

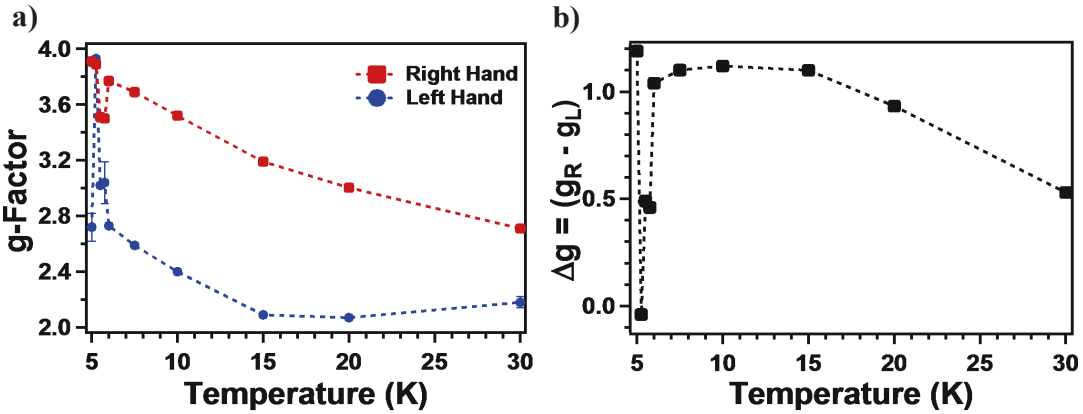

Figure 6.6: (a) Temperature dependence of the AFR g-factors excited by right and left hand circular polarizations. (b) Temperature dependence of the difference in g-factors found by subtracting the left hand g-factors from the right hand g-factors at each temperature.

at 20K. One can see that g-factors in HMO are unexpectedly *asymmetric*, with the high energy branch possessing a g-factor that is significantly lower than that of the low energy branch. Interestingly, this asymmetry extends to negative fields as well, such that there is a kink in the AFR g-factor when the field is turned from positive and negative. To the best of our knowledge, such features have not been previously observed in any other hexagonal manganite.

More information can be obtained by examining the temperature dependence of the g-factors in HMO. Fig. 6.6(a) displays the temperature dependence of the g-factors for right and left hand circular polarizations obtained in positive magnetic fields. Care was taken to only fit data within the low field phase of HMO. At temperatures near T_{SR}, g-factors near the Mn only value of 2 are observed. As the temperature is decreased the g-factors monotonically increase, a trend which is con-

sistent with other hexagonal manganites which possess rare-earth magnetism [211]. However, unlike other manganites, a large renormalization of the g-factors is observed at T_{Ho}. The effect is more easily observed in the left hand channel as the AFR is well separated from nearby Ho crystal field levels. In this case we observe a dramatic increase of nearly 40% at T_{Ho}, suggesting strong interactions between Ho and Mn spins. A similar renormalization is also observed in the right hand channel as well. This effect can be attributed to a large increase in the effective internal fields at T_{Ho}. At this transition the Ho sublattices becomes easily magnetized as evidenced by the observed peak in the susceptibility at T_{Ho} [183]. The Mn sublattice then experiences an increased effective magnetic field which causes the large change in g-factor at the transition. Fig. 6.6(b) displays the temperature dependence of the difference in g-factors of the high and low energy branches of AFR, defined as $\Delta g = g_R - g_L$. One can see that the asymmetry of the g-factors appears to onset near T_{SR} which is further evidence of the onset of Ho spin fluctuations at this transition. As the temperature is reduced the asymmetry increases before saturating at $\Delta g \approx 1$ at 15K.

6.4 Discussion

Our experimental results have demonstrated that exceptionally strong and unconventional Ho-Mn spin interactions exist in HMO. In general, the low symmetry structure of HMO can in principle support a wide array of magnetic exchange mechanisms

between the Ho and Mn sublattices. One generally expects conventional Heisenberg exchange to be negligible in the ground state as Ho and Mn moments are orthogonal to one other. Instead, the broken inversion symmetry of the crystal lattice and the orthogonality of Mn and Ho spins suggests that antisymmetric Dyzaloshinkii-Moriya (DM) coupling [46, 111] may be the dominant exchange, which is believed to be the case in both $ErMnO_3$ [184] and $YbMnO_3$ [185]. However, the symmetry of the AFR g-factors from positive to negative fields suggest that the Ho-Mn interaction scales with the absolute value of magnetic field and is therefore not consistent with DM interactions.

However, more exotic exchanges have been proposed in HMO. For instance, it was recently demonstrated that much of the phase diagram, including the Mn sublattice reorientations, could be reproduced by the inclusion of a symmetry permitted fourth order trigonal anisotropy exchange mechanism in the free energy of the form:

$$H_K = K \sum_{ij} S^z_{Hi} S^y_{Mj} [3(S^x_{Mj})^2 - (S^y_{Mj})^2], \tag{6.5}$$

where S_H and S_M refer to the Ho and Mn spins respectively [48]. Such an exchange mechanism may explain the asymmetric splitting as well as the symmetry from positive to negative fields. One can see that the exchange mechanism in Eq. 6.5 is proportional to S^z_{Ho}. If the Ho spins remain paramagnetic or easily polarizable with magnetic field then we can replace S^z_{Ho} with its expectation value which will be pro-

portional to the magnetic field. Such a term would then have a definite sign for both high and low energy branches of the AFR, thereby shifting the otherwise symmetric splitting to either higher or lower energy depending on the sign. As of the writing of this thesis, we are currently collaborating with Prof. Tchernyshyov's theory group to determine if this unusual exchange mechanism, or perhaps others, can explain our experimental results.

6.5 Conclusion

In summary, high precision time domain terahertz experiments were used to probe the field dependent FIR spectra of the multiferroic $HoMnO_3$. Through careful examination of the temperature and field dependence of an antiferromagnetic resonance of the manganese sublattice, we uncovered evidence of exceptionally strong Ho-Mn spin interactions. The g-factors of this excitation were found to be asymmetric between high and low energy branches and significantly larger than the expected Mn only value. Furthermore, we observed a dramatic renormalization of the g-factors of both branches at the Ho spin ordering temperature. We speculated that these effects may be consistent with an unusual fourth order trigonal anisotropy exchange mechanism that was previously proposed in HMO. The analysis presented in this work provides a paradigm for uncovering similar unusual spin interactions between rare-earth and manganese spins in other hexagonal manganites.

Chapter 7

A Measure Of Monopole Inertia In The Quantum Spin Ice $Yb_2Ti_2O_7$

7.1 Introduction

An important and continuing theme of modern solid state physics is the realization of exotic excitations in materials (e.g. quasiparticles) that have no analogy (or have not yet been observed) in the actual physical vacuum of free space. Although they are not fundamental particles, such quasiparticles do constitute the most basic description of the excited states of the "vacuum" in which they reside [2, 40, 217]. In this regard the magnetic textures of the excited states of *spin ices*, magnetic pyrochlore oxides with dominant Ising interactions, are proposed to be modeled as effective magnetic charge monopoles [218, 219]. Recent inelastic neutron scattering experiments

have established the pyrochlore material $Yb_2Ti_2O_7$ as a quantum spin ice, where in addition to the Ising interactions there are substantial transverse terms that may induce quantum dynamics and - in principle - coherent monopole motion [220, 221].

In this chapter a comprehensive study of the dynamic magnetic susceptiblity of $Yb_2Ti_2O_7$ is reported. This project began as a time-domain THz study performed by a former postdoctoral researcher in our group LiDong Pan. His data suggested a sign change in the real part of the magnetic susceptibility at low frequencies which can only be accounted for in a model in which the magnetic monopols of $Yb_2Ti_2O_7$ possess an inertial mass. However, the frequency of this sign change could not be identified as it is below the accessible frequency range of time-domain THz spectroscopy. Therefore, I performed microwave cavity perturbation experiments on $Yb_2Ti_2O_7$ in order to determine the magnitude and sign of the magnetic susceptibility in the microwave range, thereby constraining the fit of the full frequency profile of the susceptibility. All THz data aquisition and analysis was performed by LiDong Pan, which is presented here as it is was the impetus for performing microwave measurements and constitutes the principle part of our main results. However, I performed the microwave cavity perturbation experiments as well as developed a novel data analysis procedure in which magnetic and electric effects are separated in a fashion that is independent of the geometrical factors of the cavity and sample.

Together our results observe a magnetic susceptibility that is consistent with a model of monopole motion and a magnetic monopole “conductivity” which can be

defined and measured. Using the unique phase sensitive capabilities of our techniques, a sign change in the reactive part of the magnetic response is observed. In generic models of monopole motion this is only possible through introducing inertial effects, e.g. a mass dependent term, to the equations of motion. Analogous to conventional electric charge systems, measurement of the conductivity's spectral weight allows for the determination of the magnetic monopole mass, which is found to be approximately 1800 electron masses. These results establish the magnetic monopoles of quantum spin ice as true coherently propagating quasiparticles of this system.

7.1.1 $Yb_2Ti_2O_7$ As A Quantum Spin Ice

Quantum spin ices have received considerable recent attention in the search for quantum spin liquids, as a possible realization for this novel state of matter in which highly quantum entangled spin degrees of freedom evade conventional long range order down to the lowest temperatures [217]. Magnetic pyrochlore oxides, in which magnetic ions sit at the vertices of corner sharing tetrahedra, provide a three dimensional system where spin ice states are found, when provided with appropriate spin interactions and anisotropy [222]. In classical spin ice materials, such as $Dy_2Ti_2O_7$ and $Ho_2Ti_2O_7$, large classical spins are forced by strong crystal field anisotropy in the local <111> direction, with a primarily ferromagnetic Ising spin interaction. The resulting ground state obeys the Bernal-Fowler ice rules, where each tetrahedron adopts the so-called "two-in, two-out" configuration. This is equivalent to the proton configurations in

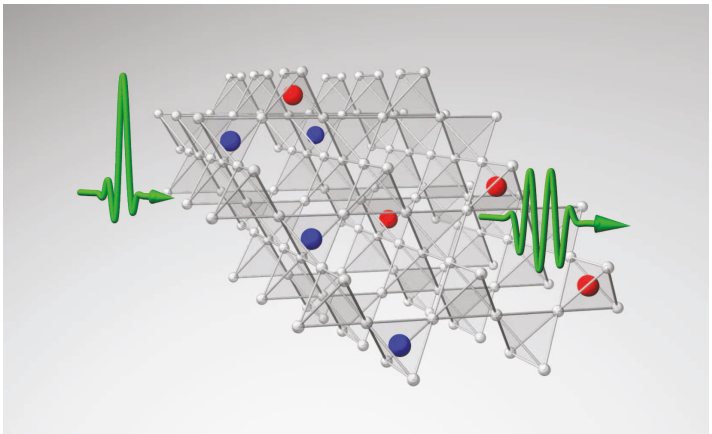

Figure 7.1: Schematic illustration of a quantum spin ice with deconfined monopole and antimonopoles (shown as red and blue spheres), together with incident and transmitted terahertz pulses. In the pyrochlore lattice, magnetic rare earth ions sit at the vertices of corner-sharing tetrahedra, which are shown as grey spheres in the figure.

water ice (two-close, two-far) and hence the classical spin ices are found to similarly possess an extensive low temperature residual entropy. Flipping a single spin (e.g, a dipole excitation) in the spin ice creates a pair of magnetic monopoles in neighboring tetrahedra, which can then subsequently be separated by additional spin flips resulting in deconfined monopoles [218, 219].

The slow dynamics of the monopoles in the classical spin ices are still a subject of investigation, but they are believed to be driven by the strong fluctuating transverse component of the dipolar field arising from thermally fluctuating neighboring spins [223]. In contrast, in materials like $Yb_2Ti_2O_7$, with the addition of finite transverse terms in the spin Hamiltonian, monopole dynamics become inherently quantum and change the situation dramatically [224, 225, 226]. The exchange interaction parameters for the magnetic pyrochlore oxide $Yb_2Ti_2O_7$ have been obtained by recent

inelastic neutron scattering (INS) at high magnetic fields [220], and later confirmed by other experimental and numerical studies [6, 221, 227]. While the largest interaction is Ising and ferromagnetic, significant non-Ising contributions exist. The crystal field structure of the material allows the well isolated ground state Kramers doublet to be treated as an effective spin 1/2 moment in the low energy sector [228, 229]. These results establish $Yb_2Ti_2O_7$ as an exchange quantum spin ice. Although the exact nature of its ground state is under debate [6, 220, 230, 231, 232, 233, 234, 235], at temperatures above a first order transition ($T_c \approx 260$ mK), $Yb_2Ti_2O_7$ is believed to be in a spin ice-like state, but one whose dynamics are determined by non-Ising terms, which allow the quantum tunneling of magnetic monopoles between tetrahedra. Despite the advances in understanding its behavior, there has been as of yet no definitive evidence for spin ice like correlations in $Yb_2Ti_2O_7$. With quantum spin liquids lacking an experimentally verified smoking gun, the characterization of the magnetic monopoles in the quantum spin ice state is a relevant and urgent task.

7.1.2 Ryzhkin model

In analogy with previous work done on proton disorder and dielectric relaxation in water ice, Ryzhkin [218] derived an expression for the magnetic relaxation through monopole motion in classical spin ices. Starting from the formalism for the local

entropy production in an irreversible process, he derived the monopole flux to be

$$\mathbf{J}_i = \mu n_{i,m}(q_{i,m}\mathbf{H} - \eta_i \Phi \mathbf{\Omega}) \tag{7.1}$$

where i refers to positive and negative monopole charge species, μ is the monopole mobility, $n_{i,m}$ is the monopole density, and $\eta_i = \pm 1$. $q_{i,m}$ is the monopole magnetic charge which is set by the condition that the spin dipole moment μ_m equals $q_m a/2$ where a is spin-spin bond length. Ryzhkin's expression differs from a simple transport model of free charge by the inclusion of the second term which includes a dependence on a configuration vector $\mathbf{\Omega}$ that is related to the system magnetization as $\mathbf{\Omega} = \mathbf{M}/q_m$. Finite magnetization reduces the entropy and provides a thermodynamic force that opposes the current. This reaction force originates in the configurational entropy of the monopole vacuum and prohibits a true dc current even in the absence of sample boundaries. $\Phi = \frac{8}{\sqrt{3}} a k_B T$ is a constant of proportionality derived in the context of water ice models that retains its relevance here [236]. As magnetic relaxation proceeds in a spin-ice through monopole motion, the configuration vector is related to the history of the monopole current as:

$$\mathbf{\Omega}(t) - \mathbf{\Omega}(0) = \int_0^t dt'(\mathbf{J}_+ - \mathbf{J}_-). \tag{7.2}$$

Substituting the Fourier transform of Eq. 7.2 into Eq. 7.1 yields a Debye-like

relaxation form for the complex susceptibility:

$$\chi_{\rm m}(\omega) = \frac{q_m^2/\Phi}{1 - i\omega\tau} \tag{7.3}$$

with a relaxation time $\tau = q_m/(n_m\mu\Phi)$ in which n_m is the total (thermally excited) monopole density $n_{+m} + n_{-m}$. The leading dependence of the susceptibility in powers of $1/(-i\omega)$ is a diagnostic for the dominant term in the equations of motion. Eq. 7.3 is characterized by a $1/(-i\omega)$ fall-off at high frequencies that reflects a dominant dissipative response. At low frequencies $\chi_{\rm m}$ is constant and real showing (e.g. the zeroth power of $1/(-i\omega)$) that the dominant effect in the dc limit comes from the reaction force. Note that both real and imaginary parts of Eq. 7.3 will be positive for all frequencies e.g. there is no sign change in χ'_m.

7.1.3 Extended Ryzhkin model

Although such Debye-like relaxation has been found to be a good description of the relaxation processes present in classical spin ice ($Ho_2Ti_2O_7$ and $Dy_2Ti_2O_7$) at the low (kHz) frequencies used in most experiments, it is not strictly speaking a fully mathematically consistent response function as it does not fall off fast enough at high ω to satisfy, for instance, the zero temperature first moment sum rule $\int_0^\infty d\omega\ \omega\chi''_{m\alpha\alpha}(\mathbf{q},\omega) = \frac{1}{2\pi N\hbar^2}\langle[S^\alpha_{\mathbf{q}},[\mathcal{H},S^\alpha_{-\mathbf{q}}]]\rangle$ for local spins [237, 238]. Here $S^\alpha_{\mathbf{q}} = \sum_j e^{-i\mathbf{q}\cdot\mathbf{R}_j} S^\alpha_j$ is the Fourier transform of lattice spin operators and $\mathcal{H}$ is a

spin Hamiltonian. The evaluation of the first moment sum rule depends on the details of the exchange interaction, but being equivalent to a double commutator of the spin Hamiltonian with spin operators, will yield some finite value.

A similar violation of the sum rule is a well-known defect of the Debye model in its application to electronic charge relaxation in dielectrics [239]. In general, the first moment of the *electric* susceptibility *must* obey the sum rule $\int_0^\infty d\omega\ \omega\chi_{\rm e}'' = \frac{\pi}{2}\frac{n_e e^2}{m_e}$ where n_e is the total charge density and m_e the electron mass. Similar to the Ryzhkin model, the Debye model does not fall off fast enough at high ω to satisfy the sum rule. The addition of inertial terms to the Debye model in the classical equations of motion does give $\chi_{\rm e}$ a high frequency asymptote that goes like $1/(-i\omega)^2$ which insures its first moment's integrability [239]. Although at low frequencies in strongly dissipative media, inertia can be neglected, at high enough frequencies it must become relevant to satisfy the sum rule. Frequently in optical studies of charge systems a restricted low energy sum rule is applicable, where the upper limit of integration is taken to be finite, but then n_e is replaced by the density of electrons in the low energy sector, and m_e is replaced by a mass that is renormalized by band and/or interaction effects.

Therefore, for spin ices, irrespective of their exact form, effects beyond Ryzhkin's treatment must become relevant at high enough frequency to satisfy the first moment sum rule. Inertial effects must be included to understand magnetic relaxation in the *quantum* spin ices. In a similar fashion to charge in dielectrics, the Ryzhkin expression Eq. 7.3 can be amended by including a phenomenological inertial term to

Eq. 7.1 as:

$$\mathbf{J}_i = \mu n_{i,m}(q_{i,m}\mathbf{H} - \eta_i \Phi \mathbf{\Omega}) - \dot{\mathbf{J}}_i/\gamma \tag{7.4}$$

where γ is a current relaxation rate.

From the standard definitions, $q_m/\mu = \gamma m$. In what follows, m will be an effective inertial mass which arises in the low energy sector through non-Ising exchanges that lead to monopole tunneling. There is no more contradiction inherent in using a classical model to describe a *quantum* spin ice than there is to use a classical model to describe the conduction of thermally excited charge in a semiconductor where classical inertia also arises through inherently quantum tunneling. Solving in the same fashion as in the above Ryzhkin case gives a classical equation of motion, the terms of which are instantly familiar and map to the form of a damped harmonic oscillator:

$$\ddot{\mathbf{M}} + \gamma \dot{\mathbf{M}} + \frac{n_m \Phi}{m}\mathbf{M} = \frac{n_m q_m^2}{m}\mathbf{H}. \tag{7.5}$$

Solving for the susceptibility we have:

$$\chi_{\mathrm{m}}(\omega) = \frac{q_m^2/\Phi}{1 - i\omega\gamma m/n_m\Phi - \omega^2 m/n_m\Phi}. \tag{7.6}$$

which in terms of τ and γ reads:

$$\chi_{\mathrm{m}}(\omega) = \frac{q_m^2/\Phi}{1 - i\omega\tau - \omega^2\tau/\gamma}. \tag{7.7}$$

With appropriate substitutions ($\omega_0^2 = n_m\Phi/m$ and $\omega_p^2 = n_m q_m^2/m$) Eq. 7.6 can be seen to be equivalent to the Drude-Lorentz equations that describe the response of a classical *electric* charge oscillator.

$$\chi_{\rm m}(\omega) = \frac{\omega_p^2}{\omega_0^2 - \omega^2 - i\omega\gamma}. \tag{7.8}$$

In the limit where $\gamma \to \infty$ Eq. 7.7 recovers Ryzhkin's expression for Debye-like relaxation. In this limit the zero crossing in χ' will move to infinity.

From Eq. 7.7 for the susceptibility and in analogy with charge conductivity we can define a magnetic monopole conductivity $\kappa(\omega) = -i\omega\chi_{\rm m}(\omega) = \kappa' + i\kappa''$. Due to mapping of our expressions Eqs. 7.6 and 7.7 to the Drude-Lorentz model, the magnetic conductivity must obey a low energy sum rule where

$$\int_0^{\omega^*} d\omega\ \kappa'(\omega) = \frac{\pi}{2}\frac{n_m q_m^2}{m}. \tag{7.9}$$

Here ω^* is a energy cut-off that must be smaller than a scale on the order of the Ising exchange parameter J_{zz}, but much larger than γ. Note that this is extension to the usual first moment sum rule for spin systems as $\kappa = -i\omega\chi_{\rm m}$. It is also important to note that this monopole conductivity κ is not the same as the spin conductivity which is defined as the response of a spin current to the magnetic field *gradient* in the small momentum limit [240, 241].

Fig. 7.1.3 plots the results of function Eq. 7.7 for both susceptibility $\chi_{\rm m}$ and the

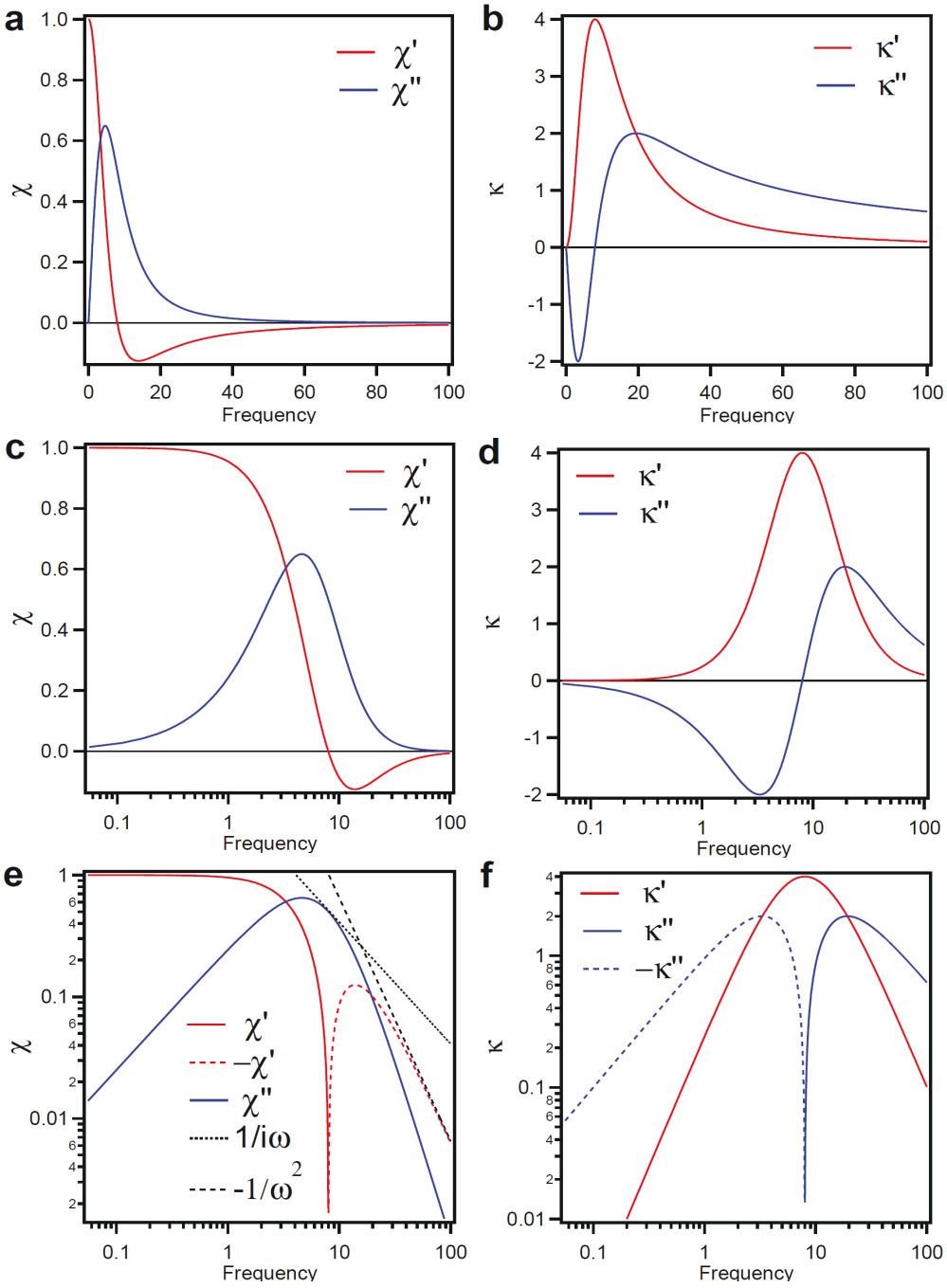

Figure 7.2: Plots of the susceptibility χ_m and the magnetic conductivity κ in the extended Ryzhkin model with parameters $1/\tau = 4$ and $\gamma = 16$ on both linear, log, and log-log scales.

magnetic conductivity κ for the range of τ and γ which is believed to be relevant to $Yb_2Ti_2O_7$. Here the example parameters $1/\tau = 4$ and $\gamma = 16$ are used and plotted on both linear, log, and log-log scales. These plots highlight the utility of analyzing both of these quantities. We see that the dissipative part of the susceptibility χ'' peaks near $1/\tau$, which is the usual Debye-like relaxation behavior. In $\chi_{\rm m}$ the scale of γ appears only as a subtle change in the high frequency power law, which manifests itself as a change of slope on the log-log plot. An experimentalist doing typical low frequency susceptibility or neutron scattering experiments (that measure only χ''_m) would be likely to be completely unaware of the high frequency scale where inertial effects become relevant. The existence of inertial effects are manifest due to the sign change in χ'_m (which are absent in the Debye-like Ryzhkin expression). The magnetic conductivity κ exhibits both frequency scales prominently. The imaginary part of κ exhibits a negative extremum at $1/\tau$. γ is seen as the frequency where $\kappa' > \kappa''$ and κ'' exhibits a maximum. The upper right panel of κ on linear scale demonstrates that if one is measuring at frequencies well above $1/\tau$ the response will be indistinguishable from a Drude-like transport and appear as a monopole metal. In that case the width of the peak in the real part of the monopole conductivity would give γ.

The lower left panel also demonstrates that the bounding behavior of $\chi_{\rm m}$ is a power law in $1/(i\omega)$, where the power indicates what term in the classical equation of motion is dominant at a particular frequency. This is because there are three "response" terms in the equation of motion, which leads to three terms in the denominator of the

susceptibility that can be written as increasing powers in $i\omega$. In different frequency regimes, different terms on the bottom of Eq. 7.7 dominate. Distinct frequency regions of $1/(i\omega)^0$, $1/(i\omega)$, and $1/(i\omega)^2$ are therefore apparent in the plots of Fig. 7.1.3.

7.2 Experimental Methods

Single crystal $Yb_2Ti_2O_7$ samples were grown via the optical floating zone method. Samples were cut into discs and then hand polished on both sides such that they possessed plane parallel sides with a near mirror finish. TDTS experiments, as described in Ch. 2, were performed by LiDong Pan down to 1.4 K, which is well below the peak in the low temperature magnetic heat capacity and within the purported quantum spin ice regime [221] (and well below the estimated scale of the mean-field $T_c \approx 3.4$ K [220]). Microwave cavity perturbation technique (MCPT) experiments were carried out by myself in the fashion described in Ch. 3. Given the separation of frequency and temperature scales of the magnetic and lattice degrees of freedom, the complex magnetic response can be extracted from both techniques. We make the reasonable assumption for an insulator at low temperatures and frequencies the index of refraction n' from dielectric effects is real, with little temperature and frequency dependence below 20 K.

7.3 Experimental Results

7.3.1 TDTS Results

Fig. 7.3.1 displays the results of the TDTS measurements on $Yb_2Ti_2O_7$. Fig. 7.3.1(a) shows an image plot of the frequency and temperature dependence of the magnitude of the complex transmission $\tilde{T}(\omega)$ in zero field. The spectra are normalized by a scan at 50 K, a temperature well above the onset of magnetic correlations. An increase in the low energy dissipation is observed as temperature decreases which is unusual for a large gap insulator. Such an effect is unlikely to come from lattice effects, as the lowest infrared active optical phonon in $Yb_2Ti_2O_7$ has an energy of 2.25 THz. Moreover, there are no reported dielectric anomalies at low temperatures [229, 242]. The feature is most pronounced for frequencies below 0.4 THz, and for temperatures below 10 K. This trend is reminiscent of the low frequency magnetic susceptibility, as this temperature range coincides with the onset of spin correlations in $Yb_2Ti_2O_7$ and the eventual crossover to the quantum spin ice state. The energy scale of this feature matches the scale of the spin interactions obtained from INS [220].

To further demonstrate the magnetic nature of the low frequency absorption, Fig. 7.3.1(b) shows the magneto-optical TDTS spectra of $Yb_2Ti_2O_7$ in the Voigt geometry. The data shows the THz transmission amplitude as a function of frequency and applied magnetic field taken at 1.6 K, normalized by the spectrum at 7 T. The

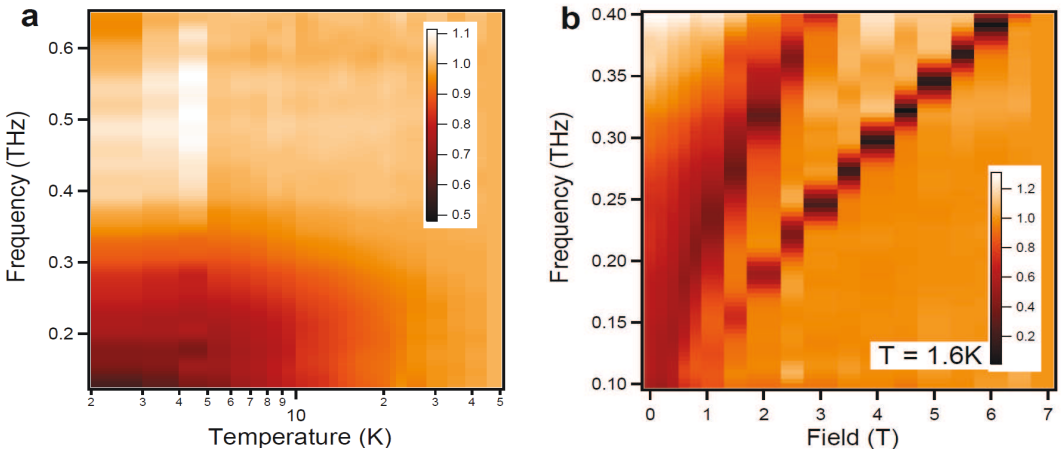

Figure 7.3: (a) The intensity plot of the transmission amplitude from TDTS measurements in zero field, as a function of frequency and temperature, normalized with the spectrum at 50 K. (b) Intensity plot of the transmission amplitude as a function of frequency and field, normalized with the spectrum at 7 T. The data in this plot are measured at 1.6 K in Voigt geometry where $\mathbf{h}_{ac} \parallel \mathbf{H}_{dc} \perp \mathbf{k}_{\mathrm{THz}}$.

field dependence of the absorption features proves the magnetic origin of the zero field dissipation at low frequencies. The behavior of this system in magnetic field has been studied in detail recently [220, 227, 230]. At high fields, $Yb_2Ti_2O_7$ is in a spin polarized state, where excitations are magnon and two-magnon excitations (two dark lines diagonally crossing Fig. 7.3.1(b)). As the field decreases, those dipole excitations crossover to weakly confined quantum string-like excitations that connect monopole - antimonopole pairs, which is signified by their increasing effective g-factors below 3 T [227]. Eventually the magnetic resonance modes lose their sharp structure and the spectra exhibit a broad, diffuse feature at zero field which is consistent with the magnetic monopoles being deconfined in the zero field quantum spin ice state. Below it is shown that, despite its apparently broad profile, this absorption exhibits features

that can be connected to coherent monopole transport.

7.3.2 MCPT Results

Microwave cavity perturbation measurements were performed on several $Yb_2Ti_2O_7$ samples to measure the complex magnetic susceptibility at a frequency lower than that available with TDTS. As will be shown below, these measurements will aid in constraining the Kramers-Kroning consistent fits of the complex magnetic susceptibility. As detailed in Ch. 3, the complex frequency shift of the TE_{011} mode of a cavity resonator upon introduction of a small perturbative sample placed at the magnetic field antinode is given by:

$$\frac{\Delta\tilde{\omega}}{\omega_0} = -\gamma_g \zeta \tag{7.10}$$

where γ_g is the geometrical factor that depends on the resonance mode of operation as well as the ratio of sample to cavity volume. As previously detailed, ζ is the complex generalized electromagnetic susceptibility of the sample which will possesses contributions from both the sample's electric (χ_{e}) and magnetic (χ_{m}) susceptibilities.

We assume that our cavity resonator measurements of insulating $Yb_2Ti_2O_7$ are strictly in the depolarization regime, where the microwaves completely penetrate the sample dimension a, in which case the sample's electromagnetic susceptibility can be

well approximated by:

$$\zeta \approx \frac{\chi_{\mathrm{m}}}{1+N_{\mathrm{M}}\chi_{\mathrm{m}}} + \frac{1}{10}\frac{\chi_{\mathrm{m}}+1}{\left(1+N_{\mathrm{M}}\chi_{\mathrm{m}}\right)^2}(k_0 a)^2\chi_{\mathrm{e}} \tag{7.11}$$

where N_{M} is the demagnetization factor of the sample and $k_0 = \omega/c$ is the microwave wavevector outside the sample. For the $Yb_2Ti_2O_7$ samples investigated here, we estimate that $k_0 a \approx 0.2$. Much like our TDTS measurements, we can separate the electric and magnetic contributions in Eq. 7.11 by assuming magnetic correlations do not onset until temperatures T < 18 K. However, our conclusions are not particularly sensitive to the choice of temperature scale, given that majority of the magnetic susceptibility signal onsets below 10 K.

For temperatures T > 18 K, for which we assume $\chi_{\mathrm{m}} = 0$, plugging Eq. 7.11 into Eq. 7.10 gives:

$$\frac{\Delta\tilde{\omega}}{\omega_0} = -\frac{\gamma_g}{10}(k_0 a)^2\chi_e, \qquad T > 18 \text{ K} \tag{7.12}$$

thus the frequency shift in this temperature range results from the sample's (primarily real) electric susceptibility. Due to the insulating nature of $Yb_2Ti_2O_7$, without any dielectric anomalies at low temperatures, we can assume that below T = 18 K the real part of χ_{e} is constant while the imaginary part is zero. In the present case, because $\chi_{\mathrm{m}} \ll 1$ and $N_{\mathrm{M}} \approx \frac{1}{2}$ the second term in Eq. 7.11 is approximately constant below

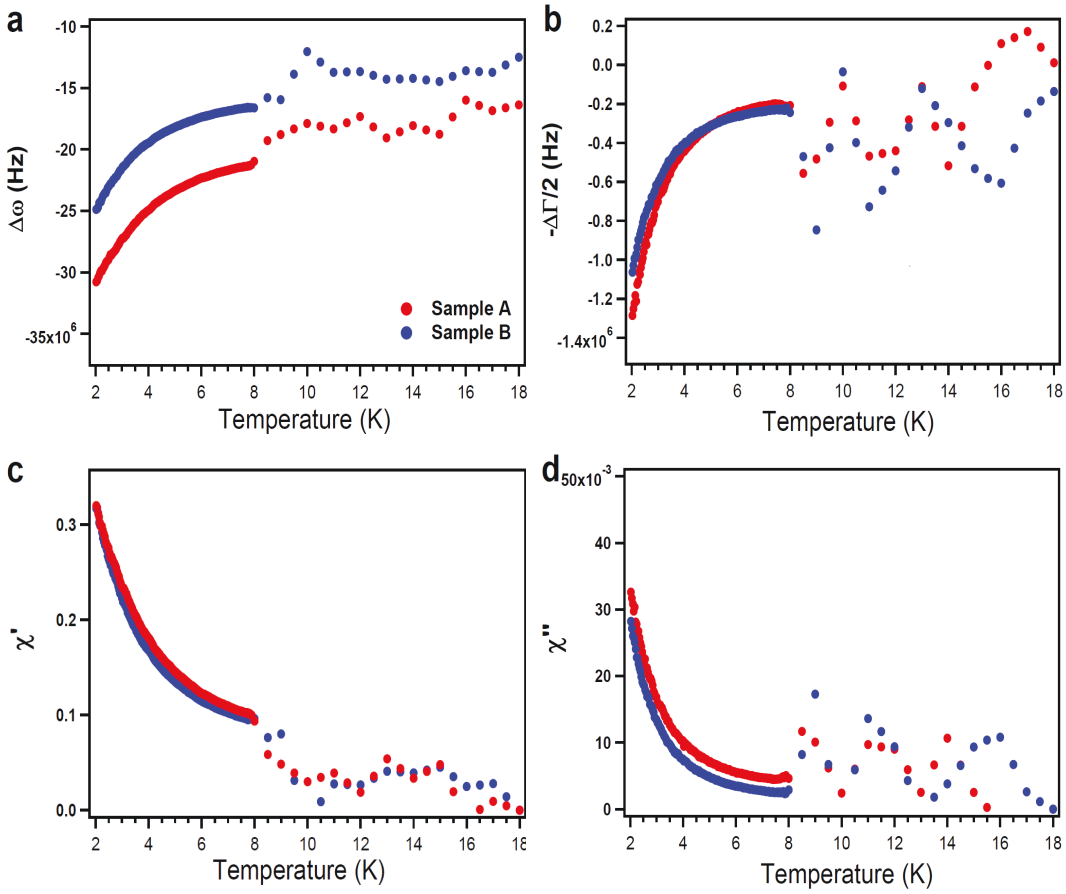

Figure 7.4: Temperature dependence of the real (a) and imaginary part (b) of the complex frequency shift for sample A (red) and sample B (blue), as well as the temperature dependence of the extracted real (c) and imaginary (d) magnetic susceptibility.

18 K. Therefore the electromagnetic susceptiblity below 18 K can be written:

$$\frac{\Delta\tilde{\omega}}{\omega_0} = -\gamma_g \frac{\chi_{\rm m}}{1 + N_{\rm M}\chi_{\rm m}} + \text{constant}, \qquad T < 18 \text{ K}. \tag{7.13}$$

Thus, $\chi_{\rm m}$ can be extracted using Eq. 7.13 if $\chi_{\rm e}$, γ_g, and $N_{\rm M}$ are all known.

In our case we extracted the electric susceptibility by linearly extrapolating our THz data into the low frequency microwave regime which we expect to be a valid method for a good electrical insulator like $Yb_2Ti_2O_7$. Our extrapolations result in values of $\chi_{\rm e} \approx 52$ and $\chi_{\rm e} \approx 66$ at room temperature and 18 K respectively. We can then use the shift in complex frequency from room temperature to 18K of the *loaded* cavity to relate a *change* in $\Delta\omega$ to a *change* in $\chi_{\rm e}$ over this range to find γ_g:

$$\Delta(\frac{\Delta\tilde{\omega}}{\omega_0}) = -\frac{\gamma_g}{10}(k_0 a)^2 \Delta\chi_{\rm e}. \tag{7.14}$$

The absolute shift between the unloaded and loaded cavity was not used in order to reduce the error caused by a resonant frequency offset that results from removal and replacement of the cavity's bottom plate when inserting a sample. The demagnetization factors of our samples were estimated from the sample's dimensions. As it was assumed that the magnetic susceptibility of the sample was negligible above 18 K, the magnetic susceptibility below 18 K could then be calculated from Eq. 7.13 when using the relative shift between the 18 K resonant frequency and the low temperature value.

Sample	**Dimensions (mm)**	**Geo. Factor γ_g**	**Demag. Factor $N_{\mathbf{M}}$**
A	$0.95 \times 1.015 \times 0.582$	5.6×10^{-4}	0.49
B	$0.95 \times 1.015 \times 0.479$	4.9×10^{-4}	0.52

Table 7.1: Dimensions, extracted geometrical factors, and calculated demagnetization factors of the two $Yb_2Ti_2O_7$ samples measured with our cavity resonator technique.

To ensure accuracy of the microwave measurements, two $Yb_2Ti_2O_7$ samples with different thickness were measured and the results compared to each other. Table 7.1 summarizes the dimensions, measured geometrical factors, and calculated demagnetization factors of the two samples. After measuring, sample A was polished to a thickness of 0.479 mm and remeasured as sample B. Figs. 7.4(a) and (b) show the temperature dependence of the change of the resonant frequency and bandwidth from the two samples respectively. The superconducting transition of the cavity is seen at T $\approx$ 8.5 K, above which there is significantly reduced resolution. The reduced resolution above the cavity's transition does not significantly effect our extracted low temperature susceptibility as the signal was small above 8.5 K. Strong signatures from the sample's magnetic correlations are seen below T $\approx$ 8 K in both the resonant frequency and bandwidth of the loaded cavity. The difference in magnitudes of the shifts from the two samples are caused by different geometrical and demagnetization factors. However, the general shape of the curves and even more importantly, the direction of the shift is consistent between measurements. These data and the parameters summarized in table 7.1 were then used to extract the magnetic susceptibility of each sample.

In Fig. 7.4(c) and (d) we plot the temperature dependence of the extracted real and imaginary magnetic susceptibility from out microwave measurements. The data shows a general trend of increase upon cooling, which is what one expects for this material. We found less than a 10% difference in the absolute magnetic susceptibilities between the two samples in the temperature range 1.5 K $<$ T $<$ 8 K, which should be considered quite good. The difference could stem from uncertainties in the extracted geometrical factors or in the demagnetization factors resulting from approximating our rectangular prism samples as ellipsoids.

7.3.3 Magnetic Monopole Conductivity

In Fig. 7.5(a) and (b) we show the real and imaginary parts of the *magnetic monopole conductivity*, $\kappa = \omega\chi(\omega)/i$, as a function of frequency at several temperatures. Data from TDTS are shown as open symbols. Other than the increasing dissipative response at low temperature, the most striking feature of the data is the trend of the frequency dependence of the reactive response (κ''), suggesting a sign change of χ' at a frequency just below the low frequency cut off for TDTS. This sign change is further confirmed by the addition of microwave cavity measurements at 18.5 GHz, which are shown in Fig. 7.5 as solid dots. The combined zero field measurements point to the existence of a zero crossing of χ' at a frequency slightly lower than 0.1 THz. The inset to Fig. 7.5, shows the corresponding complex magnetic susceptibility at low temperatures. Also, an external dc magnetic field pushes

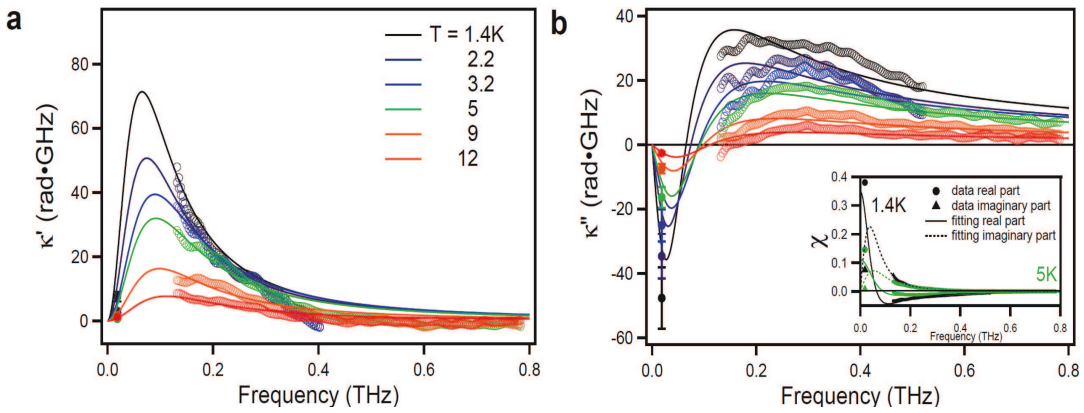

Figure 7.5: Real (a) and imaginary (b) part of the magnetic conductivity $\kappa = \omega\chi(\omega)/i$ as a function of frequency at several temperatures. Solid symbols are data obtained with microwave cavity measurements, while open symbols show data from TDTS. Solid lines are fitting curves as described in the main text. Inset shows the corresponding data and fitting of the complex magnetic susceptibility at two temperatures.

the zero crossing to higher frequencies where reliable TDTS data can be achieved, providing further support for this feature.

Fits shown in Fig. 7.5 as solid lines are obtained by *simultaneously* fitting the real and imaginary parts of $\kappa(\omega)$ including both the microwave cavity and the TDTS data to the expressions of the extended Ryzhkin model. Although the fits are not perfect, it is important to emphasize how restrictive the fitting procedure is (even despite the frequency gap between the TDTS and microwave data) due to the Kramers-Kronig relations between the real and imaginary parts of $\kappa(\omega)$. κ' at low frequency cannot be changed without affecting κ'' at higher frequency and vice versa. This simultaneous fitting of the real and imaginary parts of the data ensures that the essential physics is well captured and constrained. The ability of this model to capture the salient features provides strong support for the phenomenological description of quantum

spin ice developed here, although a more sophisticated model that incorporates a distribution of relaxation times as done recently in the classical spin ices [243] might potentially improve the fits. As the spectra themselves evolve continuously with temperature, these data were fit up to a reasonably high temperature of 10 K, which is presumably well out of the regime of any spin ice correlations. As discussed below, in the paramagnetic regime at temperatures above the mean-field T_c, we believe that fits to Eq. 7.8 should be considered only phenomenological without any correspondence of the fit parameters to monopole characteristics.

The temperature dependence of the fitting parameters is shown in Fig. 7.3.3. The excellent agreement between χ_0 obtained from the current experiment and the values reported in Ref [6] with magnetization measurement lends further support to our phenomenological model of the monopole dynamics in quantum spin ice at low temperatures. The satisfying match between the χ_0 obtained from our measurements and the dc value also suggest (due to the above mentioned Kramers-Kronig constraints) there are no significant features at even lower frequency in the magnetic susceptibility of $Yb_2Ti_2O_7$. Both relaxation rates γ and $1/\tau$ first show a slow decreasing trend upon cooling down to ≈ 4 K (of order the mean-field T_c [220]), with a faster dependence below this temperature, before apparent *saturation* below 2K and down to the lowest measured temperatures. The data can be interpreted in terms of monopole motion below the mean-field temperature scale. The magnetization relaxation rate we find at low temperature ($1/\tau \approx 230$ GHz) is consistent with the limits put on it by neutron

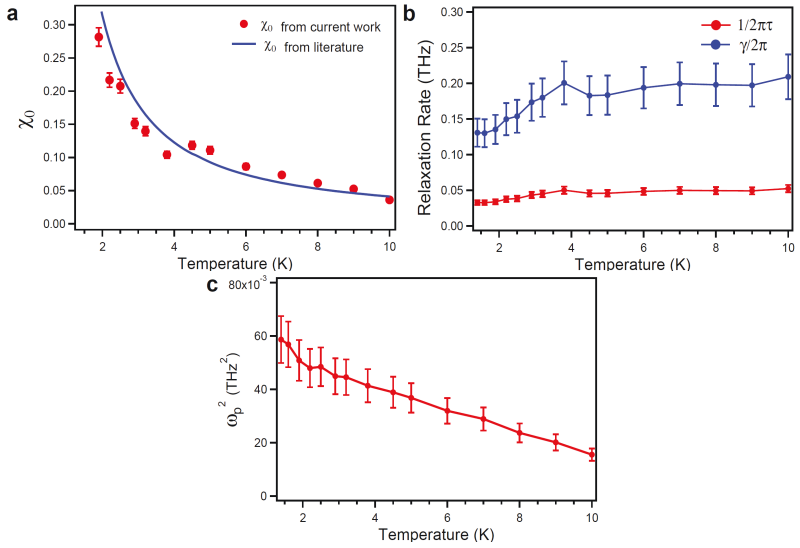

Figure 7.6: (a) χ_0 obtained from the current experiment (dots), and from dc susceptibility measurements reported in Ref. [6] (line). (b) Relaxation rates γ, τ^{-1}. In this plot, rates are divided by 2π to put in units to compare to spectral plots. To compare these quantities to relaxation in time, quantities should have the 2π removed. (c) Magnetic spectral weight (plasma frequency squared) obtained from fitting.

spin echo experiments ($1/\tau_{echo} \gtrsim 250$ GHz) [244]. At this time, the source of the temperature dependence of the momentum relaxation γ is unclear. But in analogy with charge systems, it is possible that the temperature independent offset (e.g. a residual resistivity) is caused in part by impurities. The present system has defects at the 1% level that are describable in terms of "weak stuffing" [234], and possible oxygen non-stoichiometry.

With the mapping of the form of the monopole conductivity described here to the Drude-Lorentz model, it is expected that a similar sum rule to exist for the magnetic spectral weight. To complete the analogy in the present case, the spectral weight from the fits can be extracted and related to a monopole plasma frequency and more

fundamental monopole parameters as $\omega_p^2 = n_m q_m^2/m_m$. The temperature dependence of the spectral weight is shown in Fig. 7.3.3(c), which illustrates the decreasing trend of the magnetic spectral weight upon warming. Further analysis of the fits to the susceptibility of the extended Ryzhkin model allows for the extraction of an effective mass m_m of the monopoles from the fitting parameters. Here the low temperature value of $m_m = n_m q_m^2 \tau/\chi_0\gamma$ is evaluated. The monopole density n_m from the results of Ref. [221], which used the Numerical Linked Cluster method to successfully model the heat capacity of $Yb_2Ti_2O_7$, we used here. Using this computed value for n_m, a value of $\approx 1.6 \times 10^{-27} kg$ or $\approx$1800 m_e for the monopole mass at temperatures below 4 K is determined.

As discussed earlier, the mass of the monopoles originates from their ability to tunnel between sites in the quantum spin ice systems as a consequence of the finite non-Ising exchange terms. Unfortunately, reliable theoretical estimates for the inertial mass of the monopoles in $Yb_2Ti_2O_7$ in this temperature range do not exist. However, it is believed that their tunneling rate is governed by the transverse exchange term $J_{z\pm}$ [221, 225]. A rough estimate for the monopole mass can be obtained with a tight-binding model of charges on the diamond lattice (the dual lattice of spins). In the $q \to 0$ limit a calculation gives $m \approx 4\hbar^2/(\alpha J_{z\pm} d^2)$ where d is the diamond lattice unit cell parameter and α is a temperature dependent dimensionless constant of order unity. With $\alpha = 1$, such a treatment gives an effective monopole mass of $\approx 2.0 \times 10^{-27}$ kg ($\approx$ 2200 m_e), which corresponds closely to the experimental

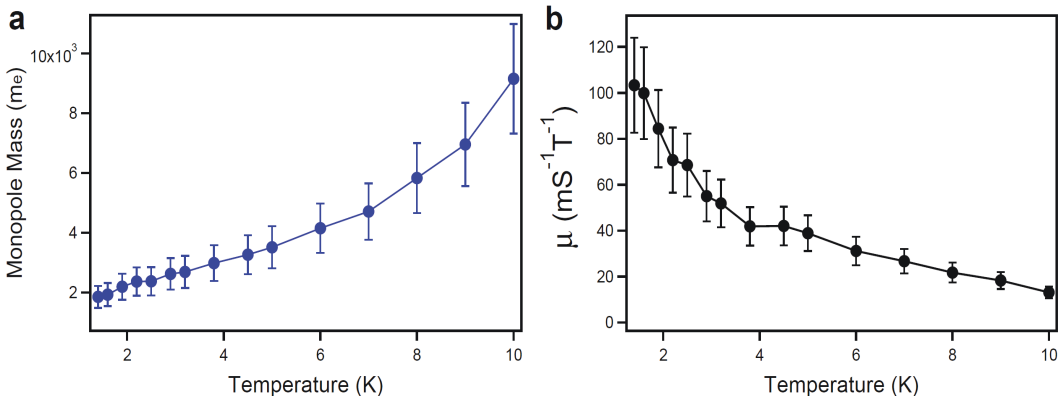

Figure 7.7: Temperature dependence of (a) the effective monopole mass in units of electron mass, and (b) the monopole mobility.

value. As noted above, the spectra evolves continuously into the high temperature paramagnetic regime. Although one can continue to fit the data to the form of Eq. 7.8, the fitting parameters become increasingly unphysical above the temperature scale of the mean-field T_c (Fig. 7.7(a)). At 10K one would determine the fitted mass is 10,000 m_e and strongly increasing, which we do not believe has any physical significance. This agreement of the fitting parameters with a monopole model at low temperatures and the disagreement at higher temperatures is further testament to the validity of our interpretation.

Following the mass determination of the monopoles and mapping to monopole conductivity, a mobility can also be obtained from an analog of the standard expression $\mu = q_m/m\gamma$, which yields a weakly temperature dependent mobility of $\approx$ 100 $ms^{-1}T^{-1}$ for the lowest temperature of our measurement at 1.4 K (Fig. 7.7(b)). This value is several orders of magnitude larger than the mobility found in classical

spin ice materials [243]. This, along with the temperature independent regime of the relaxation rates at low temperature, points to a clear distinction between the monopole transport in the two classes of spin ice materials. This supports the idea that although in principle the mass would get larger (and inertial effects naively would increase) in the classical Ising limit, quantum tunneling from transverse exchange terms is eventually superseded by incoherent monopole hopping. We note that our TDTS experiments of $Dy_2Ti_2O_7$ show no temperature or field dependent features in the spectral range reported here. The demonstration of the sign change in the reactive part of the complex magnetic response function is strong evidence of the monopoles' inertial effects in quantum spin ice.

7.4 Conclusion

In summary, a comprehensive study of $Yb_2Ti_2O_7$ was performed in which the complex magnetic susceptiblity was probed over a broad frequency range stemming from the microwave to terahertz ranges through the use of two optical spectroscopy techniques. A sign change in the real part of the susceptibility was observed and explained by adding an inertial term to the equations of motions which is equivalent to massive monopoles propagating within the quantum spin ice regime. By fitting the extracted magnetic susceptibility to this model, the mass and mobility of the magnetic monopoles was extracted. The monopole mass was found to be roughly

1800 times that of the free electron, in good agreement with the expected value from a tight binding calculation. This study further establishes magnetic monopoles as the true coherent quasiparticles of $Yb_2Ti_2O_7$.

Chapter 8

Summary

In this thesis we investigated the low energy electrodynamics of materials which display quantum magnetism through their optical responses. The techniques used in this thesis were time-domain terahertz spectroscopy and microwave cavity perturbation technique, the details of which were presented in Ch. 2 and Ch. 3 respectively. With these methods, we were able to extract the complex magnetic susceptibility of these materials from the microwave to terahertz spectral ranges, thereby attaining a holistic perspective of their low energy magnetic excitations. By comparing our experimental results to theoretical expectations we were then able to characterize the ground states of these quantum magnets.

In Ch. 4, we demonstrated the spin-orbital singlet character of the ground state of $FeSc_2S_4$ through the observation of a spin-orbital singlet-triplet excitation. Its excitation energy was found to be significantly renormalized from the expected single

ion value by magnetic exchange, in agreement with existing theories. Additionally, we showed that $FeSc_2S_4$'s close promity to a quantum critical point results in the presence of long range correlations which we demonstrated exist over a length scale of over 8 nearest neighbors. Our results establish $FeSc_2S_4$ as a spin orbital-liquid with long range entanglement.

In Ch. 5, high resolution terahertz transmission and polarimetry experiments were utilized to probe the magneto-optics of the skyrmion insulator Cu_2OSeO_3. Experiments performed throughout the magnetic phase diagram uncovered a new magnetic excitation which was shown to be folded from the zone boundary to the zone center, detected the magnetic phases including the skyrmion phase, and unveiled the unusual dynamics of the uniform precession of the field polarized phase. These observations were generally attributed to the effects of DM interactions, which are particularly strong in Cu_2OSeO_3, on the low energy magnetic response of this chiral magnet. Our results underline the need for further investigation into the effects of DM interactions in these systems.

In Ch. 6, high precision time domain terahertz experiments were used to probe the field dependent FIR spectra of the multiferroic $HoMnO_3$. Through careful examination of the temperature and field dependence of an antiferromagnetic resonance of the manganese sublattice, we uncovered evidence of exceptionally strong Ho-Mn spin interactions. The g-factors of this excitation were found to be asymmetric between high and low energy branches and significantly larger than the expected Mn

only value. Furthermore, we observed a dramatic renormalization of the g-factors of both branches at the Ho spin ordering temperature. We speculated that these effects may be consistent with an unusual fourth order trigonal anisotropy exchange mechanism that was previously proposed in HMO. The analysis presented in this work provides a guide for uncovering similar unusual spin interactions between rare-earth and manganese spins in other hexagonal manganites.

In. Ch. 7, microwave cavity perturbation experiments of the quantum spin ice $Yb_2Ti_2O_7$ aided in revealing a sign change in the real part of the susceptibility. This was explained by adding an inertial term to the equations of motions, which is equivalent to massive monopoles propagating within the quantum spin ice regime. By fitting the extracted magnetic susceptibility to this model, the mass and mobility of the magnetic monopoles was extracted. The monopole mass was found to be roughly 1800 times that of the free electron, in good agreement with the expected value from a tight binding calculation. This study further establishes magnetic monopoles as the true coherent quasiparticles of $Yb_2Ti_2O_7$.

The work presented in this thesis focused on the low energy electrodynamics of various quantum magnets. By investigating the magnetic excitations of these materials over a broad frequency range from microwaves to the far infrared, we learned that the magnetic ground states of these materials depends heavily on the local symmetries, geometries, and interactions of spins. This thesis serves as a paradigm for the future optical study of such systems.

Appendix A

Anomalous Three-Dimensional Bulk AC Conduction Within The Kondo Gap Of SmB_6 Single Crystals

A.1 Introduction

Topological states of matter have dominated the condensed matter research landscape in recent years and none more so than topological insulators. Topological insulators possess bulk band inversion due to strong spin-orbit coupling resulting in chiral spin-momentum locked surface states, which are protected by time reversal or crystal

symmetry [245, 246, 247, 248, 249, 250]. Since their prediction, a plethora of experimental evidence has corroborated their existence and investigated their corresponding physics [251, 252, 253, 254, 255]. However, this class of topological insulators are in their essence non-interacting systems. Additionally, clean samples with the Fermi energy deep within the bulk insulating gap have proven challenging to synthesize, limiting their potential applications. Merging strong electron correlations with non-trivial topology is an exciting avenue to pursue exotic many-body quantum ground states with a truly insulating bulk.

The Kondo insulator SmB_6, sometimes referred to as a mixed-valent semiconductor [256], has recently been proposed as such a correlated, topologically non-trivial state [257, 258, 259, 260, 261]. SmB_6 undergoes a crossover from metal to insulator behavior with reducing temperature which can be attributed to the opening of a bulk band gap of $\Delta_K \approx$ 15-20 meV. The gap is believed to originate from hybridization between localized $4f$ electrons near the Fermi level and itinerant $5d$ electrons [256, 262, 263]. Correspondingly, the dc resistivity shows an exponential divergence with reducing temperature, as expected for a gapped system, but then surprisingly plateaus at temperatures T $<$ 5K (Fig. A.1), suggesting a parallel conduction channel [264, 265]. Although first interpreted as stemming from impurity states [266, 267], the low temperature resistivity plateau has recently been proposed to arise from topological surface states residing within the Kondo gap, suggesting SmB_6 to be the first example of a topological Kondo insulator (TKI) [257, 258, 259, 260, 261]. Non-trivial

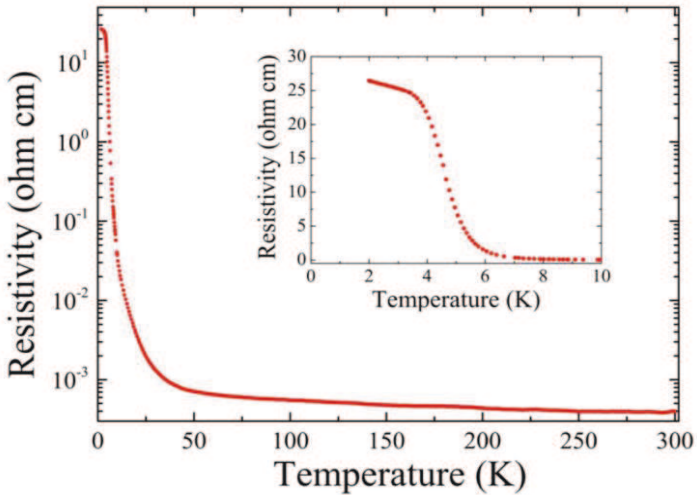

Figure A.1: Temperature dependence of the resistivity of SmB_6. The exponential divergence of the resitivity stems from the opening of a bulk band gap of $\Delta_K \approx 15-20$ meV which originates from hybridization between $4f$ and $5d$ electrons. However, the resitivity unexpectedly plateaus below 5K (inset) which has been attributed to topological surface states residing within the bulk gap. Figure adapted from Ref. [7].

topology is supported by recent calculations which propose SmB_6 possesses three Dirac cones located at high symmetry points of the Brillouin zone [258, 260, 261].

Since the TKI prediction of SmB_6, experimental evidence of surface conduction at low temperatures has been reported via transport [268, 269, 270, 271] and tunneling spectroscopy [272, 273]. Meanwhile other techniques such as torque magnetometry [274], photoemission [275, 276, 277, 278, 279], and neutron scattering [280] also report findings consistent with the TKI prediction. This has led many to hail SmB_6 as the quintessential TKI, with high mobility surface states wrapping a perfectly insulating bulk.

These claims, however, should be considered in conjunction with previous low energy ac optical conductivity experiments of SmB_6 single crystals which have claimed

evidence for *localized states* within the Kondo gap at the lowest temperatures and ac conductivities orders of magnitude higher than the dc value [281, 282, 283, 284, 285, 286]. These observed localized states are in stark contrast to the expected Drude response, indicative of free charge carries, observed from the surface states of Bi_2Se_3 [255, 287]. However, these optical experiments on SmB_6 single crystals pre-date the TKI prediction and may require reinterpretation. Additionally, results from a number of heat capacity experiments reveal a very large low temperature fermionic heat capacity with a γ coefficient that is 2-25 $mJ/mol \cdot K^2$ (the same as some correlated metals) which has been shown to be of bulk origin [288] and therefore seemingly at odds with a bulk gapped state [267, 289, 290].

While the origin of these in-gap states remains an open question, recent experiments suggest that impurities and disorder do play an important role in the low temperature physical properties of SmB_6, perhaps even in the topological aspects. Phelan *et al.* [290] demonstrated that the low temperature resistivity plateau can be tuned as a function of carbon or aluminum doping, typical impurities found in SmB_6 depending on the synthesis method and quality of seed materials. The effects of disorder in the form of $Sm^{+2,3}$ vacancies have also been examined and shown to produce significant changes in the low temperature physical properties of SmB_6 [291, 292]. Recent Raman spectroscopy measurements show that $Sm^{+2,3}$ vacancies on the order of only 1% can effectively close the bulk gap [292]. In this regard, recent theoretical calculations predict the topological properties of SmB_6 to be strongly dependent on

$Sm^{+2,3}$ valence [261], which will correlate with sample imperfections. These results suggest that synthesis method, impurity concentration, and disorder are important considerations and warrant further investigation in SmB_6.

Low energy optical experiments are well suited for investigating the in-gap conduction in SmB_6. Additionally, transmission experiments performed as a function of sample thickness can separate surface and bulk conduction and have therefore been successful in the field of topological insulators [255, 287]. However, optical transmission experiments on the rare-earth hexaborides can be exceptionally challenging due to their unusually large index of refraction. Moreover, as we discuss below, SmB_6 itself has substantial ac conduction that precludes simple transmission experiments. Therefore, the optical properties of the hexaborides have been traditionally studied via reflection techniques, [282, 284, 285] which rely on a Kramers-Kronig transform to obtain the real and imaginary parts of the response and possess substantially less signal to noise than what can be achieved in modern phase sensitive transmission experiments. Transmission experiments of SmB_6 in the far infra-red have been performed with success [286, 293] but a detailed temperature and thicknesses dependence of the optical conductivity has not been provided. Moreover, the continuous wave nature of previously used techniques can give artifacts due to standing wave resonances in the optical apparatus.

In this chapter we present a comprehensive high resolution study of the optical properties of the potential topological Kondo insulator SmB_6 in the terahertz fre-

quency range. As the gap energy, $\Delta_K \approx$ 15-20 meV, is larger than our experimental energy range, $\hbar\omega \approx$ 1-8 meV, we directly probe states within the bulk insulating gap via the optical conductivity. We compare samples grown via both optical floating zone and aluminum flux methods to examine differences originating from sample preparation, but only minor differences are found. Transmission experiments performed as a function of sample thickness determine that the conduction of the in-gap states is predominantly 3D in nature. Our results show that, although SmB_6 may be a dc insulator, the "perfectly insulating" bulk of SmB_6 in fact has significant 3D conduction at finite frequencies that is many orders of magnitude larger than any known impurity band conduction. The potential origins of these states and their coupling to the low energy spin excitons of SmB_6 are discussed. Additionally, the well defined conduction path geometry of our optical experiments allows us to place limits on the sheet resistance of potential surface states, which must lie below our detection threshold if present.

A.2 Experimental Methods

As stated in the introduction, the exceptionally high index of refraction of SmB_6, $n \approx 25$, in the THz regime presents experimental challenges for transmission measurements. One can show from the Fresnel relations that the reflection coefficient of a sample with index of refraction $n = 25$ at normal incidence is $r \approx [\frac{(n-1)}{(n+1)}]^2 \approx 85\%$.

Absorptions in the sample and reflection off the back surface drastically further reduce the transmission. Therefore, novel methods for measuring SmB_6 single crystals are needed in order to achieve sufficient signal to noise.

Correspondingly, we find SmB_6 samples are not sufficiently transmissive in the THz range until sample thicknesses of d $\leq$ 100 μm. In order to achieve such thicknesses, SmB_6 samples were first double sided polished to a mirror finish to ensure plane parallel sides. Samples were then mounted to a double side polished Al_2O_3 substrate of nominal thickness of 500 μm via mounting wax. Once mounted, SmB_6 samples were not removed from the substrate for the remainder of the experiment. Samples were then further polished to a thickness of 10's of μm as measured by a micrometer. Time domain terahertz (TDTS) transmission experiments were then performed. The thickness dependent THz response of the samples was obtained by further polishing the samples in between TDTS measurements.

TDTS transmission experiments, as described in Ch. 2, were performed using a home built spectrometer within a temperature range of 1.6K to 300K [160]. Mounting single crystals of SmB_6 to the Al_2O_3 substrates introduces a new interface which modifies the typical transmission expression presented in Eq. 2.16. In this case it is best to use an identical substrate as a reference as the transmission is then independent of the substrate's thickness. For the case of a single crystal mounted to a substrate, Eq. 2.16 is modified as

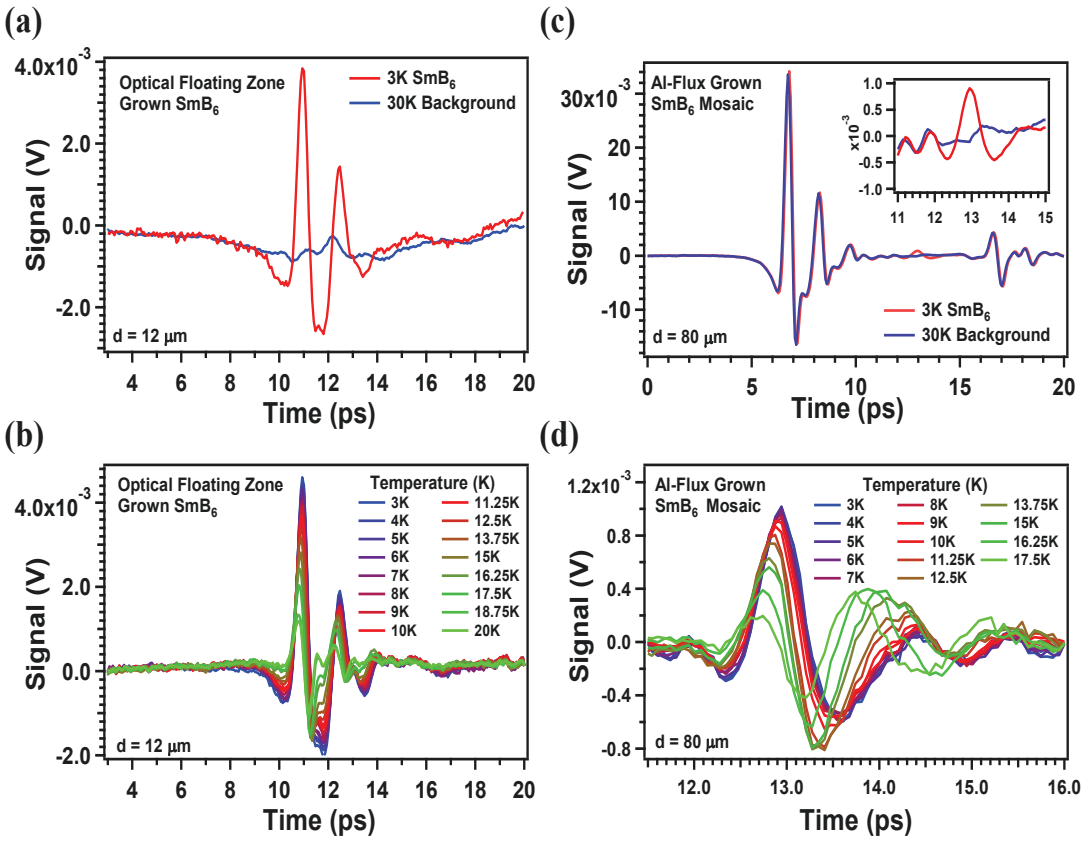

Figure A.2: (a) Transmitted electric field of an optical floating zone grown SmB_6 single crystal mounted to an Al_2O_3 substrate as a function of time at 3K and 30K. The 30K signal is identified as background "light leak" signal which is caused by diffraction of light around the sample. (b) Transmitted electric field as a function of temperature once the background signal shown in (a) is removed by subtraction. (c) Transmitted electric field of the aluminum flux grown SmB_6 mosaic at 3K and 30K. The light leak in this case is much larger due to diffraction between neighboring samples within the mosaic. The two largest signals shown stem from light only transmitted through the Al_2O_3 substrate and must be subtracted from the reference substrate's transmitted electric field. The inset shows an expanded view of the time window in which the signal from light transmitted through the SmB_6 mosaic is observed. (d) Transmitted electric field as a function of temperature once the background signal shown in (c) has been removed by subtraction. See text for more details.

APPENDIX A. ANOMALOUS THREE-DIMENSIONAL BULK AC CONDUCTION WITHIN THE KONDO GAP OF SmB_6 SINGLE CRYSTALS

$$\widetilde{T} = \frac{2\widetilde{n}(\widetilde{n}_s + 1)}{(\widetilde{n} + 1)(\widetilde{n} + \widetilde{n}_s)} e^{\frac{i\omega d}{c}(\widetilde{n}-1)} \tag{A.1}$$

where $\widetilde{n}_s$ is the *substrate's* complex index of refraction. One can verify that in the case of no substrate, $\widetilde{n}_s = 1$, Eq. 2.16 is recovered. TDTS experiments were performed on the Al_2O_3 substrate with an aperture reference where it was found that $\widetilde{n}_s$ is well approximated by a real constant in the THz range, as expected for a good insulator, with a value of $n_s = 3$.

Long wavelength THz radiation restricts TDTS to samples with fairly large cross sectional areas. Therefore, sample diameters greater than 3 mm are typically needed in order to achieve sufficient signal to noise. Optical floating zone SmB_6 samples are therefore better suited for TDTS as single crystals can often be so large. TDTS measurements on large floating zone crystals were performed on single crystal SmB_6 samples with the $\hat{c}$ [001] axis oriented out of the plane of the sample surface. SmB_6 samples grown via the aluminum flux method are generally smaller than what is required for TDTS. In order to achieve sufficient signal to noise on these samples, a "mosaic" of 10 closely packed aluminum flux grown SmB_6 samples were mounted to an identical Al_2O_3 substrate. The mosaic covered a rectangular spatial area of $\approx$ 3.5 mm $\times$ 6 mm in cross section. All aluminum flux samples were oriented with the $\hat{c}$ [001] axis out of the plane of the sample surface. One should note that the cubic symmetry of the $Pm3m$ space group of SmB_6 ensures that the linear optical response is identical for incident THz $\vec{k}$ oriented along any of the principal axes of the crystal

[75].

Additional complications can arise in very low transmissivity samples as low absolute levels of incident radiation can - even for the single crystal - be transmitted through cracks in the sample surface, through gaps in between single crystals mounted in the mosaic pattern, or around the cryostat itself. We refer to this spurious signal as a "light leak" and it must be removed from our data for accurate results. Fig. A.2 displays our methods for removing such light leak signal in the case of both single crystal optical floating zone samples and the aluminum flux grown mosaic, although both are qualitatively similar with the exception that the light leak is larger in the the case of the mosaic. We find that even the thinnest SmB_6 samples become opaque to THz radiation at temperatures T $\approx$ 30K. Presumably this stems from the bulk Kondo gap closing with increasing temperature. Yet, a very small background light leak signal is still transmitted at and above 30K. We identify this signal as the light leak as it is temperature independent from 30K to room temperature. Additionally, we find our data are not systematic until this spurious signal is removed. For the case of optical floating zone samples this signal is simply removed by subtracting the light leak signal as a function of time at T = 30K from the transmitted electric field of the sample at lower temperatures. Fig. A.2 (a) shows the transmitted THz electric field at 3K through an optical floating zone SmB_6 sample (d = 12 μm) as well as the 30K light leak signal. Fig. A.2 (b) shows the measured electric field of the same sample at temperatures below 30K once the light leak signal has been subtracted.

APPENDIX A. ANOMALOUS THREE-DIMENSIONAL BULK AC CONDUCTION WITHIN THE KONDO GAP OF SmB_6 SINGLE CRYSTALS

Removing the light leak signal from the aluminum flux grown mosaic contains an additional complication as the light leak in this case is much larger due to diffraction through spaces between neighboring samples of the mosaic. It requires some additional considerations in analysis, that we believe are applied here for the first time. In a similar manner as described above, the light leak signal as measured at 30K is subtracted from sample scans at lower temperatures. However, the additional step of subtracting the light leak signal from the measured reference substrate's electric field is taken to ensure the transmission is accurate. This step is not necessary for the optical floating zone samples as the light leak signal is substantially smaller than the transmitted substrate's electric field, $< 1\%$. However, the light leak is as large as 40% for the SmB_6 mosaic. Fig A.2 (c) shows the 3K and 30K measured electric field of the SmB_6 mosaic (d = 80 μm). The first large pulse at $\approx$ 7 ps stems from light diffracting around and between neighboring samples of the mosaic and therefore only traveling through the Al_2O_3 substrate. This signal is subtracted from the reference substrate's measured signal to correct the transmission. The next largest signal at $\approx$ 17 ps is the first echo of light which has been reflected within the substrate twice. The inset of the graph shows the signal in between these two substrate pulses where a small but finite signal of light transmitted through the SmB_6 mosaic can be seen at $\approx$ 13 ps. Fig. A.2 (d) shows the extracted transmitted electric field of the SmB_6 mosaic as a function of temperature once the light leak has been subtracted.

A.3 Experimental Results

A.3.1 Low Energy Optical Response Of SmB_6

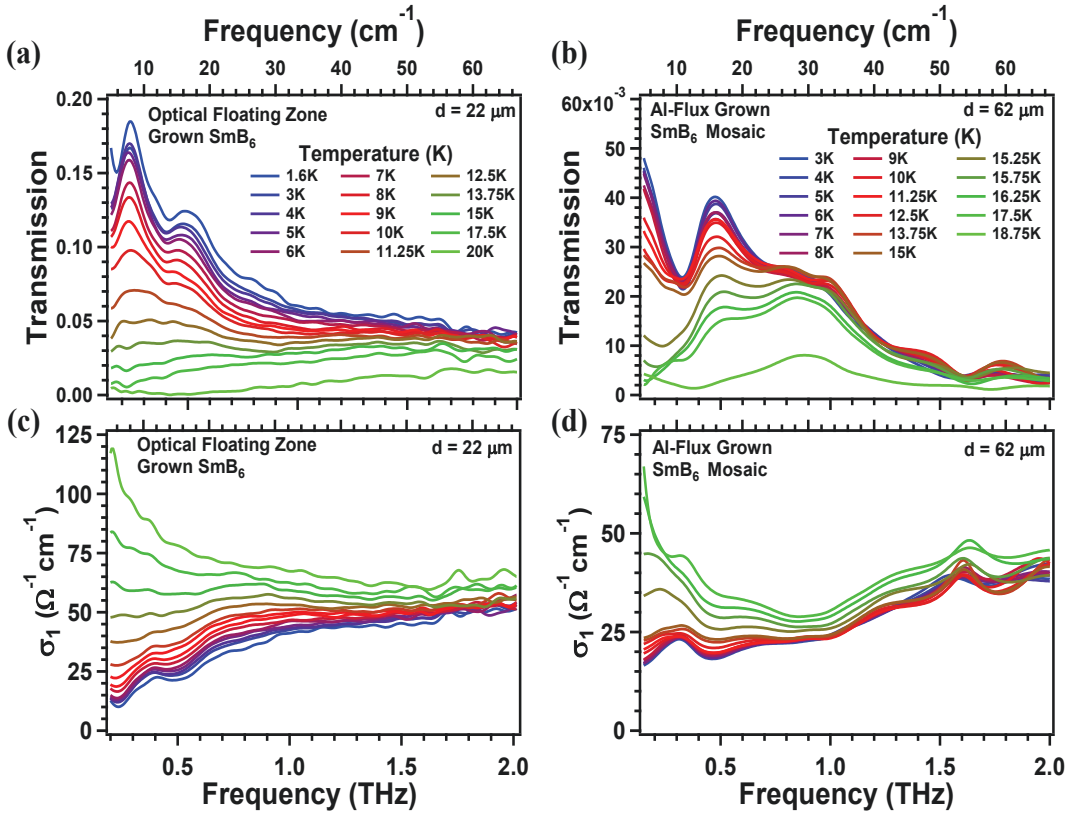

Figure A.3: (a,b) Magnitudes of the complex transmissions, as defined in Eq. A.1, as a function of frequency and temperature for representative samples grown by both (a) optical floating zone and (b) aluminum flux methods. The two samples had thicknesses of 22 μm and 62 μm respectively. (c,d) Real part of the optical conductivity. $\sigma_1(\omega, T)$, calculated from the transmissions shown in (a,b).

Figs. A.3 (a,b) display the magnitude of the complex transmission, as defined in Eq. A.1, as a function of temperature and frequency for two representative samples grown by optical floating zone (d = 22 μm) and aluminum flux methods (d = 62 μm)

respectively. Both samples show qualitatively similar behavior of the transmission. At the lowest temperatures the largest transmission, $\approx$ 5 - 20 % depending on sample thickness and synthesis method, is observed at the lowest frequencies. The transmission then quickly decreases with increasing frequency. Although both samples show the same general features, we believe that the data for the floating zone crystal is more representative of the true spectral shape of SmB_6 due to artifacts that can be introduced in the mosaic geometry. For instance, we believe the dip in transmission of the aluminum flux grown mosaic sample at $\approx$ 0.3 THz is an artifact as it is not systematic between measurements and likely stems from imperfections in our method of removing the light leak signal as described above. For both samples, the transmission gradually decreases with increasing temperature until becoming opaque in the THz range for T $\geq$ 30K for sample thicknesses d $>$ 10 μm. As we will discuss below these features are generally consistent with residual conductivity within a gap which is closing or filling in with increasing temperature.

As stated in the methods section above, the real and imaginary parts of the complex optical conductivity can be extracted from the complex transmission via numerical inversion of Eq. A.1. Figs. A.3 (c,d) display the real part of the optical conductivity, $\sigma_1(\omega, T)$, extracted from the two transmissions shown in Fig. A.3 (a,b) respectively. With some notable differences to be discussed below, the general frequency and temperature dependence of these data are in rough agreement with those of previously reported optical studies [282, 284, 285, 286], although the exceptionally

high resolution of our measurements provide new details.

A crossover from metallic to insulating behavior can be seen as a function of temperature in the conductivity of both samples, which show qualitatively similar behavior. At the highest measured temperature, T = 20K, a Drude-like response can be seen as the optical conductivity is largest at the lowest frequencies and is a decreasing function of frequency thereafter. The Drude-like response indicates the presence of free charge carriers in the conduction band. As the temperature is reduced the magnitude of the Drude response correspondingly decreases, disappearing at T $\approx$ 12K, at which point the conductivity is nearly frequency independent out to 2 THz. At lower temperatures, T $<$ 12K, the conductivity becomes an increasing function of frequency, displaying approximately linear behavior below $\approx$ 1 THz. This change in functional dependence of the conductivity with frequency signifies a shift to a new conduction mechanism. Above 1 THz the conductivity saturates and displays little dependence with temperature. The frequency dependence of the conductivity will be further addressed in the discussion below.

A.3.2 Thickness Dependence

To further investigate these in-gap states, spectra were taken as a function of sample thickness. A thickness dependent study was performed on three samples, two optical floating zone crystals and the aluminum flux mosaic comprised of 10 individual single crystals. To obtain the thickness dependence, spectroscopy was performed,

then samples were mechanically polished to a reduced thickness as measured by a micrometer, then spectroscopy was performed again, etc. As the conductivity carries the dimension of (resistance $\times$ thickness)$^{-1}$, one would expect that the optical conductivity would display thickness dependence if significant surface conduction exists. For samples with bulk 3D conductivity one expects there to be no thickness dependence of the conductivity as reducing the thickness also increases the resistance of the sample rendering the conductivity unchanged. Thus, transmission experiments performed in this fashion can separate surface and bulk conduction as has been done in Bi_2Se_3 [255, 287].

Fig. A.4 (a) displays the results of our thickness dependent study of the optical conductivity at T = 3K $\pm$ 0.1K, in the frequency range in which the highest signal to noise is achieved. However, we mention that our conclusions are not particularly dependent on this temperature or frequency range. Thickness dependence of three samples are shown. The colored regions are representative of the experimental uncertainty of our measurements which will be used for further analysis below. One can immediately observe that there is no systematic dependence with sample thickness of the extracted optical conductivity within the uncertainty of our experiment. One might argue that surface state conduction may lie at frequencies below our experimental range. However, such a prominent feature at low frequencies in the real conductivity would manifest as an obvious trend over a large frequency range in the imaginary conductivity, as the real and imaginary parts of the conductivity are re-

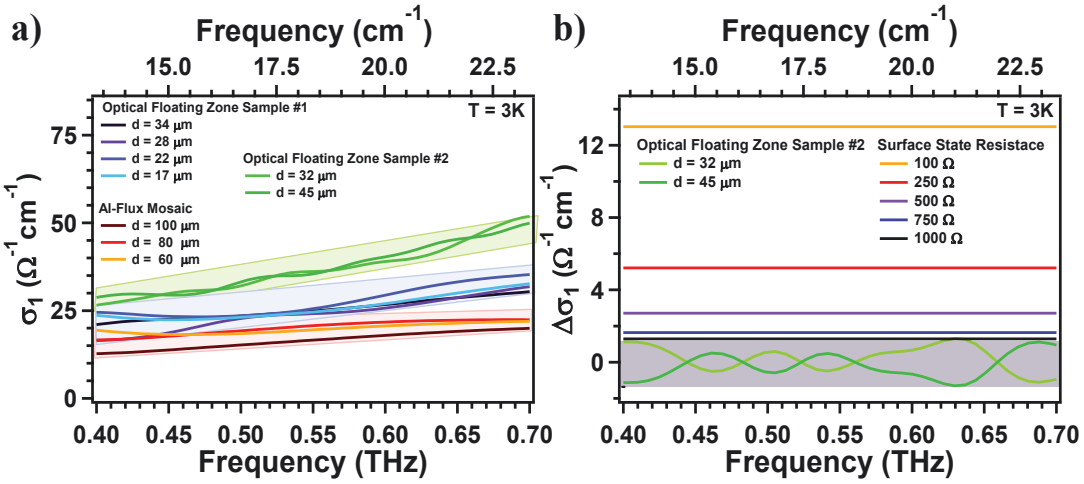

Figure A.4: (a) Thickness dependence of the optical conductivity at T = 3K ± 0.1K in the frequency range of the highest signal to noise of our measurement. Data from two different optical floating zone samples are presented as well as data from the aluminum flux grown mosaic. The colored regions represent the estimated experimental uncertainty of our measurement for each sample. One can see that no systematic dependence on thickness is observed, indicating 3D bulk conduction. (b) Change in optical conductivity expected if surface states were present with the given sheet resistance as derived from our RefFIT tri-layer model. The two lower curves are the conductivities from the optical floating zone sample #2 presented in (a) with the average of the two conductivities subtracted. The gray box represents our estimated measurement uncertainty. From this we conclude that if surface states are present then they must have a sheet resistance $R_s \geq 1000\ \Omega$. See text for details.

lated through a Karmers-Kronig transformation. We observe no such trend in the imaginary part of the conductivity for any SmB_6 sample measured in this study. We therefore conclude that the principal signal of the residual conductivity of the in-gap states stems from 3D bulk conduction.

With the 3D nature of the optical conductivity within the gap established, we now discuss how this relates to the TKI prediction of SmB_6. Our measurements are not able to exclude topological surface states residing within the bulk Kondo gap.

However, if surface states exist in the gap then they must have a conductance below the detection threshold of our measurement. Thus, an estimate of our uncertainty can be used to place limits on the potential surface state conductance. To do so, the optical transmission was modeled in RefFIT [106]. The T = 3K conductivity of the optical floating zone sample #2, shown in Fig. A.4 (a), was chosen for the model as the thickness dependence on this sample possesses the lowest experimental uncertainty. A tri-layer model of surface state - bulk - surface state was developed to model the transmssion. The bulk conductivity was given by that of the d = 32 μm sample shown in Fig. A.4 (a). The two surface states were modeled as two identical 2D Drude responses, in agreement with the surface states observed in Bi_2Se_3 [255, 287]. We assume that the conductance of these states is constant as a function of frequency in our spectral range. This is consistent with the $\approx$ 10 THz scattering rate determined in quantum oscillations experiments [274]. Therefore, the surface state conductance would manifest in the tri-layer model as a frequency independent offset to the conductivity when the thickness of the sample is varied.

The results of the model are shown in Fig. A.4 (b). Shown at the bottom are the optical conductivity at T = 3K of the optical floating zone SmB_6 sample #2 for thicknesses of d = 32 μm and 45 μm with the average of the two thicknesses subtracted. The gray box indicates our approximate uncertainty in the experiment. The horizontal lines demonstrate the expected offset in the effective optical conductivity that would be extracted if surface states with the specified resistances existed in ad-

dition to the bulk conductivity. From the model we conservatively conclude that we would be able to identify surface states with a sheet resistance $R_s \leq 1000\ \Omega$ in our experiment. Therefore, surface states with a sheet resistance below this detection threshold can be excluded.

A.3.3 Coupling Of Bulk States To Spin Excitons

The results presented above show that although SmB_6 may be a bulk dc insulator, it shows significant bulk ac conduction. Low energy 3D bulk states exist within the gap of SmB_6. These states within the gap can also greatly affect other low energy excitations of SmB_6. For instance, previous experiments indicate a magnetically active collective spin-exciton which results from the electron-hole continuum to exist within the gap of SmB_6 with an energy of ≈ 14 meV [294, 295, 296, 297]. In a recent neutron scattering study [280, 298], the width of the exciton was observed to be exceptionally narrow, ≈ 2 meV, although more recent measurements with improved resolution suggest the width of the resonance to be even narrower than that, ≈ 100 μeV [299]. The narrow width suggests the spin exciton to be an extremely long lived excitation and was speculated to be protected from decaying into electron-hole pairs by the hybridization gap in which it resides.

However, the exciton can in principle couple to states within the gap, whether they are topological Dirac states or bulk states. Coupling of the spin exciton to such states can have tremendous impact on the physics of SmB_6. The possibility of spin

excitons coupling to surface states has been discussed theoretically [300] and then reported experimentally via tunneling spectroscopy [301]. Meanwhile, evidence of coupling between spin excitons and bulk states was recently presented via Raman spectroscopy measurements [292]. In that work it was found that disorder in the form of $Sm^{+2,3}$ vacancies on the order of only 1% leads to states within the gap. The spin exciton shows a corresponding spectral broadening with increasing disorder suggesting decay through these bulk in-gap states.

While the spin exciton lies at higher energy than what our experiment can access, we can still quantify how the finite density of states within the gap couples to these collective excitations. A similar analysis has been performed previously in regards to how crystal field line widths in metallic systems and the "resonance mode" in high T_c cuprate superconductors [302] couple to a continuum of states. One may use the expression

$$\Gamma = 4\pi[gV_cD(\epsilon_F)]^2\Omega \tag{A.2}$$

where Γ is the full width at half maximum of the resonance, Ω is the exciton energy, $D(\epsilon_F)$ is the density of states at the Fermi level, and g is the coupling constant.

With the energy, $\Omega \approx 16$ meV, and width, $\Gamma \approx 2$ meV, of the spin exciton as measured in floating zone crystals by Raman experiments [292], we can extract the coupling constant if the density of states at the Fermi level is known. An estimate of the density of states can be obtained from the metallic contribution of the heat

capacity, $C_{ele} = \gamma T$. Interestingly, heat capacity measurements find a surprisingly large metallic component at low temperatures, often on the order of 10 mJ K^{-2} mol^{-1}, in agreement with the observed large low energy spectral weight [267, 289, 290]. Additionally, recent measurements indicate that the large metallic heat capacity is independent of sample surface area and is therefore of bulk origin [288]. Phelan *et al.* report a value of $\gamma = 25$ mJ K^{-2} mol^{-1} in optical floating zone samples [290]. In the simplest picture of a non-interacting Fermi gas, the density of states is proportional to γ, in the units of the given heat capacity, as, $\gamma = \frac{\pi^2 k_B^2 N_A V_c}{3} D(\epsilon_F)$, where k_B is Boltzmann's constant, N_A is Avagadro's number, and V_c is the volume of one SmB_6 formula unit. Substituting the observed value of γ into this expression and then the corresponding density of states into Eq. A.2 results in a coupling constant of $g = 9.40$ meV.

The coupling constant is more easily understood in the conventional dimensionless form, λ, which can be determined via the expression, $\lambda = \frac{2 I_0 g^2 V_c D(\epsilon_F)}{\Omega}$. Here, I_0 is the ratio of the integrated spectral weight of the excition to the total integrated spin structure factor. An $I_0 \approx 0.4$ was determined from neutron scattering experiments [280]. Substituting in the appropriate values gives $\lambda = 0.047$. This calculation shows that the coupling of the excitons to the bulk in-gap states to be very weak.

The strong dependence of the exciton's linewidth on sample disorder [292, 299] is interesting considering the relatively weak dependence of the in-gap states we probe. Moreover, the fact that the exciton is seen clearly in Raman, whereas it it is not

observed in the infrared [286] points to a well-defined selection rule associated with its excitation. In inversion symmetric systems like SmB_6 excitations are either Raman active or infrared active, but not both. We therefore speculate that the exciton is - in the ideal case - prevented by symmetry from coupling to the infrared continuum and it is only through disorder that this coupling becomes finite. In other words, the exciton's lifetime disorder dependence comes from a strong dependence of disorder on g in Eq. A.2 and not $D(E_F)$.

A.4 Discussion

Our results and the existing heat capacity data show that the low energy density of states in SmB_6 is quite large, in contrast to the assumption of a clean insulating gap. Why then do transport experiments claim to see a perfectly insulating gap with activated dc transport? First, it is important to point out that in the limit of zero temperature dc transport can only probe extended states. However, ac experiments are also sensitive to *localized* quasiparticle states, as well neutral excitations that carry a dipole moment (e.g. phonons as the least exotic example). In ac experiments, charge does not need to be transmitted across the sample as charge in localized states can still oscillate at ac frequencies on length scales smaller than the localization length and dissipate energy. Samples which display such behavior can appear as insulators in dc transport experiments but conductors at finite frequency. In this regard, we

remind the reader that the ac conductivity in the THz range in SmB_6 is orders of magnitude greater than the dc value at low temperatures [282, 284, 285, 293] in agreement with this picture.

What is the origin of the in-gap ac conduction? The most obvious explanation is that it originates from impurity states. A number of authors have pointed out the special role of impurities in Kondo insulators, which in some cases can form a Kondo hole impurity band [303, 304, 305, 306]. Yet, these scenarios predict magnetic phenomena which are not observed. However, the general phenomenology of the low temperature ac and dc conductivity of SmB_6 is somewhat similar to what is observed in some localization-driven insulators, such as the disordered electron glass Si:P [307]. In the latter systems the dc conductivity is described by a model of variable range hopping with a stretched exponential activated dependence and a power law dependence of the ac response. The expected dependencies are determined by the form of the density of states at the Fermi level [307, 308, 309]. Assuming a nearly constant density of states, one expects the dc conductivity, for 3D hopping conduction to follow the expected Mott form for Fermi glasses going with temperature as $\ln(\sigma_{dc}) \propto T^{-\frac{1}{4}}$ [308]. Indeed Gorshunov *et al.* claim such a temperature dependence for temperatures $4K \leq T \leq 10K$ with a characteristic energy scale of $T_0 = 54K$, although fitting an exponential to such a small range cannot be considered very conclusive. In such insulators where disordered induced localization is expected to be central to the physics, the expectation is that at the lowest temperatures ac conduction occurs

between *resonant* pairs of localized states. Without interactions the ac conductivity is expected to follow Mott's famous ω^2 law [310], which is clearly inconsistent with the data exhibited here. With interactions included, but at frequency scales below that of the characteristic interaction energy between electron-hole pairs, the expectation is that the conductivity is quasi-linear with $\sigma_1(\omega) = e^4 D(\epsilon_F)^2 \xi^4 [\ln(2I_0/\hbar\omega)]^3 \omega/\epsilon$ where ξ is the localization length [309]. I_0 is the characteristic scale of tunneling between localized states that is expected to be bounded by the hybridization gap energy. Our ac conductivity data (Fig. A.3) is roughly consistent with this linear dependence at our lowest measured frequencies. It is also important to point out that in principle, even the "metallic" heat capacity seen in SmB_6 is consistent with localized states as it has been emphasized that despite their insulating nature such systems can still show a $fermionic$ linear in T heat capacity (albeit of a magnitude far less than observed in the present case as discussed below) [311, 312, 313, 314].

However, despite the (partial) qualitative agreement with a picture of localized bulk states, there are important quantitative issues that need to be resolved. For instance, the magnitude of the ac conductivity in the present case is quite unlike other disordered insulators. It is approximately four orders of magnitude larger than both the impurity band conduction in Si:P (at say doped 39% of the way towards the 3D metal-insulator transition) [307] and is essentially of the scale of the ac conduction in completely amorphous Nb_xSi_{1-x} [315] alloys. Although in principle this very large scale of the ac conductivity can follow from the very large $D(E_F)$ in SmB_6, the large

heat capacity itself is unexplained. Although localized states at E_F can manifest a linear in T heat capacity, the heat capacity of SmB_6 is many orders of magnitude larger than any known localization-driven insulator ($\sim 10\mu$J K^{-2} mol^{-1} for the impurity band in Si:P at $\sim$ 50 % of the x_c for the metal-insulator transition [311, 312] and $\sim$ 0.5mJ K^{-2} mol^{-1} for amorphous glasses [313, 314]). Additionally, localized states at E_F will more generically result in stretched exponential variable range hopping style-activation and not simple activation in the transport.

Gorshunov *et al.* claim that sample imperfections manifests as a slight maximum in the real conductivity at 0.72 THz (24 cm^{-1}) [286]. Although, this is an energy scale that matches the activation energy scale of the dc resistivity above 10K, we have observed no such band in any sample measured in this study. Moreover, Gorshunov *et al.*'s band was only a weak maxima, and it is not clear (even if such a band was present) why it would manifest in the dc data with an activated temperature dependence. It has also been found that the activation energy is strongly dependent on pressure [316], which has no obvious explanation where the activated transport arises through hopping in an impurity band.

Therefore, one should consider the possibility that these in-gap states are intrinsic to SmB_6. The apparent agreement in the optical conductivity in our measurements between samples grown by different methods and under varying conditions suggests a different explanation than impurities. One can see from Figs. A.3 and Fig. A.4(a) that the low temperature conductivities of the samples measured in this study vary

by - at most - a factor of 2. Generally, insulating states induced by disorder have conductivities that are exponentially sensitive to the degree of impurities, often displaying large variation in physical properties upon even small changes to the sample composition. The apparent lack of dependence upon sample preparation and, in some cases, doping [290] suggests the intrinsic nature of these localized states. We remind the reader that the aluminum flux grown mosaic was comprised of 10 individual single crystals and is therefore likely representative of samples grown by this method.

A number of possibilities exist for ac conduction by an intrinsic mechanism at low energy. One theory suggests that a Fermi surface comprised of electrically neutral quasiparticles can exist within the Kondo gap [317, 318]. These quasiparticles, although electrical neutral, may still possess an electrical dipole moment and therefore conduct at ac frequencies [319]. A separate theory claims that these in-gap localized states may originate from intrinsic electrons in SmB_6 that become self trapped through interactions with valence fluctuations [320]. Additionally, a recent torque magnetometry experiment has claimed to observe unconventional quantum oscillations stemming from a bulk 3D Fermi surface in SmB_6 [321]. These results suggest that the potentially intrinsic nature of our observed in-gap localized states warrants further consideration and investigation.

Lastly, we discuss the limits placed on the potential surface state sheet resistance from our data. As discussed above, Fig. A.4 (b) demonstrates that the surface states of the SmB_6 samples studied must have a sheet resistance of $R \geq 1000\ \Omega$

or they would be detectable in our measurement. The reported sheet resistance of surface states in SmB_6 varies greatly between transport experiments, ranging from 0.1 - 100 Ω [268, 270, 271]. This wide discrepancy may originate from the unknown conduction paths in 4 probe measurements as current can in principle travel along all surfaces of the sample or perhaps from differences in surface preparation methods. A benefit of our optical experiments is that the conduction paths are precisely known as the measurement geometry is well-defined. Correspondingly, larger values of surface state sheet resistance are often reported from optical techniques such as R = 250 Ω [322] in SmB_6 thin films and R ≈ 200 Ω in Bi_2Se_3 [255, 287]. It is unclear if the mechanical polishing performed on the SmB_6 samples in this study can account for such a discrepancy in reported sheet resistance. However, we point out that while the floating zone single crystals were mechanically polished on both front and back surfaces, the aluminum flux grown samples present their as-grown surface on one side. If high mobility surface states existed then they would be presumably maintained on this surface of these samples and observed in our experiment. Moreover, we point out that a recent study which investigated the effects of polishing on surface state resistance found that fine polishing *increased* surface resistance as it removed conductive subsurface cracks in the sample [323]. Correspondingly, the observed surface resistance on highly polished samples was found to be 2-3 kΩ through surface sensitive Corbino measurements, in agreement with the $R/_s \geq 1$ kΩ limit found in this study [323, 324].

A.5 Conclusion

In summary, we presented a detailed study of the optical properties of SmB_6 in the THz frequency range. SmB_6 single crystals grown by both optical floating zone and aluminum flux methods were studied and found to be consistent in their optical properties. We show, through high resolution time domain terahertz measurements, that there is substantial in-gap 3D bulk ac conductivity in SmB_6. We discussed the possible origins of these states and their coupling to the low energy spin excitons of SmB_6 in which a coupling constant of $\lambda = 0.047$ was found. A modeling of the optical conductivity concluded that any potential surface states, which must lie below our detection limit if present, must have a sheet resistance of $R_s \geq 1000\ \Omega$, which is substantially larger than what has been previously reported. Our results demonstrate the hybridization gap of SmB_6 is insulating in dc transport measurements but in fact displays significant bulk conduction at finite frequencies.

Appendix B

Potential Topological Superconductivity in $Tl_4(Tl_{1-x}Sn_x)Te_3$

B.1 Introduction

Topological insulators [246] have undoubtedly revolutionized our understanding of the role that topology plays in condensed matter physics. These materials are characterized by strong spin-orbit coupling such that the bulk bands are inverted, giving rise to symmetry protected topological surface states within the bulk gap. However, topological insulators are, generally speaking, non-interacting systems. Today, there is a growing interest in the possible exotic ground states that result from the interplay

of topology and strong electron correlations. In this sense, a natural generalization can be made from a non-interacting topological insulator to a, similarly gapped but interacting, topological superconductor. It is thought that topological superconductors host exotic non-Abelian Majorana fermion excitations which have been proposed as the basis for quantum computation methods [325]. Accordingly, the discovery and characterization of potential topological superconductors has received a substantial amount of theoretical and experimental interest in recent years.

Predicting materials which will possess low temperature superconducting ground states is already a daunting task which only becomes even more difficult when topology is also considered. To date, most investigations have employed one of three methods in the search for topological superconductivity. In the first method, topological insulators, which are already known to possess strong spin-orbit coupling, are doped such that they enter a superconducting phase. The second method, based on the Kitaev model [326], proposes that Majorana fermions are localized at the ends of 1D superconducting nanowires when in proximity to a ferromagnet and under applied fields. Both of these techniques have had success with some compelling, although not conclusive, evidence for topological superconductivity [327, 328]. In the third method, which has received considerably less attention, low temperature topological superconducting ground states are searched for in strongly spin-orbit coupled metals. The idea here is that as superconductivity is often the low temperature ground state of Fermi liquids, so too might topological superconductivity be that of spin-orbit

coupled Fermi liquids [329]. This is the method of interest in this work.

In this chapter, microwave cavity perturbation experiments are performed on the potential topological superconductor Tl_5Te_3. Our measurements are consistent with an isotropically gapped Fermi surface with a zero temperature gap of $\Delta = 372$ meV. However, in contrast to the expected behavior of an s-wave superconductor, we find an unexpected large (40% the normal state value) residual conductivity at low temperatures, deep with the superconducting phase of Tl_5Te_3. As our measurement is a surface sensitive technique, we suggest that this large residual conductivity may arise from topologically protected surface states which exist within the superconducting bulk gap.

B.1.1 Potential Topological Superconductivity In $\mathbf{Tl_4(Tl_{1-x}Sn_x)Te_3}$

Recent publications [8, 9] have suggested that the strongly spin-orbit coupled correlated metal Tl_5Te_3 is topologically non-trivial, possessing bulk band inversion at the Z point and correspondingly Z_2 topologically protected surface states. Fig. B.1 displays angle resolved photoemission spectra of Tl_5Te_3 in which a single Dirac cone, in conjunction with some bulk states, is observed at the center of the surface Brillouin zone [8]. Interestingly, Tl_5Te_3 enters a superconducting phase at $T_c = 2.3$K, suggesting a possible topological superconducting ground state. Corresponding heat

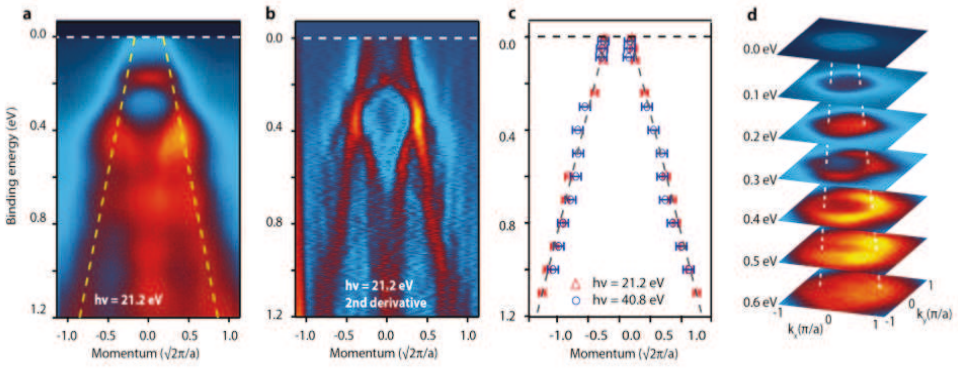

Figure B.1: Dirac-like surface states in the superconductor Tl_5Te_3. (a) APRES spectrum taken with the He Iα ($h\nu = 21.2$ eV) photons along the (0,0) - (π, π) direction showing the coexistence of prominent bulks states and a linearly dispersing surface state (yellow dashed lines) near E_F. (b) Second derivative plot of the measured experimental data in (a), where the surface state is more clearly resolved. (c) MDC fits for the data taken with the He Iα and He IIα ($h\nu = 21.2$ eV and 40.8 eV) photons, showing no substantial dependence on photon energy. (d) Momentum resolved intensity maps at a series of binding energies which show the single Dirac cone feature at the zone center. Figure adapted from Ref. [8]

capacity measurements of Tl_5Te_3 are consistent with s-wave superconductivity with an extracted bulk gap of $\Delta = 0.333$ meV and a near perfect 96% volume fraction superconductivity [8].

Additional interesting phases may be achieved upon doping Tl_5Te_3 with Sn. Fig. B.2 displays a phase diagram of $Tl_4(Tl_{1-x}Sn_x)Te_3$ as a function of temperature and Sn concentration [9]. As the amount of Sn doping is increased, a dome of superconductivity in which T_c increases and then decreases, is observed. Further increasing increasing the Sn concentration above $x > \sim 0.5$ pushes the system into an insulating state which DFT calculations predict may be a topological crystalline insulator phase. Therefore, $Tl_4(Tl_{1-x}Sn_x)Te_3$ may present the opportunity to study both topological

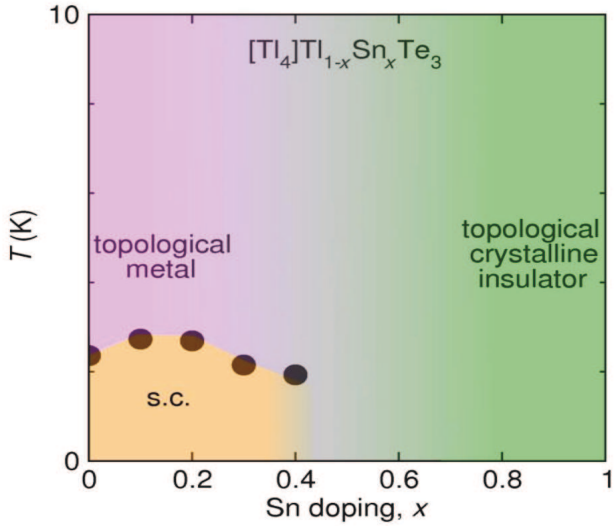

Figure B.2: Phase diagram of $[Tl_4]Tl_{1-x}Sn_xTe_3$ showing the superconducting dome proximal to a transition from a topological metal to a topological crystalline insulator. Figure adapted from Ref. [9].

superconductivity and a topological phase transition as a function of doping.

B.2 Experimental Methods

Single crystals of Tl_5Te_3 were prepared using a modified Bridgman method in an optical floating-zone furnace using 2.5% excess Te as a flux. $Tl_4(Tl_{1-x}Sn_x)Te_3$ samples were prepared by heating elemental Tl, Te, and Sn in a vacuum sealed silica ampoule to 540 C, holding for 24 h, followed by slow cooling (2 C/h). Single crystals of $Tl_4(Tl_{1-x}Sn_x)Te_3$ suitable for microwave cavity measurements were obtained from the ingot after slow cooling.

Microwave cavity perturbation measurements were then performed on the

APPENDIX B. POTENTIAL TOPOLOGICAL SUPERCONDUCTIVITY IN $Tl_4(Tl_{1-X}Sn_X)Te_3$

$Tl_4(Tl_{1-x}Sn_x)Te_3$ samples as described in Ch. 3. Recall that for highly conductive samples microwave radiation is confined to a small region near the sample surface and is therefore a direct probe of the sample's surface impedance. In this regime, known as the skin-depth regime, the complex frequency shift, $\Delta\tilde{\omega} = \Delta\omega_0 + \frac{i}{2}\Delta\Gamma$, can be related to the surface impedance by:

$$\frac{\Delta\tilde{\omega}}{\omega_0} = \xi\tilde{Z}_s + \lim_{\sigma\to\infty}\frac{\Delta\tilde{\omega}}{\omega_0} \tag{B.1}$$

where ξ, known as the "resonator constant", and $\lim \frac{\Delta\tilde{\omega}}{\omega_0}$ as $\sigma \to \infty$, known as the "metallic shift," are constants which depend on the mode of resonance, the sample geometry, and the sample position within the cavity. The complex conductivity of the sample can then be extracted from the relation:

$$\tilde{Z}_s = \sqrt{\frac{i\omega\mu_0}{\sigma_1 + i\sigma_2}} \tag{B.2}$$

Microwave cavity perturbation technique is a particularly well suited technique for characterizing superconducting samples. Not only can the complex conductivity be extracted from Eq. B.2, but the penetration depth of the superconductor is directly proportional to the sample's reactance:

$$X_s = \mu_0\omega\lambda(T). \tag{B.3}$$

which itself is proportional to the frequency shift $\Delta\omega_0$ via Eq. B.1. As the penetration depth is proportional to the density of states, the low temperature, $T < T_c/3$, functional dependence is indicative of the pairing symmetry in the superconductor. For instance, for a completely isotropic gap structure, i.e. *s*-wave superconductivity, the shift in penetration depth takes the BCS form:

$$\frac{\lambda(T) - \lambda(0)}{\lambda(0)} = \sqrt{\frac{\pi\Delta_0}{2k_BT}} \exp\left(-\frac{\Delta_0}{k_BT}\right) \tag{B.4}$$

where Δ_0 and $\lambda(0)$ are the zero temperature gap and penetration depth respectively. For higher order symmetries of the superconducting gap, for instance *p*-wave, *d*-wave, etc., the penetration depth changes from the exponential dependence of Eq. B.4 to a power law dependence with temperature. It is then the exponent of the power law which is indicative of the momentum structure of the gap. In the clean limit, power law exponents equal to two are a sign of point nodes, or places in k space where the magnitude of the superconducting gap is zero, i.e. *p*-wave superconductivity. An exponent of one is indicative of line nodes, or directions in momentum space in which the superconducting gap is zero, which is found in *d*-wave superconductivity. In this fashion the low temperature penetration depth provides insight into the superconducting properties of the material.

The complex conductivity extracted from our microwave measurements and Eq. B.2 can be compared to the expected optical conductivity of a BCS superconductor

as determined by the Mattis-Bardeen relations:

$$\frac{\sigma_1(\omega,T)}{\sigma_n} = \frac{2}{\hbar\omega}\int_{\Delta}^{\infty}\frac{[f(\epsilon)-f(\epsilon+\hbar\omega)](\epsilon^2+\Delta^2+\hbar\omega\epsilon)}{(\epsilon^2-\Delta^2)^{1/2}[(\epsilon+\hbar\omega)^2-\Delta^2]^{1/2}}d\epsilon + \frac{1}{\hbar\omega}\int_{\Delta-\hbar\omega}^{-\Delta}\frac{[1-2f(\epsilon+\hbar\omega)](\epsilon^2+\Delta^2+\hbar\omega\epsilon)}{(\epsilon^2-\Delta^2)^{1/2}[(\epsilon+\hbar\omega)^2-\Delta^2]^{1/2}}d\epsilon \tag{B.5}$$

$$\frac{\sigma_2(\omega,T)}{\sigma_n} = \frac{1}{\hbar\omega}\int_{\Delta-\hbar\omega,-\Delta}^{\Delta}\frac{[1-2f(\epsilon+\hbar\omega)](\epsilon^2+\Delta^2+\hbar\omega\epsilon)}{(\Delta^2-\epsilon^2)^{1/2}[(\epsilon+\hbar\omega)^2-\Delta^2]^{1/2}}d\epsilon \tag{B.6}$$

where $f(\epsilon)$ is the Fermi-Dirac distribution function and the conductivities have been normalized by the normal state conductivity σ_n [84].

B.3 Experimental Results

Fig. B.3(a) displays the resonant frequency and bandwidth of our cavity resonator as a function of temperature with a Tl_5Te_3 sample inserted in the magnetic field antinode of the TE_{011} mode as described in Ch. 3. Fig. B.3(b) displays the shift in both the resonant frequency and bandwidth in which the data of the empty cavity resonator has been subtracted from the data shown in (a). A clear sharp superconducting transition at $T_c = 2.3K$ can be seen in the data.

Fig. B.4(a) displays the real and imaginary parts of the complex surface impedance of Tl_5Te_3 extracted from the data shown in Fig. B.3 and Eq. B.1. The resonator constant and metallic shift were found by comparing multiple measurements of the same sample. One can see that above T_c the measured surface impedance is

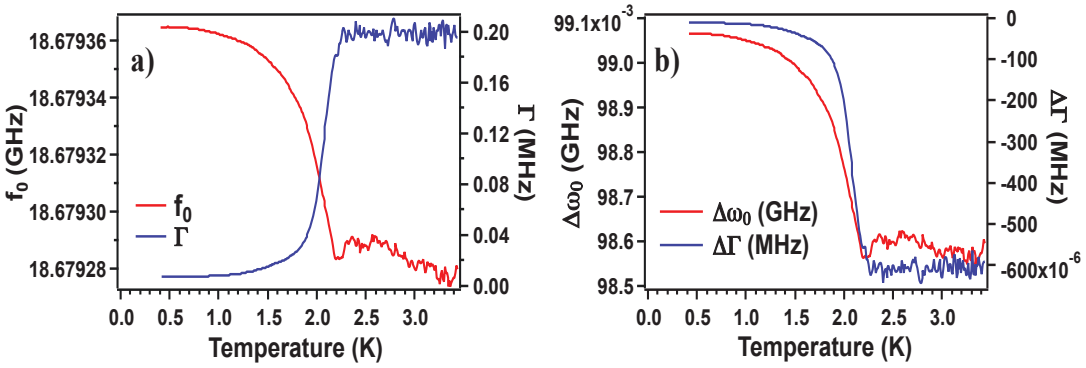

Figure B.3: (a) Temperature dependence of the resonant frequency f_0 and bandwidth Γ of our cavity resonator with a Tl_5Te_3 sample placed at the magnetic field antinode of the TE_{011} mode. A sharp transition to a superconducting state can be seen in the data at $T_c = 2.3$K. (b) Corresponding shift in resonant frequency and bandwidth found by subtracting the data of the empty cavity resonator from the data shown in (a).

consistent with the Hagens-Ruebens limit in which $X_s \approx R_s$ as expected for a metal.

Fig. B.4(b) displays the extracted change in penetration depth found from the surface reactance shown in Fig. B.4(a) and Eq. B.3. The change in penetration depth was found by subtracting the value of penetration depth at the lowest measured temperature from the rest of the data. As discussed above, the functional dependence of the change in penetration with temperature in the low temperature limit is indicative of the pairing symmetry of the superconductor. Shown in black is a fit of the data to Eq. B.4, the expected expression for a BCS s-wave superconductor. One can see that the fit is in excellent agreement with our data and therefore suggests s-wave superconductivity in Tl_5Te_3. Similar power law fits of the data yield an un-physical exponent of nearly 5, further confirming the validity of the BCS fit. From this fit we extract a zero temperature gap of $\Delta = 0.372$ meV which is in excellent agreement with

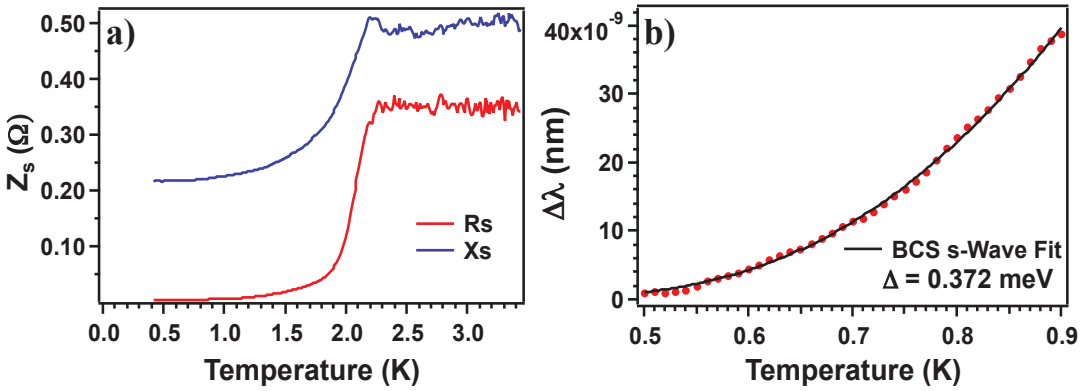

Figure B.4: (a) Temperature dependence of the real and imaginary parts of the surface impedance of Tl_5Te_3 found via Eq. B.1 and the data shown in Fig. B.3(b). (b) Temperature dependence of the extracted change in penetration depth in the temperature region $T < T_c/3$. The black solid line is the fit of the data to the expected BCS s-wave exponential form given in Eq. B.4. From this fit we extract a zero temperature gap value of $\Delta = 0.372$ meV.

the expected BCS weak coupling value of $\Delta = 0.350$ meV given by $2\Delta/k_BT_c = 3.53$. These results concur with heat capacity measurements [8] which are also consistent with s-wave superconductivity but find a slightly smaller gap of $\Delta = 0.333$ meV.

Fig. B.5(a)-(b) displays the extracted temperature dependence of the (a) real and (b) imaginary parts of the optical conductivity of Tl_5Te_3 found from the surface impedance shown in Fig. B.4(a) and Eq. B.2. Shown in red is the expected optical conductivity from the Mattis-Bardeen equations, Eq.'s B.5 and B.6, calculated with the resonant frequency of our measurement, $\omega = 18.5$ GHz, and the zero temperature gap, $\Delta = 0.372$ meV, extracted from our fit of the penetration depth. B.4. One can see that our experimental data and the prediction of Mattis-Bardeen theory agree relatively well at temperatures near T_c. Just below T_c, a well defined coherence

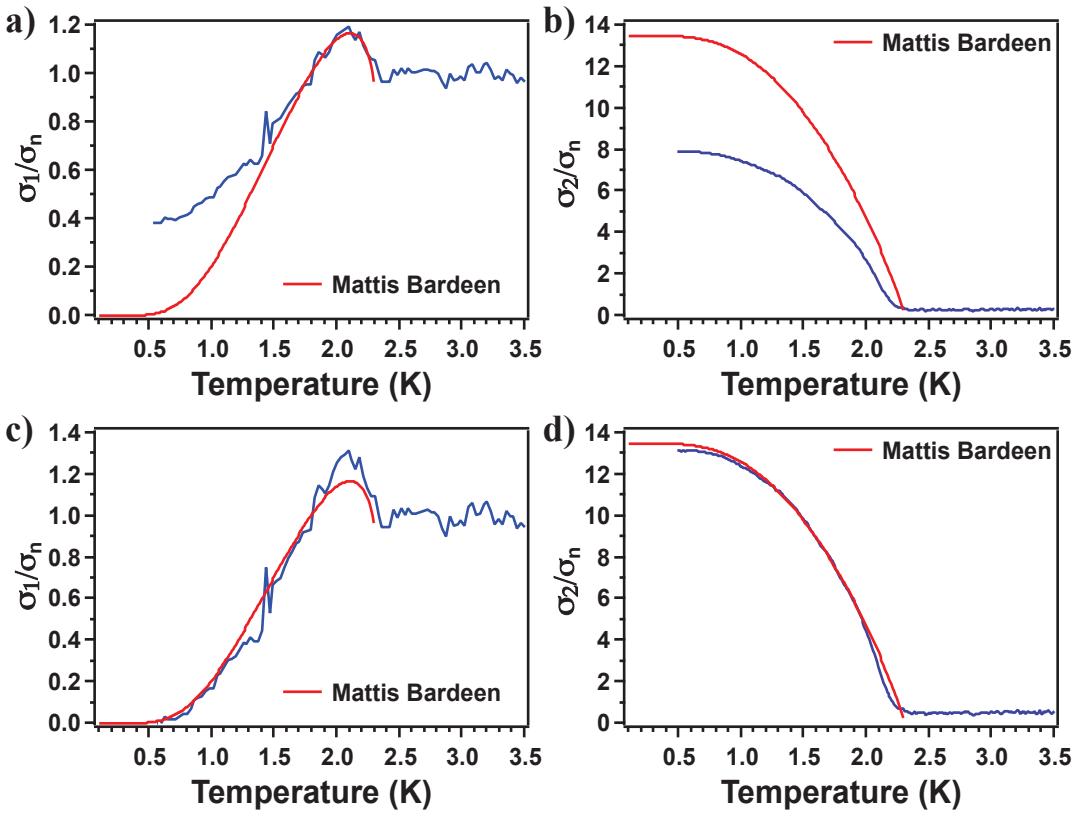

Figure B.5: Temperature dependence of the both the (a) real and (b) imaginary parts of the optical conductivity normalized by the normal state value. The red lines are the expected optical conductivity from the Mattis-Bardeen expression given in Eq.'s B.5 and B.6. One can see that a large discrepancy between the Mattis-Bardeen expression and the real and imaginary conductivities exist at low temperatures. (c)-(d) The same data as shown in (a) and (b) but with the low temperature residual conductivity subtracted from the data in which case the agreement with the Mattis-Bardeen prediction is dramatically improved.

peak can be observed in the real part of the optical conductivity, suggesting type-II coherence factors in Tl_5Te_3. However, a large discrepancy between our data and the theoretical expectation is observed as the temperature is reduced. It appears as though Tl_5Te_3 possesses a large low temperature residual conductivity which is nearly 40% the normal state value. The agreement with the Mattis-Bardeen prediction can be dramatically improved if this residual conductivity is subtracted from the data. Fig. B.5 (c)-(d) displays the identical data as B.5(a)-(b) but with the low temperature residual conductivity removed in this fashion.

B.4 Discussion

We demonstrated in our analysis that the temperature dependence of the penetration depth of Tl_5Te_3 is consistent with s-wave superconductivity and a gap of $\Delta = 0.372$ meV, both of which are in agreement with previous heat capacity measurements [8]. As further confirmation of s-wave superconductivity, a coherence peak just below T_c can be observed in the real part of the conductivity, which is generally consistent with type-II coherence factors in the sample. However, the magnitude of the coherence peak in Fig. B.5(c) is slightly larger than expected from the Mattis-Bardeen expression which may be suggestive of more unusual coherence factors which deviate from the BCS picture. This is an ongoing point of investigation in these samples and one that we hope will generate further theoretical interest.

APPENDIX B. POTENTIAL TOPOLOGICAL SUPERCONDUCTIVITY IN $Tl_4(Tl_{1-X}Sn_X)Te_3$

Of particular interest is the discrepancy of our data with the Mattis-Bardeen expectation at low temperatures. We observed a remarkably large ($\approx 40\%$ the normal state conductivity) residual conductivity in Tl_5Te_3 at low temperatures. In principle, residual conductivity could arise from either a less than 100% superconducting volume fraction or the presence of nodes in the superconducting gap. However, as mentioned above, it was found previously that Tl_5Te_3 possesses nearly perfect $\approx$ 96% volume fraction superconductivity and that the Fermi surface appears uniformly gapped. Such large residual conductivity is not explanable from only 4% normal state electrons. It may be additionally possible that such large residual conductivity arises from non-ideal surfaces which were not cleaved in vacuum prior to measurement. However, one would generally expect that any surface oxide to be an insulating dielectric and therefore does not explain the residual conductivity.

An additional, and more exciting, explanation for the low temperature residual conductivity exists. This feature is naturally explained in a scenario where Tl_5Te_3 is a topological superconductor and the residual conductivity arises from symmetry protected metallic surface states. Such a feature would likely not be seen in heat capacity measurements as any surface signal would constitute an infinitesimal contribution on top of the superconducting bulk signal. However, our microwave cavity measurements are surface sensitive, explaining why such a feature would be observed here but not previously. Fig. B.6 displays σ_1 with the potential surface state and bulk superconducting contributions distinguished. Additional evidence for this inter-

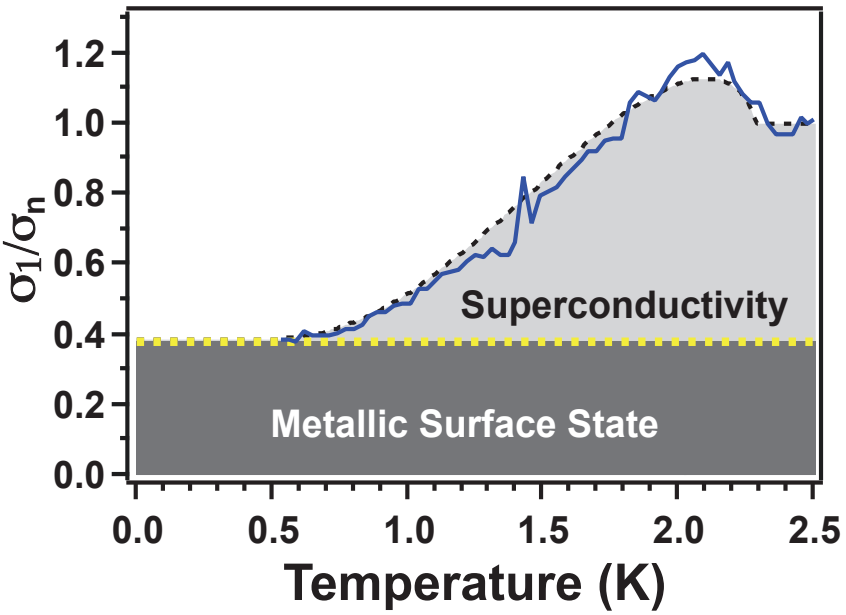

Figure B.6: A possible interpretation of the real part of the optical conductivity where the low temperature residual conductivity arises from a topological surface state.

pretation may arise out of similar measurements performed on samples doped with Sn. As of the writing of this thesis, experiments on $Tl_4(Tl_{1-x}Sn_x)Te_3$ are ongoing.

B.5 Conclusions

In summary, highly precise microwave cavity resonator measurements on the potential topological superconductor Tl_5Te_3 were performed. By examining the temperature dependence of the penetration depth, we identified Tl_5Te_3 as an s-wave superconductor with a zero temperature gap of $\Delta = 0.372$ meV, in good agreement with previous heat capacity measurements of Ref. [8]. A coherence peak that is

generally consistent with type-II coherence factors was observed in the real part of the optical conductivity. Interestingly, a large residual conductivity was observed at low temperatures which may be consistent with a topological surface state. Further measurements as a function of Sn doping are ongoing and may provide more insight into the origin of the low temperature residual conductivity. If the presence of a topological surface state can be confirmed, then it would be the first conclusive evidence of a topological superconductivity discovered to date.

Appendix C

Performing An MCPT Experiment

In this section I'll describe the finer details about how to perform a microwave cavity experiment using our system at JHU. A picture displaying the entire experimental set-up with some of the more important components labeled is shown in Fig. C.1.

C.0.1 Performing A Reference Measurement

Before measuring any sample, a reference measurement of the empty cavity must be completed. Once a reference measurement is performed, the cavity cannot be removed from the insert until all sample measurements are completed. Every effort should be made to keep as much consistent with the cavity as possible after the reference measurement. To perform a reference measurement, follow the steps below but disregard the steps pertaining to loading a sample.

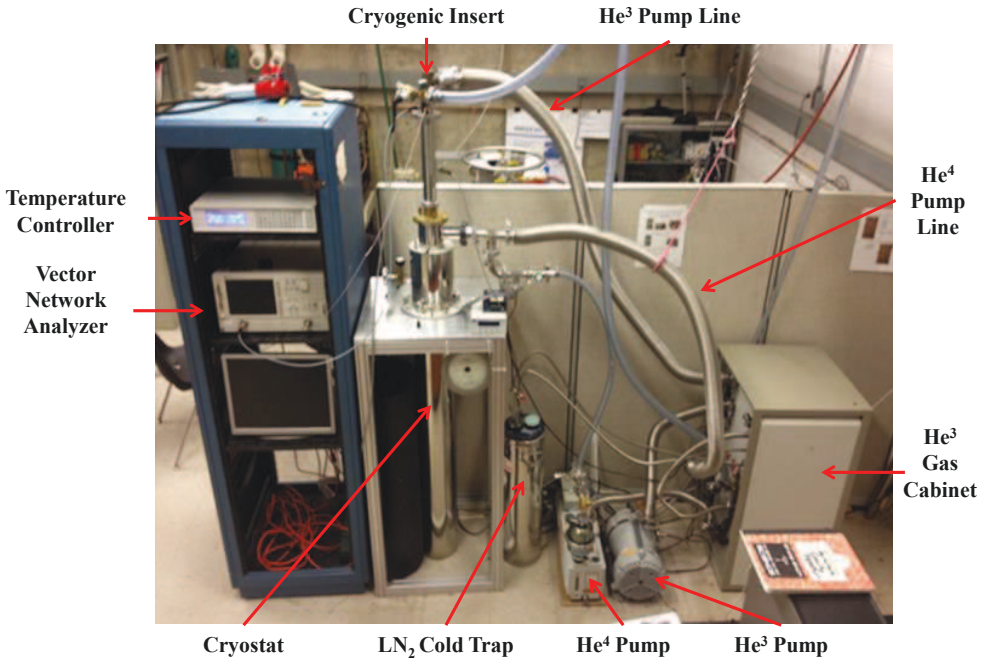

Figure C.1: Our experimental MCPT set-up at JHU with some of the more important components labeled.

C.0.2 Mounting a sample

Assuming a reference measurement of the empty cavity has been performed, the next step is to load a sample into the cavity for measurement. Before describing how this is done, I would like to give some quick advice about sample sizes and geometries. Finding the right size sample to use for a MCPT measurement is challenging. Samples that are too large will result in large frequency shifts but also often greatly reduced resolution from substantially widened resonance peaks. While samples which are too small will have very narrow resonance peaks and high resolution but potentially very small frequency shifts. The optimally sized sample is an intermediary between these two limits. My advice would be to start with samples that are roughly of ≈ 1 mm in dimensions first. It is always possible to remove some of the sample by polishing or cleaving but obviously not possible to add more sample back on.

Loading a sample into the cavity is an simple procedure. Carefully remove the cavity bottom plate by unscrewing the six Allen screws which hold it in place. Note that because the cavity cannot be removed from the insert after finishing a reference measurement you will have to remove the bottom plate while the cavity is still attached to the insert. This can be difficult and frustrating but be careful and patient, the cavity is fragile. Once removed, place the bottom plate of the cavity on a KimWipe on top of a flat surface. A small amount of Apiezon grease on top of the sapphire rod is all that is needed to hold a sample in place. I usually place the sample on the sapphire rod with very sharp tweezers while looking through a magnifying

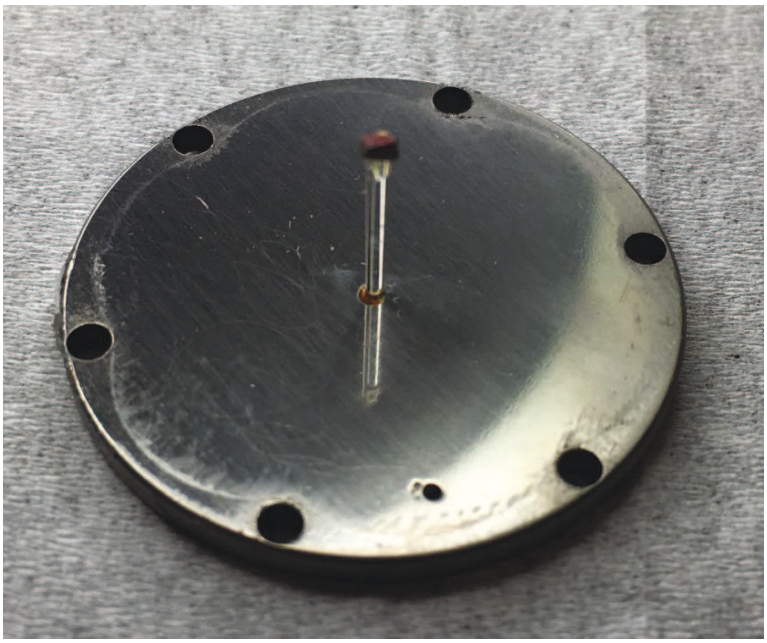

Figure C.2: A picture the bottom plate of our cavity with a small sample mounted to the end of the sapphire rod.

glass. Fig. C.2 displays the bottom plate of the cavity with a sample loaded. After the sample is mounted then the cavity should be reassembled.

C.0.3 Pumping Out The Sample Space

Once the cavity is closed again, the vacuum can should be attached to the insert with a healthy amount of vacuum grease placed on the insert's cone seal. This is generally a two person job. Someone has to keep a hand underneath the vacuum can before its pumped out so it doesn't fall off the insert. Since the vacuum can seals by tightly fitting against the cone seal of the insert, it is vital to not drop or dent the vacuum can. The other person operates the valves so that the vacuum can will be

pumped out by the He^4 pump. Make sure that the valve on top of the He^4 pump is in the position such that it releases the pumped out air to the room and not to the liquifier (Fig. C.4). Then start the pump, open valve 4a on the front of the gas cabinet, and open the small valve at the top of the insert which opens the sample space to the clear plastic pump out line. The pressure can then be monitored by the pressure gauge on top of the cryostat. Once the vacuum can has been pumped out for about 30s then it no longer needs to be held by hand, the pressure differential is enough to make sure it does not fall off.

C.0.4 Pre-Cool Down Prep

Once the vacuum can is on and is being pumped out then the next step is placing the insert into the cryostat. Place a ladder next to the cryostat to stand on. It should be noted that there is just barely enough room above the cryostat for the insert to fit. In fact, you will have to tilt it very slightly. Gently and slowly lower the insert into the cryostat. Try to keep it straight while lowering it or it will get caught on the baffles inside.

Once the insert is in place, then the He^3 line can be connected. We also need to pump out the He^3 space within the insert before cooling down or all the air in there will freeze and base temperature will not be reached. It is absolutely crucial that the these exact steps are followed. Opening an incorrect valve could result in all the He^3 being pumped to the room. You should still be pumping on the sample space at this

point, you do not need to stop that before pumping on the He^3 space. Generally, I pump on both at the same time. The goal is to use the He^4 pump to pump out the He^3 space as well. To do this, open valves, 4a (which should already be open), 1a, 7, 2, and 3. If done correctly then both the sample space and He^3 space should be in the process of being pumped out. I would leave the experiment like this overnight. When both spaces are fully pumped out then the pressure gauge on the front of the experiment will read ≈ 0.08 or so.

After pumping overnight there is only one more step before cooling down. We also need to pump out the liquid nitrogen trap to remove the impurities from the last cool down. Close the small green value at the top of the insert which connects the sample space to the pump. Then go to the front of the gas cabinet and close all the open valves. To pump out the cold trap open valves 4a, 1a, 7, 2, and 12a. Pump out the liquid nitrogen trap for about 30 mins or so. Once that is finished then close valve 12a and return to pumping out the sample space and He^3 space by following the steps above. I generally pump on these spaces while cooling the experiment down to 4K.

C.0.5 Cooling Down The Experiment

C.0.5.1 From Room Temperature To 4K

Cooling down the cavity experiment takes roughly 15 - 20 hours and occurs in several steps. A graph showing the temperature of the cavity and He^3 pot as a function of time during the cool down process is shown in Fig. C.3. The first step is to partially fill the He^4 space of the cryostat with liquid nitrogen (LN_2). The He^4 space is pretty large and it takes quite a while to fill but filling it completely is not necessary. Maybe 5 - 10 mins of filling is enough. As the cavity is in vacuum it will cool very slowly. Over the course of 5 or so hours the cavity should cool to under 150K. It is beneficial to let the system cool down as much as possible with the LN_2 as cooling with the He^4 is significantly slower and quickly burns off the He^4.

Once the system is less than 150K, the LN_2 can be removed from the He^4 space. This is accomplished by slowly inserting a long hollow tube into the He^4 space and over-pressuring with dry He^4 gas, forcing the LN_2 up the tube and out of the He^4 space. We have a special long tube with a 90 degree bend at the end for accomplishing this task. Slowly insert this tube into the He^4 space (careful! if LN_2 is still in the He^4 space then it may spray out when you insert the tube, so do it very slowly with the top pointing away from you). Once all the way in then attach the rubber hose on the end of the tube to the connection on the LN_2 space of the cryostat. The next step is to over-pressure the He^4 space with dry He^4 gas. Connect the He^4 dry gas line to the

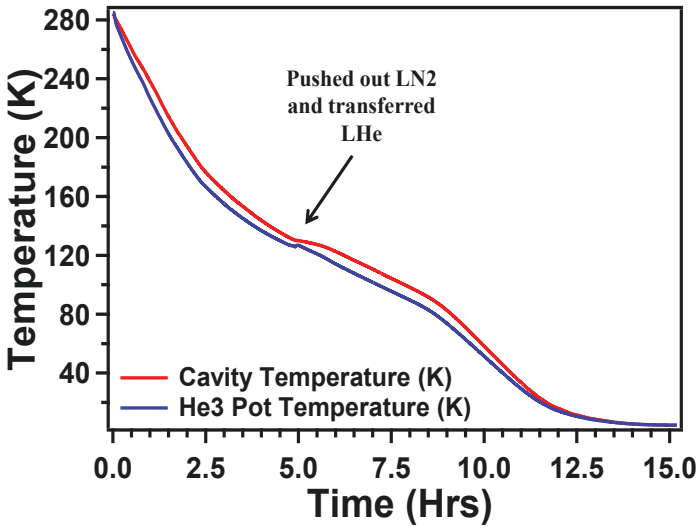

Figure C.3: A graph showing the temperature readings of the cavity system as a function of time during a typical cool down from room temperature to 4K. If proper vacuum is kept in the cavity space then the cavity temperature should be slightly higher than the He^3 pot temperature for the duration of the cool down.

other port of the He^4 space to force all the LN_2 out. The pressure is enough to force all the LN_2 out in just a matter of seconds.

Once the He^4 space no longer contains LN_2 then you're ready to transfer He^4. First, start transferring LN_2 from an external LN_2 dewar into the LN_2 space of the cryostat. Then insert the He^4 transfer line into one of the ports of the He^4 space of the cryostat. Leave the other port open until a constant flow of He^4 gas is coming out of the cryostat. This pushes any remaining nitrogen or air out of the He^4 space. After a few seconds of flushing the He^4 space in this fashion, cork the open port and open the green valve next to the cryostat to allow the He^4 exhaust to be recovered by the liquifier (Fig. C.4). Turn on the He^4 level meter to monitor the level as you

transfer. The pressure in the He^4 dewar should be fairly high, about 5 psi or so for the transfer.

If everything is done correctly then the system should fill to 108 cm within 10-15 minutes at most. It should be noted that 108 cm is the highest level that the level meter can read. In principle the cryostat can hold more than 108 cm but since you cannot monitor the level I don't recommend filling above this mark. Besides, this will be enough He^4 to last for about 3 days. Once at 108 cm, then release the pressure in the He^4 dewar by venting to the liquifier. Wait for the pressure to go down before removing the transfer line. Once removed, make sure both He^4 ports are corked. The system will likely take another 12 or so hours to cool from 150K to 4K. Remember, this entire time you are still pumping on the sample and He^3 spaces.

C.0.5.2 From 4K To 1.8K

Temperatures below 4K are reached by simply pumping on the He^4 bath. Instructions for operating the valve which connects the bath to the liquifier and directing the exhaust from the pump to the liquifier are provided in Fig. C.4. Begin by closing the valve at the top of the insert which closes off the sample space from the pump. Failure to remember this step before pumping on the He^4 will flood the sample space with He^4 and then the experiment will have to be warmed up and pumped out again. Close all the valves that control the pumping of the He^3 space as well. Close the valve connecting the liquifier to the He^4 bath and pull up the handle on the exhaust

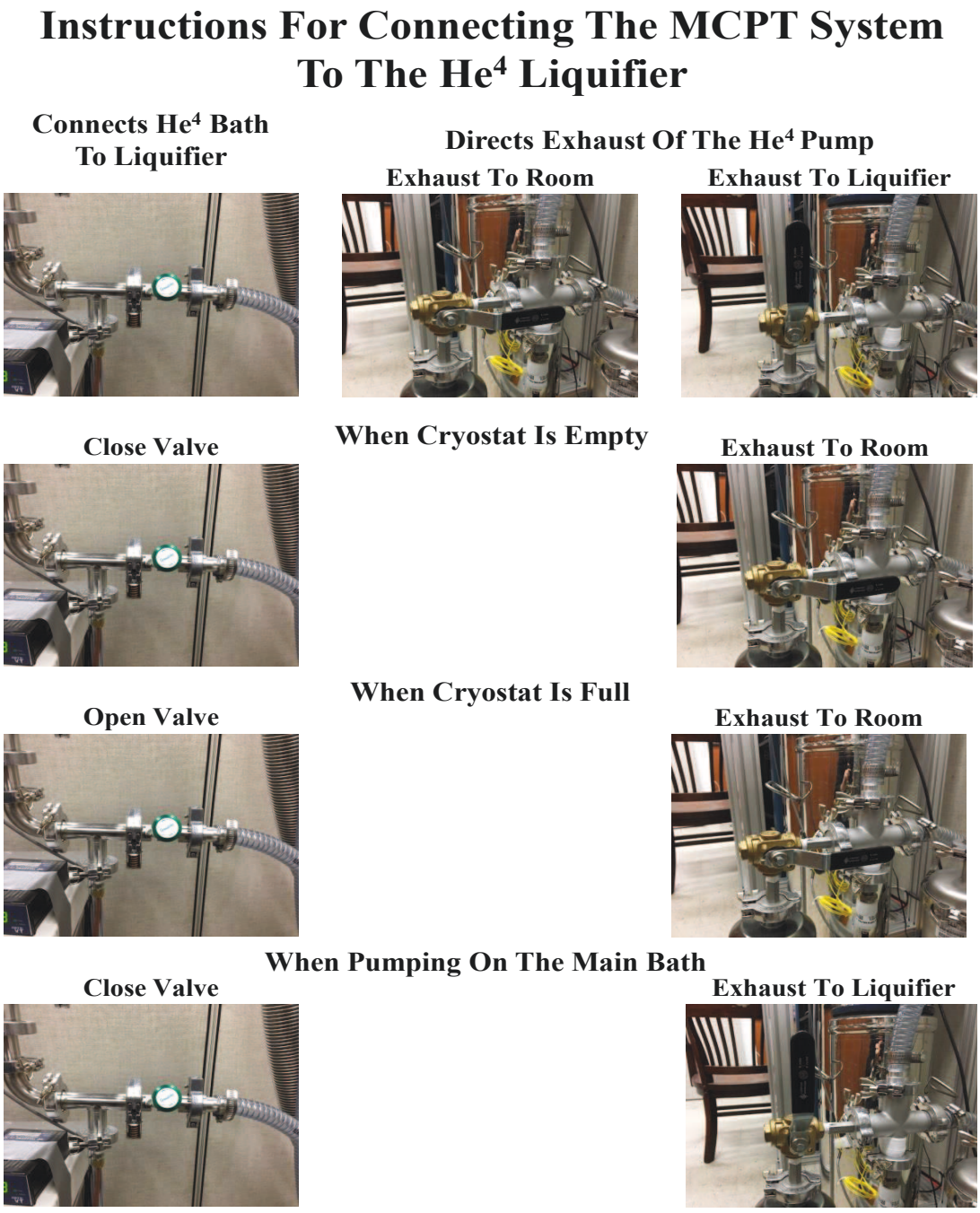

Figure C.4: Instructions for appropriately connecting the MCPT experiment to the He recovery system.

of the He^4 pump to ensure all the pumped out He^4 is directed to the liquifier (Fig. C.4). Double check that all valves are closed on the front of the gas cabinet. Now very slowly open valve 5a, thereby pumping on the He^4 bath. You will hear the pump respond immediately.

Leave the system in this configuration for about an hour or so and the cavity will reach as low as 1.8K. You can monitor the temperature of the bath by watching the large round pressure valve on the front of the experiment.

C.0.5.3 From 1.8K To 1.2K

In order to get to temperatures below 1.8K we must introduce the He^3 into the system. Before doing so you must first fill the liquid nitrogen trap with liquid nitrogen. Running the He^3 through the trap removes any impurities from the He^3 before it is inserted into the experiment. Once filled then you are ready to introduce the He^3.

Fig. C.5 displays the instructions for introducing the He^3. Once the He^3 is introduced into the experiment, you will notice the temperatures of the cavity and He^3 pot immediately increase considerably. This is a result of the warm He^3 gas entering the system. However, after the initial spike in temperature the system will cool down quickly. Wait until all the He^3 has condensed into liquid by monitoring the pressure of the right pressure gauge "G1" on the gas cabinet. The pressure will drop to zero once all the He^3 is condensed. If the above steps are performed correctly then the cavity will reach temperatures as low as 1.2K.

C.0.5.4 Below 1.2K

Now that all the He^3 has condensed we can pump on the liquid He^3 to get to the base temperature of the experiment. Follow the instructions for pumping on the He^3 as listed in Fig. C.5. It is also important to make sure the microwave power of the VNA is turned down during this step. I would set it to -40 dBm, otherwise the power of the microwaves themselves may heat the cavity. Once you begin pumping on the He^3 the system should begin cooling down rapidly. Waiting only about 30 minutes or so should be enough to get to base temperature, typically between 350 mK - 400 mK.

C.0.5.5 Returning The System Back To 4K

Recovering all the He^3 is accomplished by simply waiting long enough for all the He^3 to boil off and be pumped back into the gas cabinet. However, the hold time for the He^3 is very long, at least 12 Hrs. This process can be sped up by closing valve 5a, thereby no longer pumping on the He^4 bath and then very slowly opening the valve connecting the bath to the liquifier. This pulls warm He^4 gas from the liquifier into the cryostat, thereby heating up the bath and acting as a heat load on the He^3 pot. You may additionally want to turn on the heater to about 30% at 25 mW to even further speed up the process. Even with these heat sources, it will take about 30 minutes before all the He^3 returns to the gas cabinet. Once all the He^3 has returned, then turn off the heater and close all the valves. Begin pumping on only the sample

Steps For Introducing He^3 Into The System

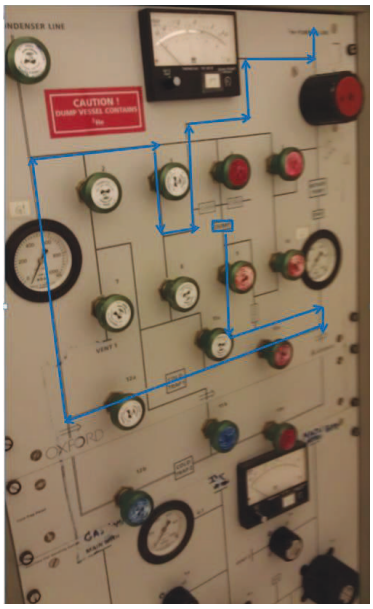

1. Open Valve 9
2. Open Valve 13a
3. Open Valve 12a
4. Open Valve 3
5. Close Valve 9
6. Open Valve 10
7. Let He^3 condense until pressure reading on the left gauge is zero

Steps For Recollecting He^3 From The System

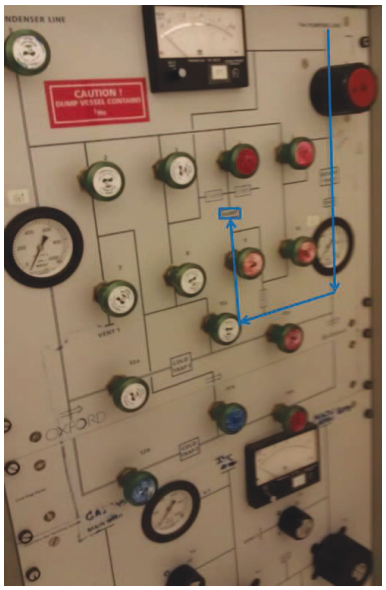

1. Close Valve 13a
2. Close Valve 10
3. Open Valve 9
4. Open Valve 6
5. Wait until all He^3 has returned to the gas cabinet by monitoring the pressure reading on the right gauge.
6. Close Valves 12a, 3, 6, & 9

Figure C.5: Instructions for operating the He^3 gas of the MCPT experiment. Blue lines indicate the path the He^3 gas takes duing the proceedure.

space again. Do not pump on the He^3 space again after introducing He^3 into the system.

C.0.6 Data Acquisition

C.0.6.1 The MCPT LabView Program

Data is retrieved from the network analyzer by a LabView program which I wrote to run the experiment. Fig. C.6 displays a screen shot of the front panel of the program. Running the program is quite simple. The "run" button at the top of the LabView window starts a loop which updates only the temperature of the cavity and He^3 pot. No data is recorded yet. This allows the user to monitor the temperatures while the experiment is cooling down without recording them. Hitting the large green button labeled "Start" to the left begins the fitting routine. Only after hitting this button is data recorded.

Table C.1 displays some of the inputted parameters of the program as well as the settings I recommend using. The program takes in as parameters the starting and ending frequency of only the first scan of the resonance peak. Typically I just center the resonance on the VNA screen and then type in the scan parameters into the LabView program before starting.

The program then averages the signal for some specified amount of time before retrieving the data and fitting to a Lorentzian function. The result of the fit, i.e.

Item	Description	Recommended Setting
Power	Outputted power by VNA	-20 dBm
Averaging Time	Time VNA averages signal before LabView retrieves the data	30s - 60s
Bandwidths To Fit	Frequency range about the center frequency for each scan	3
Starting Frequency	Starting frequency for only the first scan.	Varies
Ending Frequency	Ending frequency of for only the first scan.	Varies

Table C.1: User inputted parameters of the MCPT LabView program with some suggested values. The starting and ending frequency are the frequency scan parameters for only the first fit taken by the program. After the first fit the program runs autonomously.

resonant frequency, bandwidth, amplitude, Q-factor, etc., and the temperatures are then written to a text file which you specify in the "MCPT Data File Path:" option. An additional text file, which you specify in the "Waveform Data File Path:" option receives the raw data from the VNA, i.e. the power as a function of frequency for each scan. The program then sets the starting and ending frequency of the next scan based off of the previous fit. In this fashion the resonance peak can be followed as it changes its resonant frequency with temperature.

C.0.7 Temperature Control

The Lake Shore 340 is capable of reading both temperature sensors simultaneously as well as controlling the heater. Since the heater sits on the He^3 pot and not the cavity, which is where we are actually interested in controlling the temperature, I've found the best heating method is to ramp the manual output of the heater through a simple program written in the Lake Shore. I do not recommend using the Setpoint or PID settings to control the temperature.

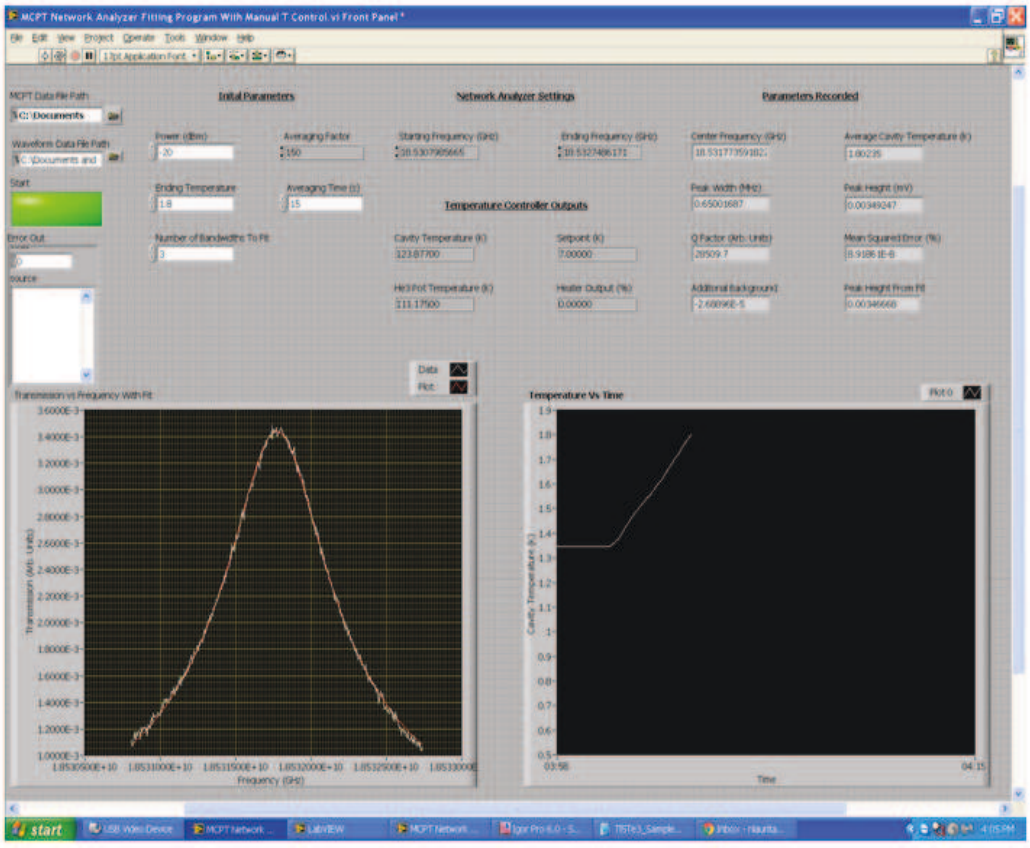

Figure C.6: A screen shot of the MCPT LabView program. The program retrieves the data from the VNA, fits it to a Lorentzian peak, records the results of the fit, and then sets the scan range for the next fit. The plot in the lower left shows the raw data from the cavity (white) and the resultant fit (red). The plot in the lower right records the cavity temperature versus time.

APPENDIX C. PERFORMING AN MCPT EXPERIMENT

Data on the MCPT system must be taken in three distinct temperature regions. The easiest is the temperature range spanning 1.8 K - 8 K, which I refer to as the "High T" data. Follow the steps for cooling down to 1.8 K listed in Sec. C.0.5.2. Do not introduce the He^3. Once at 1.8 K, start the LabView program and let it take several fits. Then PAUSE, do not stop, the LabView program and start a temperature control program in the Lake Shore by hitting "Program", then "Run Program", then scrolling the program you would like to run and hitting enter. This will ramp the manual output of the heater at some constant rate which you specify. I have found this to be the most reproducible way of taking data on the MCPT system. Once the Lake Shore program is running, then unpause the LabView program and continue recording data.

The "Mid T" data, from 1.2 K - 1.8 K, is the hardest region to take data. I have yet to find an ideal method for recording data in this range. However, the best method I have found is to cool the experiment down to 1.8 K just as if you were going to take "High T" data. Then perform all the steps necessary as if you were going to introduce the He^3. However, instead of opening valve 3 all the way, open it very slightly for only a second just so only a tiny amount of He^3 is introduced into the insert. This small amount of He^3 gas will act as transfer gas and cool down the experiment to 1.2 K. The He^3 gas is capable of absorbing an enormous amount of heat, so warming up from 1.2K is difficult and not a reproducible process. So I recommend taking data while the experiment cools down in this temperature range.

"Low T" data refers to data taken from base temperature to 1.2 K. Follow the steps for reaching base temperature listed in Sec. C.0.5.4. Then start the LabView program and let it take several fits of the data. Then pause the program, and start another program on the Lake Shore. Then close valve 6 on the gas cabinet which stops the pumping on the He^3. If this step is forgotten then the experiment will never warm up, pumping on the He^3 is just too much cooling power. Then unpause the LabView program and let it take data for the duration of the program.

C.0.8 Data Analysis

Data analysis for the MCPT experiment is in principle very simple. The idea is to simply subtract the unloaded cavity data from the loaded cavity data from which the complex response of the sample can be extracted via the equations provided in Sec. 3.3. However, small complications arise due to the fact that data on the MCPT system occurs in different temperature ranges, which different density of points, with often small frequency shifts between measurements. In order to streamline the analysis process I wrote an Igor macro capable of monitoring the data during acquisition as well as some post acquisition analysis. Fig. C.7 displays a screen shot of the control panel of the analysis program. Detailed instructions for using the code can be found at the beginning of the code itself. A brief explanation of the code will be provided here.

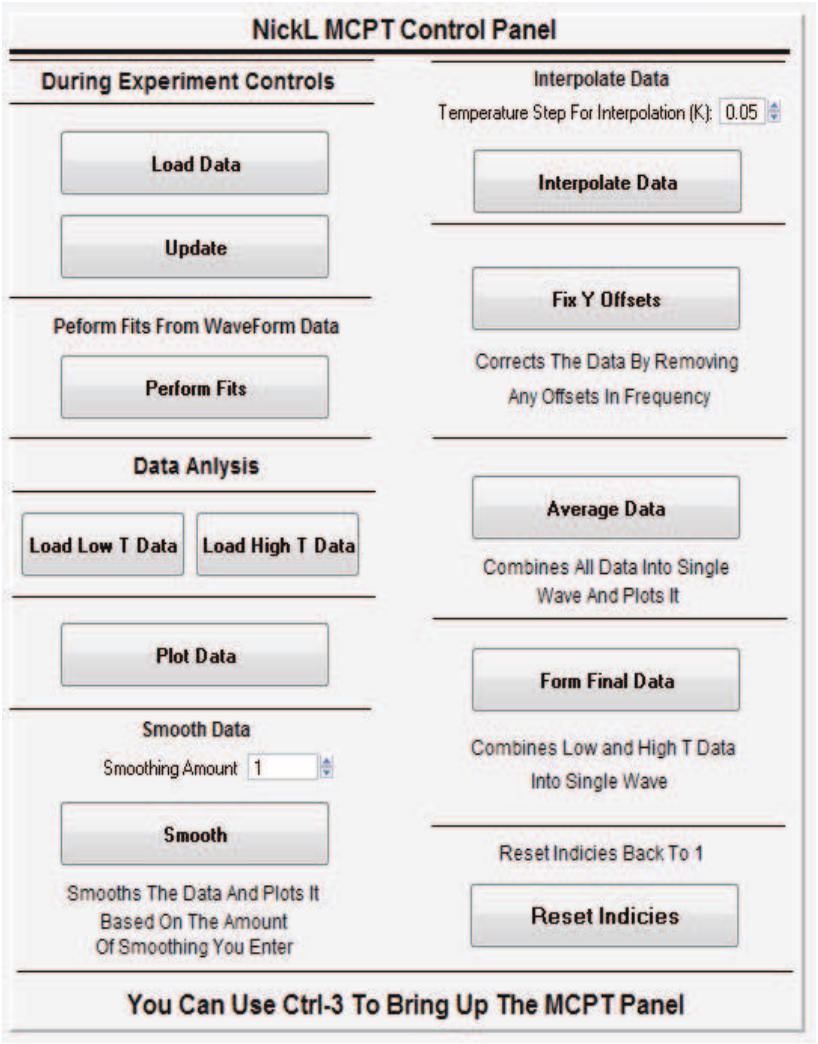

Figure C.7: A screen shot of the control panel of the automated Igor MCPT data analysis program. Detailed instructions for its use can be found at the beginning of the code itself.

C.0.8.1 Monitoring Data During The Experiment

At the top right of the control panel you will find a section labeled "During Experiment Controls" with buttons labeled "Load Data" and "Update." As the name suggests these buttons allows the user to monitor the data taken with the LabView program in real time. Pressing the "Load Data" button will pull up a window from which the user should select the "MCPT" text file of interest. An additional widow will be pulled up after the first file selection from which the user should choose the corresponding "Waveform" text file. The "Update" button will then grab the data from the "MCPT" file and create four plots to display the data. Simply repressing the "Update" button reloads all the data from the text file and updates the corresponding graphs.

C.0.8.2 Post Acquisition Data Analysis

The remainder of the controls on the panel are for analyzing the data post acquisition. The data is parsed into either "Low T" or "High T" data and analyzed separately. Load the "Mid T" data with the "High T" data. The remainder of the buttons are self explanatory. The program smooths, interpolates, and averages all the collected data. The final result is are single waves of resonant frequency and bandwidth versus temperature which can then be used for further analysis.

One final option of the Igor code is the ability to fit asymmetric peaks. Although in the ideal case the resonance peak will be a perfect Lorentzian, in real experiments

the peak may be asymmetric from a background with strong frequency dependence. This may result in poor fitting of the data in the LabView program. This is why the raw voltage versus frequency data from the VNA is recorded in the "Waveform" text file. The "Perform Fits" button on the analysis control panel loads the raw data from this text file and then fits it with a model of a Lorentzian peak on a general cubic polynomial background to account for asymmetry. I highly recommend using this function if the peak is heavily asymmetric. With this method, often unreliable looking resonant frequency and bandwidth data found by fitting to a perfect Lorentzian can be transformed into high precision data with the asymmetric model.

Bibliography

[1] W. Nolting and A. Ramakanth, *Quantum Theory of Magnetism*. Springer, 2009.

[2] L. Balents, "Spin liquids in frustrated magnets," *Nature*, vol. 464, no. 7286, pp. 199–208, 2010.

[3] M. Hoffman, "Novel techniques in thz-time-domain-spectroscopy," Ph.D. dissertation, Universit at Freiburg im Breisgau, 2006.

[4] L. S. Bilbro, "Fluctuations of superconductivity in $La_{2-x}Sr_xCuO_4$ measured with terahertz time-domain spectroscopy," Ph.D. dissertation, Johns Hopkins University, 2012.

[5] G. Chen, L. Balents, and A. P. Schnyder, "Spin-orbital singlet and quantum critical point on the diamond lattice: $FeSc_2S_4$," *Phys. Rev. Lett.*, vol. 102, p. 096406, Mar 2009.

[6] R. M. D'Ortenzio, H. A. Dabkowska, S. R. Dunsiger, B. D. Gaulin, M. J. P.

Gingras, T. Goko, J. B. Kycia, L. Liu, T. Medina, T. J. Munsie, D. Pomaranski, K. A. Ross, Y. J. Uemura, T. J. Williams, and G. M. Luke, "Unconventional magnetic ground state in $Yb_2Ti_2O_7$," *Phys. Rev. B*, vol. 88, p. 134428, Oct 2013.

[7] M. C. Hatnean, M. R. Lees, D. M. Paul, and G. Balakrishnan, "Large, high quality single-crystals of the new topological Kondo insulator SmB_6," *Scientific Reports*, vol. 3, no. 3071, 2013.

[8] K. E. Arpino, D. C. Wallace, Y. F. Nie, T. Birol, P. D. C. King, S. Chatterjee, M. Uchida, S. M. Koohpayeh, J.-J. Wen, K. Page, C. J. Fennie, K. M. Shen, and T. M. McQueen, "Evidence for topologically protected surface states and a superconducting phase in $[Tl_4](Tl_{1-x}Sn_x)Te_3$ using photoemission, specific heat, and magnetization measurements, and density functional theory," *Phys. Rev. Lett.*, vol. 112, p. 017002, Jan 2014.

[9] K. E. Arpino, B. D. Wasser, and T. M. McQueen, "Superconducting dome and crossover to an insulating state in $[Tl_4](Tl_{1-x}Sn_x)Te_3$," *APL Materials*, vol. 3, no. 4, p. 041507, 2015.

[10] D. C. Mattis, *The Theory of Magnetism*, F. Seitz, Ed. Harper & Row, 1965.

[11] W. Gilbert, *De Magnete*. Dover Publications, 1893.

[12] J. C. Maxwell, *A treatise on electricity and magnetism*, 1873.

[13] P. Zeeman, "The effect of magnetization on the nature of light emitted by a substance," *Nature*, vol. 55, p. 347, 1897.

[14] H. A. Lorentz, *The Theory of Electrons*. London: Macmillan & Co., 1909.

[15] P. Curie, "Propriétés magnétiques des crops à diverses tempèratures," *Ann. Chem. Phys.*, 1895.

[16] P. Weiss, "L'hypothése du champ moléculaire et la propriété ferromagnétique," *J. Phys. Theor. Appl.*, vol. 6, no. 1, pp. 661–690, 1907.

[17] "II. The Doctor's Dissertation (text and translation)*," in *Early Work (19051911)*, ser. Niels Bohr Collected Works, L. Rosenfeld and J. R. Nielsen, Eds. Elsevier, 1972, vol. 1, pp. 163 – 393.

[18] H.-J. Van Leeuwen, "Problèmes de la théorie électronique du magnétisme," *J. Phys. Radium*, vol. 2, no. 12, pp. 361–377, 1921.

[19] W. Gerlach and O. Stern, "Der experimentelle nachweis der richtungsquantelung im magnetfeld," *Zeitschrift für Physik*, vol. 9, no. 1, pp. 349–352, 1922.

[20] G. E. Uhlenbeck and S. Goudsmit, "Ersetzung der hypothese vom unmechanischen zwang durch eine forderung bezüglich des inneren verhaltens jedes einzelnen elektrons," *Die Naturwissenschaften*, vol. 13, no. 47, pp. 953–954, 1925.

[21] W. Pauli, "Über den zusammenhang des abschlusses der elektronengruppen im atom mit der komplexstruktur der spektren," *Zeitschrift für Physik*, vol. 31, no. 1, pp. 765–783, 1925.

[22] W. Pauli, "Zur Quantenmechanik des magnetischen Elektrons," *Zeitschrift für Physik A Hadrons and Nuclei*, vol. 43, no. 9-10, pp. 601–623, 1927.

[23] P. A. M. Dirac, "On the theory of quantum mechanics," vol. 112, no. 762, pp. 661–677, 1926.

[24] W. Heisenberg, "Mehrkörperproblem und resonanz in der quantenmechanik," *Z. Physik*, vol. 38, no. 6, pp. 411–426, 1926.

[25] N. W. Ashcroft and N. D. Mermin, *Solid State Physics*. Saunders, 1976.

[26] W. Heitler and F. London, "Interaction of neutral atoms and homopolar binding by quantum mechanics," *Zeitschrift für Physik*, vol. 44, no. 6, pp. 455–472, 1927.

[27] C. Herring, *Direct exchange between well-separated atoms*, G. T. Rado and H. Suhl, Eds. Academic Press, New York, 1965, vol. 2B.

[28] J. B. Goodenough, "Theory of the role of covalence in the perovskite-type manganites $[\mathrm{La}, m(\mathrm{II})]\mathrm{MnO}_3$," *Phys. Rev.*, vol. 100, pp. 564–573, Oct 1955.

[29] J. B. Goodenough, "An interpretation of the magnetic properties of the perovskite-type mixed crystals $\mathrm{La}_{1-x}\mathrm{SrCoO}_{3-\lambda}$," *Journal of Physics and Chemistry of Solids*, vol. 6, no. 23, pp. 287–297, 1958.

[30] J. Kanamori, "Superexchange interaction and symmetry properties of electron orbitals," *Journal of Physics and Chemistry of Solids*, vol. 10, no. 23, pp. 87 – 98, 1959.

[31] R. J. Baxter, *Exactly Solved Models In Statistical Mechanics*. Academic Press, 1982.

[32] W. Lenz, "Contributions to the understanding of magnetic properties in solid bodies," *Physikalische Zeitschrift*, vol. 21, pp. 613–315, 1920.

[33] E. Ising, "Beitrag zur theorie des ferromagnetismus," *Zeitschrift für Physik*, vol. 31, no. 1, pp. 253–258, 1925.

[34] H. Bethe, "Zur theorie der metalle," *Zeitschrift für Physik*, vol. 71, no. 3, pp. 205–226, 1931.

[35] L. Onsager, "Crystal statistics. I. a two-dimensional model with an order-disorder transition," *Phys. Rev.*, vol. 65, pp. 117–149, Feb 1944.

[36] H. A. Kramers and G. H. Wannier, "Statistics of the two-dimensional ferromagnet. part I," *Phys. Rev.*, vol. 60, pp. 252–262, Aug 1941.

[37] T. Holstein and H. Primakoff, "Field dependence of the intrinsic domain magnetization of a ferromagnet," *Phys. Rev.*, vol. 58, pp. 1098–1113, Dec 1940.

[38] J. Goldstone, A. Salam, and S. Weinberg, "Broken symmetries," *Phys. Rev.*, vol. 127, pp. 965–970, Aug 1962.

BIBLIOGRAPHY

[39] N. P. Armitage, "Quantum materials, Kitaev's exact solution approximated," *Nature Mater.*, vol. 15, pp. 701–702, 2016.

[40] C. Lacroix, P. Mendels, and F. Mila, *Introduction To Frustrated Magnetism*, ser. Springer Series in Solid-State Sciences. Springer, 2011, vol. 164.

[41] G. H. Wannier, "Antiferromagnetism. the triangular Ising net," *Phys. Rev.*, vol. 79, pp. 357–364, Jul 1950.

[42] P. Anderson, "Resonating valence bonds: A new kind of insulator?" *Materials Research Bulletin*, vol. 8, no. 2, pp. 153 – 160, 1973.

[43] P. W. Anderson, "The resonating valence bond state in La_2CuO_4 and superconductivity," *Science*, vol. 235, no. 4793, pp. 1196–1198, 1987.

[44] J. D. Bernal and R. H. Fowler, "A theory of water and ionic solution, with particular reference to hydrogen and hydroxyl ions," *The Journal of Chemical Physics*, vol. 1, no. 8, pp. 515–548, 1933.

[45] I. Dzyaloshinsky, "A thermodynamic theory of weak ferromagnetism of antiferromagnetics," *Journal of Physics and Chemistry of Solids*, vol. 4, no. 4, pp. 241 – 255, 1958.

[46] T. Moriya, "Anisotropic superexchange interaction and weak ferromagnetism," *Phys. Rev.*, vol. 120, pp. 91–98, 1960.

[47] K. I. Kugel and D. I. Khomskii, "The Jahn-Teller effect and magnetism: Transition metal compounds," *Sov. Phys. Usp*, vol. 25, no. 231, 1982.

[48] S. G. Condran and M. L. Plumer, "A model of magnetic order in hexagonal $HoMnO_3$," *Journal of Physics: Condensed Matter*, vol. 22, no. 16, p. 162201, 2010.

[49] M. C. Nuss and J. Orenstein, *Terahertz Time Domain Spectroscopy*, D. G. Gruner, Ed. Springer Berlin Heidelberg, 1998, vol. 74, no. pp 7-50.

[50] M. Tonouchi, "Cutting-edge terahertz technology," *Nat. Photonics*, vol. 1, pp. 97–105, 2007.

[51] D. H. Auston, K. P. Cheun, and P. R. Smith, "Picosecond photoconducting hertzian dipoles," *Applied Physics Letters*, vol. 3, no. 10, pp. 2006–2015, 1984.

[52] P. R. Smith, D. H. Auston, and M. C. Nuss, "Subpicosecond photoconducting dipole antennas," *Quantum Electronics*, vol. 24, no. 2, pp. 255–260, 1988.

[53] D. Grischkowsky, S. Keiding, M. van Exter, and C. Fattinger, "Far-infrared time-domian spectrocopy with terahertz beams of dielectrics and semiconductors," *Journal of the Optical Society of America B-optical Physics*, vol. 7, no. 10, pp. 2006–2015, 1990.

[54] G. Grüner, *Millimeter and Submillimeter Wave Spectroscopy of Solids*, 1998.

[55] P. F. Taday, "Applications of terahertz spectroscopy to pharmaceutical sciences," *Philosophical Transactions of the Royal Society of London A: Mathematical, Physical and Engineering Sciences*, vol. 362, no. 1815, pp. 351–364, 2004.

[56] B. B. Hu and M. C. Nuss, "Imaging with terahertz waves," *Opt. Lett.*, vol. 20, no. 16, pp. 1716–1718, Aug 1995.

[57] J. L. Johnson, T. D. Dorney, and D. M. Mittleman, "Enhanced depth resolution in terahertz imaging using phase-shift interferometry," *Applied Physics Letters*, vol. 78, no. 6, pp. 835–837, 2001.

[58] D. M. Mittleman, S. Hunsche, L. Boivin, and M. C. Nuss, "T-ray tomography," *Opt. Lett.*, vol. 22, no. 12, pp. 904–906, Jun 1997.

[59] S. Wang, B. Ferguson, D. Abbott, and X.-C. Zhang, "T-ray imaging and tomography," *Journal of Biological Physics*, vol. 29, no. 2, pp. 247–256, 2003.

[60] W. L. Chan, J. Deibel, and D. M. Mittleman, "Imaging with terahertz radiation," *Reports on Progress in Physics*, vol. 70, no. 8, p. 1325, 2007.

[61] M. Nagel, P. H. Bolivar, M. Brucherseifer, H. Kurz, A. Bosserhoff, and R. Büttner, "Integrated planar terahertz resonators for femtomolar sensitivity label-free detection of DNA hybridization," *Appl. Opt.*, vol. 41, no. 10, pp. 2074–2078, Apr 2002.

[62] M. K. Choi, A. Bettermann, and D. W. van der Weide, "Potential for detection of explosive and biological hazards with electronic terahertz systems," *Philosophical Transactions of the Royal Society of London A: Mathematical, Physical and Engineering Sciences*, vol. 362, no. 1815, pp. 337–349, 2004.

[63] M. Leahy-Hoppa, M. Fitch, X. Zheng, L. Hayden, and R. Osiander, "Wideband terahertz spectroscopy of explosives," *Chemical Physics Letters*, vol. 434, no. 46, pp. 227 – 230, 2007.

[64] E. Bründermann, H.-W. Hübers, and M. F. Kimmitt, "Terahertz techniques," *Springer*, vol. 151, 2012.

[65] D. B. Rutledge, D. P. Neikirk, and D. P. Kasilingam, "Integrated circuit antennas," *Infrared and millimeter waves*, vol. 10, no. part 2, pp. 1–90, 1983.

[66] Y.-S. Lee, *Generation and Detection of Broadband Terahertz Pulses*. Springer US, 2009.

[67] M. van Exter and D. Grischkowsky, "Characterization of an optoelectronic terahertz beam system," *Microwave Theory and Techniques, IEEE Transactions on*, vol. 38, no. 11, pp. 1684–1691, 1990.

[68] C. Brückner, G. Notni, and A. Tnnermann, "Optimal arrangement of 90° off-axis parabolic mirrors in THz setups," *Optik - International Journal for Light and Electron Optics*, vol. 121, no. 1, pp. 113 – 119, 2010.

[69] P. Arguijo and M. S. Scholl, "Exact ray-trace beam for an off-axis paraboloid surface," *Appl. Opt.*, vol. 42, no. 16, pp. 3284–3289, Jun 2003.

[70] K. Tanaka, N. Saga, and H. Mizokami, "Field spread of a diffracted gaussian beam through a circular aperture," *Appl. Opt.*, vol. 24, no. 8, pp. 1102–1106, Apr 1985.

[71] J. F. Corson, "Advances in terahertz spectroscopy of high-T_c superconductors," Ph.D. dissertation, University of California, Berkely, 2000.

[72] M. Born and E. Wolf, *Principles of optics: electromagnetic theory of propagation, interference, and diffration of light.* Cambridge University Press, 1999.

[73] W. H. Press, S. A. Teukolsky, W. T. Vetterling, and B. P. Flannery, *Numerical Recipes 3rd Edition: The Art of Scientific Computing*, 3rd ed. New York, NY, USA: Cambridge University Press, 2007.

[74] R. C. Jones, "A new calculus for the treatment of optical systems. description and discussion of the calculus," *J. Opt. Soc. Am.*, vol. 31, no. 7, pp. 488–493, Jul 1941.

[75] N. P. Armitage, "Constraints on jones transmission matrices from time-reversal invariance and discrete spatial symmetries," *Phys. Rev. B*, vol. 90, p. 035135, Jul 2014.

[76] C. M. Morris, R. V. Aguilar, A. V. Stier, and N. P. Armitage, "Polarization

modulation time-domain terahertz polarimetry," *Opt. Express*, vol. 20, no. 11, pp. 12 303–12 317, May 2012.

[77] O. Klein, S. Donovan, M. Dressel, and G. Grüner, "Microwave cavity perturbation technique: Part I: Principles," *International Journal of Infrared and Millimeter Waves*, vol. 14, no. 12, 1993.

[78] S. Donovan, O. Klein, M. Dressel, K. Holczer, and G. Grüner, "Microwave cavity perturbation technique: Part II: Experimental scheme," *International Journal of Infrared and Millimeter Waves*, vol. 14, no. 12, 1993.

[79] M. Dressel, O. Klein, S. Donovan, and G. Grüner, "Microwave cavity perturbation technique: Part III: Applications," *International Journal of Infrared and Millimeter Waves*, vol. 14, no. 12, 1993.

[80] M. Scheffler and M. Dressel, "Broadband microwave spectroscopy in Corbino geometry for temperatures down to 1.7K," *Rev. Sci. Instrum.*, vol. 76, no. 074702, 2005.

[81] J. C. Booth, D. H. Wu, and S. M. Anlage, "A broadband method for the measurement of the surface impedance of thin films at microwave frequencies," *Rev. Sci. Instrum.*, vol. 65, no. 2082, 1994.

[82] P. J. Turner, D. M. Broun, S. Kamal, M. E. Hayden, J. S. Bobowski, R. Harris, D. C. Morgan, J. S. Preston, D. A. Bonn, and W. N. Hardy, "Bolometric

technique for high-resolution broadband microwave spectroscopy of ultra-low-loss samples," *Rev. Sci. Instrum.*, vol. 75, no. 1, 2004.

[83] M. L. Stutzman, M. Lee, and R. F. Bradley, "Broadband calibration of long lossy microwave transmission lines at cryogenic temperatures using nichrome films," *Rev. Sci. Instrum.*, vol. 71, no. 4596, 2000.

[84] M. Dressel and G. Grüner, *Electrodynamics of Solids: Optical Properties of Electrons In Matter*. Cambridge University Press, 2002.

[85] R. A. Waldron, *The Theory of Wavguides and Resonant Cavities*. Maclaren & Sons Ltd. London, 1967.

[86] J. D. Jackson, *Classical Electrodynamics*. John Wiley & Sons, Ltd., 1975.

[87] H. B. G. Casimir, "On the theory of electromagnetic waves in resonant cavities," *Philips Research Reports*, vol. 6, no. 162, 1951.

[88] Z. Zhai, C. Kusko, C. Hakim, S. Sridhar, A. Revcolecschi, and A. Vietkine, "Precision microwave dielectric and magnetic susceptibility measurements of correlated electronic mateirals using superconducting cavities," *Rev. Sci. Instrum.*, vol. 71, no. 8, 2000.

[89] K. S. Champlin and R. R. Krongard, *IRE Trans. Microwave Theory Techn.*, vol. MIT-9, no. 545, 1961.

[90] M. E. Brodwin and M. K. Parsons, "New approach to the perturbation of cavity resonators by homogeneous, isotropic spheres," *J. Appl. Phys.*, vol. 36, no. 494, 1965.

[91] L. I. Buranov and I. F. Schegolev, *Intrum. & Exp. Tech.*, vol. 14, no. 528, 1971.

[92] M. Cohen, S. K. Khanna, W. J. Gunning, A. F. Garito, and A. J. Heeger, "Theory of microwave losses of one-dimensional conductors in the skin effect regime: Application of TTF-TCNQ," *Solid State Commun.*, vol. 17, no. 367, 1975.

[93] N. P. Ong, "Microwave cavity-perturbation equations in the skin-depth regime," *J. Appl. Phys.*, vol. 48, no. 2935, 1977.

[94] D.-N. Peligrad, B. Nebendahl, M. Mehring, A. Dulcic, M. Pozek, and D. Paar, "General solution for the complex frequency shift in microwave measurements of thin films," *PRB*, vol. 64, no. 224504, 2001.

[95] G. Khaliullin and S. Maekawa, "Orbital liquid in three-dimensional mott insulator: $LaTiO_3$," *Phys. Rev. Lett.*, vol. 85, pp. 3950–3953, Oct 2000.

[96] V. Fritsch, J. Hemberger, N. Büttgen, E.-W. Scheidt, H.-A. Krug von Nidda, A. Loidl, and V. Tsurkan, "Spin and orbital frustration in $MnSc_2S_4$ and $FeSc_2S_4$," *Phys. Rev. Lett.*, vol. 92, p. 116401, Mar 2004.

[97] G. Chen, A. P. Schnyder, and L. Balents, "Excitation spectrum and magnetic

field effects in a quantum critical spin-orbital system: The case of $FeSc_2S_4$," *Phys. Rev. B*, vol. 80, p. 224409, Dec 2009.

[98] P. G. L. Brossard and H. Oudet, *J. Phys. (Paris), Colloq.*, vol. 37, no. C6-23, 1976.

[99] M. Ivanov, V. Mitrofanov, L. Falkovskaya, and A. Fishman, "Random fields in disordered magnetics with Jahn-Teller ions," *Journal of Magnetism and Magnetic Materials*, vol. 36, no. 12, pp. 26 – 38, 1983.

[100] W. Low and M. Weger, "Paramagnetic resonance and optical spectra of divalent iron in cubic fields. I. theory," *Phys. Rev.*, vol. 118, pp. 1119–1130, Jun 1960.

[101] S. Wittekoek, R. P. van Stapele, and A. W. J. Wijma, "Optical-absorption spectrum of tetrahedral Fe^{+2} in $CdIn_2S_4$: Influence of a weak Jahn-Teller coupling," *Phys. Rev. B*, vol. 7, pp. 1667–1677, Feb 1973.

[102] G. A. Slack, S. Roberts, and J. T. Vallin, "Optical absorption of FeS^{2+} in CdTe in the near and far infrared," *Phys. Rev.*, vol. 187, pp. 511–524, Nov 1969.

[103] A. Krimmel, M. Mücksch, V. Tsurkan, M. M. Koza, H. Mutka, and A. Loidl, "Vibronic and magnetic excitations in the spin-orbital liquid state of $FeSc_2S_4$," *Phys. Rev. Lett.*, vol. 94, p. 237402, Jun 2005.

[104] S. Sarkar, T. Maitra, R. Valentí, and T. Saha-Dasgupta, "Comparative study

of $FeCr_2S_4$ and $FeSc_2S_4$: Spinels with orbitally active A site," *Physical Review B*, vol. 82, no. 4, p. 041105, 2010.

[105] L. Mittelstädt, M. Schmidt, Z. Wang, F. Mayr, V. Tsurkan, P. Lunkenheimer, D. Ish, L. Balents, J. Deisenhofer, and A. Loidl, "Spin-orbiton and quantum criticality in $FeSc_2S_4$," *Phys. Rev. B*, vol. 91, p. 125112, Mar 2015.

[106] A. B. Kuzmenko, "Kramerskronig constrained variational analysis of optical spectra," *Review of Scientific Instruments*, vol. 76, no. 8, 2005.

[107] G. A. Slack, F. S. Ham, and R. M. Chrenko, "Optical absorption of tetrahedral Fe^{2+} ($3d^6$) in cubic ZnS, CdTe, and $MgAl_2O_4$," *Phys. Rev.*, vol. 152, pp. 376–402, Dec 1966.

[108] L. F. Feiner, "Unified description of the cooperative Jahn-Teller effect in $FeSc_2S_4$ and the impurity Jahn-Teller effect in $CoCr_2S_4$:Fe^{+2}," *J. Phys. C.*, vol. 15, no. 7, 1982.

[109] T. Sakai, O. Cepas, and T. Ziman, "Selection rule of ESR for spin-gap systems," *Physica B: Condensed Matter*, vol. 294-295, 2001.

[110] D. Hüvonen, "Terahertz spectroscopy of low-dimensional spin systems," Ph.D. dissertation, National Institute of Chemical Physics and Biophysics, Tallinn, Estonia, May 2008.

[111] I. Dzyaloshinsky, "A thermodynamic theory of weak ferromagnetism of antiferromagnetics," *Journal of Physics and Chemistry of Solids*, vol. 4, no. 4, pp. 241 – 255, 1958.

[112] K. W. Plumb, J. R. Morey, J. A. Rodriguez-Rivera, H. Wu, A. A. Podlesnyak, T. M. McQueen, and C. L. Broholm, "Antiferromagnetic and orbital ordering on a diamond lattice near quantum criticality," *Phys. Rev. X*, vol. 6, p. 041055, 2016.

[113] A. Biffin, C. Rüegg, J. Embs, T. Guidi, D. Cheptiakov, A. Loidl, V. Tsurkan, and R. Coldea, "Magnetic field dependence of excitations near spin-orbital quantum criticality," *Phys. Rev. Lett.*, vol. 118, p. 067205, Feb 2017.

[114] T. H. R. Skyrme, "A unified field theory of mesons and baryons," *Nucl. Phys.*, vol. 31, no. 556, 1962.

[115] N. Nagaosa and Y. Tokura, "Topological properties and dynamics of magnetic skrymions," *Nature Nanotechnology*, vol. 8, pp. 899–911, 2013.

[116] A. N. Bogdanov and D. A. Yablonskii, "Thermodynamically stable "vorticies" in magnetically ordered crystals. the mixed state of magnets," *Sov. Phys. JETP*, vol. 68, no. 101, 1989.

[117] U. K. Rozler, A. N. Bogdanov, and C. Pfleiderer, "Spontaneous skrymion ground state in magnetic metals," *Nature*, vol. 442, pp. 797–801, 2006.

[118] S. Mühlbauer, B. Binz, F. Jonietz, C. Pfleiderer, A. Rosch, A. Neubauer, R. Georgii, and P. Boni, "Skrymion lattice in a chiral magnet," *Science*, vol. 323, pp. 915–919, 2009.

[119] X. Z. Yu, J. Kanazawa, Y. Onose, K. Kimoto, W. Z. Zhang, Y. Matsui, and Y. Tokura, "Near room-temperature formation of a skyrmion crystal in thin-films of the helimagnet FeGe," *Nat. Mater.*, vol. 10, pp. 106–109, 2011.

[120] X. Z. Yu, Y. Onose, J. Kanazawa, J. H. Park, J. H. Han, Y. Matsui, N. Nagaosa, and Y. Tokura, "Real-space observation of a two-dimensional skrymion crystal," *Nature*, vol. 465, pp. 901–904, 2010.

[121] W. Münzer, A. Neubauer, T. Adams, S. Mühlbauer, C. Franz, F. Jonietz, R. Georgii, P. Böni, B. Pedersen, M. Schmidt, A. Rosch, and C. Pfleiderer, "Skyrmion lattice in the doped semiconductor $Fe_{1-x}Co_xSi$," *Phys. Rev. B*, vol. 81, p. 041203, Jan 2010.

[122] T. Schulz, R. Ritz, A. Bauer, M. Halder, M. Wager, C. Franz, C. Pfleiderer, K. Everschor, M. Garst, and A. Rosch, "Emergent electrodynamics of skyrmions in a chiral lattice magnet," *Nat. Phys.*, vol. 8, pp. 301–304, 2012.

[123] F. Jonietz, S. Mühlbauer, C. Pfleiderer, A. Neubauer, W. Münzer, A. Bauer, T. Adams, R. Georgii, P. Böni, R. A. Duine, K. Everschor, M. Garst, and A. Rosch, "Spin transfer torques in mnsi at ultralow current densities," *Science*, vol. 330, no. 6011, pp. 1648–1651, 2010.

[124] S. Seki, X. Z. Yu, S. Ishiwata, and Y. Tokura, "Observation of skyrmions in a multiferroic material," *Science*, vol. 336, no. 6078, pp. 198–201, 2012.

[125] S. Seki, J.-H. Kim, D. S. Inosov, R. Georgii, B. Keimer, S. Ishiwata, and Y. Tokura, "Formation and rotation of skyrmion crystal in the chiral-lattice insulator Cu_2OSeO_3," *Phys. Rev. B*, vol. 85, p. 220406, Jun 2012.

[126] J. S. White, I. Levati, A. A. Omrani, N. Egetenmeyer, K. Pra, I. ivkovi, J. L. Gavilano, J. Kohlbrecher, M. Bartkowiak, H. Berger, and H. M. Rnnow, "Electric field control of the skyrmion lattice in Cu_2OSeO_3," *Journal of Physics: Condensed Matter*, vol. 24, no. 43, p. 432201, 2012.

[127] J. H. Yang, Z. L. Li, X. Z. Lu, M.-H. Whangbo, S.-H. Wei, X. G. Gong, and H. J. Xiang, "Strong dzyaloshinskii-moriya interaction and origin of ferroelectricity in Cu_2OSeO_3," *Phys. Rev. Lett.*, vol. 109, p. 107203, Sep 2012.

[128] D. I. Khomskii, "Classifying multiferroics: mechanisms and effects," *Physics*, vol. 2, no. 20, 2009.

[129] Y. Tokura, S. Seki, and N. Nagaosa, "Multiferroics of spin origin," *Reports on Progress in Physics*, vol. 77, no. 7, p. 076501, 2014.

[130] C. Jia, S. Onoda, N. Nagaosa, and J. H. Han, "Bond electronic polarization induced by spin," *Phys. Rev. B*, vol. 74, p. 224444, Dec 2006.

[131] C. Jia, S. Onoda, N. Nagaosa, and J. H. Han, "Microscopic theory of spin-polarization coupling in multiferroic transition metal oxides," *Phys. Rev. B*, vol. 76, p. 144424, Oct 2007.

[132] T.-H. Arima, "Ferroelectricity induced by proper-screw type magnetic order," *Journal of the Physical Society of Japan*, vol. 76, no. 7, p. 073702, 2007.

[133] J.-W. G. Bos, C. V. Colin, and T. T. M. Palstra, "Magnetoelectric coupling in the cubic ferrimagnet Cu_2OSeO_3," *Phys. Rev. B*, vol. 78, p. 094416, Sep 2008.

[134] M. Belesi, I. Rousochatzakis, M. Abid, U. K. Rößler, H. Berger, and J.-P. Ansermet, "Magnetoelectric effects in single crystals of the cubic ferrimagnetic helimagnet Cu_2OSeO_3," *Phys. Rev. B*, vol. 85, p. 224413, Jun 2012.

[135] M. Mochizuki and S. Seki, "Magnetoelectric resonances and predicted microwave diode effect of the skyrmion crystal in a multiferroic chiral-lattice magnet," *Phys. Rev. B*, vol. 87, p. 134403, Apr 2013.

[136] M. Mochizuki, "Spin-wave modes and their intense excitation effects in skyrmion crystals," *Phys. Rev. Lett.*, vol. 108, p. 017601, Jan 2012.

[137] A. Maisuradze, A. Shengelaya, H. Berger, D. M. Djokić, and H. Keller, "Magnetoelectric coupling in single crystal Cu_2OSeO_3 studied by a novel electron spin resonance technique," *Phys. Rev. Lett.*, vol. 108, p. 247211, Jun 2012.

[138] A. Maisuradze, Z. Guguchia, B. Graneli, H. M. Rønnow, H. Berger, and

H. Keller, "μSR investigation of magnetism and magnetoelectric coupling in Cu_2OSeO_3," *Phys. Rev. B*, vol. 84, p. 064433, Aug 2011.

[139] A. A. Omrani, J. S. White, K. Prša, I. Živković, H. Berger, A. Magrez, Y.-H. Liu, J. H. Han, and H. M. Rønnow, "Exploration of the helimagnetic and skyrmion lattice phase diagram in Cu_2OSeO_3 using magnetoelectric susceptibility," *Phys. Rev. B*, vol. 89, p. 064406, Feb 2014.

[140] E. Ruff, P. Lunkenheimer, A. Loidl, H. Berger, and S. Krohns, "Magnetoelectric effects in the skrymion host material Cu_2OSeO_3," *Scientific Reports*, vol. 5, no. 15025, 2015.

[141] O. Janson, I. Rousochatzakis, A. A. Tsirlin, M. Belesi, A. A. Leonov, U. K. Robler, J. van den Brink, and H. Rosner, "The quantum nature of skyrmions and half-skyrmions in Cu_2OSeO_3," *Nature Comm.*, 2014.

[142] K. H. Miller, X. S. Xu., H. Berger, E. S. Knowles, D. J. Arenas, M. W. Meisel, and D. B. Tanner, "Magnetodielectric coupling of infrared phonons in single-crystal Cu_2OSeO_3," *Phys. Rev. B*, vol. 82, p. 144107, Oct 2010.

[143] R. B. Versteeg, I. Vergara, S. D. Schäfer, D. Bischoff, A. Aqeel, T. T. M. Palstra, M. Grüninger, and P. H. M. van Loosdrecht, "Optically probed symmetry breaking in the chiral magnet Cu_2OSeO_3," *Phys. Rev. B*, vol. 94, p. 094409, Sep 2016.

[144] D. Szaller, S. Bordács, and I. Kézsmárki, "Symmetry conditions for nonreciprocal light propagation in magnetic crystals," *Phys. Rev. B*, vol. 87, p. 014421, Jan 2013.

[145] Y. Okamura, F. Kagawa, S. Seki, M. Kubota, M. Kawasaki, and Y. Tokura, "Microwave magnetochiral dichroism in the chiral-lattice magnet Cu_2OSeO_3," *Phys. Rev. Lett.*, vol. 114, p. 197202, May 2015.

[146] M. Mochizuki, "Microwave magnetochiral effect in Cu_2OSeO_3," *Phys. Rev. Lett.*, vol. 114, p. 197203, May 2015.

[147] T. Schwarze, J. Waizner, M. Garst, A. Bauer, I. Stasinopoulos, H. Berger, C. Pfleiderer, and D. Grundler, "Universal helimagnon and skyrmion excitations in metallic, semiconducting, and insulating chiral magnets," *Nature Mater.*, vol. 14, pp. 478–483, 2015.

[148] V. P. Gnezdilov, Y. Lamonova, G. Pashkevich, P. Lemmens, H. Berger, F. Bussy, and S. L. Gnatchenko, "Magneto-electricity in the ferrimagnet Cu_2OSeO_3: Symmetry analysis and Raman scattering study," *Low Temperature Physics*, vol. 36, no. 550, 2010.

[149] M. Ozerov, J. Romhányi, M. Belesi, H. Berger, J.-P. Ansermet, J. van den Brink, J. Wosnitza, S. A. Zvyagin, and I. Rousochatzakis, "Establishing the fundamental magnetic interactions in the chiral skyrmionic mott insulator Cu_2OSeO_3 by

terahertz electron spin resonance," *Phys. Rev. Lett.*, vol. 113, p. 157205, Oct 2014.

[150] P. Y. Portnichenko, J. Romhayni, Y. A. Onykiienko, A. Henschel, M. Schmidt, A. S. Cameron, M. A. Surmach, J. A. Lim, J. T. Park, A. Schneidewind, D. L. Abernathy, H. Rosner, J. van den Brink, and D. S. Inosov, "Magnon spectrum of the helimagnetic insulator Cu_2OSeO_3," *Nature Commun.*, vol. 7, no. 10725, p. 10725, 2016.

[151] J. Romhányi, J. van den Brink, and I. Rousochatzakis, "Entangled tetrahedron ground state and excitations of the magnetoelectric skyrmion material Cu_2OSeO_3," *Phys. Rev. B*, vol. 90, p. 140404, Oct 2014.

[152] K. Momma and F. Izumi, "*VESTA3* for three-dimensional visualization of crystal, volumetric and morphology data," *Journal of Applied Crystallography*, vol. 44, no. 6, pp. 1272–1276, Dec 2011.

[153] H. Effenberger and F. Pertlik, "The crystal structures of the copper(II)-oxo-selenites Cu_2OSeO_3 (cubic and monoclinic), and $Cu_4O(SeO_3)_3$ (monoclinic and triclinic)," *Chemical Monthly*, vol. 117, no. 8, pp. 887–896, 1986.

[154] M. Belesi, I. Rousochatzakis, H. C. Wu, H. Berger, I. V. Shvets, F. Mila, and J. P. Ansermet, "Ferrimagnetism of the magnetoelectric compound Cu_2OSeO_3 probed by ^{77}Se NMR," *Phys. Rev. B*, vol. 82, p. 094422, Sep 2010.

[155] G. S. Tucker, J. S. White, J. Romhányi, D. Szaller, I. Kézsmárki, B. Roessli, U. Stuhr, A. Magrez, F. Groitl, P. Babkevich, P. Huang, I. Živković, and H. M. Rønnow, "Spin excitations in the skyrmion host Cu_2OSeO_3," *Phys. Rev. B*, vol. 93, p. 054401, Feb 2016.

[156] V. Chizhikov and V. Dmitrienko, "Microscopic description of twisted magnet Cu_2OSeO_3," *Journal of Magnetism and Magnetic Materials*, vol. 382, pp. 142 – 151, 2015.

[157] T. Adams, A. Chacon, M. Wagner, A. Bauer, G. Brandl, B. Pedersen, H. Berger, P. Lemmens, and C. Pfleiderer, "Long-wavelength helimagnetic order and skyrmion lattice phase in Cu_2OSeO_3," *Phys. Rev. Lett.*, vol. 108, p. 237204, Jun 2012.

[158] I. Levatić, V. Šurija, H. Berger, and I. Živković, "Dissipation processes in the insulating skyrmion compound Cu_2OSeO_3," *Phys. Rev. B*, vol. 90, p. 224412, Dec 2014.

[159] J. Panella, B. A. Trump, G. G. Marcus, and T. M. McQueen, *In Preparation*, 2017.

[160] N. J. Laurita, B. Cheng, R. Barkhouser, V. A. Neumann, and N. P. Armitage, "A modified 8f geometry with reduced optical aberrations for improved time domain terahertz spectroscopy," *Journal of Infrared, Millimeter, and Terahertz Waves*, pp. 1–9, 2016.

[161] O. Arnold, J. Bilheux, J. Borreguero, A. Buts, S. Campbell, L. Chapon, M. Doucet, N. Draper, R. F. Leal, M. Gigg, V. Lynch, A. Markvardsen, D. Mikkelson, R. Mikkelson, R. Miller, K. Palmen, P. Parker, G. Passos, T. Perring, P. Peterson, S. Ren, M. Reuter, A. Savici, J. Taylor, R. Taylor, R. Tolchenov, W. Zhou, and J. Zikovsky, "Mantiddata analysis and visualization package for neutron scattering and {SR} experiments," *Nuclear Instruments and Methods in Physics Research Section A: Accelerators, Spectrometers, Detectors and Associated Equipment*, vol. 764, pp. 156 – 166, 2014.

[162] R. Ewings, A. Buts, M. Le, J. van Duijn, I. Bustinduy, and T. Perring, *Nuclear Instruments and Methods in Physics Research Section A: Accelerators, Spectrometers, Detectors and Associated Equipment*, vol. 834, pp. 132 – 142, 2016.

[163] G. G. Marcus *et al.*, *In Preparation.*, 2017.

[164] M. Freiser, "A survey of magnetooptic effects," *IEEE Transactions on Magnetics*, vol. 4, no. 2, pp. 152–161, 1968.

[165] S. R. Woodford, A. Bringer, and S. Blgel, "Interpreting magnetization from faraday rotation in birefringent magnetic media," *Journal of Applied Physics*, vol. 101, no. 5, 2007.

[166] A. Glazer and K. G. Cox, *Clasical linear crystal optics in International Tables for Crystallography.* John Wiley & Sons, Ltd., 2006, vol. D.

[167] L. D. Barron, *Molecular Light Scattering and Optical Activity.* Cambridge University Press, New York, 2009.

[168] I. Živković, D. Pajić, T. Ivek, and H. Berger, "Two-step transition in a magnetoelectric ferrimagnet Cu_2OSeO_3," *Phys. Rev. B*, vol. 85, p. 224402, Jun 2012.

[169] I. Živković, J. S. White, H. M. Rønnow, K. Prša, and H. Berger, "Critical scaling in the cubic helimagnet Cu_2OSeO_3," *Phys. Rev. B*, vol. 89, p. 060401, Feb 2014.

[170] U. Köbler, A. Hoser, M. Kawakami, T. Chatterji, and J. Rebizant, "An unified view of the spin dynamics in two- and three-dimensional magnetic systems," *Journal of Magnetism and Magnetic Materials*, vol. 205, no. 23, pp. 343 – 356, 1999.

[171] M. I. Kobets, K. G. Dergachev, E. N. Khatsko, A. I. Rykova, P. Lemmens, D. Wulferding, and H. Berger, "Microwave absorption in the frustrated ferrimagnet Cu_2OSeO_3," *Low Temperature Physics*, vol. 36, no. 2, pp. 176–179, 2010.

[172] N. J. Laurita, J. Deisenhofer, L. Pan, C. M. Morris, M. Schmidt, M. Johnsson, V. Tsurkan, A. Loidl, and N. P. Armitage, "Singlet-triplet excitations and long-range entanglement in the spin-orbital liquid candidate $FeSc_2S_4$," *Phys. Rev. Lett.*, vol. 114, p. 207201, 2015.

[173] M. Sparks, R. Loudon, and C. Kittel, "Ferromagnetic relaxation. I. theory of the relaxation of the uniform precession and the degenerate spectrum in insulators at low temperatures," *Phys. Rev.*, vol. 122, pp. 791–803, May 1961.

[174] E. Schlömann, "Ferromagnetic relaxation caused by interaction with thermally excited magnons," *Phys. Rev.*, vol. 121, pp. 1312–1319, Mar 1961.

[175] C. Kittel and E. Abrahams, "Relaxation process in ferromagnetism," *Rev. Mod. Phys.*, vol. 25, pp. 233–238, Jan 1953.

[176] M. E. Zhitomirsky and A. L. Chernyshev, "*Colloquium* : Spontaneous magnon decays," *Rev. Mod. Phys.*, vol. 85, pp. 219–242, Jan 2013.

[177] A. L. Chernyshev, "Field dependence of magnon decay in yttrium iron garnet thin films," *Phys. Rev. B*, vol. 86, p. 060401, Aug 2012.

[178] T. Oguchi, "Theory of spin-wave interactions in ferro- and antiferromagnetism," *Phys. Rev.*, vol. 117, pp. 117–123, Jan 1960.

[179] S. M. Rezende, "Theory of coherence in Bose-Einstein condensation phenomena in a microwave-driven interacting magnon gas," *Phys. Rev. B*, vol. 79, p. 174411, May 2009.

[180] C. L. Ordóñez Romero, B. A. Kalinikos, P. Krivosik, W. Tong, P. Kabos, and C. E. Patton, "Three-magnon splitting and confluence processes for spin-wave excitations in yttrium iron garnet films: Wave vector selective brillouin light

scattering measurements and analysis," *Phys. Rev. B*, vol. 79, p. 144428, Apr 2009.

[181] A. Kreisel, F. Sauli, L. Bartosch, and P. Kopietz, "Microscopic spin-wave theory for yttrium-iron garnet films," *The European Physical Journal B*, vol. 71, no. 1, p. 59, 2009.

[182] P. E. Wigen, *Nonlinear Phenomena and Chaos In Magnetic Materials*, P. E. Wigen, Ed. World Scientific, 1994.

[183] B. Lorenz, "Hexagonal manganites - ($RMnO_3$): Class (I) multiferroics with strong coupling of magnetism and ferroelectricity,," *ISRN Condensed Matter Physics*, vol. vol. 2013, no. 497073, 2013.

[184] M. Fiebig, C. Degenhardt, and R. V. Pisarev, "Interaction of frustrated magnetic sublattices in $ErMnO_3$," *Phys. Rev. Lett.*, vol. 88, p. 027203, Dec 2001.

[185] X. Fabrèges, I. Mirebeau, P. Bonville, S. Petit, G. Lebras-Jasmin, A. Forget, G. André, and S. Pailhès, "Magnetic order in $YbMnO_3$ studied by neutron diffraction and mössbauer spectroscopy," *Phys. Rev. B*, vol. 78, p. 214422, Dec 2008.

[186] D. Talbayev, A. D. LaForge, S. A. Trugman, N. Hur, A. J. Taylor, R. D. Averitt, and D. N. Basov, "Magnetic exchange interaction between rare-earth

and mn ions in multiferroic hexagonal manganites," *Phys. Rev. Lett.*, vol. 101, p. 247601, Dec 2008.

[187] S. Nandi, A. Kreyssig, L. Tan, J. W. Kim, J. Q. Yan, J. C. Lang, D. Haskel, R. J. McQueeney, and A. I. Goldman, "Nature of ho magnetism in multiferroic $HoMnO_3$," *Phys. Rev. Lett.*, vol. 100, p. 217201, May 2008.

[188] B. Lorenz, Y. Q. Wang, Y. Y. Sun, and C. W. Chu, "Large magnetodielectric effects in orthorhombic $HoMnO_3$ and $YMnO_3$," *Phys. Rev. B*, vol. 70, p. 212412, Dec 2004.

[189] N. Hur, I. K. Jeong, M. F. Hundley, S. B. Kim, and S.-W. Cheong, "Giant magnetoelectric effect in multiferroic $HoMnO_3$ with a high ferroelectric transition temperature," *Phys. Rev. B*, vol. 79, p. 134120, Apr 2009.

[190] B. Lorenz, A. P. Litvinchuk, M. M. Gospodinov, and C. W. Chu, "Field-induced reentrant novel phase and a ferroelectric-magnetic order coupling in $HoMnO_3$," *Phys. Rev. Lett.*, vol. 92, p. 087204, Feb 2004.

[191] C. dela Cruz, F. Yen, B. Lorenz, Y. Q. Wang, Y. Y. Sun, M. M. Gospodinov, and C. W. Chu, "Strong spin-lattice coupling in multiferroic $HoMnO_3$: Thermal expansion anomalies and pressure effect," *Phys. Rev. B*, vol. 71, p. 060407, Feb 2005.

[192] N. Iwata and K. Kohn, "Dielectric anomalies at magnetic transitions of hexag-

onal rare earth manganese oxides $RMnO_3$," *Journal of the Physical Society of Japan*, vol. 67, no. 9, pp. 3318–3319, 1998.

[193] F. Yen, C. R. dela Cruz, B. Lorenz, Y. Y. Sun, Y. Q. Wang, M. M. Gospodinov, and C. W. Chu, "Low-temperature dielectric anomalies in $HoMnO_3$: The complex phase diagram," *Phys. Rev. B*, vol. 71, p. 180407, May 2005.

[194] H. Sugie, N. Iwata, and K. Kohn, "Magnetic ordering of rare earth ions and magnetic-electric interaction of hexagonal $RMnO_3$ (R=Ho, Er, Yb or Lu)," *Journal of the Physical Society of Japan*, vol. 71, no. 6, pp. 1558–1564, 2002.

[195] M. Fiebig, C. Degenhardt, and R. V. Pisarev, "Magnetic phase diagram of $HoMnO_3$," *Journal of Applied Physics*, vol. 91, no. 10, pp. 8867–8869, 2002.

[196] M. Fiebig, D. Fröhlich, K. Kohn, S. Leute, T. Lottermoser, V. V. Pavlov, and R. V. Pisarev, "Determination of the magnetic symmetry of hexagonal manganites by second harmonic generation," *Phys. Rev. Lett.*, vol. 84, pp. 5620–5623, Jun 2000.

[197] M. Fiebig, T. Lottermoser, and R. V. Pisarev, "Spin-rotation phenomena and magnetic phase diagrams of hexagonal $RMnO_3$," *Journal of Applied Physics*, vol. 93, no. 10, pp. 8194–8196, 2003.

[198] O. P. Vajk, M. Kenzelmann, J. W. Lynn, S. B. Kim, and S.-W. Cheong, "Mag-

netic order and spin dynamics in ferroelectric $HoMnO_3$," *Phys. Rev. Lett.*, vol. 94, p. 087601, Mar 2005.

[199] T. Lonkai, D. Hohlwein, J. Ihringer, and W. Prandl, "The magnetic structures of $YoMnO_{3-\delta}$ and $HoMnO_3$," *Applied Physics A*, vol. 74, no. 1, pp. s843–s845.

[200] A. Munoz, J. A. Alonso, M. J. Martnez-Lope, M. T. Casis, J. L. Martnez, and M. T. Fernndez-Daz, "Evolution of the magnetic structure of hexagonal $HoMnO_3$ from neutron powder diffraction data," *Chemistry of Materials*, vol. 13, no. 5, pp. 1497–1505, 2001.

[201] P. J. Brown and T. Chatterji, "Neutron diffraction and polarimetric study of the magnetic and crystal structures of $HoMnO_3$ and $YMnO_3$," *Journal of Physics: Condensed Matter*, vol. 18, no. 44, p. 10085, 2006.

[202] P. J. Brown and T. Chatterji, "Determination of the magnetic structures of the field-induced phases of $HoMnO_3$," *Phys. Rev. B*, vol. 77, p. 104407, Mar 2008.

[203] S.-W. Cheong and M. Mostovoy, "Multiferroics: a magnetic twist for ferroelectricity," *Nat. Mater.*, vol. 6, pp. 13–20, 2007.

[204] B. B. Van Aken, T. T. M. Palstra, A. Filippetti, and A. Nicola, "The origin of ferroelectricity in magnetoelectric $YMnO_3$," *Nat. Mater.*, vol. 3, pp. 164–170, Feb 2004.

[205] C. J. Fennie and K. M. Rabe, "Ferroelectric transition in $YMnO_3$ from first principles," *Phys. Rev. B*, vol. 72, p. 100103, Sep 2005.

[206] P. Coeure and *et al.*, *Proc. of 1st Intl. Meeting on Ferroelectricity (Institute of Physics, Czech. Acad. Sci., Prague), p. 332*, 1966.

[207] H. Sim, J. Oh, J. Jeong, M. D. Le, and J.-G. Park, "Hexagonal $RMnO_3$: a model system for 2d triangular lattice antiferromagnets," *Acta Cryst.*, vol. B72, pp. 3–19, 2016.

[208] Y. J. Choi, N. Lee, P. A. Sharma, S. B. Kim, O. P. Vajk, J. W. Lynn, Y. S. Oh, and S.-W. Cheong, "Giant magnetic fluctuations at the critical endpoint in insulating $HoMnO_3$," *Phys. Rev. Lett.*, vol. 110, p. 157202, Apr 2013.

[209] I. Munawar and S. H. Curnoe, "Theory of magnetic phases of hexagonal rare earth manganites," *Journal of Physics: Condensed Matter*, vol. 18, no. 42, p. 9575, 2006.

[210] W. Palme, F. Mertens, O. Born, and B. L uthi, "Magnetic resonances of $CsCuCl_3$," *Solid State Commun.*, vol. 76, no. 7, pp. 873–876, 1990.

[211] E. C. Standard, T. Stanislavchuk, A. A. Sirenko, N. Lee, and S.-W. Cheong, "Magnons and crystal-field transitions in hexagonal $RMnO_3$ (R = Er, Tm, Yb, Lu) single crystals," *Phys. Rev. B*, vol. 85, p. 144422, Apr 2012.

[212] B. R. Judd, "The magnetic and spectroscopic properties of certain rare-earth

double nitrates," *Proceedings of the Royal Society of London A: Mathematical, Physical and Engineering Sciences*, vol. 232, no. 1191, pp. 458–474, 1955.

[213] A. Abragam and B. Bleaney, *Electron Paramagnetic Resonance*. Clarendon Press, Oxford, 1970.

[214] R. J. Elliott and K. W. H. Stevens, "The theory of magnetic resonance experiments on salts of the rare earths," *Proceedings of the Royal Society of London A: Mathematical, Physical and Engineering Sciences*, vol. 218, no. 1135, pp. 553–566, 1953.

[215] S. Rosenkranz, A. P. Ramirez, A. Hayashi, R. J. Cava, R. Siddharthan, and B. S. Shastry, "Crystal-field interaction in the pyrochlore magnet $Ho_2Ti_2O_7$," *Journal of Applied Physics*, vol. 87, no. 9, pp. 5914–5916, 2000.

[216] U. Ranon and K. Lee, "Paramagnetic resonance of Ho^{3+} in a trigonal site in SrF_2," *Phys. Rev.*, vol. 188, pp. 539–545, Dec 1969.

[217] M. J. P. Gringras and P. A. McClarty, "Quantum spin ice: a search for gapless quantum spin liquids in pyrochlore magnets," *Rep. Prog. Phys.*, vol. 77, no. 056501, 2014.

[218] I. Ryzhkin, "Magnetic relaxation in rare-earth pyrochlores," *J. Exp. Theor. Phys.*, vol. 101, pp. 841–486, 2005.

[219] C. Castelnovo, R. Moessner, and S. L. Sondhi, "Magnetic monopoles in spin ice," *Nature*, vol. 451, pp. 42–45, 2008.

[220] K. A. Ross, L. Savary, B. D. Gaulin, and L. Balents, "Quantum excitations in quantum spin ice," *Phys. Rev. X.*, vol. 1, no. 021002, 2011.

[221] R. Applegate, N. R. Hayre, R. R. P. Singh, T. Lin, A. G. R. Day, and M. J. P. Gingras, "Vindication of $Yb_2Ti_2O_7$ as a model exchange quantum spin ice," *Phys. Rev. Lett.*, vol. 109, p. 097205, Aug 2012.

[222] J. S. Gardner, M. J. P. Gingras, and J. E. Greedan, "Magnetic pyrochlore oxides," *Rev. Mod. Phys.*, vol. 82, pp. 53–107, Jan 2010.

[223] G. Ehlers, A. L. Cornelius, M. Orendc, M. Kajnakov, T. Fennell, S. T. Bramwell, and J. S. Gardner, "Dynamical crossover in 'hot' spin ice," *Journal of Physics: Condensed Matter*, vol. 15, no. 2, p. L9, 2003.

[224] Y. Wan and O. Tchernyshyov, "Quantum strings in quantum spin ice," *Phys. Rev. Lett.*, vol. 108, p. 247210, Jun 2012.

[225] Z. Hao, A. G. R. Day, and M. J. P. Gingras, "Bosonic many-body theory of quantum spin ice," *Phys. Rev. B*, vol. 90, p. 214430, Dec 2014.

[226] L. Savary and L. Balents, "Spin liquid regimes at nonzero temperature in quantum spin ice," *Phys. Rev. B*, vol. 87, p. 205130, May 2013.

[227] L. Pan, S. K. Kim, A. Ghosh, C. M. Morris, K. A. Ross, E. Kermarrec, B. D. Gaulin, S. M. Koohpayeh, O. Tchernyshyov, and N. P. Armitage, "Low-energy electrodynamics of novel spin excitations in the quantum spin ice $Yb_2Ti_2O_7$," *Nat. Commun.*, vol. 5, no. 4970, 2014.

[228] J. A. Hodges, P. Bonville, A. Forget, M. Rams, K. Krlas, and G. Dhalenne, "The crystal field and exchange interactions in $Yb_2Ti_2O_7$," *Journal of Physics: Condensed Matter*, vol. 13, no. 41, p. 9301, 2001.

[229] B. Z. Malkin, A. R. Zakirov, M. N. Popova, S. A. Klimin, E. P. Chukalina, E. Antic-Fidancev, P. Goldner, P. Aschehoug, and G. Dhalenne, "Optical spectroscopy of $Yb_2Ti_2O_7$ and $Y_2Ti_2O_7$:Yb^{3+} and crystal-field parameters in rare-earth titanate pyrochlores," *Phys. Rev. B*, vol. 70, p. 075112, Aug 2004.

[230] K. A. Ross, J. P. C. Ruff, C. P. Adams, J. S. Gardner, H. A. Dabkowska, Y. Qiu, J. R. D. Copley, and B. D. Gaulin, "Two-dimensional kagome correlations and field induced order in the ferromagnetic *xy* pyrochlore $Yb_2Ti_2O_7$," *Phys. Rev. Lett.*, vol. 103, p. 227202, Nov 2009.

[231] J. D. Thompson, P. A. McClarty, H. M. Rønnow, L. P. Regnault, A. Sorge, and M. J. P. Gingras, "Rods of neutron scattering intensity in $Yb_2Ti_2O_7$: Compelling evidence for significant anisotropic exchange in a magnetic pyrochlore oxide," *Phys. Rev. Lett.*, vol. 106, p. 187202, May 2011.

[232] K. A. Ross, L. R. Yaraskavitch, M. Laver, J. S. Gardner, J. A. Quilliam,

S. Meng, J. B. Kycia, D. K. Singh, T. Proffen, H. A. Dabkowska, and B. D. Gaulin, "Dimensional evolution of spin correlations in the magnetic pyrochlore $Yb_2Ti_2O_7$," *Phys. Rev. B*, vol. 84, p. 174442, Nov 2011.

[233] L.-J. Chang, S. Onoda, Y. Su, Y.-J. Kao, K.-D. Tsuei, Y. Yasui, K. Kazuhisa, and M. R. Lees, "Higgs transition from a magnetic coulomb liquid to a ferromagnet in $Yb_2Ti_2O_7$," *nat. Commun.*, vol. 3, no. 992, 2012.

[234] K. A. Ross, T. Proffen, H. A. Dabkowska, J. A. Quilliam, L. R. Yaraskavitch, J. B. Kycia, and B. D. Gaulin, "Lightly stuffed pyrochlore structure of single-crystalline $Yb_2Ti_2O_7$ grown by the optical floating zone technique," *Phys. Rev. B*, vol. 86, p. 174424, Nov 2012.

[235] N. R. Hayre, K. A. Ross, R. Applegate, T. Lin, R. R. P. Singh, B. D. Gaulin, and M. J. P. Gingras, "Thermodynamic properties of $Yb_2Ti_2O_7$ pyrochlore as a function of temperature and magnetic field: Validation of a quantum spin ice exchange hamiltonian," *Phys. Rev. B*, vol. 87, p. 184423, May 2013.

[236] I. Ryzhkin and W. R.W., "The configurational entropy in the Jaccard theory of the electrical properties of ice," *J. Phys: Condens. Matter*, vol. 9, no. 395, 1997.

[237] P. C. Hohenberg and W. F. Brinkman, "Sum rules for the frequency spectrum of linear magnetic chains," *Phys. Rev. B*, vol. 10, pp. 128–131, Jul 1974.

[238] I. A. Zaliznyak and S.-H. Lee, *Magnetic Neutron Scattering in Modern Techniques for Characterizing Magnetic Materials*. Springer, 2005.

[239] Y. Onodera, "Breakdown of debye's model for dielectric relaxation in high frequencies," *J. Phys. Soc. Jpn.*, vol. 62, pp. 4104–4107, 1993.

[240] D. J. Scalapino, S. R. White, and S. Zhang, "Insulator, metal, or superconductor: The criteria," *Phys. Rev. B*, vol. 47, pp. 7995–8007, Apr 1993.

[241] J. V. Alvarez and C. Gros, "Conductivity of quantum spin chains: A quantum monte carlo approach," *Phys. Rev. B*, vol. 66, p. 094403, Sep 2002.

[242] M. T. Vandenborre, E. Husson, J. P. Chatry, and D. Michel, "Rare-earth titanates and stannates of pyrochlore structure; vibrational spectra and force fields," *Journal of Raman Spectroscopy*, vol. 14, no. 2, pp. 63–71, 1983. [Online]. Available: http://dx.doi.org/10.1002/jrs.1250140202

[243] L. Bovo, J. A. Bloxsom, D. Prabhakaran, G. Aeppli, and S. T. Bramwell, "Brownian motion and quantum dynamics of magnetic monopoles in spin ice," *Nat. Commun.*, vol. 4, no. 1535, 2013.

[244] J. S. Gardner, G. Ehlers, N. Rosov, R. W. Erwin, and C. Petrovic, "Spin-spin correlations in $Yb_2Ti_2O_7$: A polarized neutron scattering study," *Phys. Rev. B*, vol. 70, p. 180404, Nov 2004.

[245] L. Fu, C. L. Kane, and E. J. Mele, "Topological insulators in three dimensions," *Phys. Rev. Lett.*, vol. 98, p. 106803, Mar 2007.

[246] M. Z. Hasan and C. L. Kane, "*Colloquium* : Topological insulators," *Rev. Mod. Phys.*, vol. 82, pp. 3045–3067, Nov 2010.

[247] J. E. Moore and L. Balents, "Topological invariants of time-reversal-invariant band structures," *Phys. Rev. B*, vol. 75, p. 121306, Mar 2007.

[248] X.-L. Qi and S.-C. Zhang, "Topological insulators and superconductors," *Rev. Mod. Phys.*, vol. 83, pp. 1057–1110, Oct 2011.

[249] R. Roy, "Topological phases and the quantum spin hall effect in three dimensions," *Phys. Rev. B*, vol. 79, p. 195322, May 2009.

[250] L. Fu, "Topological crystalline insulators," *Phys. Rev. Lett.*, vol. 106, p. 106802, Mar 2011.

[251] D. Hsieh, D. Qian, L. Wray, Y. S. Hor, R. J. Cava, and M. Z. Hasan, "A topological dirac insulator in a quantum spin hall phase," *Nature*, vol. 452, pp. 970–974, 2008.

[252] H. Zhang, C.-X. Liu, X.-L. Qi, X. Dai, Z. Fang, and S.-C. Zhang, "Topological insulators in Bi_2Se_3, Bi_2Te_3, and Sb_2Te_3 with a single dirac cone on the surface," *Nature Phys.*, vol. 5, pp. 438–442, 2009.

[253] T. Zhang, P. Cheng, X. Chen, J.-F. Jia, X. Ma, K. He, L. Wang, H. Zhang, X. Dai, Z. Fang, X. Xie, and Q.-K. Xue, "Experimental demonstration of topological surface states protected by time-reversal symmetry," *Phys. Rev. Lett.*, vol. 103, p. 266803, Dec 2009.

[254] Y. Okada, C. Dhital, W. Zhou, E. D. Huemiller, H. Lin, S. Basak, A. Bansil, Y.-B. Huang, H. Ding, Z. Wang, S. D. Wilson, and V. Madhavan, "Direct observation of broken time-reversal symmetry on the surface of a magnetically doped topological insulator," *Phys. Rev. Lett.*, vol. 106, p. 206805, May 2011.

[255] R. Valdés Aguilar, A. V. Stier, W. Liu, L. S. Bilbro, D. K. George, N. Bansal, L. Wu, J. Cerne, A. G. Markelz, S. Oh, and N. P. Armitage, "Terahertz response and colossal kerr rotation from the surface states of the topological insulator Bi_2Se_3," *Phys. Rev. Lett.*, vol. 108, p. 087403, Feb 2012.

[256] C. M. Varma, "Mixed-valence compounds," *Rev. Mod. Phys.*, vol. 48, pp. 219–238, Apr 1976.

[257] M. Dzero, K. Sun, V. Galitski, and P. Coleman, "Topological Kondo insulators," *Phys. Rev. Lett.*, vol. 104, p. 106408, Mar 2010.

[258] T. Takimoto, "SmB_6: A promising candidate for a topological insulator," *Journal of the Physical Society of Japan*, vol. 80, no. 12, p. 123710, 2011.

[259] M. Dzero, K. Sun, P. Coleman, and V. Galitski, "Theory of topological Kondo insulators," *Phys. Rev. B*, vol. 85, p. 045130, Jan 2012.

[260] F. Lu, J. Zhao, H. Weng, Z. Fang, and X. Dai, "Correlated topological insulators with mixed valence," *Phys. Rev. Lett.*, vol. 110, p. 096401, Feb 2013.

[261] V. Alexandrov, M. Dzero, and P. Coleman, "Cubic topological Kondo insulators," *Phys. Rev. Lett.*, vol. 111, p. 226403, Nov 2013.

[262] B. Coqblin and A. Blandin, "Stabilit des moments magntiques localiss dans les mtaux," *Advances in Physics*, vol. 17, no. 67, pp. 281–366, 1968.

[263] N. F. Mott, "Rare-earth compounds with mixed valencies," *Philosophical Magazine*, vol. 30, no. 2, pp. 403–416, 1974.

[264] A. Menth, E. Buehler, and T. H. Geballe, "Magnetic and semiconducting properties of SmB_6," *Phys. Rev. Lett.*, vol. 22, pp. 295–297, Feb 1969.

[265] J. C. Nickerson, R. M. White, K. N. Lee, R. Bachmann, T. H. Geballe, and G. W. Hull, "Physical properties of smb_6," *Phys. Rev. B*, vol. 3, pp. 2030–2042, Mar 1971.

[266] A. Kebede, M. Aronson, C. Buford, P. Canfield, J. H. Cho, B. Coles, J. Cooley, J. Coulter, Z. Fisk, J. Goettee, W. Hults, A. Lacerda, T. McLendon, P. Tiwari, and J. Smith, "Proceedings of the international conference on strongly corre-

lated electron systems studies of the correlated electron system SmB_6," *Physica B: Condensed Matter*, vol. 223, pp. 256 – 259, 1996.

[267] S. Gabáni, K. Flachbart, E. Konovalova, M. Orendáč, Y. Paderno, V. Pavlík, and J. Šebek, "Properties of the in-gap states in SmB_6," *Solid State Communications*, vol. 117, no. 11, pp. 641 – 644, 2001.

[268] D. J. Kim, S. Thomas, T. Grant, J. Botimer, Z. Fisk, and J. Xia, "Surface hall effect and nonlocal transport in SmB_6: Evidence for surface conduction," *Scientific Reports*, vol. 3, no. 3150, 2013.

[269] D. J. Kim, J. Xia, and Z. Fisk, "Topological surface state in the Kondo insulator samarium hexaboride," *Nature Materials*, vol. 13, pp. 466–470, 2014.

[270] S. Wolgast, C. Kurdak, K. Sun, J. W. Allen, D.-J. Kim, and Z. Fisk, "Low-temperature surface conduction in the Kondo insulator SmB_6," *Phys. Rev. B*, vol. 88, p. 180405, Nov 2013.

[271] F. Chen, C. Shang, Z. Jin, D. Zhao, Y. P. Wu, Z. J. Xiang, Z. C. Xia, A. F. Wang, X. G. Luo, T. Wu, and X. H. Chen, "Magnetoresistance evidence of a surface state and a field-dependent insulating state in the Kondo insulator SmB_6," *Phys. Rev. B*, vol. 91, p. 205133, May 2015.

[272] X. Zhang, N. P. Butch, P. Syers, S. Ziemak, R. L. Greene, and J. Paglione,

"Hybridization, inter-ion correlation, and surface states in the Kondo insulator SmB_6," *Phys. Rev. X*, vol. 3, p. 011011, Feb 2013.

[273] M. M. Yee, Y. He, A. Soumyanarayanan, D.-J. Kim, Z. Fisk, and J. E. Hoffman, "Imaging the Kondo insulating gap of SmB_6," *arXiv:1308.1085*, 2013.

[274] G. Li, Z. Xiang, F. Yu, T. Asaba, B. Lawson, P. Cai, C. Tinsman, A. Berkley, S. Wolgast, Y. S. Eo, D.-J. Kim, C. Kurdak, J. W. Allen, K. Sun, X. H. Chen, Y. Y. Wang, Z. Fisk, and L. Li, "Two-dimensional fermi surfaces in Kondo insulator SmB_6," *Science*, vol. 346, no. 6214, pp. 1208–1212, 2014.

[275] M. Neupane, N. Alidoust, S.-Y. Xu, T. Kondo, Y. Ishida, D. J. Kim, C. Liu, I. Belopolski, Y. J. Jo, T.-R. Chang, H.-T. Jeng, T. Durakiewicz, L. Balicas, H. Lin, A. Bansil, S. Shin, Z. Fisk, and M. Z. Hasan, "Surface electronic structure of the topological Kondo-insulator candidate correlated electron system SmB_6," *Nature Comm.*, vol. 4, no. 2991, 2013.

[276] H. Miyazaki, T. Hajiri, T. Ito, S. Kunii, and S.-i. Kimura, "Momentum-dependent hybridization gap and dispersive in-gap state of the Kondo semiconductor SmB_6," *Phys. Rev. B*, vol. 86, p. 075105, Aug 2012.

[277] Z. Xu, P. K. Biswas, J. H. Dil, D. R. S., G. Landolt, S. Muff, C. E. Matt, X. Shi, N. C. Plumb, M. Radovic, E. Pomjakushina, K. Conder, A. Amato, B. S. V., R. Yu, H.-M. Weng, Z. Fang, X. Dai, J. Mesot, H. Ding, and M. Shi, "Direct

observation of the spin texture in SmB_6 as evidence of the topological kondo insulator," *Nature Comm.*, vol. 5, no. 4566, 2014.

[278] J. Jiang, S. Li, T. Zhang, Z. Sun, F. Chen, Z. R. Ye, M. Xu, Q. Q. Ge, S. Y. Tan, X. H. Niu, M. Xia, B. P. Xie, Y. Li, X. H. Chen, H. H. Wen, and D. L. Feng, "Obersvation of possible topological in-gap sufrace states in the Kondo insulator SmB_6 by photoemission," *Nature. Comm.*, vol. 4, no. 3010, 2013.

[279] E. Frantzeskakis, N. de Jong, B. Zwartsenberg, Y. K. Huang, Y. Pan, X. Zhang, J. X. Zhang, F. X. Zhang, L. H. Bao, O. Tegus, A. Varykhalov, A. de Visser, and M. S. Golden, "Kondo hybridization and the origin of metallic states at the (001) surface of SmB_6," *Phys. Rev. X*, vol. 3, p. 041024, Dec 2013.

[280] W. T. Fuhrman, J. Leiner, P. Nikolić, G. E. Granroth, M. B. Stone, M. D. Lumsden, L. DeBeer-Schmitt, P. A. Alekseev, J.-M. Mignot, S. M. Koohpayeh, P. Cottingham, W. A. Phelan, L. Schoop, T. M. McQueen, and C. Broholm, "Interaction driven subgap spin exciton in the Kondo insulator SmB_6," *Phys. Rev. Lett.*, vol. 114, p. 036401, Jan 2015.

[281] S. von Molnar, F. Holtzberg, A. Benoit, A. Briggs, J. Floquet, and J. L. Tholence, *Valence Instabilities*, P. Wachter and H. Boppart, Eds. Amsterdam: North-Holland, 1982.

[282] G. Travaglini and P. Wachter, "Intermediate-valent SmB_6 and the hybridization model: An optical study," *Phys. Rev. B*, vol. 29, pp. 893–898, Jan 1984.

[283] C. M. Jackson, G. Grüner, Z. Fisk, and S. von Molnar, "Microwave conductivity of SmB_6," *Phys. Rev. B*, vol. 29, pp. 4786–4788, Apr 1984.

[284] S.-I. Kimura, T. Nanba, S. Kunii, and T. Kasuya, "Low-energy optical excitation in rare-earth hexaborides," *Phys. Rev. B*, vol. 50, pp. 1406–1414, Jul 1994.

[285] T. Nanba, H. Ohta, M. Motokawa, S. Kimura, S. Kunii, and T. Kasuya, "Gap state of SmB_6," *Physica B: Condensed Matter*, vol. 186, pp. 440 – 443, 1993.

[286] B. Gorshunov, N. Sluchanko, A. Volkov, M. Dressel, G. Knebel, A. Loidl, and S. Kunii, "Low-energy electrodynamics of SmB_6," *Phys. Rev. B*, vol. 59, pp. 1808–1814, Jan 1999.

[287] L. Wu, M. Brahlek, R. V. Aguilar, A. V. Stier, C. M. Morris, Y. Lubashevsky, L. S. Bilbro, N. Bansal, S. Oh, and N. P. Armitage, "A sudden collapse in the transport lifetime across the topological phase transition in $(bi_{1-x}in_x)_2se_3$," *Nature Phys.*, vol. 9, pp. 410–414, 2013.

[288] N. Wakeham, P. F. S. Rosa, Y. Q. Wang, M. Kang, Z. Fisk, F. Ronning, and J. D. Thompson, "Low-temperature conducting state in two candidate topological Kondo insulators: SmB_6 and $Ce_3Bi_4Pt_3$," *Phys. Rev. B*, vol. 94, p. 035127, Jul 2016.

[289] K. Flachbart, S. Gabni, K. Neumaier, Y. Paderno, V. Pavlk, E. Schuberth, and

N. Shitsevalova, "Specific heat of SmB_6 at very low temperatures," *Physica B: Condensed Matter*, vol. 378380, pp. 610 – 611, 2006.

[290] W. A. Phelan, S. M. Koohpayeh, P. Cottingham, J. W. Freeland, J. C. Leiner, C. L. Broholm, and T. M. McQueen, "Correlation between bulk thermodynamic measurements and the low-temperature-resistance plateau in smb_6," *Phys. Rev. X*, vol. 4, p. 031012, Jul 2014.

[291] W. A. Phelan, S. M. Koohpayeh, P. Cottingham, J. A. Tutmaher, J. C. Leiner, M. D. Lumsden, C. M. Lavelle, X. P. Wang, C. Hoffman, M. A. Siegler, N. Haldolaarachchige, D. P. Young, and T. M. McQueen, "On the chemistry and physical properties of flux and floating zone grown SmB_6 single crystals," *Scientific Reports*, vol. 6, 2016.

[292] M. E. Valentine, S. Koohpayeh, W. A. Phelan, T. M. McQueen, P. F. S. Rosa, Z. Fisk, and N. Drichko, "Breakdown of the Kondo insulating state in SmB_6 by introducing sm vacancies," *Phys. Rev. B*, vol. 94, p. 075102, Aug 2016.

[293] H. Ohta, R. Tanaka, M. Motokawa, S. Kunii, and T. Kasuya, "Far-infrared transmission spectra of SmB_6," *Journal of the Physical Society of Japan*, vol. 60, no. 4, pp. 1361–1364, 1991.

[294] P. A. Alekseev, V. N. Lazukov, R. Osborn, B. D. Rainford, I. P. Sadikov, E. S. Konovalova, and Y. B. Paderno, "Neutron scattering study of the intermediate-

valent ground state in SmB_6," *EPL Europhysics Letters*, vol. 23, no. 5, p. 347, 1993.

[295] P. A. Aleskeev, J. M. Mignot, J. Rossat-Mignod, V. N. Lazukov, and I. P. Sadikov, "Magnetic excitations in SmB_6 single crystals," *Physica B Condensed Matter*, vol. 186, pp. 384–386, may 1993.

[296] J.-M. Mignot, P. Alekseev, J. Rossat-Mignod, V. Lazukov, and I. Sadikov, "Local singlet bound state and magnetic excitations in mixed-valence SmB_6," *Physica B: Condensed Matter*, vol. 199, pp. 430 – 432, 1994.

[297] P. A. Alekseev, J. M. Mignot, J. Rossat-Mignod, V. N. Lazukov, I. P. Sadikov, E. S. Konovalova, and Y. B. Paderno, "Magnetic excitation spectrum of mixed-valence SmB_6 studied by neutron scattering on a single crystal," *Journal of Physics: Condensed Matter*, vol. 7, no. 2, p. 289, 1995.

[298] W. T. Fuhrman and P. Nikolić, "In-gap collective mode spectrum of the topological Kondo insulator SmB_6," *Phys. Rev. B*, vol. 90, p. 195144, Nov 2014.

[299] Private Communication with W. Fuhrman.

[300] G. A. Kapilevich, P. S. Riseborough, A. X. Gray, M. Gulacsi, T. Durakiewicz, and J. L. Smith, "Incomplete protection of the surface Weyl cones of the Kondo insulator SmB_6: Spin exciton scattering," *Phys. Rev. B*, vol. 92, p. 085133, Aug 2015.

[301] W. K. Park, L. Sun, A. Noddings, D.-J. Kim, Z. Fisk, and L. H. Greene, "Topological surface states interacting with bulk excitations in the Kondo insulator SmB_6 revealed via planar tunneling spectroscopy," vol. 113, no. 24, pp. 6599–6604, 2016.

[302] H.-Y. Kee, S. A. Kivelson, and G. Aeppli, "Spin˘1 neutron resonance peak cannot account for electronic anomalies in the cuprate superconductors," *Phys. Rev. Lett.*, vol. 88, p. 257002, Jun 2002.

[303] R. Sollie and P. Schlottmann, "Local density of states in the vicinity of a Kondo hole," *Journal of Applied Physics*, vol. 70, no. 10, pp. 5803–5805, 1991.

[304] P. Schlottmann, "Impurity bands in Kondo insulators," *Phys. Rev. B*, vol. 46, pp. 998–1004, Jul 1992.

[305] P. Schlottmann, "Influence of a Kondo-hole impurity band on magnetic instabilities in Kondo insulators," *Phys. Rev. B*, vol. 54, pp. 12 324–12 331, Nov 1996.

[306] P. S. Riseborough, "Collapse of the coherence gap in Kondo semiconductors," *Phys. Rev. B*, vol. 68, p. 235213, Dec 2003.

[307] E. Helgren, N. P. Armitage, and G. Grüner, "Frequency-dependent conductivity of electron glasses," *Phys. Rev. B*, vol. 69, p. 014201, Jan 2004.

[308] N. F. Mott, "Conduction in glasses containing transition metal ions," *Journal of Non-Crystalline Solids*, vol. 1, no. 1, pp. 1–17, 1968.

[309] B. I. Shklovskiĭ and A. L. Éfros, "Zero-phonon ac hopping conductivity of disordered systems," *Eksp. Toer. Fiz.*, vol. 81, pp. 406–415, 1981.

[310] N. F. Mott and E. A. Davis, *Electronis Processes in Non-Crytalline Materials*. Oxford: Oxford University Press, 1979.

[311] N. Kobayashi, S. Ikehata, S. Kobayashi, and W. Sasaki, "Specific heat study of heavily P doped Si," *Solid State Communications*, vol. 24, no. 1, pp. 67–70, 1977.

[312] S. Wagner, M. Lakner, and H. v. Löhneysen, "Specific heat of Si:(P, B) at low temperatures," *Physical Review B*, vol. 55, no. 7, p. 4219, 1997.

[313] D. Mael, S. Yoshizumi, and T. H. Geballe, "Specific heat of amorphous Mo_xGe_{1-x} through the metal-insulator transition," *Phys. Rev. B*, vol. 34, pp. 467–470, Jul 1986.

[314] A. Y. Rogatchev and U. Mizutani, "Hopping conductivity and specific heat in insulating amorphous Ti_xSi_{100-x} alloys," *Physical Review B*, vol. 61, no. 23, p. 15550, 2000.

[315] E. Helgren, G. Grüner, M. R. Ciofalo, D. V. Baxter, and J. P. Carini, "Mea-

surements of the complex conductivity of Nb_xSi_{1-x} alloys on the insulating side of the metal-insulator transition," *Phys. Rev. Lett.*, vol. 87, p. 116602, 2001.

[316] J. Cooley, M. Aronson, Z. Fisk, and P. Canfield, "SmB_6: Kondo insulator or exotic metal?" *Physical review letters*, vol. 74, no. 9, p. 1629, 1995.

[317] P. Coleman, E. Miranda, and A. Tsvelik, "Are Kondo insulators gapless?" *Physica B: Condensed Matter*, vol. 186, pp. 362 – 364, 1993.

[318] G. Baskaran, "Majorana fermi sea in insulating SmB_6: A proposal and a theory of quantum oscillations in Kondo insulators," *arXiv:1507.03477*, 2015.

[319] T.-K. Ng and P. A. Lee, "Power-law conductivity inside the Mott gap: Application to κ-$(BEDT\text{-}TTF)_2cu_2(CN)_3$," *Phys. Rev. Lett.*, vol. 99, p. 156402, Oct 2007.

[320] S. Curnoe and K. A. Kikoin, "4electron self-trapping in intermediate-valent SmB_6," *Phys. Rev. B*, vol. 61, pp. 15 714–15 725, Jun 2000.

[321] B. S. Tan, Y.-T. Hsu, B. Zeng, M. C. Hatnean, N. Harrison, Z. Zhu, M. Hartstein, M. Kiourlappou, A. Srivastava, M. D. Johannes, T. P. Murphy, J.-H. Park, L. Balicas, G. G. Lonzarich, G. Balakrishnan, and S. E. Sebastian, "Unconventional fermi surface in an insulating state," *Science*, vol. 349, no. 6245, pp. 287–290, 2015.

[322] J. Zhang, J. Yong, I. Takeuchi, R. L. Greene, and R. D. Averitt, "Ultrafast

terahertz spectroscopy study of Kondo insulating thin film SmB_6: evidence for an emergent surface state," *arXiv:1509.04688*, 2015.

[323] S. Wolgast, Y. S. Eo, C. Kurdak, D. J. Kim, and Z. Fisk, "Conduction through subsurface cracks in bulk topological insulators," *arXiv:1506.08233ArXiv*, 2015.

[324] Private Communication with C. Kurdak.

[325] M. Leijnse and K. Flensberg, "Introduction to topological superconductivity and majorana fermions," *Semiconductor Science and Technology*, vol. 27, no. 12, p. 124003, 2012.

[326] A. Y. Kitaev, "Unpaired majorana fermions in quantum wires," *Physics-Uspekhi*, vol. 44, no. 10S, p. 131, 2001.

[327] S. Sasaki, M. Kriener, K. Segawa, K. Yada, Y. Tanaka, M. Sato, and Y. Ando, "Topological superconductivity in $Cu_xBi_2Se_3$," *Phys. Rev. Lett.*, vol. 107, p. 217001, Nov 2011.

[328] V. Mourik, K. Zuo, S. M. Frolov, S. R. Plissard, E. P. A. M. Bakkers, and L. P. Kouwenhoven, "Signatures of majorana fermions in hybrid superconductor-semiconductor nanowire devices," *Science*, vol. 336, no. 6084, pp. 1003–1007, 2012.

[329] L. Fu, "Parity-breaking phases of spin-orbit-coupled metals with gyrotropic,

ferroelectric, and multipolar orders," *Phys. Rev. Lett.*, vol. 115, p. 026401, Jul 2015.

Vita

Nicholas J. Laurita was born in Oceanside, NY and raised in Lakeland, FL. He attended the University of South Florida, receiving a B.Sc. degree in Applied Physics in 2011, graduating *summa cum laude*. In 2011, he enrolled in the physics Ph.D. program at Johns Hopkins University where his research focused on examining the low energy electrodynamics of quantum magnets. While a graduate student at JHU, he was awarded an Owen fellowship, received the Rowland prize for innovation and excellence in teaching, and received two Achievement Rewards for College Scientists scholarships. He has published multiple papers in peer-reviewed journals, including: Nature Physics, Physical Review Letters, and Physical Review B. Beginning in summer of 2017, Nick will be joining the Institute of Quantum Information and Matter at the California Institute of Technology as an Institute of Quantum Information and Matter Postdoctoral Fellowship recipient.